Measurement of dijet production in neutral current deep inelastic scattering at high Q^2 and determination of α_s at HERA

by

Enrico Tassi

Measurement of dijet production in neutral current deep inelastic scattering at high Q^2 and determination of α_s at HERA

DISSERTATION

zur Erlangung des Doktorgrades
des Fachbereichs Physik
der Universität Hamburg

vorgelegt von

Enrico Tassi
aus Rom

Hamburg
2001

Abstract

Dijet production has been studied in neutral current deep inelastic e^+p scattering for $470 < Q^2 < 20000$ GeV^2 with the ZEUS detector at HERA using an integrated luminosity of 38.4 pb^{-1}. Dijet differential cross sections are presented in a kinematic region where both theoretical and experimental uncertainties are small. Next-to-leading-order (NLO) QCD calculations describe the measured differential cross sections well. A QCD analysis of the measured dijet fraction as a function of Q^2 allows both a precise determination of $\alpha_s(M_Z)$ and a test of the energy-scale dependence of the strong coupling constant. A detailed analysis provides an improved estimate of the uncertainties of the NLO QCD cross sections arising from the parton distribution functions of the proton. The value of $\alpha_s(M_Z)$, as determined from the QCD fit, is $\alpha_s(M_Z) = 0.1166 \pm 0.0019$ (stat.)$^{+0.0024}_{-0.0033}$ (exp.)$^{+0.0057}_{-0.0044}$ (th.).

Zusammenfassung

Die Erzeugung von Zwei-Jet-Ereignissen wurde in tiefunelastischer e^+p Streuung fuer $470 < Q^2 < 20000$ GeV^2 mit dem ZEUS Detektor bei HERA untersucht. Dafür wurden Ereignisse des neutralen Stroms mit einer integrierten Luminosität von 38.4 pb^{-1} verwendet. Die differentielle Wirkungsquerschnitte der Zweit-Jet-Produktion wurden in einem kinematischen Bereich untersucht, in dem sowohl theoretische als auch experimentelle Unsicherheiten gering sind. Die gemessenen differentiellen Wirkungsquerschnitte konnten gut durch Next-to-leading-order (NLO) QCD-Berechnungen beschrieben werden. Eine QCD-Analyse der gemessenen Rate von Zweit-Jet-Ereignissen als Funktion von Q^2 erlaubte sowohl eine genaue Bestimmung der Kopplungskonstanten $\alpha_s(M_Z)$ der starken Wechselwirkung, als auch einen Test ihrer Abhängigkeit von der Energieskala. Die Unsicherheiten der Vorhersagen der NLO QCD-Berechnungen für die untersuchten Wirkungsquerschnitte sind durch die Verteilungsfunktionen der Partonen im Proton bedingt. Diese detailierte Analyse erlaubt eine verbesserte Abschätzung dieser Unsicherheiten. $\alpha_s(M_Z)$ wurde mit Hilfe der QCD-Analyse zu $\alpha_s(M_Z) = 0.1166 \pm 0.0019$ (stat.)$^{+0.0024}_{-0.0033}$ (exp.)$^{+0.0057}_{-0.0044}$ (th.) bestimmt.

A Juan Terrón

Contents

List of Figures

iv

List of Tables

Chapter 1

Introduction

Experimental studies of Quantum Chromodynamics (QCD) in the high-energy regime have now left the phase of crude testing of QCD, and have stepped into the phase of rather accurate measurements. Results obtained in the last few years at the LEP, TEVATRON, and HERA colliders have overall strengthened our belief that QCD is indeed the best candidate for a theory of the strong interactions.

A priori, the strong coupling constant is the only parameter relevant to the high-energy regime of QCD that needs to be determined, as, in principle, everything else can be calculated from first principles. The strong coupling is one of the fundamental 'constants' of nature, and, as such, there is no limit to the accuracy with which we would like to know its value. Beside setting the overall precision of any fixed-order perturbative QCD (pQCD) calculation, an accurate knowledge of α_s is, for example, necessary to extract electroweak parameters from precise e^+e^- data, as well as to explore scenarios in which all forces of nature are unified at some large energy scale. Upon closer scrutiny, one quickly realises that this ideal situation is far from reality. Since the observable final states are made out of hadrons, and not of quarks and gluons, understanding of the interface between perturbative (hard) and non-perturbative (soft) QCD cannot be escaped even when we consider high-energy processes. This is particularly true for colliders where at least one of the initial interacting particles is a proton. As a result, ancillary information such as parton densities in the proton and Monte Carlo hadronisation models, is needed for all practical cases.

The vast physics program being presently carried out at the electron-proton collider HERA is playing a major role in the above mentioned activity of testing of QCD, as well as in revealing new information on the structure of the proton. Very precise measurements of the neutral current inclusive e^+p and e^-p cross sections, performed by the H1 and ZEUS collaborations, have enormously improved our knowledge of the partonic structure of the proton, resulting in such an important discovery as the steep rise of the sea and gluon densities in the proton at low values of the x-Bjorken (x_{Bj}) variable. The interpretation of these measurements at the lowest attainable values of x_{Bj} and Q^2 ($x_{Bj} \sim 10^{-7}$ for $Q^2 \sim 0.05$ GeV^2), where Q^2 is the virtuality of the exchanged boson, presently challenges our understanding of QCD. On the other hand, pQCD analyses of these very precise data, when restricted to phase-space regions characterized by not too small values of Q^2 and x_{Bj} are now beginning to allow the simultaneous determination of the parton densities in the proton and of the strong coupling constant with significant precision.

In addition to this considerable progress achieved in the measurements of the inclusive cross sections and their interpretation within the framework of pQCD, the last couple of years have also witnessed a remarkable progress in the description of more exclusive observables, namely multi-jet cross sections in neutral current (NC) deep inelastic scatering (DIS) at HERA. These observables are perfectly suited to test the dynamics of the underlying QCD hard processes and, due to their *direct* sensitivity to α_s and (in the low x_{Bj} region) the gluon density in the proton,

to provide complementary information on the strong coupling and the gluon density.

This dissertation presents a study of dijet production in NC DIS at HERA at high Q^2 and a determination of the strong coupling constant α_s. Measurements of the differential cross sections for dijet production are presented and compared with next-to-leading-order (NLO) pQCD predictions, after correcting the latter for hadronisation effects. The phase-space region is restricted to high-Q^2 values, $470 < Q^2 < 20000$ GeV^2. In this region, the experimental uncertainties in the reconstruction of both the scattered positron and the hadronic final state are smaller than at lower Q^2. In addition, the theoretical uncertainties due to the modelling of the hadronic final state, to the parton distribution functions (PDFs) of the proton, and to the higher-order contributions are minimised.

The comparison of the differential cross sections with the NLO calculations has allowed the test of the description of dijet production by the underlying QCD hard processes. A QCD analysis has been performed that takes fully into account the correlation between the value of $\alpha_s(M_Z)$ used in the determination of the proton PDFs and that used in the calculation of the partonic cross sections. Furthermore, a detailed study of the uncertainties in the theoretical predictions has been carried out which includes the statistical and correlated systematic uncertainties from the data sets used in the determination of the proton PDFs. The QCD analysis results into a precise determination of $\alpha_s(M_Z)$ as well as a study of the energy-scale dependence of the strong coupling constant[1].

<div align="center">*****</div>

This dissertation is organised as follows:

The next chapter gives a short description of the basic calculational framework of pQCD. The important concepts of renormalised strong coupling constant, parton distribution functions of the proton, infrared (IR) singularities and IR-safe observables, as well as the subleties present in the calculation of NLO jet cross sections are discussed there. The chapter also contains a short review of the recent most precise determinations of the strong coupling constant.

The third chapter describes the calculation of all the NLO predictions used in the comparison with the measured inclusive and dijet cross sections. Particular emphasis is placed on an accurate evaluation of theoretical uncertainties and a phase-space region is selected in order to minimise them. In particular, a novel result is represented by one of the first attempts to fully quantify the uncertainties of the NLO jet cross sections arising from the uncertainties in the parton distribution functions of the proton.

A short description of the HERA collider and the ZEUS detector is presented in chapter 4.

In chapter 5 we give a complete description of the measurement of the inclusive and dijet differential cross sections and their associated uncertainties. Starting from the selection of the event samples, the quality of the reconstruction of the kinematic and jet variables and the unfolding procedure are discussed, followed by a detailed study of the main sources of systematic uncertainty.

Chapter 6 presents the final results on the measured cross sections and the comparison with the QCD predictions. In this chapter we also describe the QCD analysis performed in order to determine the strong coupling constant, which is determined both at the reference scale provided by Z^0 boson mass and as a function of Q.

The last chapter summarise the results obtained and ends this thesis with an outlook.

Chapter 2

Theoretical framework

In this chapter we introduce the concepts of renormalized strong coupling constant and parton densities functions of the proton and give an overview of the general structure of DIS cross sections in pQCD. Emphasis is placed on the description of a general algorithm which has been developed in order to overcome the complex pattern of infrared (soft and collinear) singularities encountered in the calculation of NLO pQCD jet cross sections. The chapter ends with a short review of the recent most precise determinations of the strong coupling constant.

2.1 The strong coupling constant

2.1.1 QCD and asymptotic freedom

Quantum Chromodynamics, the non-Abelian gauge field theory which describes the interactions of coloured quarks and gluons, emerged as viable theory of the strong interaction in the 1970s as the result of the assembling of many theoretical ideas and experimental results. It is nowadays regarded as one of the cornerstones of the Standard Model of elementary particles and their interactions.

The most fundamental tenet of QCD is that hadrons are color-singlet bound states of quarks, anti-quarks and gluons. A quark of specific flavor (such as a charm quark) comes in three colors; gluons, the spin-one gauge bosons carriers of the colour interaction, come in eight colours.

The Lagrangian density of QCD is of a Yang-Mills type and is given (up to gauge-fixing terms) by:

$$L_{QCD} = -\frac{1}{4}F_{\mu\nu}^{(a)}F^{(a)\mu\nu} + \sum_q \overline{\psi}_q^i \left(i\slashed{D}_{ij} - m_q\right)\psi_q^j, \tag{2.1}$$

where

$$F_{\mu\nu}^a = \partial_\mu A_\nu^a - \partial_\nu A_\mu^a + g_s f^{abc} A_\mu^b A_\nu^c \tag{2.2}$$

is the gluon field strength tensor,

$$(D_\mu)_{ij} = \delta_{ij}\partial_\mu - ig_s A_\mu^a T_{ij}^a \tag{2.3}$$

is the gauge covariant derivative, T^a are the $SU(3)$ representation matrices (normalized so that $\text{tr}\,(T^a T^b) = \delta^{ab}/2$), and the f^{abc} are the structure constants of SU(3) defining its associated algebra. The $\psi_q^i(x)$ are the 4-component dirac spinors associated with each quark field of color i and flavor q, and the A_ν^a are the gluon fields. In the Eq. (2.1) the sum on q is over the six different flavors (u, d, s, c, b, t) of quarks. It is the third non-Abelian term on the right-hand-side of Eq. (2.2) which distinguishes QCD from Quantum Electrodynamics (QED), giving rise to triplet and quartic gluon self-interactions and ultimately, as we will see, to the property of asymptotic freedom.

At the classical level, and in the limit in which quark-mass effects can be neglected, the QCD Lagrangian depends on a single dimensionless parameter: this is the gauge coupling, g_s, which determines the strength of the interaction between coloured quanta. The *strong coupling constant* is defined, in analogy with the fine structure constant of QED, as

$$\alpha_s = \frac{g_s^2}{4\pi}. \tag{2.4}$$

Predictions for a QCD observable associated to a given scattering process are obtained by perturbative methods using the Feynman rules which can be derived from the QCD lagrangian density. As is typical in a quantum field theory, Feynman diagrams containing loops produce ultraviolet (UV) divergences (originating from the integration over the unconstraint loop momenta) which need to be removed via a *renormalisation procedure*. As a consequence of the renormalisation of the theory the strong coupling constant α_s become dependent, on a calculable manner, to an additional momentum scale: the renormalisation scale μ_R. This quantity can be regarded as the momentum scale at which the subtractions needed to remove the UV divergencies are performed. Since μ_R is an arbitrary and unphysical parameter, the value of any physical observable R (if calculated to all orders in α_s) has to be independent of μ_R. This simple physics requirement is expressed mathematically by the renormalisation group equation

$$\mu_R^2 \frac{\partial R}{\partial \mu_R^2} \;=\; \left[\mu_R^2 \frac{\partial}{\partial \mu_R^2} \;+\; \mu_R^2 \frac{\partial \alpha_s}{\partial \mu_R^2} \frac{\partial}{\partial \alpha_s} \right] R \;=\; 0, \tag{2.5}$$

which clearly show that, in order to keep the observable R independent from μ_R, a change in the subtraction point (μ_R) must be compensated by an appropriate change in the renormalized strong coupling constant $\alpha_s(\mu_R)$.

The renormalisation scale dependence of the strong coupling constant is determined by the Callan-Symanzik β-function of QCD which is defined by:

$$\mu_R^2 \frac{\mathrm{d}}{\mathrm{d}\mu_R^2} a(\mu_R) \;\;=\;\; \beta\left(a(\mu_R)\right), \tag{2.6}$$

where in the Eq. (2.6) we have defined the couplant $a(\mu_R) = \alpha_s(\mu_R)/\pi$. The β-function is calculated by performing a perturbative expansion in powers of a:

$$\beta\left(a(\mu_R)\right) = -\sum_{i \geq 0} \beta_i \left(a(\mu_R)\right)^{i+2}, \tag{2.7}$$

and then extracting the coefficients, β_i, from the higher-order (loop) corrections to the bare vertices of the theory.

The calculation of the one-loop coefficient, β_0, performed almost 30 years ago [2] has led to the discovery of the property of *asymptotic freedom* of QCD:

$$a(\mu_R) \to 0 \quad \text{as} \quad \mu_R \to \infty. \tag{2.8}$$

The renormalized strong coupling constant, according to asymptotic freedom, gets smaller at high energies, and it is only in this domain that high-precision tests, similar to those in QED, can be performed using the methods of perturbation theory.

One of the triumphs of modern particle physics and quantum field theory has been indeed, mostly thanks to the property of asymptotic freedom, the extend to which QCD has successfully accounted for the strong interaction processes observed at colliders; most notably the striking phenomenon of hadronic jet production and the short-distance partonic structure of the proton.

2.1.2 The renormalised strong coupling constant

The Callan-Symanzik β-function of QCD is presently known to four-loops accuracy[1]

$$\mu_R^2 \frac{d}{d\mu_R^2} a = \beta(a) = -\sum_{i \geq 0} \beta_i (a)^{i+2} = -\beta_0 a^2 - \beta_1 a^3 - \beta_2 a^4 - \beta_3 a^5 + \mathcal{O}(a^6). \quad (2.9)$$

The coefficients are given by [2, 3, 4, 5]

$$
\begin{aligned}
\beta_0 &= \frac{1}{4}\left[11 - \frac{2}{3}n_f\right], \\
\beta_1 &= \frac{1}{16}\left[102 - \frac{38}{3}n_f\right], \\
\beta_2 &= \frac{1}{64}\left[\frac{2857}{2} - \frac{5033}{18}n_f + \frac{325}{54}n_f^2\right], \\
\beta_3 &= \frac{1}{256}\left[\frac{149753}{6} + 3564\zeta_3 + \left(-\frac{1078361}{162} - \frac{6508}{27}\zeta_3\right)n_f \right. \\
&\quad \left. + \left(\frac{50065}{162} + \frac{6472}{81}\zeta_3\right)n_f^2 + \frac{1093}{729}n_f^3\right].
\end{aligned}
\quad (2.10)
$$

where n_f is the number of active flavours, and ζ is Riemann's zeta function with values $\zeta_2 = \pi^2/6$ and $\zeta_3 \approx 1.202\,057$.

In the class of schemes where the beta function is mass independent, which includes the minimal subtraction (MS) schemes of dimensional regularization [6], β_0 and β_1 [3] are universal. The results for β_2 [4] and β_3 [5] are available in the modified MS ($\overline{\text{MS}}$) scheme [7]. For the reader's convenience, the coefficients of the beta function, β_i ($i = 0, \ldots, 3$), are listed for the n_f values of practical interest in Table 2.1.

In solving the Eq. (2.9) for α_s, a constant of integration has to be introduced: this is the fundamental constant of QCD that must be determined from experiment. The most sensible choice for this constant is the value of α_s at a fixed-reference scale μ_R^{ref}. It has become standard to choose $\mu_R^{\text{ref}} = M_Z$, where $M_Z = 91.1882$ GeV is the mass of the Z^0 boson which is very precisely measured ($\Delta M_Z = \pm 0.0022$ GeV), safely in the perturbative region ($\alpha_s(M_Z) \ll 1$), and far away from the quark thresholds ($m_b \ll M_Z \ll m_t$).

It is also convenient to introduce an additional dimensional parameter, Λ, which provides a direct parameterisation of the μ_R dependence of α_s. Integrating Eq. (2.9) leads to

$$
\begin{aligned}
\ln \frac{\mu_R^2}{\Lambda^2} &= \int \frac{da}{\beta(a)} \\
&= \frac{1}{\beta_0}\left[\frac{1}{a} + b_1 \ln a + (b_2 - b_1^2)a + \left(\frac{b_3}{2} - b_1 b_2 + \frac{b_1^3}{2}\right)a^2\right] + C, \quad (2.11)
\end{aligned}
$$

where an expansion in a has been performed, and to simplify the notation we have defined $b_i = \beta_i/\beta_0$ ($i = 1, 2, 3$). The integration constant is here conveniently split into Λ, the so-called asymptotic scale parameter, and C. The conventional $\overline{\text{MS}}$ definition of Λ, which we shall adopt in the following, corresponds to choosing $C = (b_1/\beta_0)\ln\beta_0$ [8, 9].

Iteratively solving Eq. (2.11) yields [10]

$$
\begin{aligned}
a &= \frac{1}{\beta_0 L} - \frac{b_1 \ln L}{(\beta_0 L)^2} + \frac{1}{(\beta_0 L)^3}\left[b_1^2(\ln^2 L - \ln L - 1) + b_2\right] \\
&\quad + \frac{1}{(\beta_0 L)^4}\left[b_1^3\left(-\ln^3 L + \frac{5}{2}\ln^2 L + 2\ln L - \frac{1}{2}\right) - 3b_1 b_2 \ln L + \frac{b_3}{2}\right], \quad (2.12)
\end{aligned}
$$

---

[1]In the following we will omit the label μ_R in the couplant, $a(\mu_R)$, wherever confusion is impossible.

where $L = \ln(\mu_R^2/\Lambda^2)$ and terms of $\mathcal{O}(1/L^5)$ have been neglected. The property of asymptotic freedom is immediately manifest in the Eq. (2.12) already at 1-loop accuracy (i.e. $b_1 = b_2 = b_3 = 0$): α_s depends logarithmically on μ_R and slowly approches zero as μ_R becomes large.

QCD matching conditions at flavour thresholds

In the discussion above we have ignored quark-mass effects, i.e., we have assumed an idealized situation where quarks of mass greater than μ_R are neglected completely.

When considering heavy-quark effects in MS-like renormalization schemes, particular care must be placed, however, in the implementation of the matching conditions across heavy-flavour thresholds. This is due to the fact that in MS-like schemes, the Appelquist-Carazzone decoupling theorem [11] does not in general apply to quantities that do not represent physical observables, such as the β-function or the coupling constant, i.e., quarks with masses much larger than the considered energy scale do not automatically decouple. The standard procedure to circumvent this problem is to render decoupling explicit by using the language of effective field theory. Let us consider QCD with $n_l = n_f - 1$ massless quark flavours and one heavy flavour h, with mass m_h which is supposed to be much larger than the energy scale. One can construct an effective n_l-flavour theory by requiring consistency with the full n_f-flavour theory[2] at an energy scale comparable to m_h, the heavy-quark threshold $\mu_R^{(n_f)} = \mathcal{O}(m_h)$. This leads to a nontrivial matching condition between the couplings and light masses, m_q, of the two theories. Although, $\alpha_s^{(n_l)}(m_h) = \alpha_s^{(n_f)}(m_h)$ and $m_q^{(n_l)}(m_h) = m_q^{(n_f)}(m_h)$ at leading and next-to-leading order, this relation does not generally hold at higher orders in the $\overline{\text{MS}}$ scheme.

The connection between the strong coupling constant in the effective and the full theory is given by

$$\alpha_s^{(nf-1)}(\mu) \quad = \quad \zeta_g^2 \alpha_s^{(n_f)}(\mu), \tag{2.13}$$

where ζ_g is known up to the three-loop order [10, 15]:

$$
\begin{aligned}
\left(\zeta_g^{MS}\right)^2 &= 1 + \frac{\alpha_s^{(n_f)}(\mu)}{\pi}\left(-\frac{1}{6}\ln\frac{\mu^2}{m_h^2}\right) + \left(\frac{\alpha_s^{(n_f)}(\mu)}{\pi}\right)^2\left(\frac{11}{72} - \frac{11}{24}\ln\frac{\mu^2}{m_h^2} + \frac{1}{36}\ln^2\frac{\mu^2}{m_h^2}\right) \\
&\quad + \left(\frac{\alpha_s^{(n_f)}(\mu)}{\pi}\right)^3\left[\frac{564731}{124416} - \frac{82043}{27648}\zeta_3 - \frac{955}{576}\ln\frac{\mu^2}{m_h^2} + \frac{53}{576}\ln^2\frac{\mu^2}{m_h^2}\right. \\
&\quad \left. -\frac{1}{216}\ln^3\frac{\mu^2}{m_h^2} + n_l\left(-\frac{2633}{31104} + \frac{67}{576}\ln\frac{\mu^2}{m_h^2} - \frac{1}{36}\ln^2\frac{\mu^2}{m_h^2}\right)\right].
\end{aligned}
\tag{2.14}
$$

In this equation the $\overline{\text{MS}}$ mass $m_h(\mu)$ is chosen for the parameterization of the heavy quark mass. From the Eq. (2.14) and (2.12) is then straigthforward to derive the relation between $\Lambda^{(n_f-1)}$ and $\Lambda^{(n_f)}$.

Solutions of the renormalisation group equation

There are various approaches that can be used to compute $\alpha_s(\mu_R)$ when $a(\mu_R^{\text{ref}})$ is given for a fixed number of flavours:

a) In the first approach $\alpha_s(\mu_R)$ is evaluated by solving numerically the differential equation Eq. (2.9) using $\alpha_s(M_Z)$ as initial condition.

---

[2]By *requiring consistency* here we mean that the values $\alpha_s^{(n_f-1)}$ and $\alpha_s^{(n_f)}$ should be related so that a physical quantity calculated in both 'theories' gives the same result.

b) In this method a two-steps procedure is applied. First the quantity Λ is calculated from Eq. (2.11) with $\mu_{\mathrm{R}} = M_Z$, and then the Eq. (2.12) is used to obtain $\alpha_{\mathrm{s}}(\mu_{\mathrm{R}})$ at any other scale μ_{R}.

c) The third approach, which is also the one adopted by the Particle Data Group (PDG), exploits the Eq. (2.12) both to determine Λ (via an iterative procedure) and then to compute $\alpha_{\mathrm{s}}(\mu_{\mathrm{R}})$.

The first method has the advantage to give an exact (numerical) solution of the renormalisation group equation avoiding altogether the introduction of the Λ parameter at intermediate steps. The other approaches do use the Λ parameter (and are hence dependent on the exact definition of Λ, as the $\overline{\mathrm{MS}}$ given above), but have the advantage of providing an explicit parameterisation of the μ_{R}-dependence of α_{s}; here Λ plays the role of a universal parameter which sets the characteristic scale of QCD.

In Tab. 2.2 the influence of the adopted evolution equation and number of loops included, is studied in the evaluation of $\alpha_s^{(5)}$ at the scale provided by the bottom mass, $m_b = 4.7$ GeV, using $\alpha_s^{(5)}(M_Z)$ as an input. It can be seen that the inclusion of β_1 leads to a significant jump in $\alpha_s^{(5)}(M_b)$ whereas the effect of the three- and four-loop coefficients, i.e. β_2 and β_3, is only marginal. Similar conclusions are drawn from Fig. 2.1 where the strong coupling constant $\alpha_{\mathrm{s}}(\mu_{\mathrm{R}})$ (at 1-, 2-, and 3-loop accuracy) is plotted in the region $5 < \mu_{\mathrm{R}} < 110$ GeV, assuming $\alpha_{\mathrm{s}}(M_Z) = 0.118$, and using the approach c) described above for the evolution.

In all the NLO pQCD calculations presented in this thesis the running of the strong coupling constant has been calculated using the method c) outlined above with the Eq. (2.12) truncated (for consistency reasons) at two loops.

2.2 General structure of the DIS cross sections in NLO pQCD

In this section we describe the general structure of the NLO QCD cross sections in NC DIS. Emphasis is placed in describing those properties that a particular physical observable has to fulfil in order to be perturbatively calculable in QCD.

2.2.1 QCD-improved parton model and factorisation

The calculational framework for computing a generic cross section in a deep inelastic e^+p hard-scattering process (i.e. a process characterized by the presence of at least a large momentum scale) is based on the *QCD-improved parton model*. According to this model, as quantitatively expressed by the factorization theorems of QCD[16] and perturbation theory, a NC DIS differential cross section[3], $d\sigma$, can be written as

$$d\sigma = \sum_{a=q,\overline{q},g} \int dx f_a(x, \mu_{\mathrm{F}}^2) d\hat{\sigma}_a(xP, \alpha_{\mathrm{s}}(\mu_{\mathrm{R}}), \mu_{\mathrm{R}}^2, \mu_{\mathrm{F}}^2) \cdot (1 + \delta_{\mathrm{had}}) . \qquad (2.15)$$

The cross section has the form of a convolution, with respect to the fraction x of the proton four-momentum (P) taken by the incoming parton, of the partonic hard cross sections ($d\hat{\sigma}_a$) with the parton distribution functions ($f_a(x, \mu_{\mathrm{F}}^2)$) of the colliding proton. The partonic cross sections describe the short-distance structure of the interaction and are calculable, thanks to the property of asymptotic freedom of QCD, as power series expansions in the renormalization scale

---

[3]Unless indicated otherwise in the following we will use the same symbol $d\sigma$ to indicate both the DIS inclusive ($d\sigma_{tot}$) and the dijet ($d\sigma_{2+1}$) differential cross sections. The same symbols with the superscript NLO will indicate only the perturbative component (the first term on the right-hand side of Eq. 2.15) which does not contain non-perturbative (δ_{hadr}) contributions.

(μ_{R}) dependent strong coupling constant. The parton distribution functions (PDFs) contain the description of the long-distance structure of the incoming proton. Although they are not predicted by pQCD their evolution with the factorization scale (μ_{F}) at which they are probed follows the DGLAP equations [17].

We have isolated into δ_{had}, in the Eq. (2.15), the contribution of the hadronisation processes that account for transformation of the final state partons into the observed colourless hadrons. These effects take place long after the hard scattering and involve long distances (small momentum transfers) and as such can not be described within the realm of pQCD. One is hence forced to use QCD-inspired phenomenological models.

In the following, we will describe only the perturbative component of the cross section and leave the discussion of these non perturbative effects to the next chapter.

2.2.2   Parton densities

The predictive power of the factorization formula Eq. (2.15) follows from the *universality* of the parton densities: once extracted from the data in one process (or more generally in a set of processes), they can be used to derive an absolute prediction for any other hard-scattering process, provided the corresponding partonic cross sections are known.

The dependence of the parton densities $f_a(x, \mu_{\mathrm{F}}^2)$ on the momentum fraction x and their absolute value at any fixed scale μ_{F}^2 are not computable in perturbation theory. However, their scale dependence is perturbatively controlled by the DGLAP evolution equations:

$$\frac{\partial f_a(x, \mu_{\mathrm{F}}^2)}{\partial \ln \mu_{\mathrm{F}}^2} = \frac{\alpha_{\mathrm{s}}(\mu_{\mathrm{R}})}{2\pi} \sum_{b=q,\overline{q},g} \int_x^1 \frac{dz}{z} P_{ab}(\alpha_{\mathrm{s}}(\mu_{\mathrm{R}}^2), z) \, f_a(x/z, \mu_{\mathrm{F}}^2) \; . \tag{2.16}$$

The kernels $P_{ab}(\alpha_{\mathrm{s}}, z)$ are the Altarelli–Parisi (AP) splitting functions. As the partonic cross sections (to be discussed in the next section), they are computable as power series expansions in α_{s}:

$$P_{ab}(\alpha_{\mathrm{s}}, z) = P_{ab}^{(0)}(z) + \frac{\alpha_{\mathrm{s}}(\mu_R)}{2\pi} \left[P_{ab}^{(1)}(z) - \beta_0 \ln \frac{\mu_{\mathrm{F}}^2}{\mu_{\mathrm{R}}^2} P_{ab}^{(0)}(z) \right] + \mathcal{O}(\alpha_{\mathrm{s}}^2) \; , \tag{2.17}$$

where $P_{ab}^{(0)}(z)$ and $P_{ab}^{(1)}(z)$ are the LO and NLO splitting functions[18] respectively, and β_0 is defined in Eq.(2.10).

The parton densities are determined by performing global DGLAP fits to data from deep-inelastic scattering, Drell–Yan (DY), prompt-photon and jet production. The method consists in parameterizing the parton densities at some input scale Q_0 and then adjusting the parameters to fit the evolved PDFs to the data. The parameters are usually constrained by imposing the positivity of the parton densities ($f_a(x, \mu_{\mathrm{F}}^2) \geq 0$) and the momentum sum rule ($\sum_a \int_0^1 dx \, x \, f_a(x, \mu_{\mathrm{F}}^2) = 1$). Having determined $f_a(x, Q_0^2)$ at a given input scale $\mu_{\mathrm{F}}^2 = Q_0^2$, the evolution equations (Eq. (2.16)) can be used to compute the parton densities at different perturbative scales μ_{F}^2 and momentum fractions x.

All densities decrease at large x. At small x, the valence quark densities vanish and the gluon density dominates. The sea-quark densities also increase at small x because they are driven by the strong rise of the gluon density and the splitting of gluons in $q\bar{q}$ pairs. Note that the quark densities are not flavour-symmetric either in the valence sector ($u_v \neq d_v$) or in the sea sector ($\bar{u} \neq \bar{d}$).

In the next chapter we will review in detail the present knowledge on the parton densities, and discuss the important issue of their theoretical and experimental associated uncertainties.

2.2.3   Partonic cross sections

Basic structure

The calculation of hard-scattering cross sections requires, besides that of the parton densities, the knowledge of the partonic cross sections $d\hat{\sigma}_a$. The latters are expressed as a power series expansion in the renormalized strong coupling constant, and are evaluated by calculating the relevant Feynman diagrams up to a given order in α_s. The NLO pQCD partonic cross sections are obtained truncating the perturbative series after the second term:

$$d\hat{\sigma}_a{}^{NLO} = d\hat{\sigma}_a^{(0)} + d\hat{\sigma}_a^{(1)} . \tag{2.18}$$

The LO cross section $d\hat{\sigma}^{(0)}$ is obtained by integrating the fully exclusive Born-level cross section $d\hat{\sigma}^B$ over the phase space for the corresponding physical observable. Let us suppose that this LO calculation involves m partons with momenta p_k $(k = 1, ..., m)$ in the final state (see Fig. 2.2). Thus, we write

$$d\hat{\sigma}_a^{(0)} = \int_m d\hat{\sigma}_a^B , \tag{2.19}$$

where the Born-level cross section is:

$$d\hat{\sigma}_a^B = d\Phi^{(m)}(\{p_k\}) \, |\mathcal{M}_m(\{p_k\})|^2 \, F_J^{(m)}(\{p_k\}) , \tag{2.20}$$

and $d\Phi^{(m)}$ and $\mathcal{M}_m$ denote the full phase space and the tree-level QCD matrix element to produce m final-state partons, respectively. These are the factors that depend on the process.

The function $F_J^{(m)}$ defines the physical quantity that we want to compute, possibly including the experimental cuts. Thus, for example, in the case of a jet cross section, $F_J^{(m)}$ is the functional representation (in terms of the four-momenta of the m partons in the final state) of the adopted jet algorithm. We will discuss shortly below the requirements that $F_J^{(m)}$ has to fulfill in order to be able to compute finite cross sections.

The evaluation of the LO cross section does not present any particular difficulty. Even if $d\hat{\sigma}^{(0)}$ cannot be computed analytically (because $\mathcal{M}_m$ is too cumbersome or the phase-space cuts in $F_J^{(m)}$ are very involved), one can straightforwardly use numerical integration techniques, for instance, a Monte Carlo program where the function $F_J^{(m)}$ is given as 'user routine'.

To calculate the NLO contribution, $d\hat{\sigma}_a^{(1)}$, one has to consider the exclusive cross section $d\sigma_a^R$ with $m + 1$ partons in the final state (real corrections) and the one-loop correction $d\sigma_a^V$ to the process with m partons in the final state (virtual corrections):

$$d\hat{\sigma}_a^{(1)} = \int_{m+1} d\hat{\sigma}_a^R + \int_m d\hat{\sigma}_a^V + \int_m d\hat{\sigma}_a^C . \tag{2.21}$$

The exclusive cross sections $d\hat{\sigma}_a^R$ and $d\hat{\sigma}_a^V$ have the same structure as the Born-level cross section in Eq. (2.20):

$$d\hat{\sigma}_a^R = d\Phi^{(m+1)} \, |\mathcal{M}_{m+1}(\{p_k\})|^2 \, F_J^{(m+1)}(\{p_k\}) , \tag{2.22}$$

$$d\hat{\sigma}_a^V = d\Phi^{(m)} \, |\mathcal{M}_m(\{p_k\})|^2_{(1-loop)} \, F_J^{(m)}(\{p_k\}) , \tag{2.23}$$

where $|\mathcal{M}_m|^2_{(1-loop)}$ denotes the *renormalized* QCD amplitude to produce m final-state partons evaluated in the one-loop approximation:

$$|\mathcal{M}_m|^2_{(1-loop)} = \mathcal{M}_m \cdot (\mathcal{M}_m^{loop})^* + \mathcal{M}_m^{loop} \cdot (\mathcal{M}_m)^* , \tag{2.24}$$

and $d\Phi^{(m+1)}$ and $\mathcal{M}_{m+1}$ indicate the phase-space and matrix element to produce the $m+1$ final state partons, respectively.

The third contribution, $d\hat{\sigma}_a^C$, in the Eq. (2.21) is the collinear-subtraction counterterm that arises from the redefinition of the bare parton densities into factorisation-scale dependent PDFs; We will explain the origin of this term shortly below.

Infrared singularities and infrared safe observables

As is well known, the calculations of the virtual[4] and real cross sections leads to a rather complicated pattern of *soft* and *collinear* singularities. These singularities arise from phase-space regions characterized by a parton (either virtual, that is exchanged in a loop, or real, that is emitted and contributing to the partonic final state) becoming soft or collinear to another parton present in the initial or final state. Regularizing the phase-space integrals on the r.h.s. of Eq. (2.21) in a number of space-time dimensions $d = 4 - 2\epsilon$ allows to express these divergencies simply in terms of double ($1/\epsilon^2$) and single ($1/\epsilon$) poles. In order to obtain a finite result for $d\hat{\sigma}_a^{(1)}$ these poles must cancel between the virtual and real contributions, and the collinear counter term. This cancellation, however, is not guaranteed by QCD for *any* observable $F_J^{(m)}$, but only for a special class of them: these are the observables that are infrared-safe and allow the factorizability of initial-state collinear singularities.

By infrared-safe observable $F_J^{(m)}$ we mean a physical quantity that is independent of the number of soft and collinear particles in the final state. Qualitatively we should have:

$$F_J^{(m+1)} \to F_J^{(m)} \quad , \tag{2.25}$$

in any case where the $m + 1$-parton final state contains either a soft parton or a pair of collinear partons.

Formally, this implies that F_J has to fulfill the following properties:

$$F_J^{(m+1)}(p_1, .., p_j = \lambda q, .., p_{m+1}) \to F_J^{(m)}(p_1, ..., p_{m+1}) \quad \text{if} \ \lambda \to 0 \ , \tag{2.26}$$

$$F_J^{(m+1)}(p_1, .., p_i, .., p_j, .., p_{m+1}) \to F_J^{(m)}(p_1, .., p, .., p_{m+1}) \quad \text{if} \ p_i \to zp \ , \ p_j \to (1-z)p \tag{2.27}$$

and

$$F_J^{(m)}(p_1, ..., p_m) \to 0 \quad \text{if} \ p_i \cdot p_j \to 0 \ . \tag{2.28}$$

Note that the m-parton jet function $F_J^{(m)}$ on the right-hand side of Eq. (2.26) is obtained from the original $F_J^{(m+1)}$ by removing the soft parton p_j, and the one on the right-hand side of Eq. (2.27) by replacing the collinear partons $\{p_i, p_j\}$ with a parton of four-momentum $p = p_i + p_j$. Equation (2.28) defines the leading-order cross section, that is, it ensures that the Born-level cross section $d\hat{\sigma}^B$ in Eq. (2.19) is well-defined (i.e. finite after integration) in $d = 4$ dimensions.

In addition to the property of infrared-safety the phase-space function must fulfil also the property of factorizability of initial-state collinear singularities. We should have:

$$F_J^{(m+1)}(p_1, .., p_i, .., p_{m+1}; p_a) \to F_J^{(m)}(p_1, ..., p_{m+1}; xp_a) \ , \quad \text{if} \ p_i \to (1-x)p_a \tag{2.29}$$

where $F_J^{(m)}$ is obtained from $F_J^{(m+1)}$ by removing the final-state parton i collinear to the initial-state parton of flavour a and momentum p_a.

If F_J fulfils these conditions than the soft singularities and the the collinear singularities *in the final state* cancel between the virtual and real cross sections (owing to the Kinoshita-Lee-Nauenberg theorem[19]), and the collinear singularities from the initial state can be consistently absorbed into 'redefined' (μ_F-dependent) parton densities. The factorization scale is the technical scale at which this redefinition of the PDFs is performed. Qualitatively speaking it can be considered as a cutoff for the transverse momentum ($p_\perp$) of the parton emitted from the initial state: for $p_\perp > \mu_F$, the parton is assumed to contribute to the final state; for $p_\perp < \mu_F$, the parton contributes to the definition of the PDFs.

---

[4]In the following we will assume that the *ultraviolet* singularities encountered in the calculation of the loop integral in $|\mathcal{M}_m|^2_{(1-loop)}$ have been cured by carrying out the the usual renormalization procedure.

In the factorization formula Eq. (2.15) we have already expressed, as is done in the standard literature, the hadronic cross section in term of the μ_F-dependent PDFs and so as a consequence we have added to the virtual and real corrections the initial-state collinear counterterm, $d\hat{\sigma}^C$, in order to guarantee the cancellation of all (soft and collinear) singularities within the sole partonic cross section. This counterterm can be expressed in a very general form. In the $\overline{\text{MS}}$ factorisation scheme and $d = 4 - 2\epsilon$ dimensions it reads:

$$d\hat{\sigma}_a^C(\mu_{\rm R}^2, \mu_{\rm F}^2) = -\frac{\alpha_{\rm s}(\mu_{\rm R})}{2\pi} \frac{1}{\Gamma(1-\epsilon)} \sum_b \int_0^1 dz \left[-\frac{1}{\epsilon} \left(\frac{4\pi\mu_{\rm R}^2}{\mu_{\rm F}^2} \right)^\epsilon P_{ab}^{(0)}(z) \right] d\hat{\sigma}_b^B(zp_a) . \qquad (2.30)$$

where the functions $P_{ab}^{(0)}(z)$ are the LO Altarelli-Parisi splitting functions. We note here that the complete μ_F dependence of the NLO partonic cross section is contained in this collinear counterterm. Since the parton densities $f_a(x, \mu_{\rm F}^2)$ are also factorisation-scale dependent, this dependence largely cancel in the hadronic cross section.

NLO partonic cross sections and determination of $\alpha_{\rm s}$

The importance of taking into account the NLO corrections can be seen from the fact that only including them one can have reliable pQCD predictions and hence perform a reliable determination of the strong coupling constant. In order to understand why this is so, it is convenient to rewrite the NLO partonic cross section Eq. (2.18) in a form that explicitly shows its $\alpha_{\rm s}$, μ_R, and μ_F dependences:

$$d\hat{\sigma}_a^{(1)} = \alpha_{\rm s}^k(\mu_{\rm R}) \left\{ \hat{c}_a^{(0)} + \alpha_{\rm s}(\mu_{\rm R})\hat{c}_a^{(1)}(\mu_{\rm R}^2, \mu_{\rm F}^2) \right\} , \qquad (2.31)$$

where in Eq. (2.31) the integer power $(k = 0, 1, 2, \dots)$ of the overall $\alpha_{\rm s}^k(\mu_{\rm R})$ term depends on the particular observable being considered.

The LO term $\hat{c}_a^{(0)}$ can give only an estimate of the order of magnitude of the partonic cross section, because, at this order, $\alpha_{\rm s}$ is not unambiguously defined. Equivalently, we can say that since $\hat{c}_a^{(0)}$ does not depend on $\mu_{\rm R}$, the size of its contribution can be varied quite arbitrarily by changing $\mu_{\rm R}$ in its coefficient $\alpha_{\rm s}^k(\mu_{\rm R})$. A 'reliable' estimate of the partonic cross section (and the strong coupling $\alpha_{\rm s}$) requires instead the knowledge of (at least) the NLO term $\hat{c}_a^{(1)}$. This term explicitly depends on $\mu_{\rm R}$ and this dependence begins to compensate that of $\alpha_{\rm s}^k(\mu_{\rm R})$.

It is worth noting here that the partonic cross sections do not contain the full $\alpha_{\rm s}$ dependence of the hadronic cross section. The PDFs of the proton, via the DGLAP evolution equations, also depend on $\alpha_{\rm s}$. Any QCD analysis aiming at a determination of the strong coupling in a QCD fit must hence take the full $\alpha_{\rm s}$-dependence into account as well as the existing correlations between $\alpha_{\rm s}$ and PDFs.

An important issue associated to the calculation of the partonic cross sections is the one related to the corresponding uncertainty due to the uncalculated higher-order (i.e. beyond NLO) terms. We will discuss this issue in the next chapter together with the other sources of theoretical uncertainty on the QCD predictions.

2.3   The NLO program DISENT

Owing to the complicated structure of the phase-space function F_J associated to a given infrared-safe observable, the *analytical* calculation of the corresponding NLO predictions is in practice impossible for all but the simplest (i.e. fully inclusive) quantities, thus making the use of numerical methods essential. However, even the application of numerical integration techniques is far from trivial, because the separate integration of the NLO real and virtual contributions

over the associated $m+1$- and m-partons phase-space regions in Eq. (2.21) cannot be performed before having first removed the singularities which affect both integrals.

Any attempt to construct a numerical program for the calculation of NLO jet observables must hence somehow be able to set up a hybrid numerical/analytical procedure where the analytical cancellations of the singularities is achieved at the integrand level and the remaining complex but finite phase-space integrals are then evaluated numerically.

In the last few years, several such NLO programs [31, 30, 32, 33] for the calculations of infrared-safe observables in DIS have appeared. They have greatly enhanced the possibility to perform detailed QCD phenomenological studies of jet production in DIS at HERA. First of all, the numerical approach allows to calculate any number and any type of observables simultaneously by simply histogramming the appropriate quantities, moreover, using the numerical approach, it is easy to implement different experimental conditions, for example detector acceptances and experimental cuts.

The aim of this section is to give a pictorial description of the main theoretical ingredients which have allowed the practical implementation of one of these NLO programs: DISENT[31]. This program has been used to obtain the NLO pQCD predictions for all the cross sections studied in this thesis[5].

DISENT is based on two key ingredients: the *subtraction method* for the numerical cancellation of the divergences among different contributions and the *dipole factorization formulae* for the universal (process- and observable-independent) analytical treatment of individual divergent terms.

2.3.1 Subtraction method

The general idea of the subtraction method is to use the *exact* identity

$$d\hat{\sigma}_a^{(1)} = \int_{m+1} \left[d\hat{\sigma}_a^R - d\hat{\sigma}_a^A \right] + \int_m d\hat{\sigma}_a^V + \int_{m+1} d\hat{\sigma}_a^A + \int_m d\hat{\sigma}_a^C \ , \qquad (2.32)$$

which is obtained by subtracting and adding back the 'fake' cross section contribution $d\hat{\sigma}_a^A$ to the NLO contribution, $d\hat{\sigma}_a^{(1)}$, in Eq. (2.21). The cross section $d\hat{\sigma}_a^A$ has to fulfil two main properties.

i) It must be a proper approximation of $d\hat{\sigma}_a^R$ such as to have the same *pointwise* singular behaviour (in d dimensions) as $d\hat{\sigma}_a^R$ itself. Thus, $d\hat{\sigma}_a^A$ acts as a *local* counterterm for $d\hat{\sigma}_a^R$ and one can safely perform the limit $\epsilon \to 0$ under the integral sign in the first term on the right-hand side of Eq. (2.32). This defines a cross section contribution $d\hat{\sigma}_a^{(1)\,\{m+1\}}$, with $m+1$-parton kinematics, that can be integrated numerically in four dimensions:

$$d\hat{\sigma}^{(1)\,\{m+1\}} = \int_{m+1} \left[\left(d\hat{\sigma}_a^R \right)_{\epsilon=0} - \left(d\hat{\sigma}_a^A \right)_{\epsilon=0} \right] . \qquad (2.33)$$

ii) The second property of $d\hat{\sigma}_a^A$ is its analytic integrability (in d dimensions) over the one-parton subspace leading to the soft and collinear divergences. In this case, we can rewrite the last three terms on the right-hand side of Eq. (2.32) as follows

$$d\hat{\sigma}_a^{(1)\,\{m\}} = \int_m \left[d\hat{\sigma}_a^V + \int_1 d\hat{\sigma}_a^A + d\hat{\sigma}_a^C \right]_{\epsilon=0} . \qquad (2.34)$$

Performing the analytic integration $\int_1 d\hat{\sigma}_a^A$, one obtains ϵ-pole contributions that can be combined with those in $d\hat{\sigma}_a^V$ and $d\hat{\sigma}_a^C$, thus cancelling (by trivial addition) all the divergences. The

---

[5]A numerical comparison of the DISENT predictions with those obtained using other DIS NLO programs presently available on the market will be presented in the next chapter.

remainder is finite in the limit $\epsilon \to 0$ and thus defines the integrand of a cross section contribution $d\hat{\sigma}_a^{(1)\,\{m\}}$, with m-parton kinematics, that can be integrated numerically in four dimensions.

The final structure of the NLO partonic cross section is then as follows

$$d\hat{\sigma}_a^{NLO} = d\hat{\sigma}_a^{(0)\,\{m\}} + d\hat{\sigma}_a^{(1)\,\{m+1\}} + d\hat{\sigma}_a^{(1)\,\{m\}} \quad , \tag{2.35}$$

and can be easily implemented in a 'partonic Monte Carlo' program, which generates *appropriately weighted* events with $m + 1$ and m final-state partons.

Note that, using the subtraction method, no approximation is actually performed in the evaluation of the NLO cross section. Rather than approximating the cross section, the subtracted contribution $d\hat{\sigma}_a^A$ defines a fake cross section that has the same dynamical singularities as the real one and whose kinematics are sufficiently simple to permit its analytic integration over the one-parton subspace leading the infrared singularities.

From the above discussion it is clear that the crucial step in the practical implementation of the subtraction method is the construction of an appropriate contribution $d\hat{\sigma}_a^A$. In the program DISENT this is achieved by exploiting the dipole formalism first introduced by Catani and Seymour [21].

2.3.2 The dipole formalism and the universal subtraction term

The dipole factorization formulae provide an effective framework to relate the singular behaviour of $|\mathcal{M}_{m+1}|^2$, the tree-level amplitude with $m + 1$ partons, to $|\mathcal{M}_m|^2$. They have the following symbolic structure:

$$|\mathcal{M}_{m+1}(p_1, ..., p_{m+1})|^2 = |\mathcal{M}_m(\widetilde{p}_1, ..., \widetilde{p}_m)|^2 \otimes \boldsymbol{V}_{ij} + ... \quad . \tag{2.36}$$

The dots on the right-hand side stand for contributions that are not singular in the soft and collinear limits (i.e. when $p_i \cdot p_j \to 0$). The dipole splitting functions $\boldsymbol{V}_{ij}$ are universal (process-independent) singular factors which reproduce all the soft and collinear limits of $|\mathcal{M}_{m+1}|^2$ and depend on the momenta and quantum numbers of the m partons in the tree-level matrix element $|\mathcal{M}_m|^2$. Colour and helicity correlations are denoted by the symbol $\otimes$. The set $\widetilde{p}_1, ..., \widetilde{p}_m$ of modified momenta on the right-hand side of Eq. (2.36) is defined starting from the original $m + 1$ parton momenta in such a way that the m partons in $|\mathcal{M}_m|^2$ are physical, that is, they are on-shell and energy-momentum conservation is implemented exactly[6]:

$$\widetilde{p}_i^2 = 0 \, , \quad \widetilde{p}_1 + ... + \widetilde{p}_m = p_1 + ... + p_{m+1} \, . \tag{2.37}$$

In particular, they can be chosen in such a way to obey *exact* phase-space factorization:

$$d\Phi^{(m+1)}(p_1, ..., p_{m+1}) = d\Phi^{(m)}(\widetilde{p}_1, ..., \widetilde{p}_m) \, d\varphi_{(\{\widetilde{p}_k\})}(p_i + p_j) \, , \tag{2.38}$$

where $d\varphi$ is a single-particle subspace that, for fixed $\widetilde{p}_1, ..., \widetilde{p}_m$, depends only on the dipole momenta p_i and p_j. Apart from the presence of colour and helicity correlations, the left hand side of Eq. (2.36) can thus be considered as a truly factorized expression.

These main features of the dipole formulae allow to construct a universal subtraction term with the following form:

$$d\hat{\sigma}_a^A = d\Phi^{(m+1)} \sum_{ij} |\mathcal{M}_m(\{\widetilde{p}_k\})|^2 \otimes \boldsymbol{V}_{ij} \, F_J^{(m)}(\{\widetilde{p}_k\}) \, , \tag{2.39}$$

which fulfils, as we will now see, the properties *i)* and *ii)* listed above.

---

[6]The detailed expressions for these parton momenta and for the dipole splitting functions are given in Ref. [21].

As for the property i), we observe that there are several dipole terms on the right-hand side of Eq. (2.39). Each of them mimics one of the $m + 1$-parton configurations in $d\hat{\sigma}_a^R$ that are kinematically degenerate with a given m-parton state. Any time the $m + 1$-parton state in $d\hat{\sigma}_a^R$ approaches a soft and/or collinear region, there is a corresponding dipole factor in $d\hat{\sigma}_a^A$ that approaches the same region with exactly the same probability as in $d\hat{\sigma}_a^R$. The equality of the two probabilities directly follows from Eq. (2.39), from the limiting behaviour of the $m+1$ amplitude in Eq. (2.36), and the property of infrared-safeness of the physical observable previiuosly discussed. In this manner $d\hat{\sigma}_a^A$ acts as a local counterterm for $d\hat{\sigma}_a^R$. Note, in particular, that the cancellation mechanism is completely independent of the actual form of the jet-defining function and works for any jet observable (i.e. for any quantity that fulfils Eq. (2.25)).

As for the property ii), we start by noting that $d\hat{\sigma}_a^A$ (likewise $d\hat{\sigma}_a^R$) depends on the $m + 1$ parton momenta $p_1, ..., p_{m+1}$. However, owing to the exact phase-space factorization Eq. (2.38) and to the fact that the fake cross section in Eq. (2.39) is proportional to the jet quantity calculated from the modified m-parton configuration, the integration of the singular dipole contributions can be completely factorized (modulo colour and helicity correlations) with respect to a term that exactly reproduces the Born-level cross section:

$$\int_{m+1} d\sigma^A = \int_m d\Phi^{(m)}(\{\widetilde{p}_k\}) \, |\mathcal{M}_m(\{\widetilde{p}_k\})|^2 \, \otimes \, \boldsymbol{I}(\{\widetilde{p}_k\}) F_J^{(m)}(\{\widetilde{p}_k\}) = \int_m d\sigma^B \otimes \boldsymbol{I}(\{\widetilde{p}_k\}) \; . \quad (2.40)$$

The factor $\boldsymbol{I}$ in Eq. (2.40) is defined by

$$\boldsymbol{I}(\{\widetilde{p}_k\}) \equiv \sum_{ij} \int_1 d\varphi_{(\{\widetilde{p}_k\})}(p_i + p_j) \, \boldsymbol{V}_{ij}, \quad (2.41)$$

and contains all the soft and collinear singularities that are necessary to compensate those in the virtual cross section $d\hat{\sigma}_a^V$ and the collinear counterterm $d\hat{\sigma}_a^C$. Owing to the convenient definition of the dipole splitting function $\boldsymbol{V}_{ij}$, it is possible to carry out analytically the integration in Eq. (2.41) over the dipole phase space in d dimensions. This leads to an explicit expression for the factor $\boldsymbol{I}$, which is again independent from $F_J^{(m)}$, and calculable (as the dipole splitting functions) once and for all.

2.3.3   Numerical implementation

In order to summarize the final results of the DISENT algorithm and to describe its numerical implementation, we start by recalling how the LO cross section in Eq. (2.19) is evaluated by using a Monte Carlo program. One first generates an m-parton event in the phase-space region $d\Phi^{(m)}$ and gives it the weight $|\mathcal{M}_m|^2$. Then this weighted event is analysed by a user routine according to the actual definition of the phase-space function $F_J^{(m)}$ and inserted into a corresponding histogram bin.

Following the decomposition in Eq. (2.35), the NLO cross section is obtained by adding to the LO result, $d\hat{\sigma}_a^{(0)}$, two contributions (which are not necessarily positive definite) with m-parton and $m + 1$-parton kinematics, respectively. As we have seen, unlike the original real and virtual contributions, these two terms are separately finite and can directly be integrated in four space-time dimensions.

The NLO contribution with m finale-state partons, $d\hat{\sigma}_a^{(1)\,\{m\}}$, has a very simple structure. It is identical to the LO partonic cross section in Eq. (2.19) but with the amplitude $|\mathcal{M}_m|^2$ replaced by an effective one, $\mathcal{F}_m$, which is the finite reminder resulting from the sum of the one-loop amplitude $|\mathcal{M}_m|^2_{(1-loop)}$, of the amplitude $|\mathcal{M}_m|^2 \otimes \boldsymbol{I}$ (arising from $\int_1 d\hat{\sigma}_a^A$), and of the amplitude of the collinear-counterterm in the Eq. (2.30) (including its $1/\epsilon$-pole):

$$d\hat{\sigma}_a^{(1)\,\{m\}} = \int_m d\Phi^{(m)} \, F_J^{(m)}(\{p_k\}) \, \mathcal{F}_m(\{p_k\}) \; . \quad (2.42)$$

As a result, this term can be evaluated in a Monte Carlo program exactly as the LO cross section except for using as a weight of the m-parton configuration $\mathcal{F}_m$ instead of $|\mathcal{M}_m|^2$.

The NLO contribution with $m+1$-parton kinematics, which is obtained by subtracting the fake cross section in Eq. (2.39) from the real cross section in Eq. (2.22), has the following explicit expression:

$$d\hat{\sigma}_a^{(1)\,\{m+1\}} = \int_{m+1} d\Phi^{(m+1)} \tag{2.43}$$

$$\cdot \left\{ |\mathcal{M}_{m+1}(\{p_k\})|^2 \; F_J^{(m+1)}(\{p_k\}) - \sum_{ij} |\mathcal{M}_m(\{\widetilde{p}_k\})|^2 \otimes \boldsymbol{V}_{ij} F_J^{(m)}(\{\widetilde{p}_k\}) \right\} .$$

The terms in the curly bracket define an effective matrix element that is again finite and integrable in four space-time dimensions. Knowing the tree-level matrix elements and the dipole splitting functions, the Monte Carlo integration of Eq. (2.43) is straightforward. One simply generates an $m+1$-parton configuration and uses it to define an event with positive weight $+|\mathcal{M}_{m+1}|^2$ and several counter-events, each of them with the negative weight $-|\mathcal{M}_m|^2 \otimes \boldsymbol{V}_{ij}$. Then these event and counter-events are analysed by the user routine. The role of the two different jet functions $F_J^{(m+1)}$ and $F_J^{(m)}$ is that of binning the weighted event and counter-events into different bins of the jet observable. Any time that the generated $m+1$-parton configuration approaches a singular region, the event and one counter-event fall into the same bin and the cancellation of the large positive and negative weights takes place.

Having described the general structure of the NLO pQCD cross sections in NC DIS and their practical implementation in the program DISENT we can now specialize to the two classes of observables we will be studying in this thesis: the total inclusive and dijet differential cross sections.

2.4 Inclusive cross section

The NLO cross section for the inclusive NC e^+p deep inelastic scattering process:

$$e^+(l) + p(P) \rightarrow e^+(l') + X \tag{2.44}$$

receives contributions from the LO $\mathcal{O}(\alpha_s^0)$ simple quark-parton model (QPM) subprocess (see Fig. 2.3a):

$$e^+(l) + q_i(p_0) \longrightarrow e^+(l') + q_i(p_1) \tag{2.45}$$

and from the NLO $\mathcal{O}(\alpha_s)$ one-loop virtual corrections to the LO processes (see Fig. 2.3b) as well as from the real corrections due to the subprocesses with two partons in the final state shown in Fig. 2.4:

$$e^+(l) + q_i(p_0) \quad \longrightarrow \quad e^+(l') + q_i(p_1) + g(p_2) \tag{2.46}$$

$$e^+(l) + g(p_0) \quad \longrightarrow \quad e^+(l') + q_i(p_1) + \bar{q}_i(p_2) \; . \tag{2.47}$$

In the Eq. (2.44) to Eq. (2.46) the particles and partons four-momenta are indicated in parentheses; in the partonic processes, i labels the quark flavour ($i = u, d, s, c, \dots$) and the corresponding anti-quark processes obtained for $q_i \leftrightarrow \bar{q}_i$ are implied. Each process can proceed via the exchange of a photon or a Z^0 boson with four-momentum q.

For a given e^+p centre-of-mass energy ($\sqrt{s} = \sqrt{(l+P)^2}$), the kinematic of the process is completely specified by two variables. They are selected among the four-momentum transfer Q^2, the Bjorken scaling variable x_{Bj} and the inelasticity variable y, which are defined respectively as

$$Q^2 = -q^2 = -(l - l')^2, \quad x_{Bj} = \frac{Q^2}{2P \cdot q} \quad \text{and} \quad y = \frac{P \cdot q}{P \cdot l}. \tag{2.48}$$

Due to the completely inclusive nature of this observable, the NLO double differential inclusive cross section, $d\sigma_{tot}/dx_{Bj}dQ^2$, can be presented in closed analytical form and is conveniently expressed in terms of three *structure functions*:

$$\frac{d^2\sigma^{NC}(e^+p)}{dx_{Bj}dQ^2} = \frac{2\pi\alpha^2}{x_{Bj}Q^4}\left[Y_+ F_2(x_{Bj},Q^2) - y^2 F_L(x_{Bj},Q^2) - Y_- x_{Bj}F_3(x_{Bj},Q^2)\right] \qquad (2.49)$$

where $Y_\pm \equiv 1 \pm (1-y)^2$ and the NLO structure functions read:

$$\begin{aligned}
F_2(x_{Bj},Q^2) &= \sum_i A_i(Q^2)x_{Bj}f_{2,i}^{NLO}(x_{Bj},Q^2)\\
F_L(x_{Bj},Q^2) &= \sum_i A_i(Q^2)x_{Bj}f_{L,i}^{NLO}(x_{Bj},Q^2)\\
x_{Bj}F_3(x_{Bj},Q^2) &= \sum_i B_i(Q^2)x_{Bj}f_{3,i}^{NLO}(x_{Bj},Q^2)
\end{aligned} \qquad (2.50)$$

In this equation the sums run over the number of *active* quark flavours: $i = d,u,s,\ldots$.

The functions f_i $(i = 2,L,3)$ are expressed in terms of convolutions of the NLO parton densities with appropriate perturbative coefficient functions. Introducing the following combinations of quark and anti-quark densities

$$\begin{aligned}
xq_i^+ &= x(q_i + \bar{q}_i)\\
xq_i^- &= x(q_i - \bar{q}_i)
\end{aligned}$$

we have:

$$\begin{aligned}
xf_{2,i} &= xq_i^+ + \frac{\alpha_s(Q^2)}{2\pi}\left[C_{2,q}\otimes xq_i^+ + C_{2,g}\otimes xg\right]\\
xf_{L,i} &= \frac{\alpha_s(Q^2)}{2\pi}\left[C_{L,q}\otimes xq_i^+ + C_{L,g}\otimes xg\right]\\
xf_{3,i} &= xq_i^- + \frac{\alpha_s(Q^2)}{2\pi}\left[C_{3,q}\otimes xq_i^-\right]
\end{aligned} \qquad (2.51)$$

where xg is the gluon density and the convolution integrals are defined as:

$$C \otimes f(x,Q^2) = \int_x^1 \frac{dy}{y}\,C(x/y)\,f(y,Q^2). \qquad (2.52)$$

In the $\overline{\text{MS}}$ scheme (used in this analysis) the coefficient functions are:

$$\begin{aligned}
C_{2,q}^{\overline{\text{MS}}}(x) &= \frac{4}{3}\left[\frac{1+x^2}{1-x}\left(\ln\frac{1-x}{x} - \frac{3}{4}\right) + \frac{1}{4}(9+5x)\right]_+\\
C_{2,g}^{\overline{\text{MS}}}(x) &= \left[x^2 + (1-x)^2\right]\ln\left(\frac{1-x}{x}\right) - 1 + 8x(1-x)\\
C_{L,q}^{\overline{\text{MS}}}(x) &= \frac{8}{3}x\\
C_{L,g}^{\overline{\text{MS}}}(x) &= 4x(1-x)\\
C_{3,q}^{\overline{\text{MS}}}(x) &= C_{2,q}^{\overline{\text{MS}}}(x) - \frac{4}{3}(1+x)
\end{aligned} \qquad (2.53)$$

where the so-called '+' prescription is defined by:

$$[f(x)]_+ = f(x) - \delta(1-x)\int_0^1 f(y)dy. \qquad (2.54)$$

The coefficients A_i and B_i are given by [81]

$$
\begin{aligned}
A_i(Q^2) &= e_{q_i}^2 + 2e_e v_e e_{q_i} v_{q_i} P(Q^2) + (v_e^2 + a_e^2)(v_{q_i}^2 + a_{q_i}^2) P^2(Q^2) \\
B_i(Q^2) &= 2e_e a_e e_{q_i} v_{q_i} P(Q^2) + 4v_e a_e v_{q_i} a_{q_i} P^2(Q^2).
\end{aligned}
\tag{2.55}
$$

Here v and a are the vector and axial vector couplings which can be expressed in terms of the Weinberg angle θ_W through

$$
v_f = T_{3f} - 2e_f \sin^2 \theta_W \quad a_f = T_{3f}.
\tag{2.56}
$$

In Eq. (2.56) e_f is the charge of fermion f (being it quark or lepton) in units of the proton charge and T_{3f} is the z component of the weak isospin.

The function $P(Q^2)$ is proportional to the ratio of the propagators for Z^0 and γ exchange

$$
P(Q^2) = \frac{1}{4 \sin^2 \theta_W \cos^2 \theta_W} \frac{Q^2}{Q^2 + M_Z^2}.
\tag{2.57}
$$

The three terms of A_i in Eq. (2.55) correspond to the γ exchange, γZ^0 interference and Z^0 exchange contributions to F_2, respectively. The latter two contributions are strongly suppressed at low Q^2 by the Z^0 propagator and become important only at Q^2 values above a few thousand GeV^2. Likewise, the xF_3 contribution to NC $e^+ p$ scattering can be neglected at low Q^2.

The *electromagnetic*[7] structure function $F_2^{\text{em}}(x_{Bj}, Q^2)$ measured by the ZEUS collaboration is presented, for the low Q^2 region, in Fig. 2.5. The most remarkable feature of these measurement is the steep rise of $F_2^{\text{em}}(x_{Bj}, Q^2)$ in the low x_{Bj} region, resulting in a strong rise of the gluon and sea densities. In Fig. 2.6 the ZEUS, H1, and fixed-target measurements of $F_2^{\text{em}}(x_{Bj}, Q^2)$ are presented as a function of Q^2 for fixed x_{Bj} values. The data clearly show the well known pattern of *scaling violations*: at a fixed value of x_{Bj} the structure function $F_2^{\text{em}}(x_{Bj}, Q^2)$ increases or decreases (depending on the x_{Bj} value) as a function of Q^2.

The NLO QCD predictions for F_2^{em} obtained using different PDFs are also presented in Fig. 2.6 and show a remarkable agreement with the measurements. The $\mathcal{O}(\alpha_s)$ QCD processes discussed above are crucial in order to correctly reproduce the scaling violations, as it is immediately evident observing that:

$$
\frac{\partial F_2^{\text{em}}(x, Q^2)}{\partial Q^2} \sim \alpha_s(Q^2) x g(x, Q^2).
\tag{2.58}
$$

The observed scaling violations in the structure functions can hence be exploited in order to determine the strong coupling and the gluon density in the proton.

The high accuracy reached in structure function measurements at HERA has indeed allowed recently the *simultaneous* determination of the strong coupling constant $\alpha_s(M_Z)$ and the PDFs of the proton, with significative precision. The $\alpha_s(M_Z)$ values obtained by the H1 and ZEUS collaborations via a DGLAP fit of the measured structure functions are[8]:

$$
\alpha_s(M_Z) = 0.1150 \pm 0.0017 \text{ (exp.)} \, ^{+0.0009}_{-0.0005} \text{ (model)} \pm 0.0050 \text{ (th.)} \quad \text{H1}
\tag{2.59}
$$

$$
\alpha_s(M_Z) = 0.1172 \pm 0.0008 \text{ (stat.)} \pm 0.0054 \text{ (syst.)} \qquad \text{ZEUS Prel.}
\tag{2.60}
$$

The gluon densities extracted simultaneously to $\alpha_s(M_Z)$ are presented in Fig. 2.7.

---

[7]That is including only γ-exchange processes.

[8]The ZEUS preliminary result does not yet contain an estimate of the theoretical uncertainty on $\alpha_s(M_Z)$.

2.5   Dijet production in NC DIS

In this section we will consider the NC DIS process characterized by the presence of two high transverse energy hadronic jets in the final state:

$$e^+(l) + p(P) \longrightarrow e^+(l') + \text{Jet}_1 + \text{Jet}_2 + \text{X}. \tag{2.61}$$

The measurement of the differential cross sections relative to this process, as already shortly discussed in the introduction, is important because it allows to test the dynamics of the underlying QCD partonic processes (up to $\mathcal{O}(\alpha_s^2)$) at a more *exclusive* level with respect to, for example, the inclusive NC cross section discussed in the previous section. In the latter case the higher-order QCD processes produce a well defined pattern of scaling violations in the structure functions but give a rather indirect information on the energy and angle distributions of the finale-state partons. Provided that the hadronisation effects (responsible for the confinement of the partons in the final state into colourless hadrons) are small, the dijet cross sections are instead more suitable observables to obtain such detailed information. This is due to the preconfinement (or local parton-hadron duality) [20] property of QCD according to which the hadronic flow should follow the partonic flow quite closely, with transfers of momentum and other quantum numbers that is local in phase-space.

In order to quantitatively discuss the dijet cross sections we have to address the problem of the definition of a suitable jet algorithm, necessary to identify from the NC DIS events those with a dijet topology, and that of the optimal choice of the reference frame where to perform the jet-clustering procedure.

2.5.1   The Breit frame

Following the discussion given above, a high transverse energy hadronic jet should originate from a large transverse momentum parent parton. As a consequence, the most appropriate choice of the reference frame where to perform the jet-clustering would appear to be the one which allows the most natural separation between the high-p_T particles originating from the hard-scattering process from other soft particles present in the final state. The Breit frame[25], defined as the frame where $2x_{Bj}\mathbf{P} + \mathbf{q} = \mathbf{0}$, is characterized exactly by this property.

In the Breit frame, a purely space-like gauge boson (γ/Z^0) with four momentum $q_{\gamma/Z} = \{0, 0, 0, -Q\}$ collides head-on with a parton from the proton while the initial and scattered positron balance in p_T. Because in this frame (contrary to the HERA laboratory frame) the presence of the scattered positron does not bias the p_T distributions of the other final state partons, any high transverse momentum final state particle must necessarily come from the hard scattering process. Thus, in a QPM process, the incoming quark is back-scattered into the negative z direction (Fig. 2.8, left) and no transverse energy is produced. Only starting with $O(\alpha_s)$ partonic processes the final state contains partons of large transverse momentum (Fig. 2.8,right) which can be then identified by the jet algorithm. A cross section for the production of one or more high E_T jet in the Breit frame receives hence no contributions from the QPM processes and is directly sensitive to the strong coupling constant. From the above discussion it should be also clear that, in the Breit frame, the separation between the hard jets and the proton remnant is maximized.

The hadronic center-of-mass frame, being related to the Breit Frame by a longitudinal boost along the z direction, would provide an equally good choice. The choice of a jet algorithm which is invariant under longitudinal boosts (see next section) makes these two frames equivalent, as far as the calculation of dijet cross sections is concerned.

2.5.2 The longitudinally invariant $K_\perp$-cluster algorithm

The jet algorithm adopted in this analysis is the longitudinally invariant $K_\perp$-cluster algorithm [26] applied in the inclusive mode proposed by Ellis and Soper [27].

The clustering, which is performed in the Breit frame, proceeds according to the following prescription [9]:

1. for every pair of particles in the final state (i,j), a distance parameter is defined according to

$$d_{ij} = min(E_{Ti}^2, E_{Tj}^2) \cdot R_{ij}^2 \, , \qquad (2.62)$$

   where $R_{ij}^2 = (\eta_i - \eta_j)^2 + (\phi_i - \phi_j)^2$;

2. for every single particle i, the distance to the beam is defined as

$$d_i = E_{Ti}^2 R^2 \, , \qquad (2.63)$$

   where R is here chosen to be 1;

3. if, of all the values d_{ij} and d_i, d_{kl} is the smallest, the particles k and l are merged according to the Snowmass convention:

$$E_{Tkl} = E_{Tk} + E_{Tl} \ , \ \ \eta_{kl} = \frac{E_{Tk}\eta_k + E_{Tl}\eta_l}{E_{Tk} + E_{Tl}} \ , \ \ \phi_{kl} = \frac{E_{Tk}\phi_k + E_{Tl}\phi_l}{E_{Tk} + E_{Tl}} \ . \qquad (2.64)$$

   If instead d_k is the smallest of all values, then particle k is removed from the list of particles and added to the list of jets;

4. the steps 1 to 3 are repeated until all particles are assigned to jets.

5. from the complete list of jets obtained at the end of this iterative procedure, the final jets are then selected as the ones with the highest transverse energies in a given pseudorapidity region.

The choice of this jet algorithm is motivated on the ground of its theoretical and phenomenological superiority with respect to jet algorithms of the cone or JADE-like types.

The $K_\perp$-clustering algorithm is considered to be theoretically more sound:

- it is based on a jet resolution variable, namely the minimal relative transverse momentum between particles, which is naturally suggested by the present understanding of the pQCD evolution of partonic systems. The use of such a resolution variable, strongly reduce unnatural assignment of particles to jets and is particularly suitable to perform resummation of soft-gluon effects;

- as can be easily proved from the definition of the jet resolution variables in Eq. (2.62) and Eq. (2.63), this jet algorithm is infrared and collinear safe to all orders in α_s and allows the factorisation of the initial-state collinear singularities into the PDFs. Properties that, as we have already discussed, are crucial in order to be able to compute jet cross section at NLO.

Particularly relevant for a meaningful comparison between data and theory are also the following properties:

---

[9]In what follows E_{Ti}, η_i, and ϕ_i denote the transverse energy (with respect to the proton direction), pseudorapidity, and azimuthal angle of particle i in the Breit frame, respectively. The pseudorapidity is defined as $\eta = -\log(\tan(\frac{\theta}{2}))$, where θ is the polar angle with respect to the proton direction.

- by construction the algorithm avoids configurations with overlapping jets;

- an identical clustering procedure is used in experimental analyses and/or theoretical calculations. Thus, the set of four-momenta used by the algorithm can be the one associated with the partons in a NLO program or the one reconstructed from the energy deposits and/or tracks measured in the detector.

- Monte Carlo studies demonstrate that jet cross sections obtained with the $K_\perp$ algorithm are affected by smaller hadronisations corrections.

These properties of the $K_\perp$-cluster algorithm are by now largely documented in the literature (see e.g. [26, 28, 29]) and will be not further discussed here.

2.5.3   Dijet cross sections

Having defined the adopted jet algorithm, we can now discuss the partonic processes that contribute to the NLO dijet cross sections in the Breit frame.

LO processes

At leading order, the dijet cross sections receive contributions from the $\mathcal{O}(\alpha_\mathrm{s})$ QCD-Compton

$$e^+(l) + q_i(p_0) \longrightarrow e^+(l') + q_i(p_1) + g(p_2) \tag{2.65}$$

and Boson-Gluon fusion (BGF)

$$e^+(l) + g(p_0) \longrightarrow e^+(l') + q_i(p_1) + \bar{q}_i(p_2) \tag{2.66}$$

processes (see Fig. 2.4) that we have already encountered in the discussion of the inclusive DIS cross section. In addition to the standard variables x_{Bj} and Q^2, we need three further variables to the describe the kinematic of the LO processes. These are usually chosen to be z_p, x_p (or alternatively ξ), and ϕ. The variable ϕ denotes the azimuthal angle between the leptonic and partonic planes in the boson-parton center-of-mass frame. The remaining variables are defined as

$$z_p = \frac{p_0 \cdot p_1}{p_0 \cdot q} \,, \quad x_p = \frac{Q^2}{2p_0 \cdot q} \quad \text{and} \quad \xi = x_{Bj} \cdot (1 + \frac{M_{12}^2}{Q^2}) \tag{2.67}$$

where M_{12} is the invariant mass of the two final-state partons. At LO the variable ξ represents the fraction of the proton four-momentum carried by the uncoming parton.

In terms of these variables the soft and collinear singularities of the LO amplitudes for the QCD-Compton and BGF processese are easily exhibited:

$$|\mathcal{M}_2^{QCDC}|^2 \quad \sim \quad \alpha_\mathrm{s} \cdot \frac{x_p^2 + z_p^2}{(1 - z_p)(1 - x_p)} \tag{2.68}$$

$$|\mathcal{M}_2^{BGF}|^2 \quad \sim \quad \alpha_\mathrm{s} \cdot \frac{\left[x_p^2 + (1 - x_p)^2\right]\left[z_p^2 + (1 - z_p)^2\right]}{z_p(1 - z_p)} \tag{2.69}$$

These amplitudes diverge for $z_p \to 0, 1$ and $x_p \to 1$, which correspond to the following kinematic configurations

$$
\begin{aligned}
p_1 \ \text{collinear to} \ p_0 \ &\Rightarrow \ z_p \to 0 \,, \\
p_2 \ \text{collinear to} \ p_0 \ &\Rightarrow \ z_p \to 1 \,, \\
p_1 \ \text{collinear to} \ p_2 \ &\Rightarrow \ x_p \to 0 \,, \\
p_1 \ \text{soft} \ &\Rightarrow \ z_p \to 0 \,, \\
p_2 \ \text{soft} \ &\Rightarrow \ z_p, x_p \to 1 \,.
\end{aligned}
\tag{2.70}
$$

These divergencies are, however, harmless because the $K_\perp$-cluster algorithm always require the application of a minimum transverse energy cut on the reconstructed jets:

$$E_T^{jet} > E_{T,min}^{jet} > 0. \qquad (2.71)$$

which has the effect of removing, from the integration of the LO partonic cross sections over the two-parton final state, the singular regions in (2.70). The requirement Eq. (2.71) represents the practical implementation, in the case of the $K_\perp$-cluster algorithm, of the safety condition Eq. (2.28) discussed on a general basis for the jet function, F_J, in section 2.2.

The final LO cross section is finally obtained convoluting the integrated partonic cross section with PDFs. An inportant qualitative difference between the dijet and inclusive cross sections is that the former are directly (i.e already at LO) sensitive to strong coupling constant and, via the BGF process, to the gluon density in the proton. The dijet cross section hence provide, in principle, an ideal observable to determine both the strong coupling constant and the gluon density.

NLO processes

In order to make quantitative prediction for the dijet cross sections it is necessary, as already discussed, to include at least the NLO contributions. At NLO one has to consider the $\mathcal{O}(\alpha_{\mathrm{s}}^2)$ real and virtual corrections to the LO QCDC and BGF processes. The real corrections (see Fig. 2.9) are a first step in the modeling of the internal structure of the jet, introducing thus a dependence of the jet cross sections on the exact definition of the jet algorithm. The virtual corrections (see Fig. 2.10) have the effect of introducing a dependence of the perturbative cofficient functions on the renormalization scale which cancel part of the dependence in α_{s}.

In the next chapter we will present the DISENT NLO pQCD predictions obtained for a large set of single differential dijet cross sections calculated on a phase-space region carefully selected in order to minimize their associated theoretical uncertainties. More precisely we will present predictions for the dijet cross sections as a function of the jets transverse energies ($E_{T,B}^{\text{jet1,2}}$) and pseudorapidities ($\eta_B^{\text{jet1,2}}$) in the Breit frame, as well as a function of Q^2, z_p, x_{Bj}, ξ, and the dijet invariant mass M_{jj}. The dijet fraction

$$R_{2+1}(Q^2) = \frac{d\sigma_{2+1}/dQ^2}{d\sigma_{\text{tot}}/dQ^2}, \qquad (2.72)$$

will prove, in particular, to be very well suited to reduce *both* theoretical and experimental uncertainties.

The comparison of these NLO QCD predictions with corresponding measured observables will allow to perform a detailed test of the framework provided by the QCD-improved parton model, to test the dynamics of the $\mathcal{O}(\alpha_{\mathrm{s}}^2)$ partonic processes, and to achieve a precise determination the strong coupling constant.

2.6 Summary on α_{s}

One of the goals of the present analysis is the determination of the strong coupling constant at the reference scale provided by the mass of the Z^0 boson, $\alpha_s(M_Z)$, and a test of its energy scale dependence. We would like then to conclude this chapter by briefly mentioning the results of the two most recent estimates provided by the Particle Data Group [22](PDG) and S. Betkhe [23] of the world average value for $\alpha_s(M_Z)$.

A large number of high-energy physics processes and observables, in conjunction with a wide range of QCD analysis methods, have been used to determine α_{s} and new determinations are

continually being reported. Significant determinations of the strong coupling have been obtained from DIS and e^+e^- annihilation processes, as well as from the energy levels of heavy quarkonia systems calculated using lattice QCD. Without entering into a detailed discussion of the various determinations of α_s (for which we refer to [22, 23]) we present in Table 2.4 and Fig. 2.11 the α_s determinations used by Bethke in order to quote his α_s world average (a similar set of results has been used in the PDG analysis). In the table, the results are given both at the relevant energy scale of the process $\alpha_s(Q)$ and at the standard reference scale of the Z^0 mass. In the latter case the experimental and theoretical uncertainty are presented separately. The last column of the table indicates the level of the QCD theoretical calculations on which these results are based. The results for $\alpha_s(Q)$ are presented in Fig. 2.12 together with the 4-loop QCD predictions for the running α_s (with 3-loop matching at the quark pole masses). The data are in good agreement with the theoretical expectation, and significantly prove the running of the strong coupling.

The uncertainties of most of the α_s results are dominated by theoretical uncertainties which are estimated using different methods. The significance of these (mostly non-gaussian) errors is largely unclear. As a consequence, the estimate of a world average value for $\alpha_s(M_Z)$ and in particular its associated uncertainty is a highly non trivial task, which strongly depend on the statistical treatment adopted in the averaging procedure. In Table 2.5 (again taken from [23]), we present the results on the α_s averages obtained under different criteria adopted for the selection of the input α_s values and different averaging strategies. The average values obtained under different selection criteria do not show significant biases within the corresponding uncertainties. Alternative averaging methods result in an uncertainty on $\alpha_s(M_Z)$ which approximately ranges from ± 0.0020 to ± 0.0060.

Using the five most significant determinations of α_s based on full NNLO pQCD analyses, Bethke quotes as the currently best estimate of the world average value of $\alpha_s(M)$:

$$\alpha_s(M_Z) = 0.1184 \pm 0.0031 \quad \text{(Bethke : NNLO pQCD).} \tag{2.73}$$

A very similar average is obtained by the PDG:

$$\alpha_s(M_Z) = 0.1181 \pm 0.0020 \quad \text{(PDG : NLO and NNLO pQCD),} \tag{2.74}$$

which has a slightly smaller uncertainty due to the PDG assumption to treat all the α_s values used in the average as uncorrelated. Because these final uncertainties are mostly dominated by theoretical errors and given the above remarks on the difficulty of a realistic estimate of the latter it is likely that the above quoted uncertainties represent only a lower limit of the real uncertainty.

Although the present uncertainty on $\alpha_s(M_Z)$ is a success for QCD, it has to be pointed out that the strong coupling constant is among the other couplings of the Standard Model (SM) the one known with lowest precision (see Table 2.3). There are various reasons that suggest to put a large experimental and theoretical effort in order to achieve an improved determination of $\alpha_s(M_Z)$:

1. The strong coupling is the basic parameter of QCD in the high-energy perturbative regime and its precision limits the precision of any observable computed via a fixed order perturbative expansion.

2. In the wider frame of the Standard Model of the strong and electroweak interactions $SU(3) \otimes SU(2) \otimes U(1)$, an improved determination of the strong coupling would be also highly desirable. The very precise data sets collected at the LEP collider are now putting under a very stringent test the SM predictions. The precision of this data is such that the simple tree level SM predictions are not sufficient in order to describe a large set of e^+e^- observables and full electro-weak and QCD radiative corrections have to be included. In

this context an improved determination of the strong coupling and the mass of the top quark, which affect the SM model predictions via the QCD radiative corrections, would certainly allow more stringent limits on the mass of the yet undiscovered Higgs boson (see e.g. Fig. 2.13) or alternatively could help in revealing internal inconsistencies of the SM in its present form.

3. Finally, a more accurate determination of $\alpha_s(M_Z)$, would have a profound impact on the possibility to discriminate between possibile extentions of the SM. A testing ground of grand unified theories (GUT) is in fact the very appealing idea of strict unification of the three coupling constants of the SM:

$$\alpha_1 = \frac{5}{3}\frac{\alpha_{em}}{\cos(\theta_W)^2} \tag{2.75}$$

$$\alpha_2 = \frac{\alpha_{em}}{\sin(\theta_W)^2} \tag{2.76}$$

$$\alpha_3 = \alpha_s(M_Z) \tag{2.77}$$

at some high energy scale (M_{GUT}), given their values at the Z^0-pole mass (see Fig. 2.14 and Fig. 2.15). While a large class of supersymmetric or string based theories predict couplings unification, the possibility to discriminate among the various models (or among possible realizations of this unification within a given model) is presently strongly hampered by the still large uncertainty on α_s.

n_f	$\beta_0^{(n_f)}$	$\beta_1^{(n_f)}$	$\beta_2^{(n_f)}$	$\beta_3^{(n_f)}$
3	$\frac{9}{4}$	4	$\frac{3863}{384}$	$\frac{445}{32}\zeta(3) + \frac{140599}{4608}$
4	$\frac{25}{12}$	$\frac{77}{24}$	$\frac{21943}{3456}$	$\frac{78535}{5184}\zeta(3) + \frac{4918247}{373248}$
5	$\frac{23}{12}$	$\frac{29}{12}$	$\frac{9769}{3456}$	$\frac{11027}{648}\zeta(3) - \frac{598391}{373248}$
6	$\frac{7}{4}$	$\frac{13}{8}$	$-\frac{65}{128}$	$\frac{11237}{576}\zeta(3) - \frac{63559}{4608}$

Table 2.1: $\overline{\text{MS}}$ values of $\beta_i^{(n_f)}$ for variable n_f.

number of loops	highest coefficient in β function	$\alpha_s^{(5)}(m_b)$		
		(a)	(b)	(c)
1	β_0	0.2059	0.2059	0.2059
2	β_1	0.2123	0.2173	0.2161
3	β_2	0.2166	0.2164	0.2167
4	β_3	0.2174	0.2173	0.2169

Table 2.2: $\alpha_s^{(5)}(m_b)$ computed from $\alpha_s^{(5)}(M_Z) = 0.118$ using different evolution equations and number of loops (see text for details).
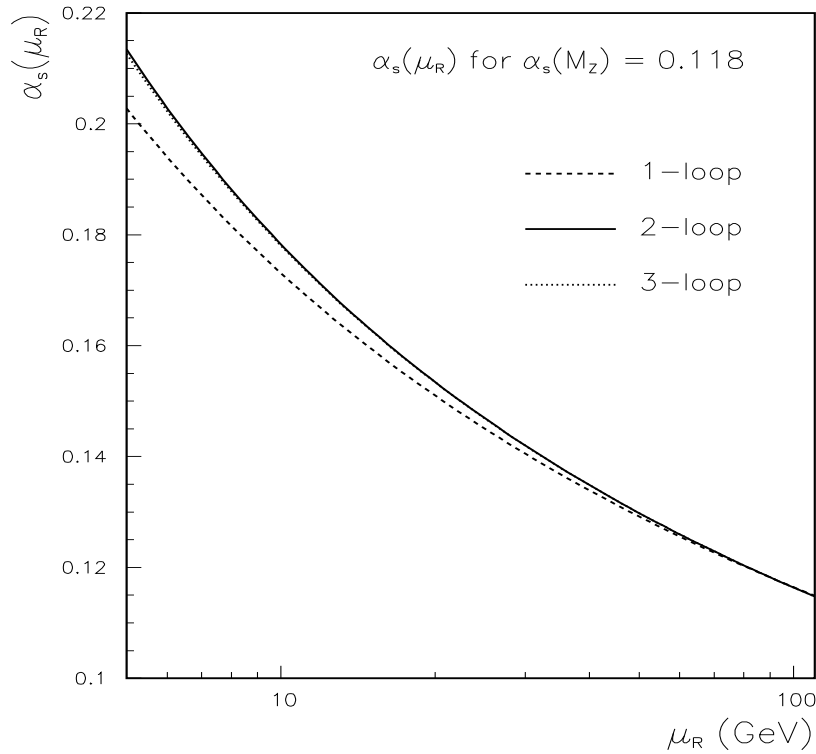
Figure 2.1: A comparison of the 1-,2-, and 3-loop $\overline{\text{MS}}$ solutions of the Callan-Symanzik equation for $\alpha_s(M_Z) = 0.118$.
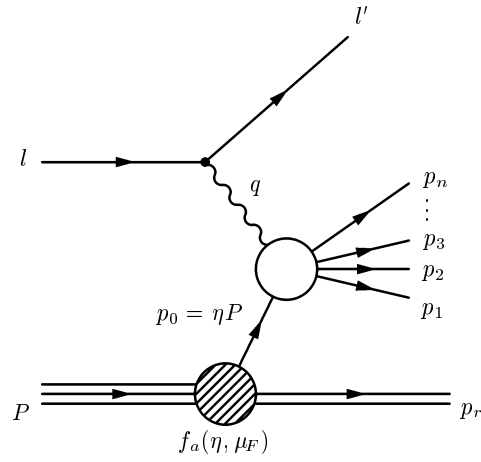
Figure 2.2: A NC DIS process with n partons in the final state.
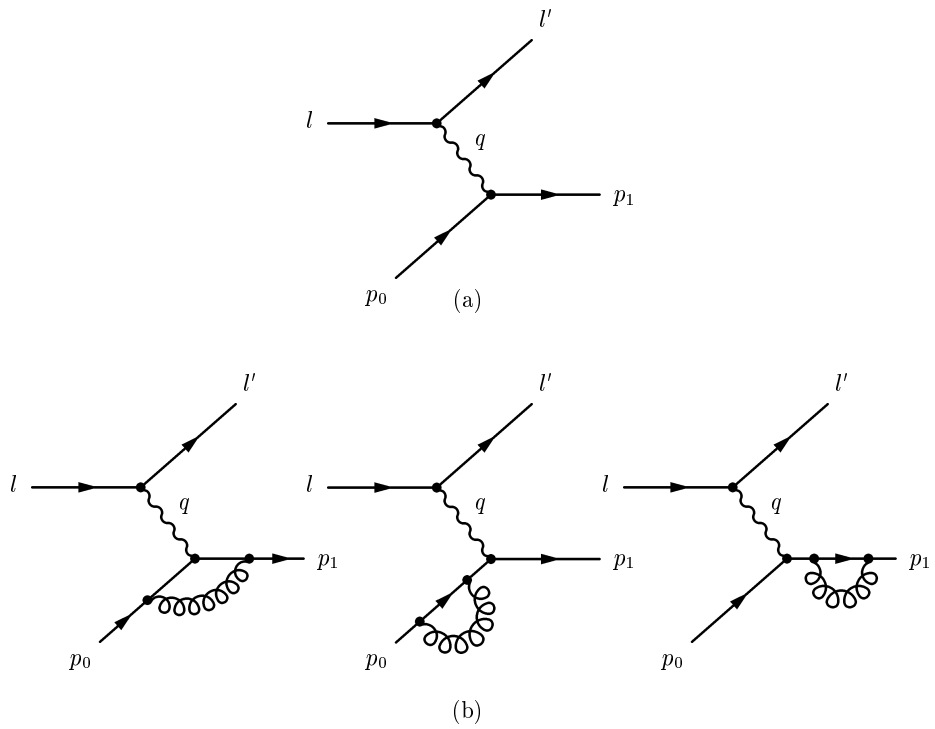
Figure 2.3: (a) The Quark parton model (QPM) diagram and (b) its virtual gluon corrections.
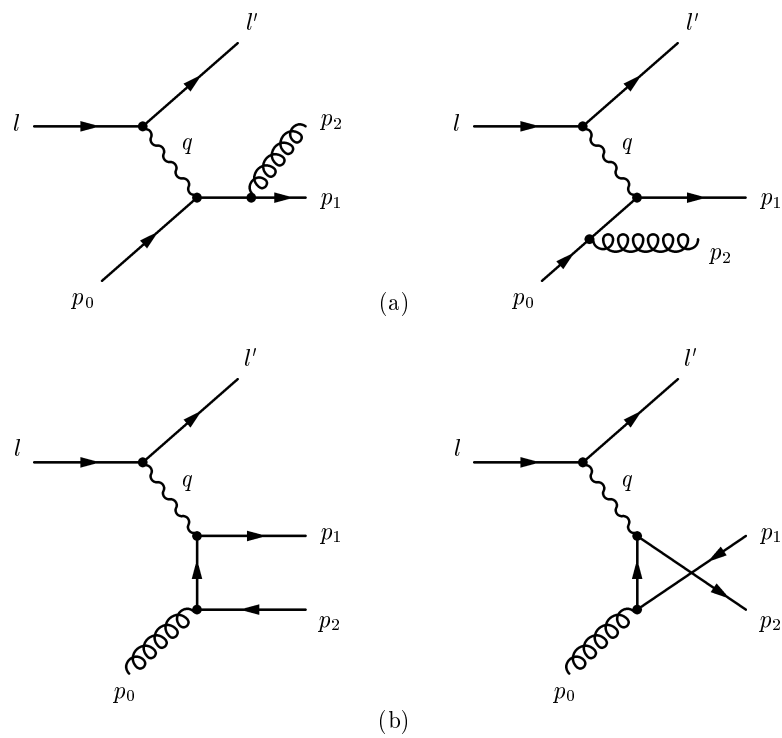
Figure 2.4: (a) The QCD-Compton diagrams and (b) the Boson-gluon fusion diagrams.
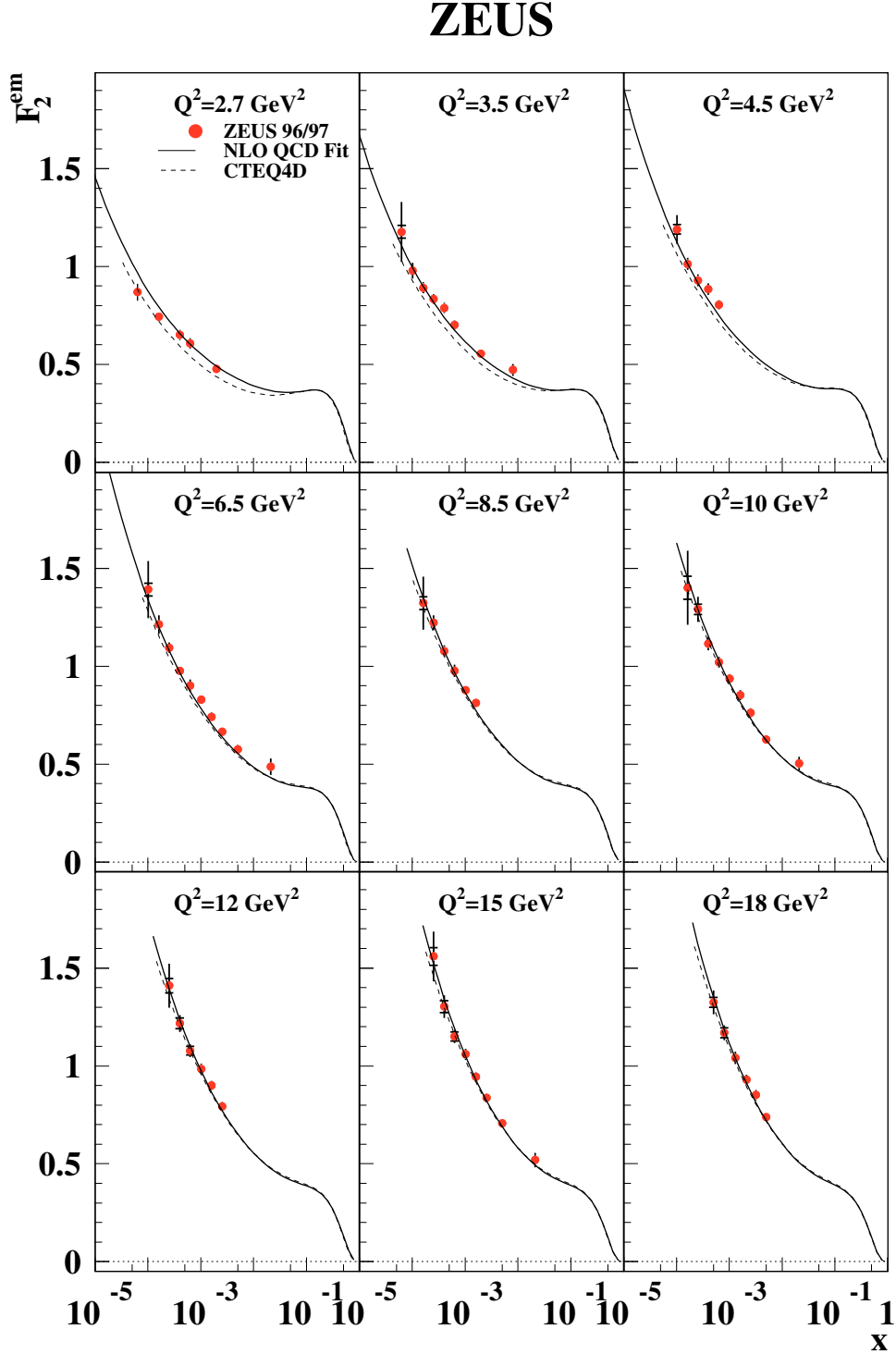
ZEUS

Figure 2.5: The ZEUS measured electromagnetic structure function F_2^{em} (black dots) as a function of x for nine Q^2 bins. The full curves show results from the ZEUS NLO QCD fit and the dashed curves show the predictions from CTEQ4D. The inner error bars indicate the statistical uncertainties; the outer ones show the statistical and systematic uncertainties added in quadrature.
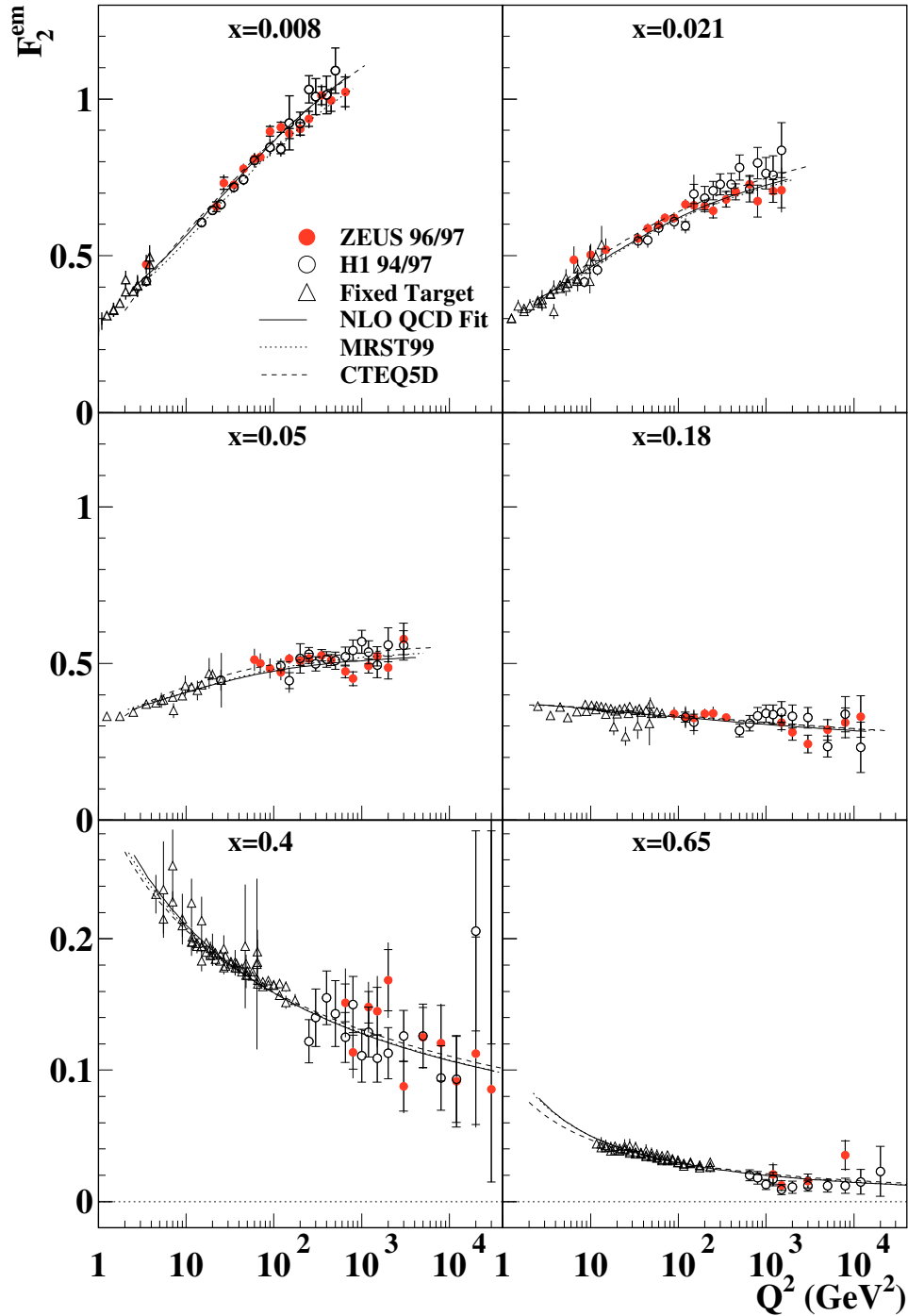
Figure 2.6: The ZEUS measurements for F_2^{em} versus Q^2, for six bins at fixed x, are compared with the results from NMC,BCDMS, E665 (triangles) and the recently published H1 results (open symbols). The inner error bars indicate the statistical uncertainties; the outer ones show the statistical and systematic uncertainties added in quadrature.
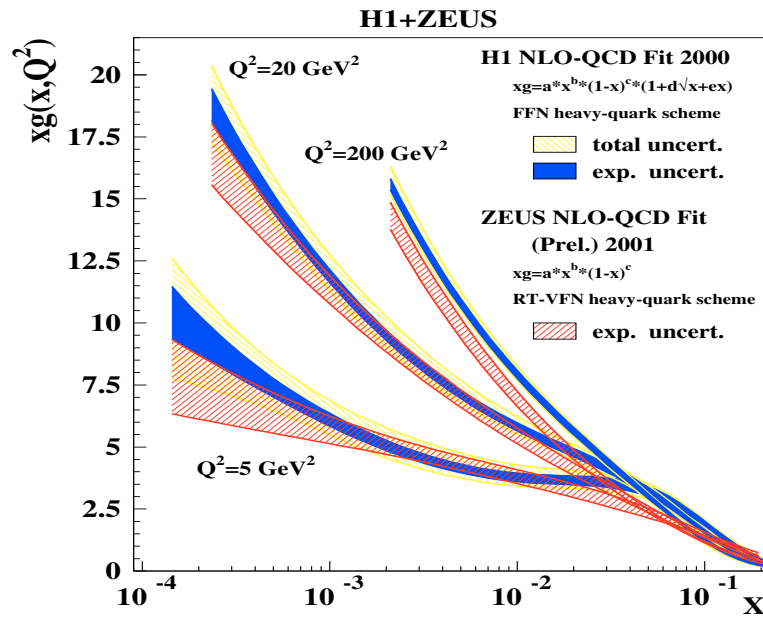
Figure 2.7: The ZEUS (preliminary) and H1 gluon densities as obtained from a DGLAP fit of HERA and fixed-target data. In the fit the PDFs were determined simultaneously with strong coupling constant α_{s}.
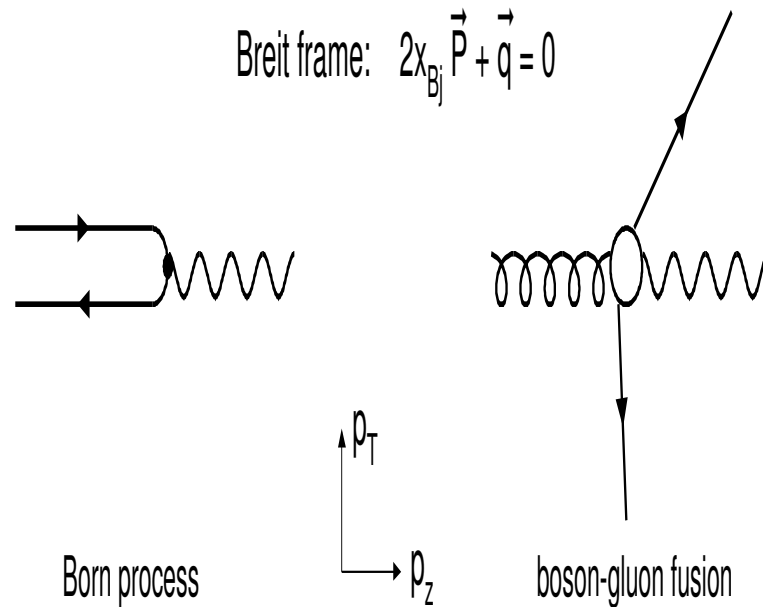
Figure 2.8: DIS processes in the Breit frame: $O(\alpha_{\mathrm{s}}^0)$ QPM process (left) and $O(\alpha_{\mathrm{s}})$ Boson-gluon fusion (right).
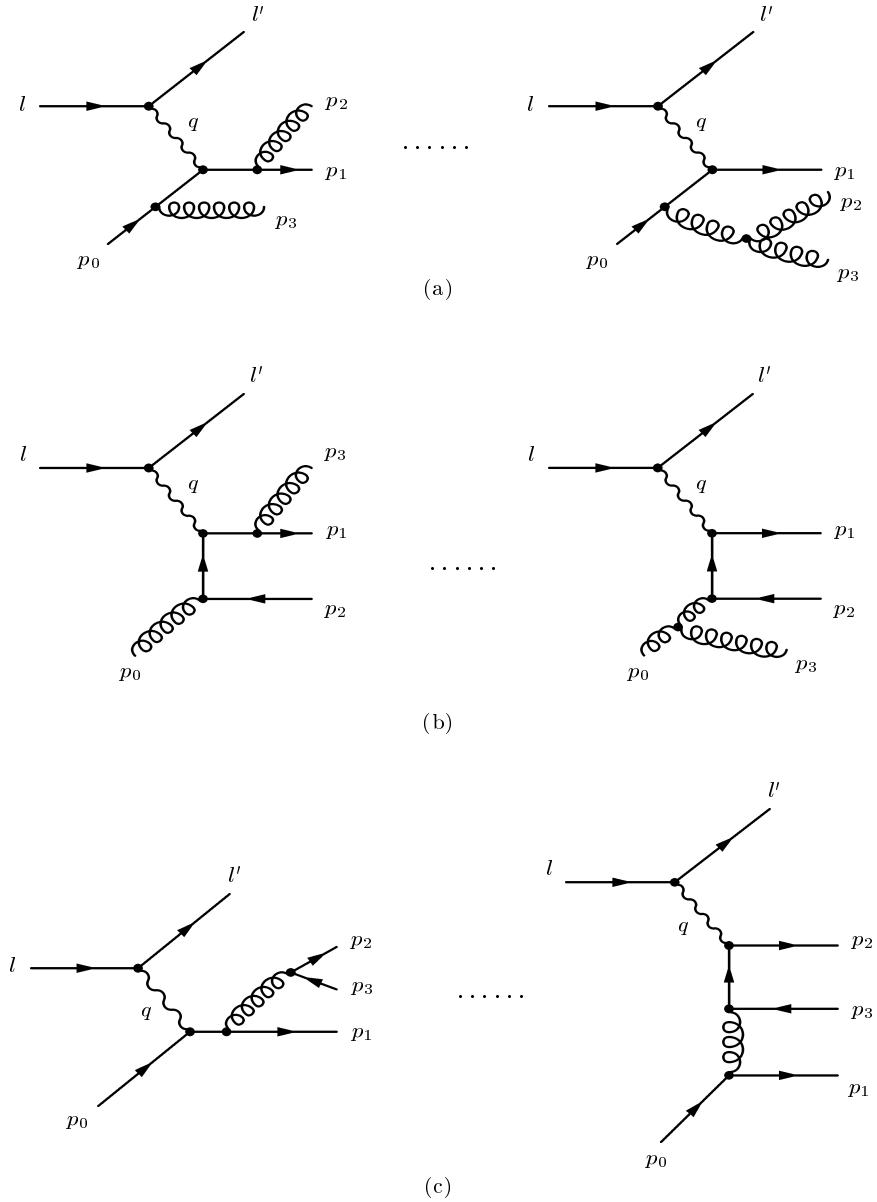
Figure 2.9: Real corrections to the QCD-Compton and BGF processes. Only two out of eight diagrams are shown for each class.
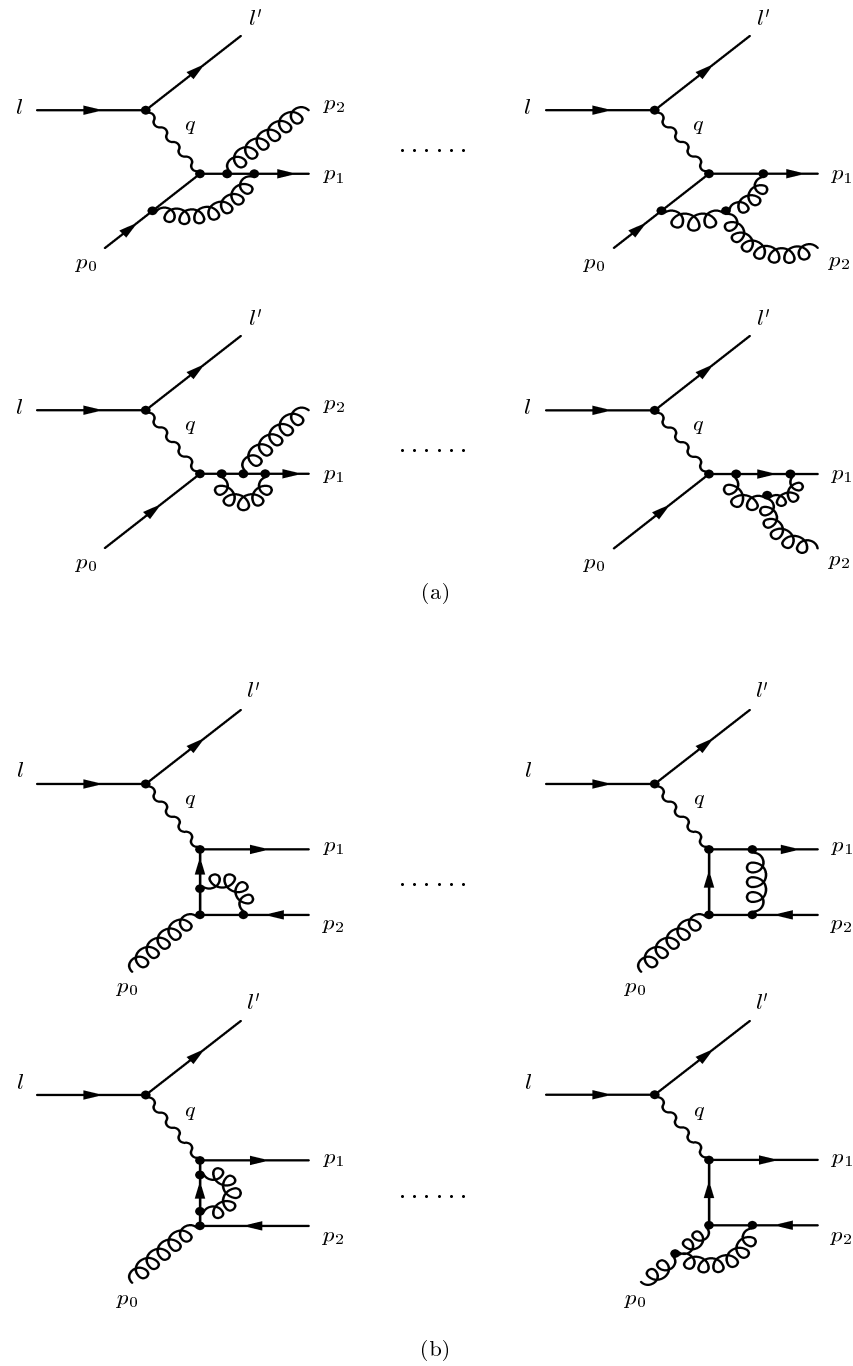
Figure 2.10: Virtual-gluon corrections to the QCD-Compton and BGF processes.

Constant	Value	Uncertainty (ppb)
$\alpha_{em}(0)$	1/137.03599976(50)	3.7
$\sin^2(\theta_W)(M_Z)$	0.23117(16)	7×10^5
$\alpha_s(M_Z)$	0.1181(20)	1.7×10^7

Table 2.3: The coupling constants of the Standard Model. The figures in parentheses after the values give the one-standard deviation uncertainty; the corresponding uncertainties in part per billion (ppb) are given in the last column (from [22]).

| Process	Q [GeV]	$\alpha_s(Q)$	$\alpha_s(M_{Z^0})$	$\Delta\alpha_s(M_{Z^0})$ exp.	theor.	Theory
DIS [pol. strct. fctn.]	0.7 - 8		$0.120 \; {}^{+\,0.010}_{-\,0.008}$	${}^{+0.004}_{-0.005}$	${}^{+0.009}_{-0.006}$	NLO
DIS [Bj-SR]	1.58	$0.375 \; {}^{+\,0.062}_{-\,0.081}$	$0.121 \; {}^{+\,0.005}_{-\,0.009}$	$-$	$-$	NNLO
DIS [GLS-SR]	1.73	$0.280 \; {}^{+\,0.070}_{-\,0.068}$	$0.112 \; {}^{+\,0.009}_{-\,0.012}$	${}^{+0.008}_{-0.010}$	0.005	NNLO
τ-decays	1.78	0.323 ± 0.030	0.1181 ± 0.0031	0.0007	0.0030	NNLO
DIS [ν; xF_3]	5.0	0.214 ± 0.021	0.118 ± 0.006	0.005	0.003	NNLO
DIS [e/μ; F_2]	2.96	0.252 ± 0.011	0.1172 ± 0.0024	0.0017	0.0017	NNLO
DIS [e-p; jets]	6 - 100		0.118 ± 0.011	0.002	0.011	NLO
$Q\overline{Q}$ states	4.1	0.216 ± 0.022	0.115 ± 0.006	0.000	0.006	LGT
Υ decays	4.75	0.22 ± 0.02	0.118 ± 0.006	$-$	$-$	NNLO
e^+e^- [σ_{had}]	10.52	$0.20 \; \pm 0.06$	$0.130 \; {}^{+\,0.021}_{-\,0.029}$	${}^{+\,0.021}_{-\,0.029}$	0.002	NNLO
e^+e^- [jets & shapes]	22.0	$0.161 \; {}^{+\,0.016}_{-\,0.011}$	$0.124 \; {}^{+\,0.009}_{-\,0.006}$	0.005	${}^{+0.008}_{-0.003}$	resum
e^+e^- [jets & shapes]	35.0	$0.145 \; {}^{+\,0.012}_{-\,0.007}$	$0.123 \; {}^{+\,0.008}_{-\,0.006}$	0.002	${}^{+0.008}_{-0.005}$	resum
e^+e^- [σ_{had}]	42.4	0.144 ± 0.029	0.126 ± 0.022	0.022	0.002	NNLO
e^+e^- [jets & shapes]	44.0	$0.139 \; {}^{+\,0.011}_{-\,0.008}$	$0.123 \; {}^{+\,0.008}_{-\,0.006}$	0.003	${}^{+0.007}_{-0.005}$	resum
e^+e^- [jets & shapes]	58.0	0.132 ± 0.008	0.123 ± 0.007	0.003	0.007	resum
$p\bar{p} \to b\bar{b}X$	20.0	$0.145 \; {}^{+\,0.018}_{-\,0.019}$	0.113 ± 0.011	${}^{+\,0.007}_{-\,0.006}$	${}^{+\,0.008}_{-\,0.009}$	NLO
$p\bar{p}$, pp $\to \gamma X$	24.3	$0.135 \; {}^{+\,0.012}_{-\,0.008}$	$0.110 \; {}^{+\,0.008}_{-\,0.005}$	0.004	${}^{+\,0.007}_{-\,0.003}$	NLO
$\sigma(p\bar{p} \to$ jets)	30 - 500		0.121 ± 0.010	0.008	0.005	NLO
e^+e^- [$\Gamma(Z^0 \to$ had.)]	91.2	0.124 ± 0.005	0.124 ± 0.005	0.004	${}^{+0.003}_{-0.002}$	NNLO
e^+e^- scaling viol.	14 - 91.2		0.125 ± 0.011	${}^{+\,0.006}_{-\,0.007}$	0.009	NLO
e^+e^- [jets & shapes]	91.2	0.121 ± 0.006	0.121 ± 0.006	0.001	0.006	resum
e^+e^- [jets & shapes]	133.0	0.113 ± 0.008	0.120 ± 0.007	0.003	0.006	resum
e^+e^- [jets & shapes]	161.0	0.109 ± 0.007	0.118 ± 0.008	0.005	0.006	resum
e^+e^- [jets & shapes]	172.0	0.104 ± 0.007	0.114 ± 0.008	0.005	0.006	resum
e^+e^- [jets & shapes]	183.0	0.109 ± 0.005	0.121 ± 0.006	0.002	0.005	resum
e^+e^- [jets & shapes]	189.0	0.110 ± 0.004	0.123 ± 0.005	0.001	0.005	resum

Table 2.4: World summary of α_s measurements (DIS = deep inelastic scattering; GLS-SR = Gross-Llewellyn-Smith sum rule; Bj-SR = Bjorken sum rule; (N)NLO = (next-to-)next-to-leading order perturbation theory; LGT = lattice gauge theory; resum = resummed NLO).
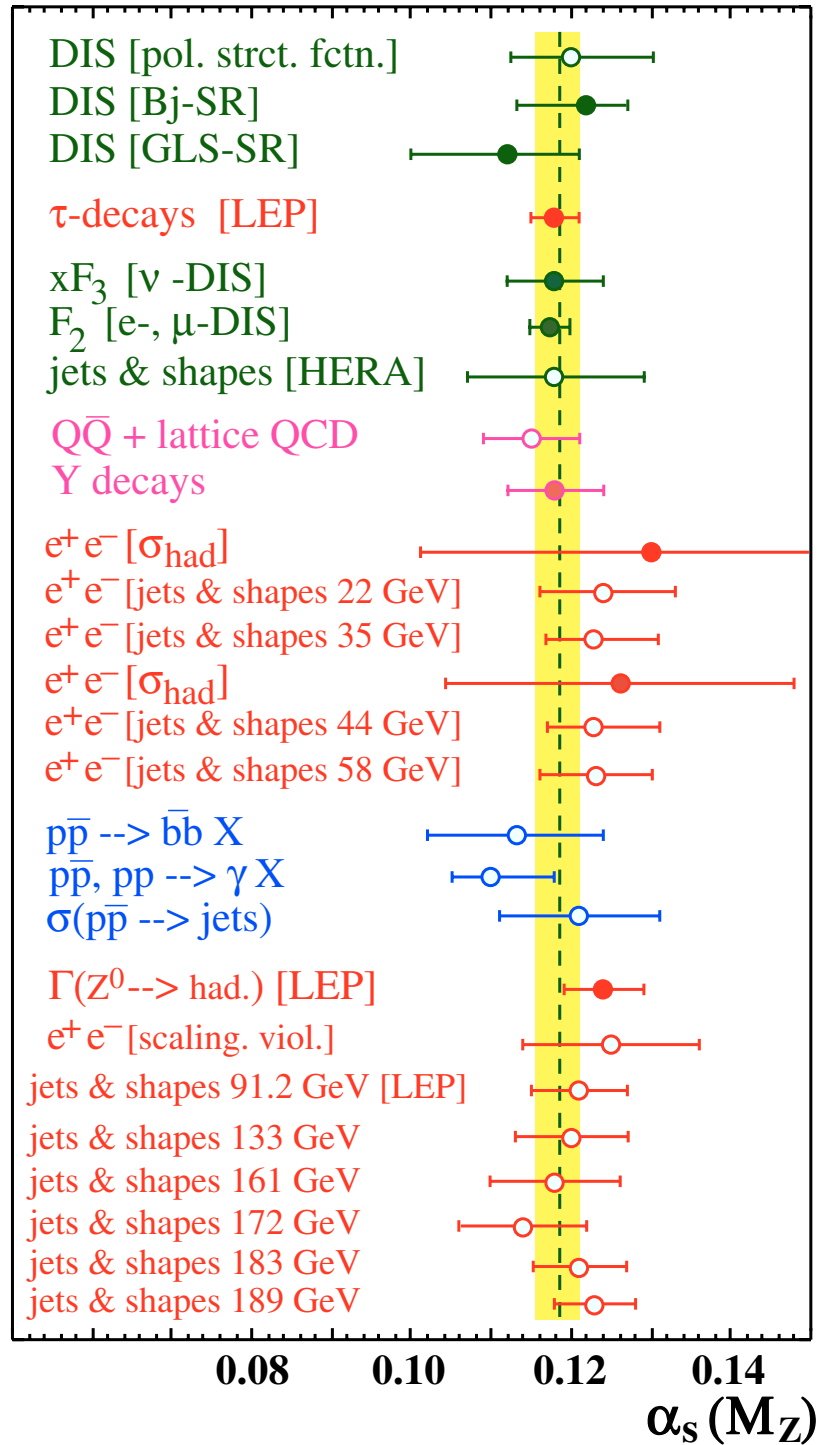
Figure 2.11: Summary of $\alpha_s(M_Z)$

row	sample (entries)	$\overline{\alpha_s}(M_{Z^0})$	opt. corr. $\Delta\overline{\alpha_s}$	overall correl.	uncorrel. $\Delta\overline{\alpha_s}$	simple rms $\Delta\overline{\alpha_s}$	rms box $\Delta\overline{\alpha_s}$
1	all (26)	0.1191	0.0045	0.71	0.0012	0.0043	0.0057
2	$\Delta\alpha_s \le 0.010$ (20)	0.1191	0.0041	0.66	0.0012	0.0037	0.0051
3	$\Delta\alpha_s \le 0.008$ (18)	0.1190	0.0039	0.62	0.0012	0.0038	0.0050
4	$\Delta\alpha_s \le 0.006$ (9)	0.1188	0.0033	0.64	0.0014	0.0029	0.0038
5	$\Delta\alpha_s \le 0.005$ (4)	0.1189	0.0022	0.28	0.0017	0.0034	0.0033
6	NNLO only (9)	0.1185	0.0035	0.78	0.0016	0.0045	0.0048
7	$\Delta\alpha_s \le 0.008$ (6)	0.1184	0.0031	0.68	0.0016	0.0026	0.0032
8	$\Delta\alpha_s \le 0.005$ (3)	0.1184	0.0022	0.27	0.0018	0.0037	0.0028
9	$\Delta\alpha_s \le 0.004$ (2)	0.1175	0.0026	0.95	0.0019	0.0006	0.0019
10	only DIS (6)	0.1178	0.0040	0.94	0.0020	0.0014	0.0047
11	only e^+e^- (15)	0.1209	0.0051	0.79	0.0016	0.0038	0.0054
12	only $p\overline{p}$ (3)	0.1135	0.0074	0.60	0.0051	0.0059	0.0068
13	$Q \le 10$ GeV (9)	0.1177	0.0040	0.93	0.0016	0.0017	0.0042
14	$10 < \frac{Q}{\text{GeV}} < 90$ (9)	0.1202	0.0064	0.56	0.0029	0.0062	0.0077
15	$Q \ge 90$ GeV (8)	0.1213	0.0056	0.78	0.0023	0.0035	0.0050

Table 2.5: Average values of $\overline{\alpha_s}(M_{Z^0})$ and averaged uncertainties, for several methods to estimate the latter, and for several subsamples of the available data.
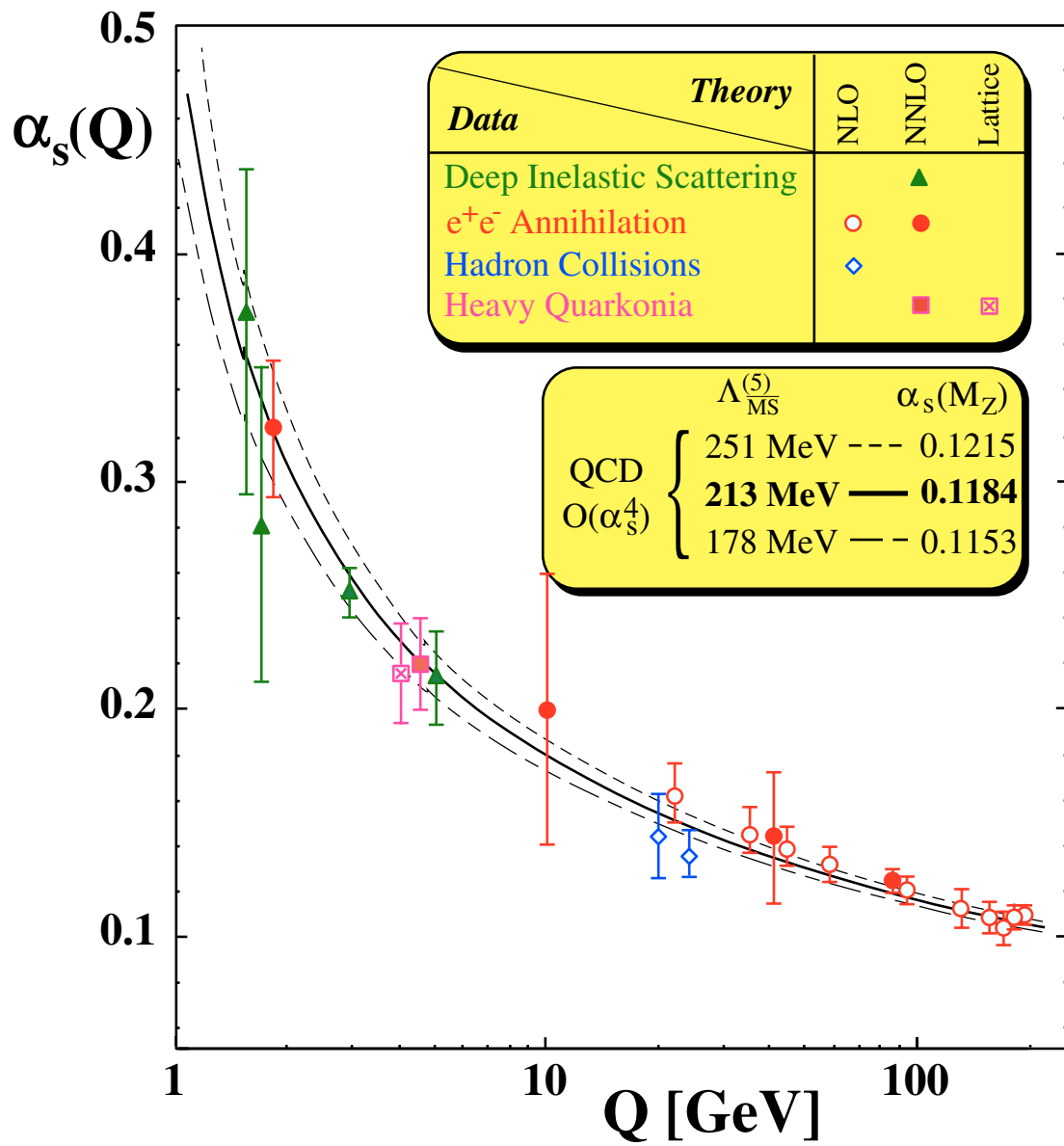
Figure 2.12: Summary of $\alpha_s(Q)$
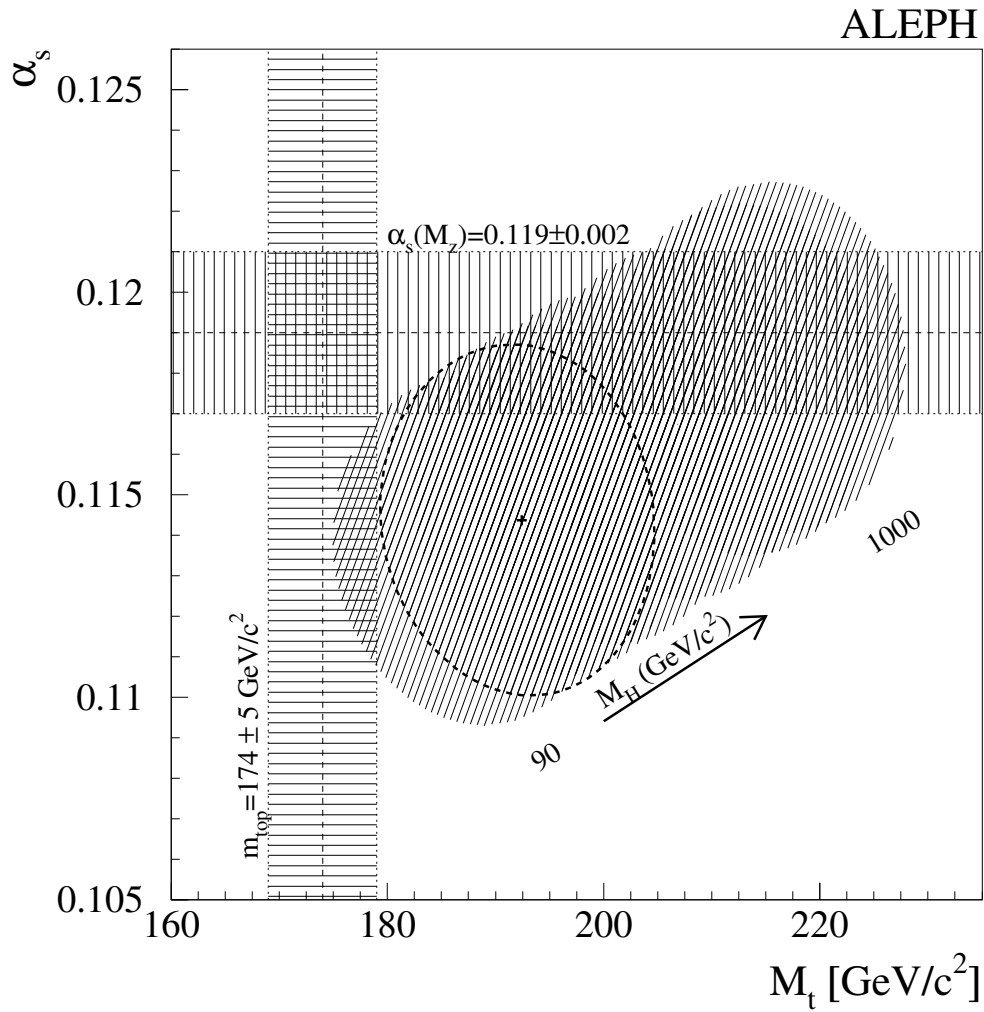
Figure 2.13: A simultaneus fit of $\alpha_s(M_Z)$, m_{top}, and the Higgs mass M_H from ALEPH.
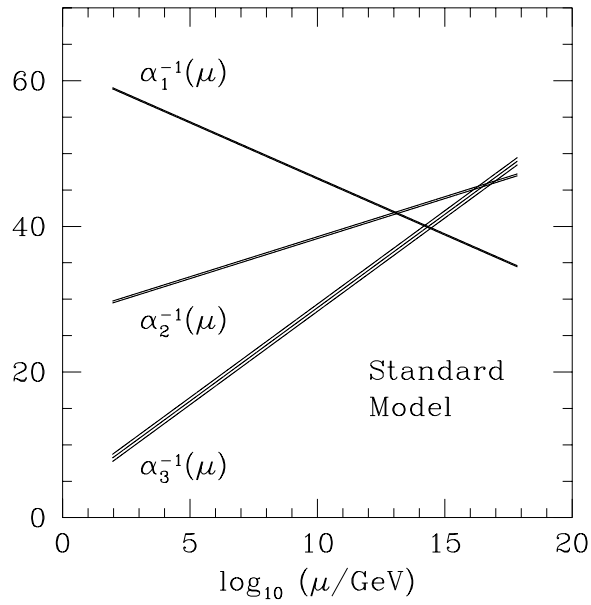
Figure 2.14: Gauge couplings unification picture in the Standard Model.
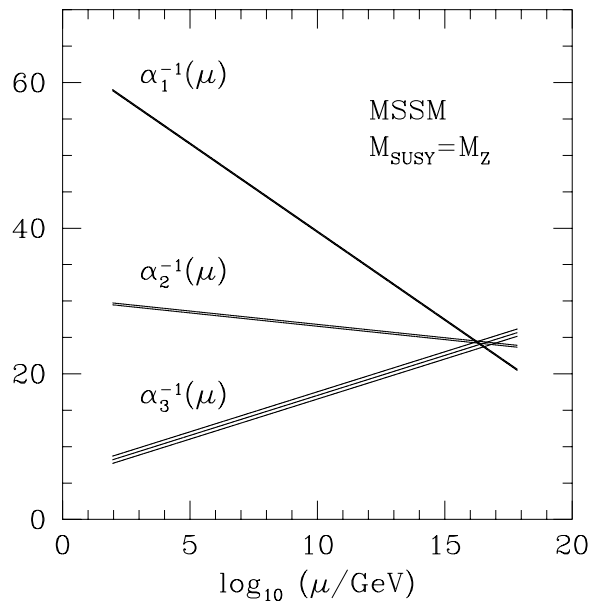
Figure 2.15: Gauge couplings unification picture in the Minimal Supersymmetric Standard Model (MSSM).

Chapter 3

QCD predictions and related uncertainties

3.1 Introduction

The aim of the measurement presented in this thesis is twofold:

1. To make a stringent quantitative comparison of the differential dijet cross sections measured with the ZEUS detector at HERA with the corresponding QCD predictions.

2. To determine the value of the strong coupling constant at the reference momentum scale provided by the Z^0 boson mass, $\alpha_s(M_Z)$, and test its energy scale dependence via a QCD analysis of the measured dijet fraction:

$$R_{2+1}(Q^2) = \frac{d\sigma_{2+1}/dQ^2}{d\sigma_{tot}/dQ^2}. \qquad (3.1)$$

In order to achieve these goals an essential requirement is the selection of a phase-space region where the QCD predictions for the differential dijet cross sections are reliable and least affected by theoretical uncertainties. In this chapter we will carefully study the various sources of uncertainty on the theoretical predictions and, as a result of this study, we will select a phase-space region in order to minimize them.

Specifically, we will estimate the uncertanties of the dijet cross sections associated with:

- the parton distribution functions (PDFs) in the proton;

- the residual renormalization/factorization scale dependence of the NLO cross sections;

- the assumed value for the strong coupling constant in the NLO calculations;

- the hadronisation process.

One arrives to consider the above sources of uncertainties by simply examining the factorisation formula that we have discussed in detail in the previous chapter, and that here we re-write for the reader's convenience:

$$d\sigma = \sum_{a=q,\bar{q},g} \int dx f_a(x, \mu_{\mathrm{F}}^2; \alpha_{\mathrm{s}}(\mu_{\mathrm{R}}); \{\pi\}) d\hat{\sigma}_a(xP, \alpha_{\mathrm{s}}(\mu_{\mathrm{R}}), \mu_{\mathrm{R}}^2, \mu_{\mathrm{F}}^2)(1 + \delta_{hadr}). \qquad (3.2)$$

In the above formula we have explicitly expressed the dependence of the cross section on all the relevant quantities (α_{s}, scales, etc.) which need to be considered in a discussion of the

uncertainties affecting the theoretical predictions. In particular, we have collectively denoted with $\{\pi\}$ the parameters used to model the PDFs' x dependence at a Q_0^2 scale. These parameters, as we will describe shortly below, will be very important for the estimate of the uncertainty of the pQCD jet cross sections arising from the PDFs of the proton.

In addition to evaluate the uncertainties associated to the QCD predictions, in this chapter we will also discuss the level of agreement achieved so far among the different NLO programs, which play such an important role in the analysis presented here.

3.2 Comparisons among different NLO programs for DIS

Presently four different programs are available for the computation of jet cross sections in DIS to NLO accuracy in the strong coupling constant: `DISENT`[31], `DISASTER++`[32], `MEPJET`[30], and `JetVip`[33]. Since all these programs are based on exact calculations, they should produce (within numerical accuracy) identical results. Given the complexity of the QCD calculations and the differences present among the actual implementations, a thorough comparison of the predictions of these programs is a mandatory requirement.

3.2.1 Overview of the programs

Only a brief overview of the NLO programs is given here (see table 3.1). For a detailed description we refer to the program manuals.

Besides the extent to which the exchange of weak gauge bosons and polarized processes are implemented, the programs differ in the technique which is used to cancel the infrared and collinear singularities. Two methods are used: the phase-space slicing method and the subtractions method. The phase-space slicing method uses a small technical cut-off y_{cut} (or s_{min}) to separate the soft and collinear regions. The introduction of this cut-off has the practical consequence that the cut-off independence has to be checked for every investigated observable. No such technical parameter is required for the subtraction method, where the concellation of the singularities take place locally in the phase space, as we have already explained at length in the previous chapter.

DISENT

In `DISENT`, singularities are handled by means of the subtraction method. The subtraction terms are obtained via the dipole factorization formulae discussed in section 2.3. The factorization scale can only be chosen proportional to the photon virtuality Q^2 or at a fixed value. Out of the four programs under consideration, DISENT is the fastest.

DISASTER++

This is a `C++` class library with a `FORTRAN` interface. The cancellation of singularities is achieved by means of the subtraction method implemented via a generalized partial-fractioning formula. DISASTER++ is the only program that allows arbitrary choices of the factorization/renormalization scales and the number of flavour N_f to be changed on an event-by-event basis.[1]

MEPJET

This was the first program for calculating general infrared safe quantities in DIS. It employs the phase-space slicing method with an invariant cut-off parameter s_{min}. `MEPJET` is at present

---

[1]A feature, this, that is extremely valuable when crossing heavy-flavour thresholds.

the only program that includes Z^0 and W exchange, polarized cross sections and leading-order quark mass effects.

`JetVip`

The phase space method with a cut-off parameter y_{cut} is used. This program includes photo-production ($Q^2 \sim 0$) and DIS processes. A special feature of the program is the possibility to include resolved virtual photon processes covering the phase space region of small, but non-zero Q^2. The full azimuthal dependence of the matrix elements for DIS processes is presently available only at leading order.

3.2.2   Numerical comparisons and choice of the default program

During the DESY workshop on *Monte Carlo Generators for HERA Physics* a rather extensive comparison of these NLO programs has been performed. The details of the technical settings for the comparison can be found in[34]. Basically total dijet cross sections predictions, obtained using the longitudinally invariant $K_\perp$-algorithm in the Breit frame, were compared in different DIS phase-space regions and for different jet selection scenarios.

The results can be summarized as follows:

- At leading order, excellent agreement among all programs was found within their statistical precision (± 0.2 %).

- At NLO, `DISENT`, `DISASTER++` and `JetVip` were found to agree among themselves at 1-2% level. In the case of the program `JetVip` a certain dependence on the assumed value of the technical cut-off was noticed. Systematic deviations up 5-8% were instead reported for `MEPJET`.

On the basis of the above results we have decided to use `DISENT` as the default program and `DISASTER++` to cross check the `DISENT` results. Our preference for `DISENT` is dictated by the significantly larger CPU time needed in a typical `DISASTER++` run.

As an additional cross check of the results obtained in the study just mentioned we have compared the `DISENT` and `DISASTER++` NLO predictions for the differential dijet cross sections used in this analysis. The results of this comparison are presented in Fig. 3.1 and Fig. 3.2. The calculations are performed in the $\overline{\text{MS}}$ renormalization and factorization scheme with the number of massless active flavours set to 5, $\mu_{\text{R}} = \mu_{\text{F}} = Q$, and refer to a high-$Q^2$ phase-space region to be defined in the next section. Although the results show a substantial agreement, the DISASTER++ predictions are still, despite the large statistics used, clearly affected by large (up to 10%) statistical fluctuations. In order to perform a more stringent test we have repeated the comparison, only for the inclusive and dijet cross cross sections as a function of Q^2, calculating the DISASTER++ predictions (using a very high statistics run) in each Q^2 bin. The results of this additional comparison, which are presented in Fig. 3.3, show that the two NLO programs indeed agree at the 1-2% level, in agreement with the conclusions of the DESY Monte Carlo Workshop.

3.3   The selection of the phase-space region

A phase-space region for the calculation of the NLO DIS inclusive differential cross sections can be simply selected in terms of standard DIS variables Q^2 and x (or y). In the case of the dijet differential cross sections special care must be placed in the definition of the jet selection criteria in order to avoid *infrared sensitive* regions of the phase space, where predictions of the NLO programs are unreliable.

3.3.1 Infrared sensitive and insensitive E_T^{jet} cut scenarios

Experience gained in the recent past in the use of NLO programs for dijet production has shown that, while based on algorithms that guarantee an exact cancellations of the soft and collinear singularities, these programs have problems in predicting reliable cross sections at the exclusive boundaries of the phase space[35].

In the case of the $K_\perp$-cluster algorithm, where the selection criteria are based on the transverse energies and pseudorapidities of the jets, the troublesome regions are those associated with a symmetric cut on the transverse energy of the jets:

$$E_{TB}^{jet1} \ , \ E_{TB}^{jet2} > E_{TB,min}^{jet}. \tag{3.3}$$

In order to illustrate the nature of the problem we will consider in the following three different jet cut scenarios:

1. Symmetric Cut Scenario:

$$E_{TB}^{jet1} \ , \ E_{TB}^{jet2} > 8 \text{ GeV} \quad \text{and} \quad -1 < \eta_{Lab}^{jet1,2} < 2 \tag{3.4}$$

2. Sum Cut Scenario:

$$E_{TB}^{jet1} \ , \ E_{TB}^{jet2} > 5 \text{ GeV} \ \text{ and } \ E_{TB}^{jet1} + E_{TB}^{jet2} > 17 \text{ GeV} \quad \text{and} \quad -1 < \eta_{Lab}^{jet1,2} < 2 \tag{3.5}$$

3. Asymmetric Cut Scenario:

$$E_{TB}^{jet1} > 8 \text{ GeV} \ \text{ and } \ E_{TB}^{jet2} > 5 \text{ GeV} \quad \text{and} \quad -1 < \eta_{Lab}^{jet1,2} < 2 \tag{3.6}$$

In all the scenarios the jets are ordered according to decreasing transverse energy (in the Breit frame) and refer to the following DIS phase space region:

$$470 < Q^2 < 20000 \ \text{ GeV}^2 \quad \text{and} \quad 0 < y < 1. \tag{3.7}$$

Although the values of the total dijet cross sections obtained for the three scenarios are roughly comparable, the E_{TB}^{jet} region considered being rather similar, the performance of a NLO program changes rather drastically between the first two and the third scenarios. It turns out that the first two scenarios are infrared sensitive and the NLO predictions, while being finite, are unreliable. The problem is that there is not enough phase space available in the vicinity of the $E_{TB}^{jet1} = E_{TB}^{jet2} = E_{TB,min}^{jet}$ point for the NLO algorithm to work properly. This can be understood in terms of the $(E_{TB}^{jet1}, E_{TB}^{jet2})$ planes which are shown for the three scenarios in the first row of Fig. 3.4.The argument goes qualitatively as follows. The NLO cross section receives contributions from the O(α_s) Born (positive) cross section and the O(α_s^2) virtual (negative) and real (positive) corrections. For the Born term and virtual corrections there are only two partons in the final state so that the condition $E_{TB}^{jet1} = E_{TB}^{jet2}$ is always fulfilled. In the case the available phase space reduces to the thick line shown on the $(E_{TB}^{jet1}, E_{TB}^{jet2})$ planes. As far as these contributions are concerned all the cut scenarios are of course equivalent. In the case of the real corrections there are three partons in the final state and the available phase space is represented by the shaded bands in Fig. 3.4. The infrared sensitivity of the first two scenarios comes from the fact that there is not enough three-body phase space available in the vicinity of the $E_{TB}^{jet1} = E_{TB}^{jet2}$ region for the compensation between the real and virtual contributions to take place. An explicit way to see this is to study the total dijet cross section as a function of the transverse energy of the leading jet :

$$E_{TB}^{jet1} = E_{TB,min}^{jet1} + n\Delta \ , \tag{3.8}$$

where $\Delta = 200$ MeV and $n = 1, \ldots, 10$.

We have calculated the total NLO dijet cross section for the three scenarios and the results are presented in the second row of Fig. 3.4. Physically meaningful cross sections should decrease for incresing E_{TB}^{jet1} (or n) values. Instead for the first two scenarios the cross sections first increase and then decreases, a clear unphysical behaviour signalling that not enough positive cross section is added to the final prediction. In the asymmetric cut scenario the cross section has instead a physical behaviour thanks to the larger phase-space region available to the emission of a third parton.

3.3.2   Two working scenarios

In accordance with the previous study we will adopt in all the following NLO calculations the asymmetric jet cut selection:

$$E_{TB}^{jet1} > 8 \; GeV \qquad E_{TB}^{jet2} > 5 \; GeV \quad \text{and} \quad -1 < \eta_{Lab}^{jet1,2} < 2 \tag{3.9}$$

The jet selection will refer to one of two possible DIS phase space regions:

- high-Q^2 Region:

$$470 < Q^2 < 20000 \; \text{GeV} \quad 0 < y < 1, \tag{3.10}$$

- low-Q^2 Region:

$$30 < Q^2 < 20000 \; \text{GeV} \quad 0 < y < 1, \tag{3.11}$$

which we will consider in order to study the Q^2 dependence of the theoretical uncertainties on the differential cross sections. This dependence is particular relevant given our goal to determine the strong coupling constant from a QCD analysis of the measured dijet fraction, $R_{2+1}(Q^2)$, as a function of Q^2:

$$R_{2+1}(Q^2) = \frac{d\sigma_{2+1}/dQ^2}{d\sigma_{tot}/dQ^2}. \tag{3.12}$$

3.4   Uncertainty due to the PDFs

The parton momentum density distributions of the proton are, as demonstrated by the Eq. (3.2), an essential ingredient in the calculation of any cross section in DIS. These parton momentum distributions have been determined by several groups (GRV [36], MRS [37, 38], CTEQ [39, 40]) by parameterising the distributions at some fixed $Q^2 = Q_0^2$ value and extrapolating the results to higher Q^2 values using the NLO DGLAP evolution equations. The parameters are fitted to data from lower energy fixed-target DIS experiments and from HERA, and, in addition, to data measured at the TEVATRON on lepton-pair production (Drell-Yan), direct photon production, W production, and inclusive jet cross-sections. The sources of uncertainty in these fits can be divided into two main groups: uncertainties in the measurements used in the fit and uncertainties in the QCD evolution equations. For the former, the statistical and systematic uncertainties are typically available from each experiment. For the latter, the theoretical uncertainties can be estimated by varying various fit assumptions (see below).

Although the comprehensive parton momentum distribution fits from GRV, MRS, and CTEQ groups make the most extensive use of available data, they lack a complete estimate of the uncertainties in the parton distribution functions. This situation represents a severe limitation to any attempt to realistically estimate the uncertainty associated to a given DIS QCD observable due to the uncertainty on the parton distribution functions. We point out in particular that the standard practice to assume as such an uncertainty the spread of the observable's predictions obtained using different input PDFs cannot be assumed as a realistic estimate given the fact that these NLO QCD fits are performed using almost identical data sets under very similar theoretical assumptions.

3.4.1 The MBFIT analysis

In order to obtain a realistic estimate of the uncertainties of the proton parton distributions functions a NLO DGLAP fit [41, 42] was recently performed. Included in the fit were the statistical and, as much as available, the correlated systematic errors from each experiment. Here we will give a short description of this QCD fit and will use the resulting PDFs (hereafter referred as MBFIT PDFs) with their associated uncertainties to quantify the corresponding uncertainty of the NLO predictions for the inclusive and dijet cross sections. For a detailed description of the fit itself and of the performed error analysis we refer the reader to Ref. [41].

Data samples and corrections

The following measurements were included in the fit:

1. HERA data on F_2^p from ZEUS [43] and H1 [44] ('1994 nominal vertex').

2. Fixed target measurements of F_2^p and F_2^d by E665 [45], NMC [46], BCDMS [47] and SLAC [48].

3. The ratio F_2^d/F_2^p from NMC [49].

4. Data on $xF_3^{\nu Fe}$ from CCFR [50].

5. Data on $x(\bar{d} - \bar{u})$ from E866 [51]. This difference is obtained from the ratio of Drell-Yan production cross sections in pp and pd scattering.

In addition to the statistical errors the following systematic errors were taken into account: for the ZEUS nominal vertex the 6 contributions as parameterised in [43] were included. The SLAC and BCDMS systematic errors were taken to be those used in [54]. For the other data sets all systematic uncertainties were included as published (for H1 and E665 only the normalization error and the total systematic error are available; the CCFR systematic errors are given in [57]). In total 57 independent sources of systematic error were propagated taking into account the correlations between those of the NMC data sets.

   Corrections for nuclear effects were applied to the data on xF_3, F_2^d and F_2^d/F_2^p. These corrections were parameterised as

$$F_i^A = F_i^N \left[1 + K_A(R_A - 1)\right] , \qquad (3.13)$$

where F_i^A is the structure function (per nucleon) measured on nucleus A, F_i^N is the structure function on a free nucleon (taken to be the average of proton and neutron) as predicted by the QCD fit and R_A is a parameterisation of the ratio of the structure function (per nucleon) in nucleus A to that of a free nucleon. The parameter K_A controls the size of the nuclear correction applied, e.g. if $K_A = 1$ (0) then $F_i^A/F_i^N \equiv R_A$ ($F_i^A/F_i^N \equiv 1$). In the case of $xF_3^{\nu Fe}$ the nuclear correction to the valence quark distribution $x(q - \bar{q}) \propto xF_3^{\nu N}$, calculated for $A = 56$ from the recent parameterisation of Eskola et al. [52], was chosen for R_{Fe}. For this nuclear correction K_{Fe} was fixed to 1 and an error $\Delta K_{Fe} = \pm 0.5$ on this parameter was allowed. For the nuclear corrections to F_2^d and F_2^d/F_2^p, R_{D_2} was taken from fits to the nuclear dependence of electron–nucleon scattering measured at SLAC [53]. For these nuclear corrections $K_{D_2} = 1 \pm 1$.

   In addition to the nuclear corrections the proton and deuteron structure functions were corrected for higher-twist contributions which become important at high x and low Q^2. For this purpose the structure functions were described as

$$F_2^{HT} = F_2^{LT}[1 + H(x)/Q^2] , \qquad (3.14)$$

where F_2^{LT} obeys the NLO QCD evolution equations and where $H(x)$ is phenomenologically parameterised as a fourth degree polynomial in x with five free parameters:

$$H(x) = h_0 + h_1 x + h_2 x^2 + h_3 x^3 + h_4 x^4. \tag{3.15}$$

It was assumed that $H(x)$ is the same for the proton and the deuteron [54] which implies that the ratio F_2^d/F_2^p is not affected by higher twist contributions. The data was not corrected for target mass effects [55] so that these effectively are included in $H(x)$. Higher-twist, target-mass or slow-rescaling [55, 56] corrections were not applied to $xF_3^{\nu Fe}$.

In addition, the following cuts were made on the data:

1. Discard data with $x < x_{min} = 0.001$. This cut was introduced because a simplified scheme was adopted (see below) to describe charm production which is known to give a large contribution ($\sim 25\%$) to the cross sections at low x. For the CCFR xF_3 data the cut was raised to $x_{\min} = 0.1$ to reduce the sensitivity to nuclear corrections at low x.

2. Discard data with $Q^2 < Q_{min}^2 = 3$ GeV^2. This cut reduces the sensitivity to QCD corrections beyond NLO and higher-twist contributions. Because the QCD evolution of the ratio F_2^d/F_2^p is small, a lower Q^2 cut of 1 GeV^2 was applied to these data.

3. Discard data with $W^2 < W_{min}^2 = 7$ GeV^2 to reduce the sensitivity to higher-twist contributions and target mass effects.

QCD fit

The input scale of the DGLAP evolutions was chosen to be $Q_0^2 = 4$ GeV^2. The gluon (xg), the sea quark (xS), the difference of down and up anti-quarks $(x\bar{\Delta})$ and the valence (xu_v, xd_v) distributions were parameterised as follows:

$$
\begin{aligned}
xg(x, Q_0^2) &= A_g x^{\delta_g}(1-x)^{\eta_g}(1+\gamma_g x) \\
xS(x, Q_0^2) &\equiv 2x(\bar{u} + \bar{d} + \bar{s}) = A_s x^{\delta_s}(1-x)^{\eta_s}(1+\gamma_s x) \\
x\bar{\Delta}(x, Q_0^2) &\equiv x(\bar{d} - \bar{u}) = A_\Delta x^{\delta_\Delta}(1-x)^{\eta_\Delta} \\
xu_v(x, Q_0^2) &\equiv x(u - \bar{u}) = A_u x^{\delta_u}(1-x)^{\eta_u}(1+\gamma_u x) \\
xd_v(x, Q_0^2) &\equiv x(d - \bar{d}) = A_d x^{\delta_d}(1-x)^{\eta_d}(1+\gamma_d x).
\end{aligned}
\tag{3.16}
$$

The QCD predictions for the parton densities at an arbitrary scale Q^2 were obtained by solving numerically[2] the DGLAP evolution equations at NLO in the $\overline{MS}$ scheme [58]. The evolution is performed in the *variable flavour number scheme*, where all quarks are assumed to be massless and charm and bottom are dynamically generated above some given thresholds Q_c^2 and Q_b^2 (set to 4 and 30 GeV^2 respectively). The input value of the strong coupling constant was set to $\alpha_s(M_Z^2) = 0.118 \ (\pm 0.005)$, which is consistent with the present world average of 0.119 [63]. In the fit, it is assumed that the strange quark distribution $x(s + \bar{s}) \equiv 2x\bar{s}$ is a given fraction $K_s = 0.20 \ (\pm 0.03)$ of the sea at the scale $Q_0^2 = 4$ GeV^2, which is consistent with the measurements of CCFR [64]. As mentioned above the charm $(2x\bar{c})$ and bottom $(2x\bar{b})$ densities start to contribute to the sea quark distribution $(xS(x, Q^2))$ above their respective thresholds. An error of ± 1 GeV^2 on Q_c^2 is allowed.

---

[2]The evolution was calculated with the program Qcdnum [65]

The normalizations A_g, A_u and A_d were fixed by the momentum and valence sum rules:

$$\int_0^1 (xg + x\Sigma)\, dx = 1$$
$$\int_0^1 xu_v\, dx/x = 2 \tag{3.17}$$
$$\int_0^1 xd_v\, dx/x = 1,$$

where $x\Sigma \equiv xS + xu_v + xd_v$ is the sum of the quark densities (singlet density).

From the evolved parton densities the relevant structure functions were calculated in NLO and fitted to the data. The normalizations of the ZEUS, H1 and NMC data sets were kept fixed to unity whereas those of E665, BCDMS, SLAC and CCFR xF_3 were left free (7 parameters). There are thus in total 28 free parameters in the fit. The χ^2 minimization and the calculation of the covariance matrices, which will be described below, were based on Minuit [66]. The fit yielded a good description of the data with $\chi^2 = 1540$ for 1578 data points and 28 free parameters. The χ^2 values for each data set separately are listed in Table 3.2. The values of the fitted parameters at the initial Q_0^2 scale are given in Table 3.3.

χ^2 and propagations of the uncertainties

The propagation of the statistical and systematic uncertainties of the measured structure functions into uncertainties of the PDFs parameters was based on linear error propagation. That implies that asymmetries in the input uncertainties are ignored[3] and that the output statistical and systematic uncertainties are, by definition, symmetric.

In the analysis the effects of the point-to-point correlated experimental systematic uncertainties were incorporated in the model prediction for the structure functions. This model prediction, calculated at the kinematic point (x_i, Q_i^2), was defined as

$$F_i(\{\pi\}, \{s\}) = F_i^{QCD}(\{\pi\}) \cdot (1 + \sum_j s_j \Delta_{ij}^{syst}) \tag{3.18}$$

where $F_i^{QCD}(\{\pi\})$ is the QCD prediction and Δ_{ij}^{syst} is the relative systematic uncertainty on data point i stemming from source j. In Eq. (3.18) $\{\pi\}$ denotes the set of parameters describing the input parton densities (see Eq. (3.16)) and $\{s\}$ is a set of systematic parameters. Notice that the experiments, by giving central values and one standard deviations systematic uncertainties, provide 'measurements' of these systematic parameters: $s_j = 0 \pm 1$.

Assuming that the parameters s_j are uncorrelated and gaussian distributed with zero mean and unit variance, the χ^2 can be written as

$$\chi^2 = \sum_i \left(\frac{F_i(\{\pi\}, \{s\}) - f_i}{\Delta f_i} \right)^2 + \sum_j (s_j)^2 \tag{3.19}$$

where f_i is the measured structure function and Δf_i is the statistical uncertainty with the point-to-point *uncorrelated* systematic uncertainties added in quadrature.

In order to propagate the statistical and systematic uncertainties, two Hessian matrices M and C were evaluated (with Minuit) at the minimum χ^2:

$$M_{ij} = \frac{1}{2} \frac{\partial^2 \chi^2}{\partial \pi_i \partial \pi_j}\ , \quad C_{ij} = \frac{1}{2} \frac{\partial^2 \chi^2}{\partial \pi_i \partial s_j}\ . \tag{3.20}$$

---

[3]If a systematic uncertainty was asymmetric the average of the upper and lower uncertainties was taken.

The statistical covariance matrix of the fitted parameters is then, as usual, given by

$$V^{stat} = M^{-1} \; . \tag{3.21}$$

A systematic covariance matrix of the fitted parameters can also be defined as

$$V^{syst} = M^{-1}CC^{T}M^{-1} \; . \tag{3.22}$$

Once the covariance matrices are known the uncertainty on any function F of the PDFs parameters $\{\pi\}$ can be calculated using the standard formula

$$(\Delta F)^2 = \sum_a \sum_b \frac{\partial F}{\partial \pi_a} V_{ab} \frac{\partial F}{\partial \pi_b} \tag{3.23}$$

provided that the derivatives $\partial F / \partial \pi_a$ are known either analytically or numerically.

The `epdflib` package

The `epdflib` package is a fortran program that provides access to the results of the MBFIT analysis described above. The input to `epdflib` is a file which contains the statistical and systematic covariance matrices of the fitted PDFs parameters and, as function of x and Q^2, the central values of all parton momentum densities as well as the derivatives of these densities to the fitted parameters. Tools are provided that allow to calculate, using Eq. (3.23), the uncertainty associated to any smooth function of the PDFs.

Also stored in `epdflib` are the PDFs resulting from a variety of additional DGLAP fits. These additional fits were performed in order to either check the stability of the central fit results with respect to different theoretical assumptions during the QCD evolution or to provide the user with phenomenologically useful additional PDFs.

Here we list for each performed additional DGLAP fit the condition/assumption that was varied with respect to the central fit:

- The quadratic sum of the statistical and systematic errors was used in the definition of the χ^2 instead of taking the statistical errors only.

- The momentum sum rule constraint was released. In this fit the total momentum fraction carried by quarks and gluons was found to be 1.03.

- The value of Q_0^2 was set to 7 instead of 4 GeV^2.

- The Q_{min}^2 cut was lowered from 3 to 2 GeV^2 and the W_{min}^2 cut from 7 to 5 GeV^2.

- The Q_{min}^2 cut was raised from 3 to 4 GeV^2 and the W_{min}^2 cut from 7 to 10 GeV^2.

- The lower x cut of 0.1 on the CCFR xF_3 data was removed.

- The normalization of the CCFR xF_3 data was fixed (to $N = 1.009$, see Table 3.2) and K_{Fe} was left as a free parameter in the fit which gave $K_{Fe} = 0.8$, consistent with the input value of 1.0 ± 0.5.

- The MRST parameterisation (instead of Eskola et al.) was used to correct the CCFR xF_3 data for nuclear effects.

- The normalization of the NMC data was left free (one parameter for the 8 NMC data sets) so that *all* fixed target data are re-normalized with respect to HERA. This resulted in $N_{\mathrm{NMC}} = 1.007$ while the normalizations of the other data sets changed by less than 0.01, compared to the central fit.

- The d_v density was pameterized as recently suggested by Bodek an Yang [67]:

$$xd' = xd + Bx(1 + x)xu. \tag{3.24}$$

Leaving the parameter B free in the fit yielded $B = -0.02 \pm 0.01$ (stat.), close to zero.

An uncertainty band, here called *parameterisation uncertainty*, is defined as the envelope of the results from the central fit and the above ten additional fits.

A second uncertainty band, here called *input uncertainty*, is defined as the envelope of the results from the central fit and the following four additional fits:

- The input value of the strong coupling constant $\alpha_s(M_Z^2)$ was varied by $\Delta\alpha_s(M_Z) = \pm 0.005$ around the central value $\alpha_s = 0.118$.

- The strange quark content of the proton $x(s + \bar{s})$, assumed to be a fraction $K_s = 0.2$ of the sea at the scale Q_0^2, was varied by $\Delta K_s = \pm 0.03$.

- The parameters (K_{Fe}, K_{D_2}) that control the size of the nuclear correction applied to xF_3 and F_2^d were varied by $\Delta K_{Fe} = \pm 0.5$ and $\Delta K_{D_2} = \pm 1$ around their central values.

- The charm threshold, $Q_c^2 = 4$ GeV^2, was varied by $\Delta Q_c^2 = \pm 1$ GeV^2.

In all the MBFIT PDFs mentioned above the renormalization (μ_R) and factorization (μ_F) scales are chosen according to: $\mu_R = \mu_F = Q$. Four additional sets are also provided in order to study the dependence of the results of the DGLAP fit on μ_R and μ_F:

- The renormalization scale was set to $\mu_R^2 = Q^2/2$ and $\mu_R^2 = 2Q^2$ while keeping the factorization scale μ_F^2 fixed to Q^2.

- The factorization scale was set to $\mu_F^2 = Q^2/2$ and $\mu_F^2 = 2Q^2$ while keeping the renormalization scale μ_R^2 fixed to μ_F^2.

In the following we will define as total uncertainty on the PDFs the sum in quadrature of the:

1. statistical and systematic uncertainties, which were propagated as described above,

2. parameterisation uncertainty, and

3. input uncertainty.

The additional PDFs sets obtained using different $\alpha_s(M_Z)$ input values will prove extremely useful in order to describe in a consistent way the α_s-dependence of the dijet cross sections and dijet fraction.

MBFIT PDFs: central predictions and related uncertainties.

In Fig. 3.5 and Fig. 3.6 the central predictions for the MBFIT PDFs together with their associated total uncertainty, as defined above, are shown as a function of x for $Q^2 = 10$ GeV^2 and $Q^2 = 500$ GeV^2 respectively. Also shown in the figures are the MRST and CTEQ5 parton densities. There is, within the quoted uncertainty, an overall good agreement among these sets of PDFs. The most noticeable difference is in the gluon density $xg(x, Q^2)$, which is steeper in the MBFIT than the MRST and CTEQ5 gluon densities. For x not to small ($x \geq 5 \cdot 10^{-3}$) the MRST and CTEQ5 gluon densities agree with that of the MBFIT within the quoted gluon uncertainty.

In Fig. 3.7 and Fig. 3.8 the relative uncertainties related to the different sources of uncertainty of the PDFs examined before, are shown for $xg(x, Q^2)$ and the singlet density $x\Sigma(x, Q^2)$ for $Q^2 = 10$ GeV^2 and $Q^2 = 500$ GeV^2. Also presented in these figures are the uncertainties associated with the renormalization and factorization scales, which are not included in the total error of the MBFIT PDFs.

It is seen that, as expected, the gluon uncertainties are typically larger than the quark uncertainties and that both are strongly reduced as Q^2 increases from 10 to 500 GeV^2. At low Q^2 the singlet density uncertainty is dominated by the scale uncertainty which however becomes very small at high Q^2.

The uncertainties associated to the strange content of the proton, to the nuclear correction to F_2^d and F_3, and to the charm threshold (see Fig. 3.8) are very small.

3.4.2 Uncertainties of the inclusive and dijet cross sections

As already mentioned the `epdflib` package gives full access for the user to the statistical and systematic covariance matrices of the fitted PDFs parameters as well as, as a function of x and Q^2, to the derivatives of the PDFs with respect to the fitted parameters. With this information available it is then, in principle, straightforward to propagate the uncertainties of the PDFs into the calculated cross section.

For each NLO differential cross section, $d\sigma^{NLO}$, the corresponding uncertainty reads:

$$\Delta(d\sigma^{NLO}) = \sqrt{\sum_{i=1}^{N_p} \sum_{j=1}^{N_p} \frac{\partial(d\sigma^{NLO})}{\partial\pi_i} \frac{\partial(d\sigma^{NLO})}{\partial\pi_j} V_{ij}} \tag{3.25}$$

with

$$\frac{\partial d\sigma^{NLO}}{\partial\pi_a} = \sum_{k=q,\bar{q},g} \int d\xi \left[\frac{\partial f_k(\xi, \mu_F^2; \{\pi\})}{\partial\pi_a}\right] d\hat{\sigma}_k(\xi P, \dots), \tag{3.26}$$

and where V_{ij} is the total covariance matrix element of the fitted parameters π_i and π_j, and N_p is the total number of PDF's parameters. The covariance matrix V can be the statistical, the systematic or, if the total error is to be calculated, the sum of both covariance matrices.

The implementation of the formula Eq. (3.25) within a NLO program is in practice a non-trivial problem. Particular care must be placed in order not to spoil the internal working algorithm of the NLO program, which is designed so as to cancel the infrared and collinear singularities. It proved also necessary to provide a faster access to the `epdflib` information so as not to add additional overhead to already high cpu-time consuming programs. These rather technical issues will be not discussed here, and we will limit ourselves to present the resulting uncertainties on the dijet differential cross sections obtained via the use of Eq. (3.25). All the results presented in the following refer, unless stated otherwise, to the high-Q^2 phase-space region defined before and have been obtained with at least ten milions DISENT events. The relative numerical accuracy associated with a typical DISENT run is shown in Fig. 3.9 for all the NLO QCD differential cross sections.

In Fig. 3.10 we present the relative uncertainties on the differential cross section due to the experimental (statistical and systematic) uncertainties of PDFs. The resulting uncertainties are typically 5% (2.5%) for the dijet (total DIS) differential cross sections. They increase up to 10% in the region of high jet transverse energies and dijet mass.

In order to illustrate the importance of taking into account the correlations among the PDFs parameters $\{\pi\}$ when evaluating the uncertainties on the dijet cross sections, we present again in Fig. 3.11, plotted as shaded bands, the uncertainties of $d\sigma_{tot}/dQ^2$, $d\sigma_{2+1}/dQ^2$, and the dijet fraction $R_{2+1}(Q^2)$ obtained using Eq. (3.25). Together with them (superimposed as a hatched band) we also plot the uncertainties of the same observables obtained neglecting the

correlations mentioned above. The latter uncertainties have been calculated simply repeating the NLO calculations using two PDFs sets, $f_i^{(p),Up}(\xi, Q^2)$ and $f_i^{(p),Dn}(\xi, Q^2)$, obtained raising and lowering the MBFIT central PDFs by the associate uncertainty $\Delta f_i^{(p)}(\xi, Q^2)$

$$f_i^{(p),Up}(\xi, Q^2) = f_i^{(p)}(\xi, Q^2) + \Delta f_i^{(p)}(\xi, Q^2) , \qquad (3.27)$$

and

$$f_i^{(p),Dn}(\xi, Q^2) = f_i^{(p)}(\xi, Q^2) - \Delta f_i^{(p)}(\xi, Q^2) . \qquad (3.28)$$

The effect of neglecting the correlations during the propagation of the uncertainties produces an uncertainty on $d\sigma_{tot}/dQ^2$ which is almost twice bigger. Also the uncertainty on $d\sigma_{2+1}/dQ^2$ increases though to a lesser extent. When ignoring correlations the uncertainties on $d\sigma_{tot}/dQ^2$ and $d\sigma_{2+1}/dQ^2$ are essentially equal and, as a consequence, the uncertainty of $R_{2+1}(Q^2)$ comes out unrealistically small. Using Eq. (3.25) the dijet cross section has a larger uncertainty than the inclusive cross section (as one would naively expect due to the more significant role played by gluon-initiated processes on the dijet observable) and in the ratio the uncertainties do not completely cancel leaving an uncertainty on $R_{2+1}(Q^2)$ at the level of 1-1.5%.

Given the extremely small PDFs-related uncertainty of $R_{2+1}(Q^2)$, this observable appears to be particularly suited to extract α_s.

In addition to the uncertainties of the dijet cross sections associated to the experimental uncertainties on the MBFIT PDFs, it is important to check the effect of using as input in the calculation of the dijet cross sections different PDFs sets obtained from the additional fits discussed in the previous section. What we are testing in this case is the stability of the results under different assumptions made in the DGLAP fit. In Fig. 3.12 we present the uncertainty on the differential cross sections due to the *PDFs parameterisation uncertainty* defined in Section 3.4.1. The corresponding uncertainties of the cross section are at 1-2% level. As a cross-check only, the uncertainties of the QCD NLO differential cross sections obtained varying the renormalization and factorization scales *only* in the PDFs are shown in the Fig. 3.13 and Fig. 3.14 , respectively.

The use of different MBFIT PDFs obtained under different assumptions on the strange content of the proton, on the nuclear correction to xF_3, F_2^d, as well as on the charm threshold produced negligible variations on the inclusive and dijet cross sections.

In the following we will define as total PDFs-related uncertainty on each calculated differential cross section, the sum in quadrature of the uncertainties obtained in correspondence of the experimental and parameterisation uncertainties of the MBFIT PDFs. The total PDFs-related relative uncertaintes for the NLO QCD differential cross sections are presented in Fig. 3.15. Also shown in the figure are the relative ratios, with respect to the central MBFIT PDFs predictions, of the cross sections obtained using the CTEQ4, CTEQ5 and MRST PDFs.

3.5   Residual renormalization-scale dependence

In any DIS pQCD calculation two momentum scales must necessarily be introduced: the renormalization (μ_R) and factorization (μ_F) scale. These two scales have a purely technical (and unphysical) origin and in a full (i.e. to all orders) perturbative calculation the result should be independent of them. In practice however, due to our present ability to calculate only the first few terms of the perturbative series, we are forced to truncate the expansion. This truncated expansion does exhibit in general renormalization- and factorization-scale dependencies.

The problem then arises, in *any* fixed-order DIS pQCD calculation, to make a choice for μ_R and μ_F (within a specified renormalization/factorization scheme) in order to get a definite pQCD prediction. As a consequence, it becomes also necessary to estimate the theoretical uncertainty related to the residual scale dependence.

In the following we will limit our discussion only to the renormalization scale dependence of the NLO cross sections, the factorization-scale dependence being almost negligible (see e.g. [34]).

3.5.1 General remarks on the choice of the renormalization scale

Even though the renormalization and factorization scales are unphysical parameters a fixed order perturbative prediction depend of course on the specific values assumed for them. The question then naturally arises if some specific scale choices are, from a theoretical point of view, to be preferred respect to others.

Theoretically optimized scales

Since the appearence of the first NLO pQCD calculations several different *theoretically motivated* choices for the renormalization scale have been suggested.

Among the most used approaches we recall:

1. The Physical Scale argument[68].

2. The Principle of Minimum Sensitivity (PMS)[69].

3. The Method of Effective Charges (ECH)[70].

4. The Method of Brodsky-Lepage-MacKenzie (BLM)[71].

Without entering in a detailed discussion of the proposed approaches (for which we refer the reader to the above references) we simply remark that after almost twenty years since the problem was clearly formulated in [69] the subject has yet to produce consensus in the theoretical community.

The physical scale argument is certainly the more widespread in the literature and in the standard phenomenological practice. According to this viewpoint the renormalization scale should be chosen to be equal or close to the typical energy scale(s) which characterize the hardness of the process under consideration.

Experimentally optimized scales

In addition to the above theoretically optimized scale choices a completely different approach has recently attracted renewed interest. In this approach the renormalization scale is not chosen according to a given theoretical prescription but is instead obtained by fitting the pQCD prediction (with the renormalization scale assumed as a free parameter) to the corresponding measured observable. This approach has been mostly used by the LEP experiments in their α_s measurements based on NLO QCD fits of several infrared and collinear-safe event shape observables (see e.g. ref.[72] for a recent DELPHI α_s measurement that fully exploits and advocates this particular method). It is intriguing that the values of α_s extracted from each observable using this approach show a remarkable level of agreement, while the α_s values obtained using a renormalization scale equal to $\sqrt{s}$ are much more dispersed. While this convergence is tantalising it must be said that such an optimization procedure has as yet no theoretical basis. The critical point here is to understand if this procedure could cause, because of this amazing convergence of the results, a bias on the central α_s fitted value.

Our choice

In the following we will assume Q, in line with the physical scale argument mentioned above, as the central choice for the renormalization and factorization scales:

$$\mu_{R,0} = \mu_{F,0} = Q, \tag{3.29}$$

where with $\mu_{R,0}$ and $\mu_{F,0}$ we have indicate the central values for μ_R and μ_F, respectively. We point out here that the same choice is adopted in all the NLO DGLAP fits (MBFIT, CTEQ, MRST) performed in order to determine the PDFs.

In order to study the dependence of the NLO QCD predictions on a renormalization scale that involves the transverse energies of the jets, we will also compare the results obtained with the central $\mu_R = \mu_F = Q$ choice with those obtained for $\mu_R = (E_{TB}^{jet,1} + E_{TB}^{jet,2})$ and $\mu_F = Q$.

3.5.2   Renormalization-scale dependence of the dijet cross sections

On general grounds one expects the residual renormalization-scale dependence to be reduced the more higher-order terms are included in the calculation of a given QCD observable. That this is actually true is demonstrated in Fig. 3.16 which shows the LO and NLO total dijet cross sections as a function of the renormalization-scale variation factor, x_μ, defined as

$$\mu_{\mathrm{R}} = x_\mu \cdot \mu_{R,0} \ \ \text{with} \ \ \mu_{R,0} = \mu_{F,0} = Q. \tag{3.30}$$

In the large x_μ range examined the LO cross section (obtained using LO matrix elements and LO definition of α_{s} and PDFs) shows a huge dependence on the renormalization scale, showing as a LO calculation can only predict the order of magnitude and crude features of a given observable but cannot be used for a precise test of QCD. The NLO cross section shows instead a much less pronounced scale dependence. A similar conclusion is drawn when using as a renormalisation scale the sum of the jet transverse energies (see Fig. 3.17).

In the following the μ_{R}-related uncertainty of the DIS inclusive and dijet cross sections will be defined as the one obtained for a variation of the renormalization-scale factor in the range: $0.5 < x_\mu < 2$.

In Fig. 3.18 this uncertainty is shown, as a function of Q^2 and for the low-Q^2 region defined in Section 3.3.2, for the inclusive and dijet differential cross sections, and for the dijet fraction $R_{2+1}(Q^2)$. The results for $d\sigma_{2+1}/dQ^2$ and $R_{2+1}(Q^2)$ show an increasing residual μ_{R}-dependence as Q^2 decreases; for $Q^2 \sim 50$ GeV^2 the uncertainty amounts to $\pm$ 20-30%. In this kinematic region the NLO dijet cross sections are not predictive since contributions from higher-orders in α_{s} are presumably very large. For this reason in the following we will limit our analysis to the high-Q^2 region defined before. A further motivation for this choice is the reduced uncertainty due to the PDFs already discussed in the previous section.

The μ_{R}-related uncertainties for all the NLO QCD differential cross sections in the high-Q^2 region are presented in Fig. 3.19. The uncertainties, which are typically at the 5% level in most of the phase-space, increase (up to 20%) in the low ξ, E_{TB}^{jet} and dijet mass regions, as well as in the forward jet pseudorapidity region. As a cross-check the relative ratio:

$$(d\sigma(\mu_{\mathrm{R}} = Q) - d\sigma(\mu_{\mathrm{R}} = E_{TB}^{jet,1} + E_{TB}^{jet,2}))/d\sigma(\mu_{\mathrm{R}} = Q)$$

is also shown (as a dashed line) in the same figure.

3.6   Uncertainty due to the strong coupling constant

In this section we address the issue of estimating the uncertainty of the differential inclusive and dijet cross sections due to the uncertainty on the strong coupling constant.

The natural method to get such an estimate is that of varying in the NLO program the value of $\alpha_s(M_Z)$ over a range which reasonably represents the uncertainty on $\alpha_s(M_Z)$.

Particular care must be placed, however, when implementing such a variation in order to:

1. consider the complete $\alpha_s(M_Z)$ dependence in the cross section $d\sigma^{NLO}(\alpha_s)$;

2. not to spoil the correlations between the assumed $\alpha_s(M_Z)$ value and the PDFs, in particular the gluon density, built-in in the DGLAP evolution equations.

In order to take into account the complete $\alpha_s(M_Z)$-dependence of $d\sigma^{NLO}$, one must vary *simultaneously* the value of $\alpha_s(M_Z)$ used in the partonic cross section and in the PDFs evolution equations. It is hence necessary to have different sets of PDFs obtained fitting the same set of data but assuming different $\alpha_s(M_Z)$ values.

Both the MBFIT described above and the CTEQ4 and MRST analyses provide PDFs sets obtained for different $\alpha_s(M_Z)$ values. The MBFIT α_s-series cover a range in $\alpha_s(M_Z)$ between $\alpha_s(M_Z) = 0.113$ and $\alpha_s(M_Z) = 0.123$ which, according to the discussion in section 2.6, fairly represents the present uncertainty on the strong coupling constant. These PDFs have been used hence to obtain the uncertainties of the differential inclusive and dijet cross sections. These resulting uncertainties are presented in Fig. 3.20: they amount to 5 - 10 % and increase in the low E_{TB}^{jet} and low dijet mass regions, as well as in the forward pseudorapidity region of the Breit frame. As a cross check in the same figure we also present (as a hatched band) the uncertainties obtained using the MRST α_s-series which cover an identical α_s range of variation.

3.7 Hadronisation effects

The NLO QCD predictions for the dijet cross sections obtained in this chapter refer to a partonic final state composed of coloured quarks and gluons. In QCD on the other hand, due to the confinement property of the strong force, coloured partons can never be observed as free particles in the final state. What we can observe and measure are hadrons: relativistic color-singlet bound states of confined quarks and gluons.

The problem then arises of how to perform a meaningful comparison of the measured dijet cross sections (which, once corrected for detector effects, refer to hadrons in final state) with the NLO predictions described above.

The approach adopted here has been that of estimating the effect of the hadronisation process on the NLO QCD dijet differential cross sections, using phenomenological (i.e. Monte Carlo) hadronisation models, and then to correct for it the NLO cross sections.

We point out here that an estimate of the hadronisation effects based on a renormalon approach, á la Dokshitzer-Marchesini, which has attracted recently a certain theoretical and experimental interest can not be attempted due to the lack of analitical predictions for the dijet cross sections in DIS.

3.7.1 The cluster and string hadronisation models

The hadronisation process takes place long after the hard scattering occurs. It involves long-distances (small momentum transfers) and, as consequence, can not be quantitatively described within the realm of pQCD. One is forced to use phenomenological models. There are two different models on the market: the string model (as implemented in JETSET) and the cluster model (as implemented in HERWIG). Both hadronisations models are based on the *local parton-hadron duality* hypothesis according to which the flows of energy-momentum and flavour quantum numbers at the hadron level should follow those at the parton level. Thus, for example, the flavour of the quark initiating a jet should be found in a hadron near the jet axis. The extent to which

the hadronic flow deviates from the partonc flow reflects the irreducible smearing of order Λ_{QCD} due to hadron formation.

The cluster model

The preconfinement property of the parton-branching process is used in HERWIG by assuming a cluster model which is local in colour and independent of the hard scale Q. After the perturbative parton-branching process, all outgoing gluons are split non-perturbatively, as shown in Fig. 3.21, into quark-antiquark pairs. Neighboring quarks and antiquarks are then combined into colour singlets. The resulting cluster mass spectrum is universal and steeply falling at high masses. Its precise form is determined by the QCD scale Λ_{MC} (used during the perturbative parton branching phase), the perturbative cutoff Q_0, and to a lesser extent the gluon splitting mechanism. Typical cluster masses are normally two or three times Q_0. The clusters thus formed then decay into hadrons. If a cluster is too light to decay into two hadrons, it is taken to represent the lightest single hadron of its flavour. Its mass is shifted to the appropriate value by an exchange of momentum with a neighbouring cluster. Those clusters massive enough to decay into two hadrons undergo simple isotropic decay into pairs of hadrons, chosen according to the density of states with appropriate quantum numbers. This model has few parameters and a natural mechanism for generating transverse momenta. However it has difficulties in dealing with the decay of very massive clusters, and in adequately suppressing baryon production.

The string model

This model is based on the dynamics of a relativistic string which represents the colour flux stretched between the initial $q\bar{q}$ (see Fig. 3.21). The string produces a linear confinement potential and an area law for matrix elements:

$$|M(q\bar{q} \rightarrow h_1 \cdots h_n)|^2 \propto e^{-bA}$$

where A is the space-time area swept out (Fig. 3.23). The string breaks up into hadrons via $q\bar{q}$ pair production in its intense colour field. Gluons produced in the parton shower give rise to 'kinks' on the string. The model has extra parameters for the transverse momentum distribution and heavy particle suppression. It has some problems describing baryon production, but less than the cluster model.

Hadron yields

Both the cluster and string hadronisation models have a few adjustable parameters that have been mainly tuned on precisely measured hadron yields at LEP. In order to illustrate the present ability of these hadronisation models to describe hadron production we compare in Table 3.4 and 3.5 the meson and baryon yields predictions with the corresponding yields measured by the LEP and SLC experiments: the overall agreement is rather good. As stated earlier, the remaining problems are in the baryon sector, especially for HERWIG. It is remarkable that most of the measured yields (except for the 0^- mesons, which have special status as Goldstone bosons) lie on the family of curves

$$< n >= a(2J + 1)e^{-M/T}$$

where M is the mass and $T \simeq 100$ MeV (fig. 3.24). This suggests that mass, rather than quantum numbers, is the primary factor in determining the production rates.

3.7.2 Hadronisation correction for the dijet cross sections

The hadronisation-correction factors are defined as the ratio of the dijet cross sections before and after the hadronisation process

$$C_{had} = \frac{d\sigma_{2+1}^{partons}}{d\sigma_{2+1}^{hadrons}} \; . \tag{3.31}$$

Their final values are taken as the mean of the cluster and string model predictions and the associated uncertainties are defined as half the spread between the models. In Fig. 3.25 we show the size of the hadronisation-corrections factors for all the dijet cross sections. The corrections are reasonably small for most of the dijet distributions (between 3% and 10%) and decrease for increasing Q^2 and E_T^{jet}. They are somewhat larger in the rear pseudorapidity and low dijet mass regions. In the high-Q^2 region considered here the string and cluster models give very similar results.

The correction factors thus obtained are used to correct bin-by-bin the NLO cross sections for the hadronisation effects according to:

$$d\sigma_{2+1} = d\sigma_{2+1}^{NLO} \cdot C_{had}^{-1} \; . \tag{3.32}$$

The approach described above is certainly an approximated one. Apart from the intrinsic uncertainties of the hadronisation models, there is an additional uncertainty related to the fact that these hadronisation programs are applied to a parton cascade that does not match the partonic final state of a NLO program. Its approximate validity rests on the assumptions that the hadronisation-correction factors are small and that the MC partonic final state give a reasonable description of the shape of the NLO cross sections. That the latter conditions is in fact fulfilled is proved in the Fig. 3.26 and Fig. 3.27, which show a comparison of the NLO dijet cross sections with the parton level predictions of the LEPTO, ARIADNE and HERWIG MC programs.

3.8 Summary

In this chapter we have gone through a rather long and detailed analysis of the NLO QCD predictions and their associated uncertainties for the differential dijet cross sections and dijet fraction in DIS processes at HERA. It is hence useful at this point to summarize the main results obtained.

A final phase space was selected according to the DIS region:

$$470 < Q^2 < 20000 \; \text{GeV}^2 \quad \text{and} \quad 0 < y < 1 \; , \tag{3.33}$$

and jet selection criteria

$$E_{TB}^{jet1} > 8 \; \text{GeV} \quad \text{and} \quad E_{TB}^{jet2} > 5 \; \text{GeV} \tag{3.34}$$

$$-1 < \eta_{1,2}^{jet} \, (\text{Lab}) < 2 \; . \tag{3.35}$$

This choice was dictated by the goal to reduce as much as possible the theoretical uncertainties associated with the NLO QCD predictions. As will be described in the following chapters, this phase space choice will prove to be particularly suited also from an experimental point of view.

The restriction to a high-Q^2 region was chosen mainly in order to avoid the extremely large renormalization-scale dependence of the dijet cross sections and dijet fraction at low Q^2. Restricting the phase space to high-Q^2 also decreases the uncertainty on the parton distribution

functions, in particular the gluon density. In the high-Q^2 region considered here the gluon-initiated processes constitute approximately only the 30-40 % of the total dijet cross section.

The asymmetric cut on the E_T of the jets avoids infrared sensitive regions where the NLO programs are, as we have seen, not reliable.

All the NLO calculations are based on the program DISENT and make use of a set of PDFs obtained in the MBFIT analysis described in Section 3.4 and available via the `epdflib` package. The calculations are performed in the $\overline{\text{MS}}$ renormalization and factorization scheme with the number of massless active flavours set to 5 and $\mu_R = \mu_F = Q$. The final theoretical results for the differential dijet cross sections and dijet rate are obtained from the corresponding NLO predictions correcting the latter for the hadronisation effects using the correction factors and procedure described in Section 3.7.

The decision to use the PDFs provided by the `epdflib` package is motivated by the fact that this package contains also the necessary information (correlation matrices and derivatives of the PDFs with respect to the fitted PDFs parameters) necessary to perform a complete propagation of the uncertainties of the PDFs on the NLO QCD differential dijet cross sections. In the phase space considered here the NLO cross sections obtained using these PDFs were found to be within 5 % compatible with the ones obtained using the CTEQ5 and MRST sets. To our knowledge the approach presented in this chapter represents one of the first attempts to a *realistic* evaluation of the uncertainty of the NLO jet cross sections due to the PDFs' uncertainties.

The use of the dijet fraction $R_{2+1}(Q^2)$ proved particularly effective in reducing the theoretical uncertainty associated with the PDFs, the relative uncertainty on $R_{2+1}(Q^2)$ due to the PDFs being only 1-1.5 %. This make this observable particularly suitable to extract α_s.

We conclude this chapter presenting the final QCD predictions for the differential dijet cross sections and dijet fraction. The differential dijet cross sections as functions of z_p, x_{Bj}, ξ, and the dijet invariant mass Mjj are presented in Fig. 3.28. Fig. 3.29 shows the differential cross sections as a function of the jets transverse energies and pseudorapidities in the Breit Frame. The theoretical uncertainty associated with each cross section is shown as shaded band underneath each plot and has been obtained adding in quadrature the four sources of uncertainty that we have being discussing in this chapter:

- Parton Distribution Functions,

- renormalization-scale dependence,

- assumed value for the strong coupling constant, and

- hadronisation models.

The differential inclusive and dijet cross sections and the dijet fraction, all as function of Q^2, are presented in Fig. 3.30. In Fig. 3.30 the uncertainty bands do not contain the uncertainty due to the strong coupling constant. Instead in this case the theoretical predictions obtained using three different $\alpha_s(M_Z^2)$ values and the corresponding PDFs sets are presented. These results will be used (as described in chapter 6) to parameterise, in each Q^2 bin, the α_s dependence of the dijet fraction $R_{2+1}(Q^2)$ in order to extract the strong coupling constant via a QCD fit of the corresponding measured observable. The complete results obtained in this chapter on the QCD cross sections and the associated uncertainties will be presented in tabular form, together with measured cross sections, in chapter 6.

	MEPJET[30]	DISENT[31]	DISASTER++[32]	JETVIP[33]
version	2.2	0.1	1.0.1	1.1
method	PS slicing	subtraction	subtraction	PS slicing
1+1,2+1	NLO	NLO	NLO	NLO
3+1	LO	LO	LO	LO
4+1	LO	—	—	—
full event record	yes	yes	yes	(yes)
scales	all	factorization: Q^2, fixed renormalization: all	all	all
flavour dependence	switch	switch	full	switch
quark masses				
in LO x-section	LO	—	—	—
resolved γ contribution				
in LO/NLO x-section	—	—	—	NLO
electroweak contribution				
in LO/NLO x-section	LO	—	—	—
polarized x-section	NLO	—	—	—

Table 3.1: A comparison of the different features of the DIS NLO QCD programs.
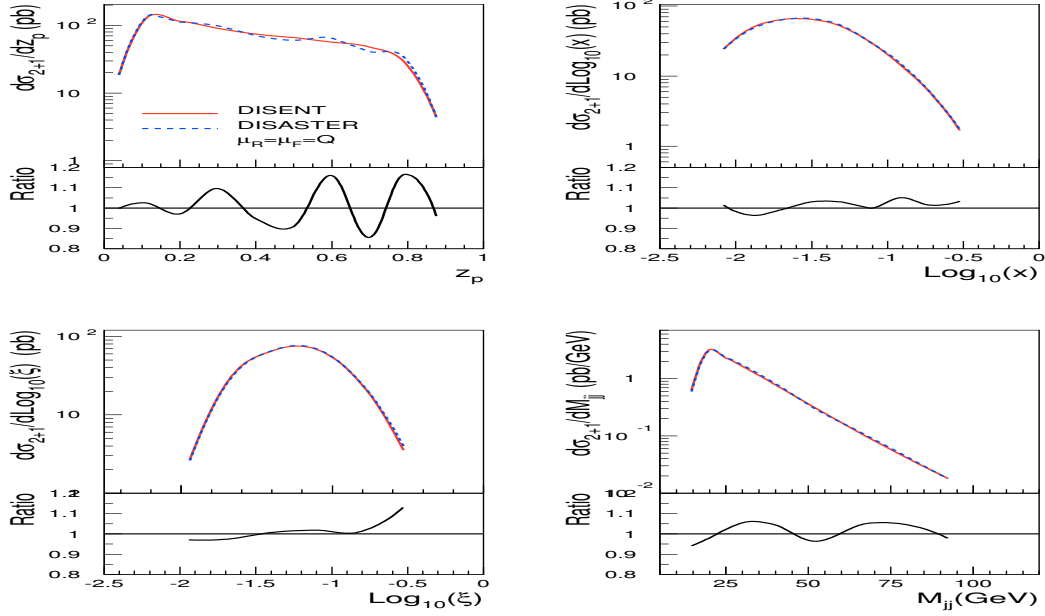
Figure 3.1: The comparison of the DISENT and DISASTER++ NLO QCD predictions, for the dijet cross sections as a function of z_p, $\log_{10}(x_{Bj})$, $\log_{10}(\xi)$, and M_{jj}.
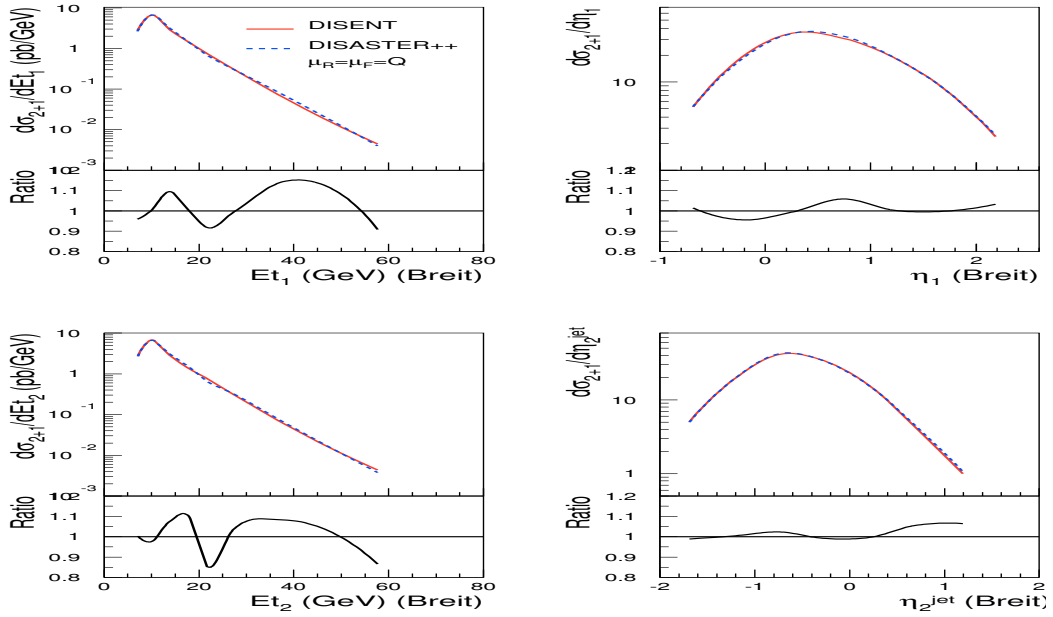

Figure 3.2: The comparison of the DISENT and DISASTER++ NLO QCD predictions, for the dijet cross sections as a function of the transverse energy and pseudorapidity of the jets.
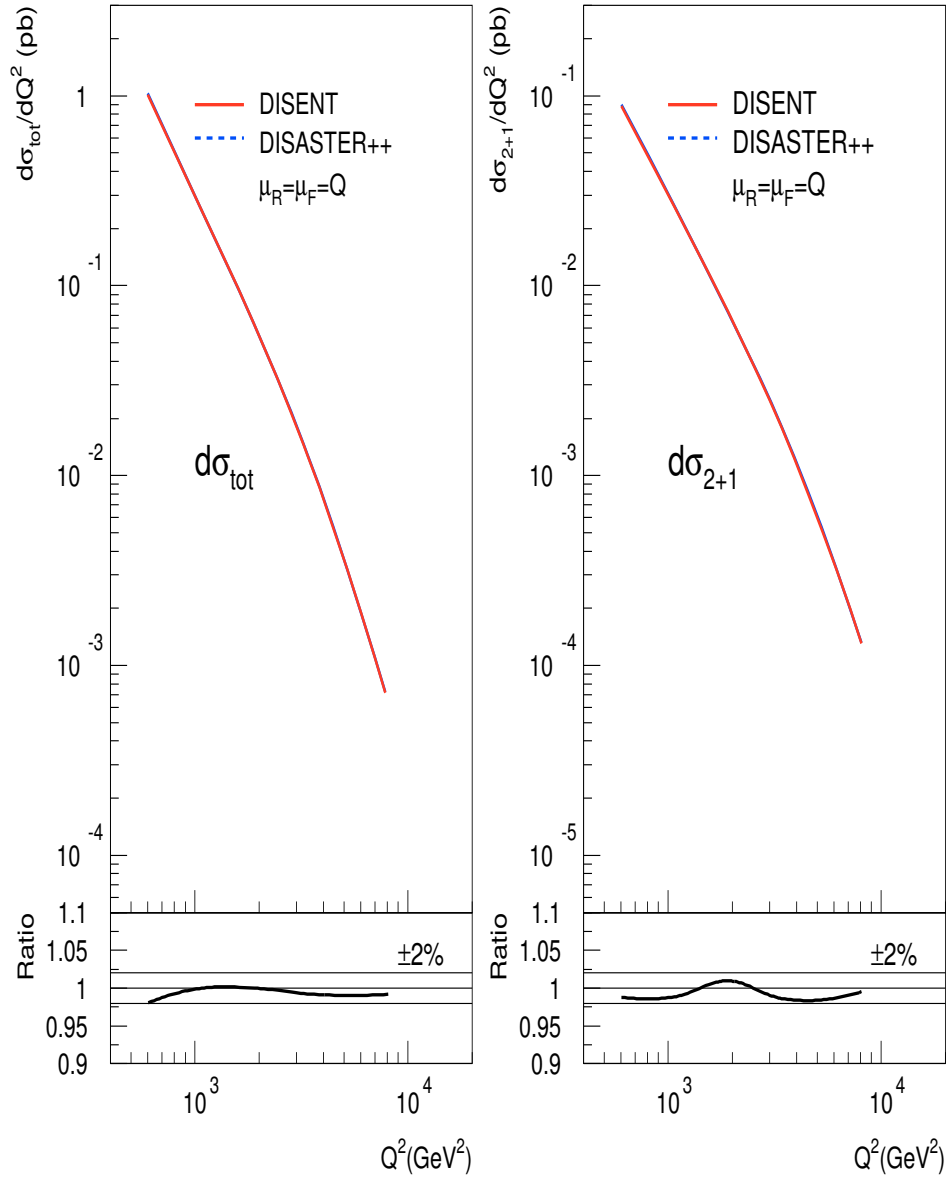
Figure 3.3: The comparison of the DISENT and DISASTER++ NLO QCD predictions, for $d\sigma_{tot}/dQ^2$ and $d\sigma_{2+1}/dQ^2$.
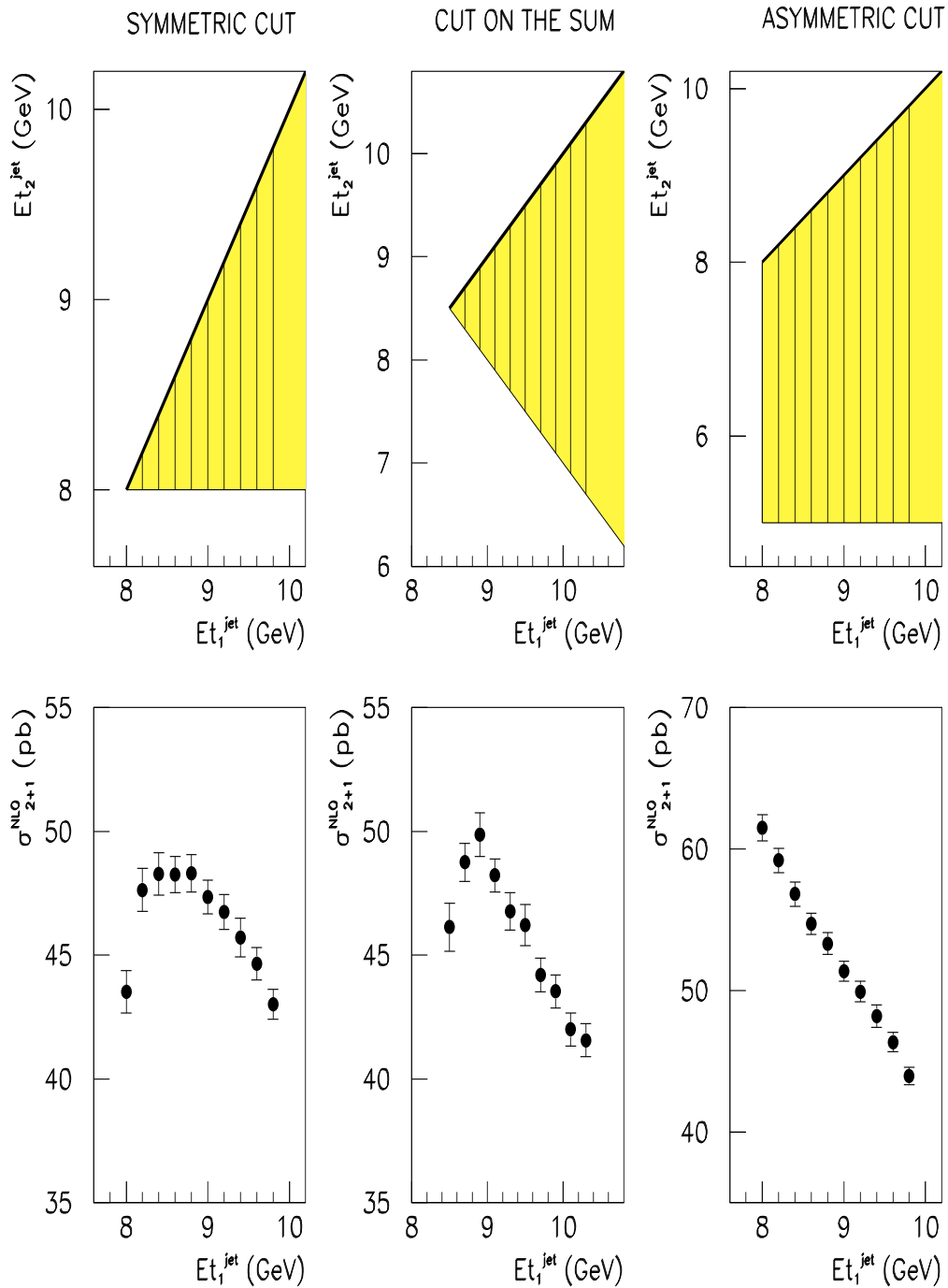
Figure 3.4: Infrared sensitive and insensitive jet cut scenarios. See text for a full explanation.

Dataset	χ^2	points	χ^2/point	Norm.
SLAC P	61.9	56	1.10	0.988
SLAC D	52.1	57	0.91	0.984
BCDMS P	155.9	177	0.88	0.979
BCDMS D	159.4	159	1.00	1.000
NMC E090 P	46.3	44	1.05	1.0
NMC E120 P	64.8	53	1.22	1.0
NMC E200 P	75.4	64	1.18	1.0
NMC E280 P	65.2	72	0.91	1.0
NMC E090 D	47.1	44	1.07	1.0
NMC E120 D	43.3	53	0.82	1.0
NMC E200 D	48.2	64	0.75	1.0
NMC E280 D	51.4	72	0.71	1.0
E665 P	53.4	41	1.30	1.018
E665 D	43.8	41	1.07	1.002
ZEUS NV94	235.2	147	1.60	1.0
H1 NV94	97.7	150	0.65	1.0
NMC D/P	188.6	205	0.92	1.0
CCFR	33.5	68	0.49	1.009
E866	16.8	11	1.53	1.0
Total	1539.8	1578	0.98	

Table 3.2: The χ^2 values of the MBFIT analysis described in Section 3.4.1, calculated with the statistical and systematic errors added in quadrature.

Parameter	$xg(x)$	$xS(x)$	$x\bar{\Delta}(x)$	$xu_v(x)$	$xd_v(x)$
A	1.357	0.807	0.306	2.739	1.994
δ	−0.255	−0.149	0.565	0.617	0.654
η	5.338	3.925	7.493	3.890	3.082
γ	−0.522	−1.332		2.753	−0.813

h_0	h_1	h_2	h_3	h_4
−0.043	−2.461	14.324	−46.758	55.834

Table 3.3: The values of the PDFs parameters at the initial scale Q_0^2, obtained from the MBFIT analysis. The parameters are defined in Eq. (3.16).
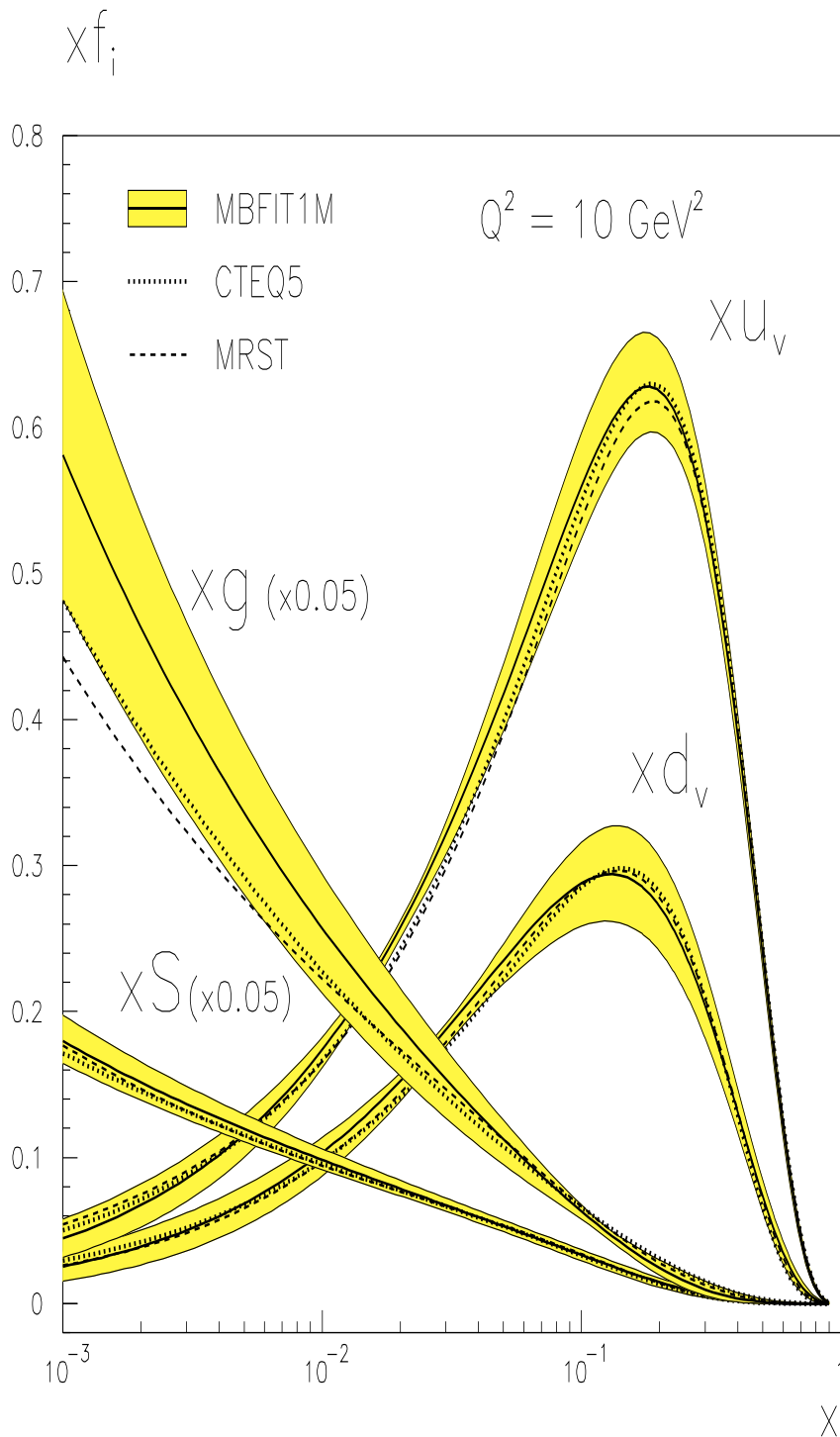
Figure 3.5: The MBFIT PDFs xg, xS (both divided by a factor 20), xu_v and xd_v and their associated uncertainties as a function of x for $Q^2 = 10$ GeV^2. Also shown as dotted (dashed) curves are the PDFs from CTEQ5 and MRST respectevely.
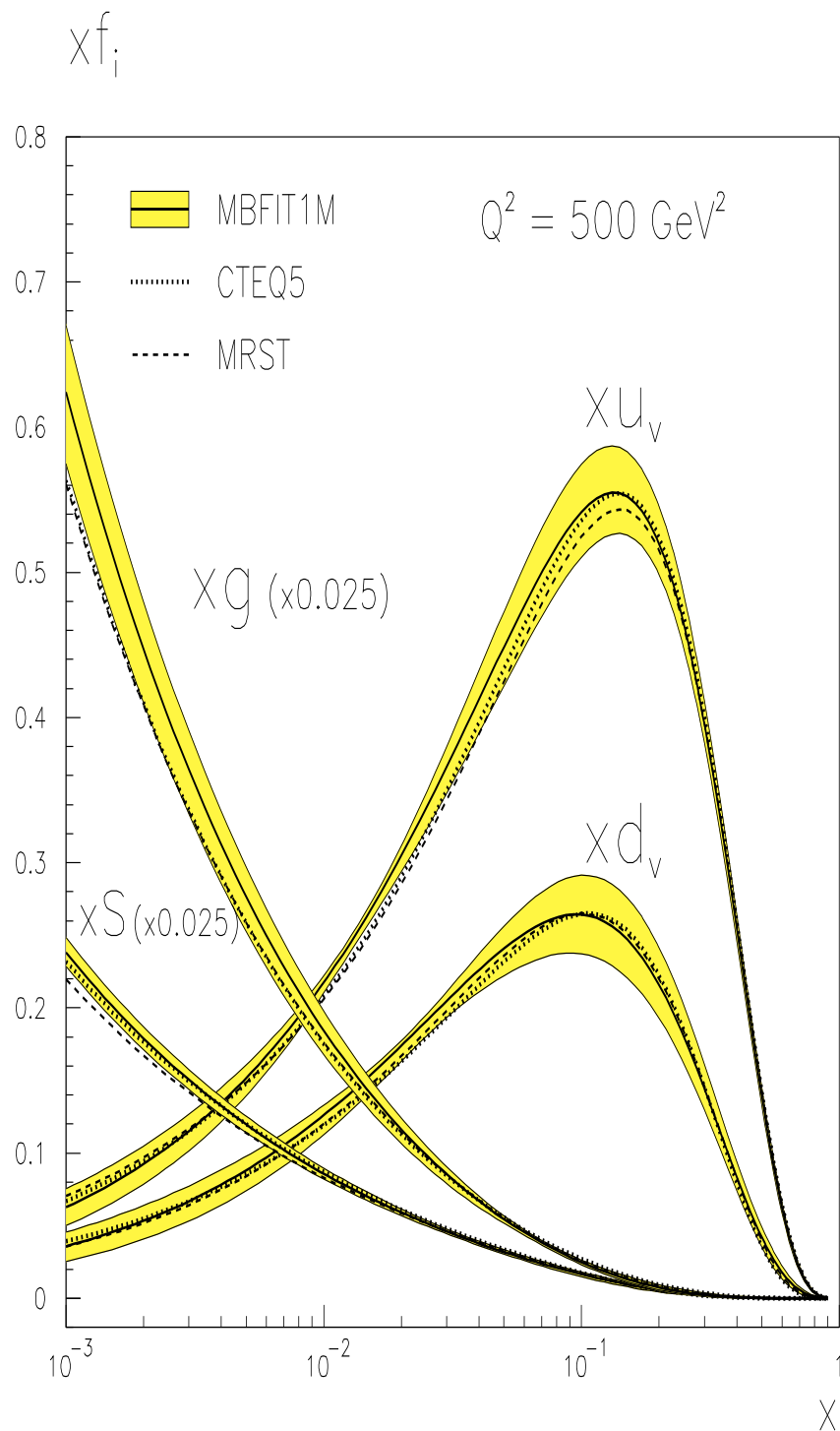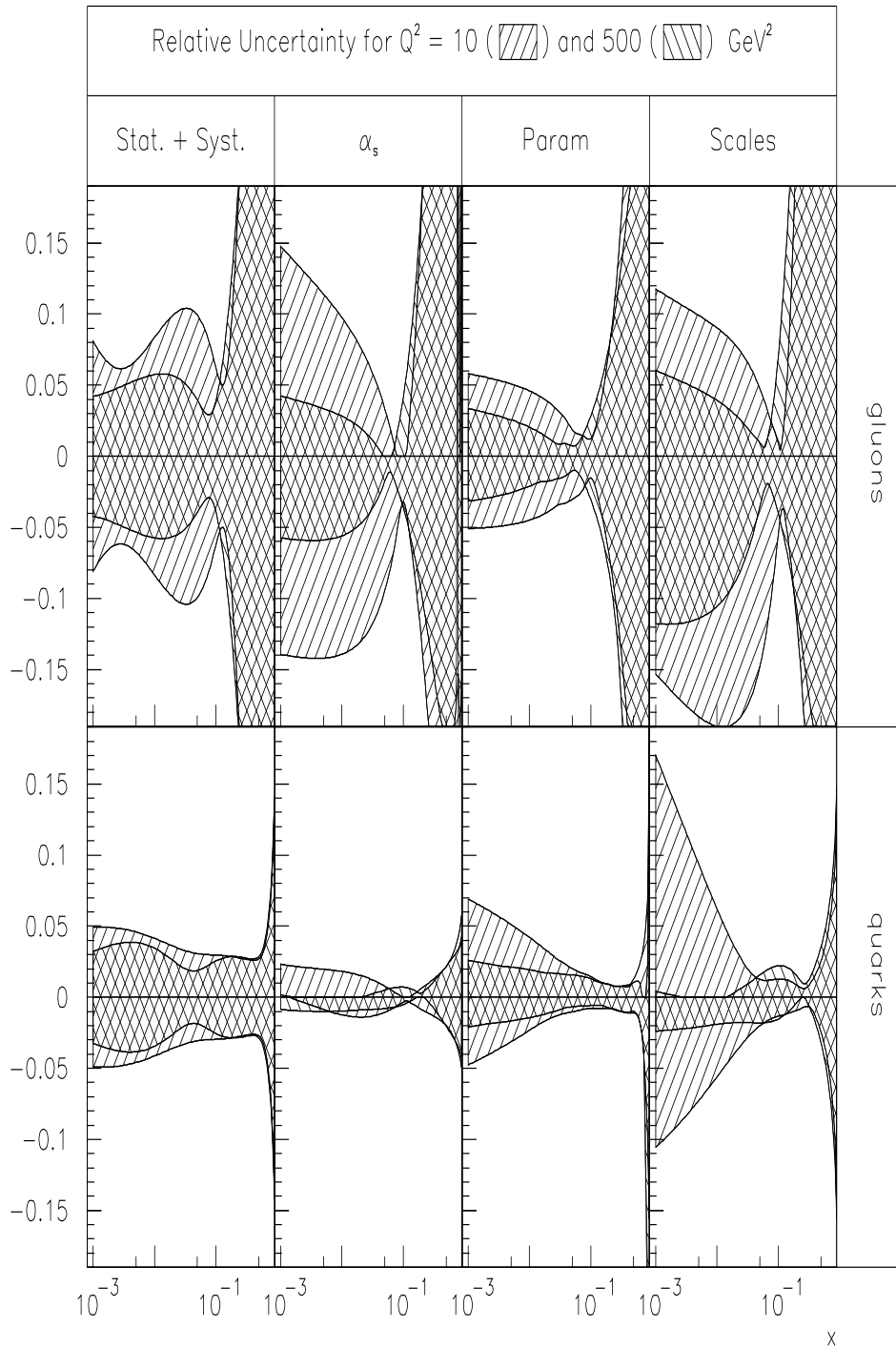
Figure 3.6: The NLOFIT PDFs xg, xS (both divided by a factor 40), xu_v and xd_v and their associated uncertainties as a function of x for $Q^2 = 500$ GeV^2. Also shown as dotted (dashed) curves are the PDFs from CTEQ5 and MRST respectevely.

Figure 3.7: The relative uncertaintes on the gluon and singlet (sum of quarks and anti-quarks) densities, plotted as a function of x for $Q^2 = 10$ and $Q^2 = 500 \text{ GeV}^2$, due to four different sources of uncertainty (left to right column): statistical and systematic uncertainties added in quadrature, assumed α_s input value, parameterisation uncertainty, renormalization and factorization scale uncertainties added in quadrature. See text for further explanation.
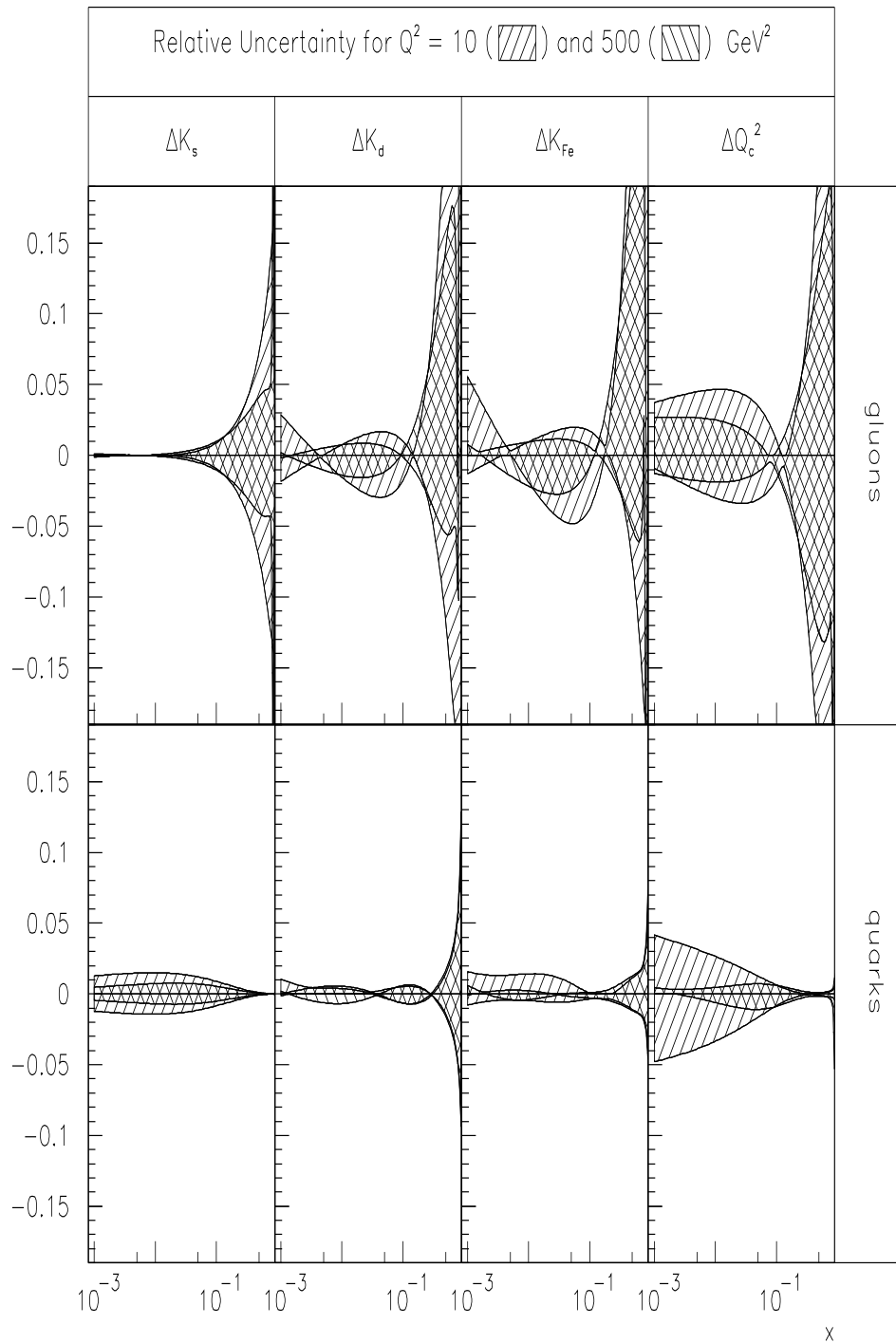
Figure 3.8: As Fig. 3.7, but for four additional sources of uncertainty (left to right column): strange content of the proton, deuteron correction, iron correction and charm threshold. See text for further explanation.
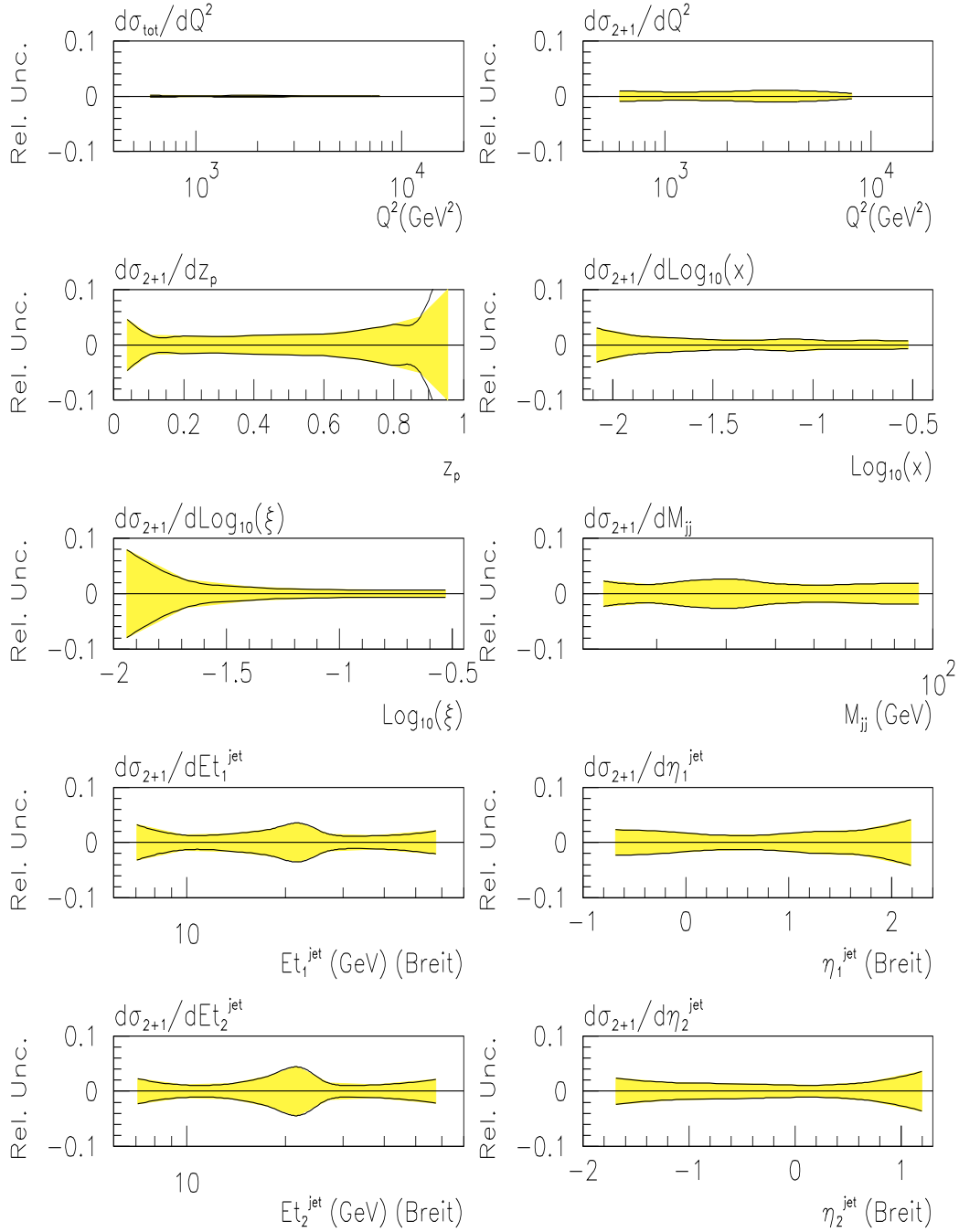
Figure 3.9: The relative numerical uncertainty, associated to a typical DISENT run, for the NLO differential cross sections.
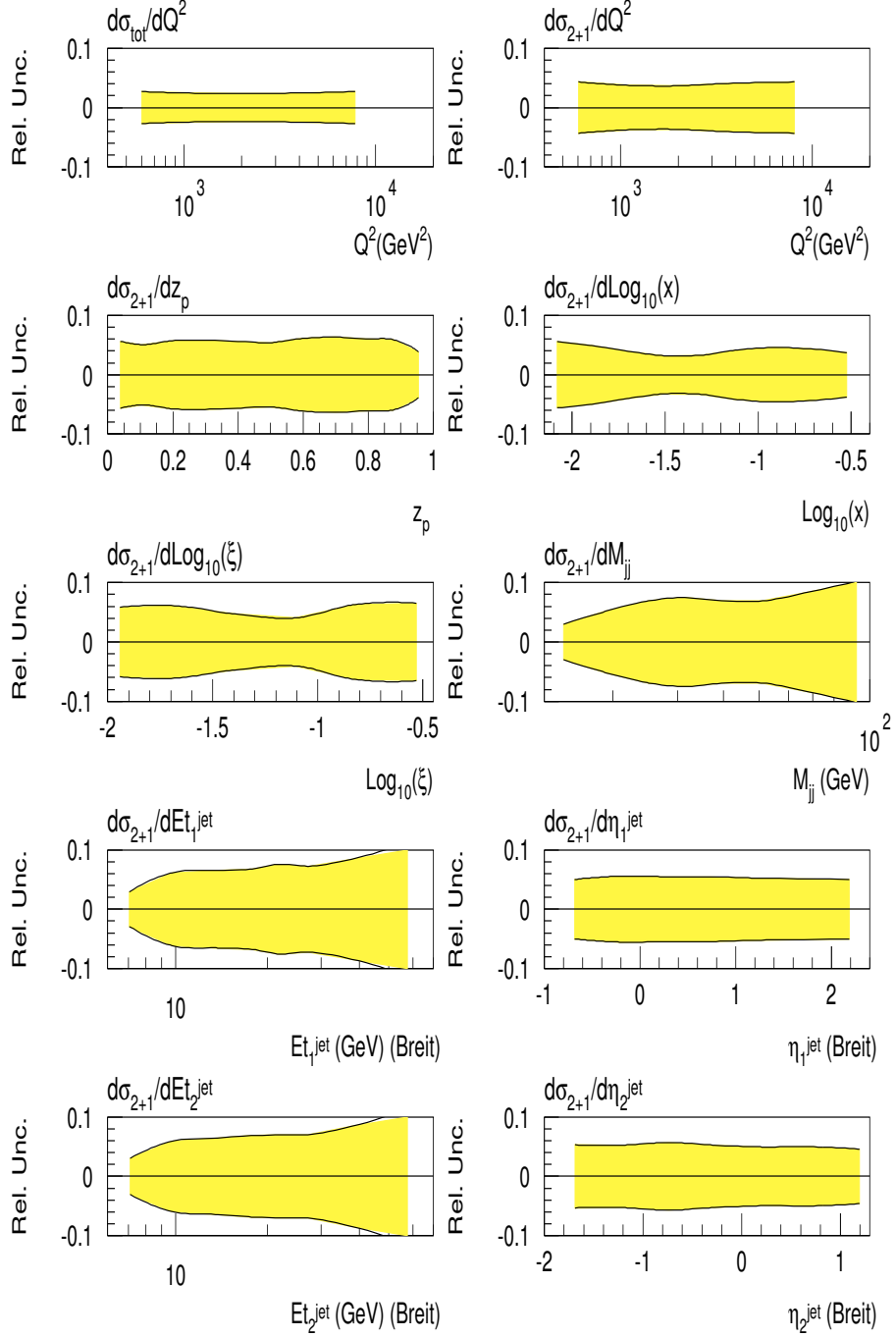
Figure 3.10: Relative uncertainties of the differential dijet cross sections due to the experimental (stat. + syst.) uncertainty of the PDFs.
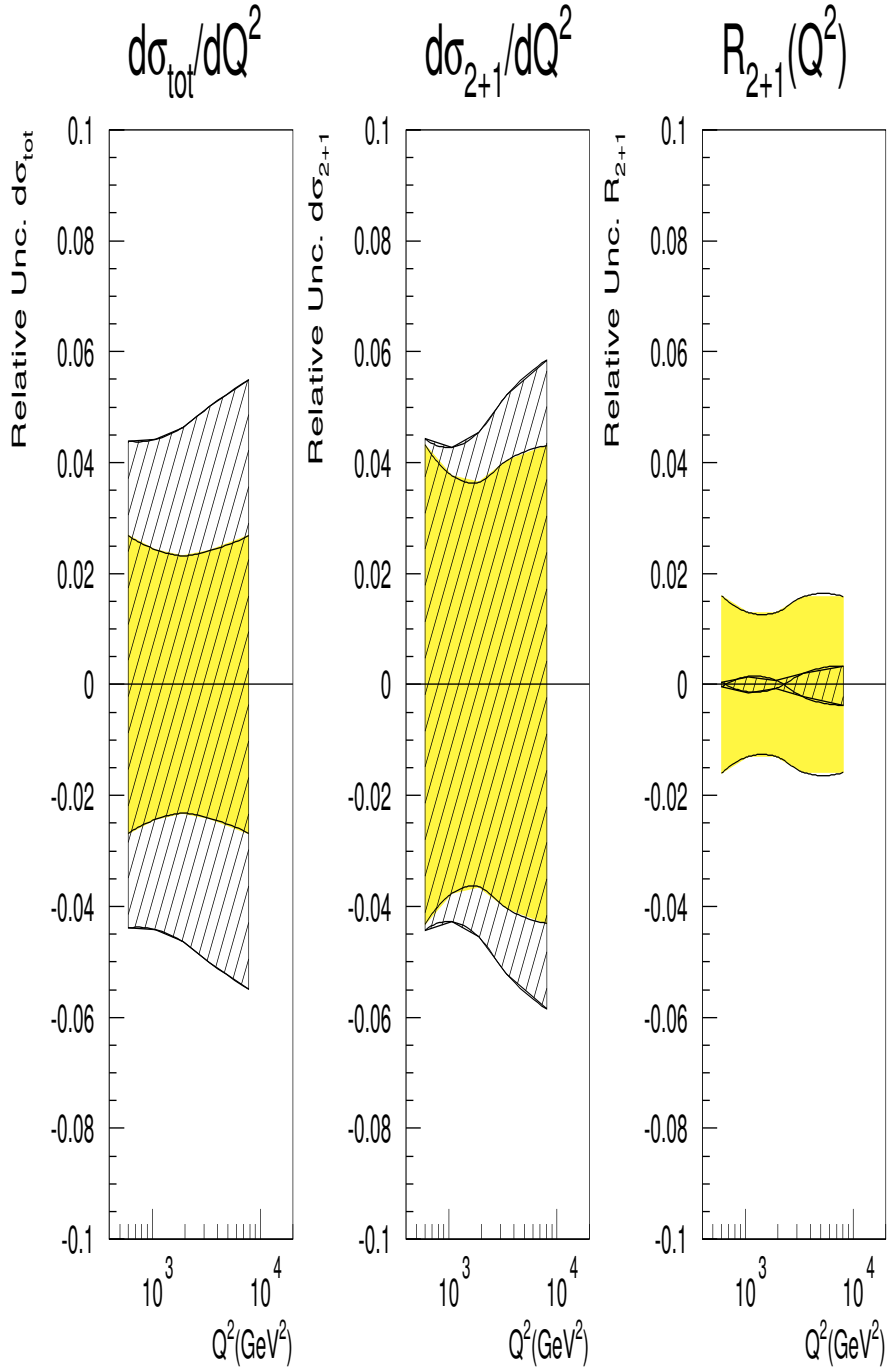
Figure 3.11: Relative uncertainties of the inclusive $d\sigma_{tot}/dQ^2$ (left), dijet $d\sigma_{2+1}/dQ^2$ (middle) cross sections and dijet fraction $R_{2+1}(Q^2)$ (right) as a function of Q^2.
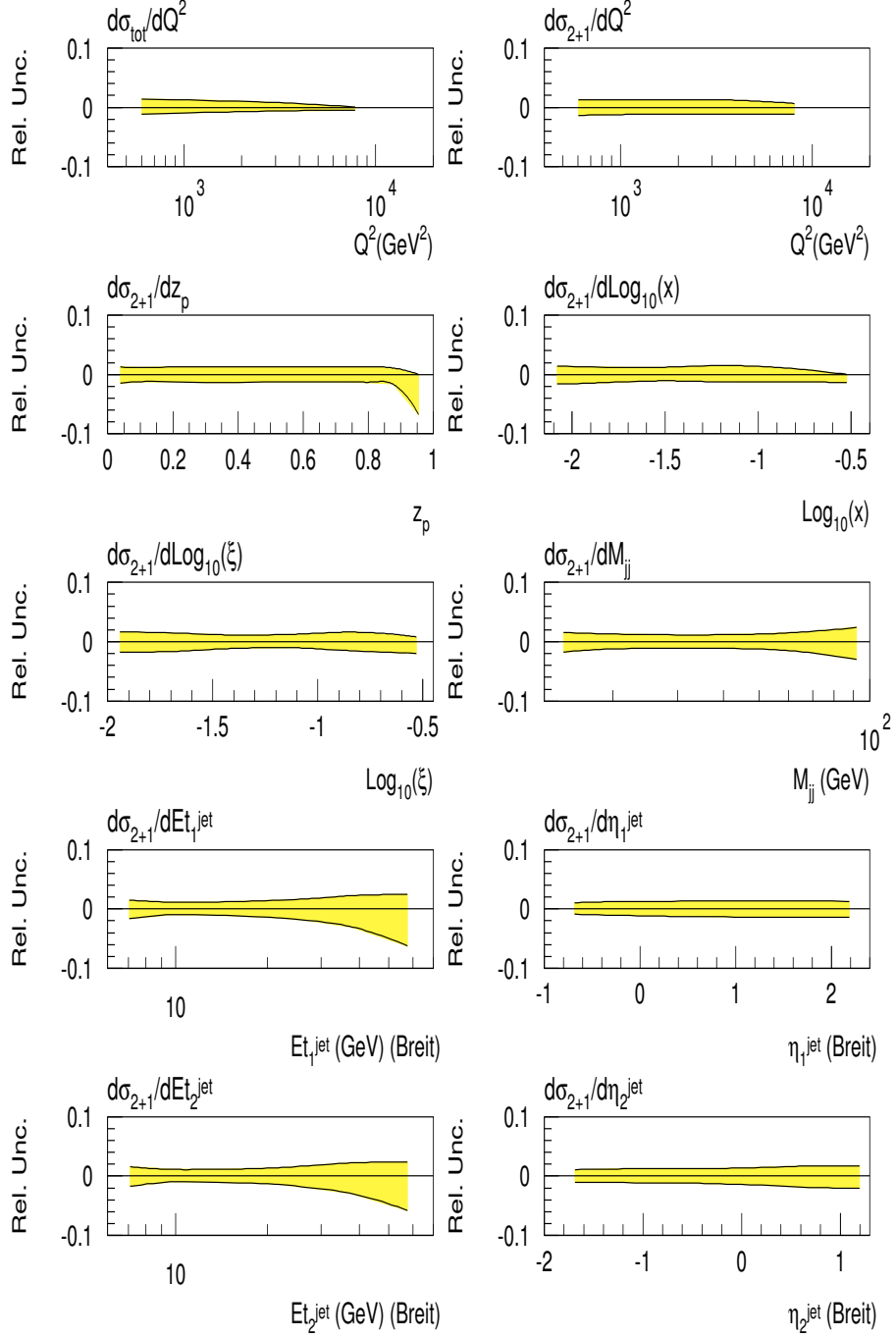
Figure 3.12: Relative uncertainties of the differential dijet cross sections due to the *parameterisation uncertainty* of the PDFs.
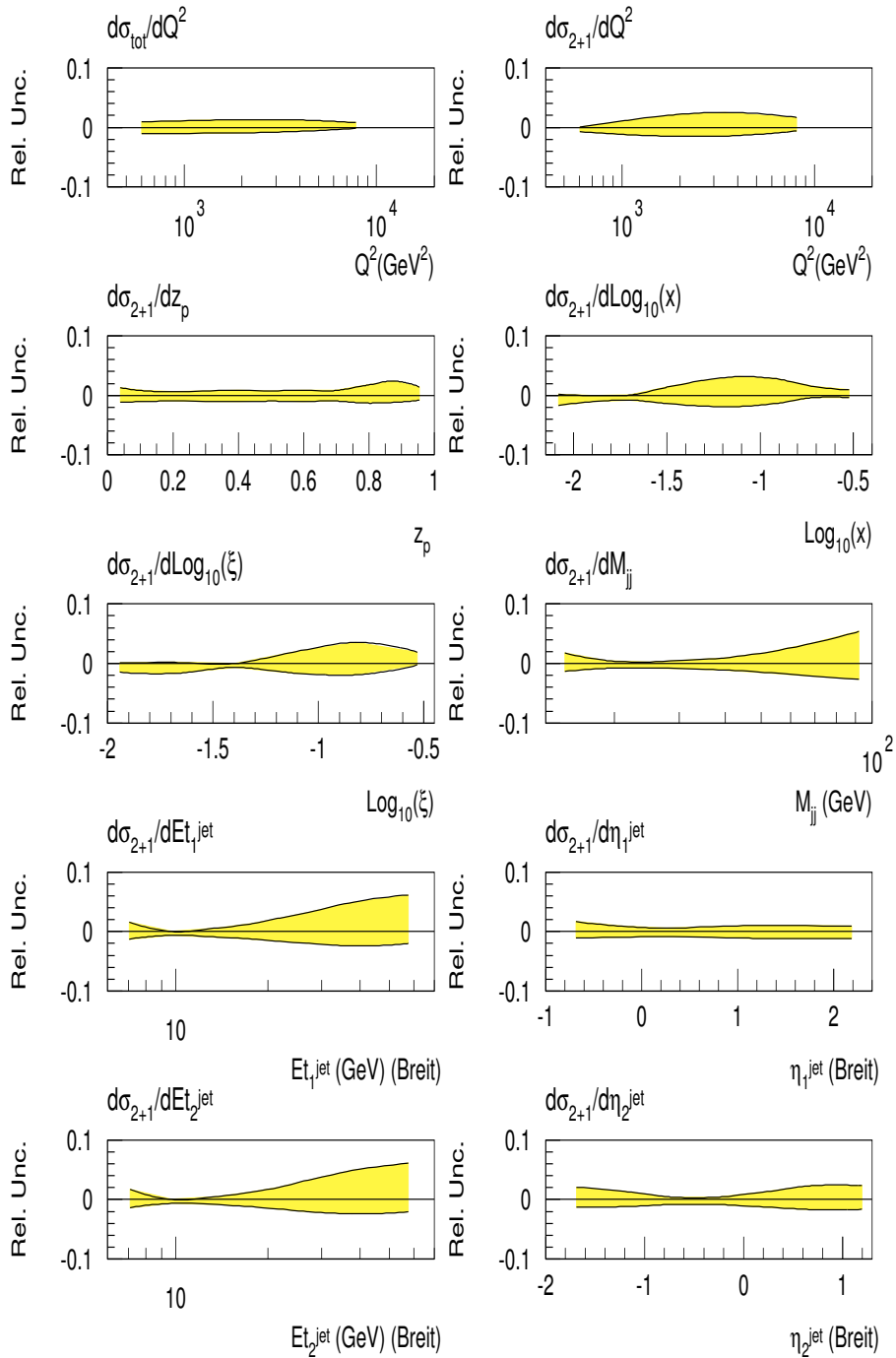
Figure 3.13: Relative uncertainties on the differential dijet cross sections obtained varying the factorization scale *only* in the PDFs.
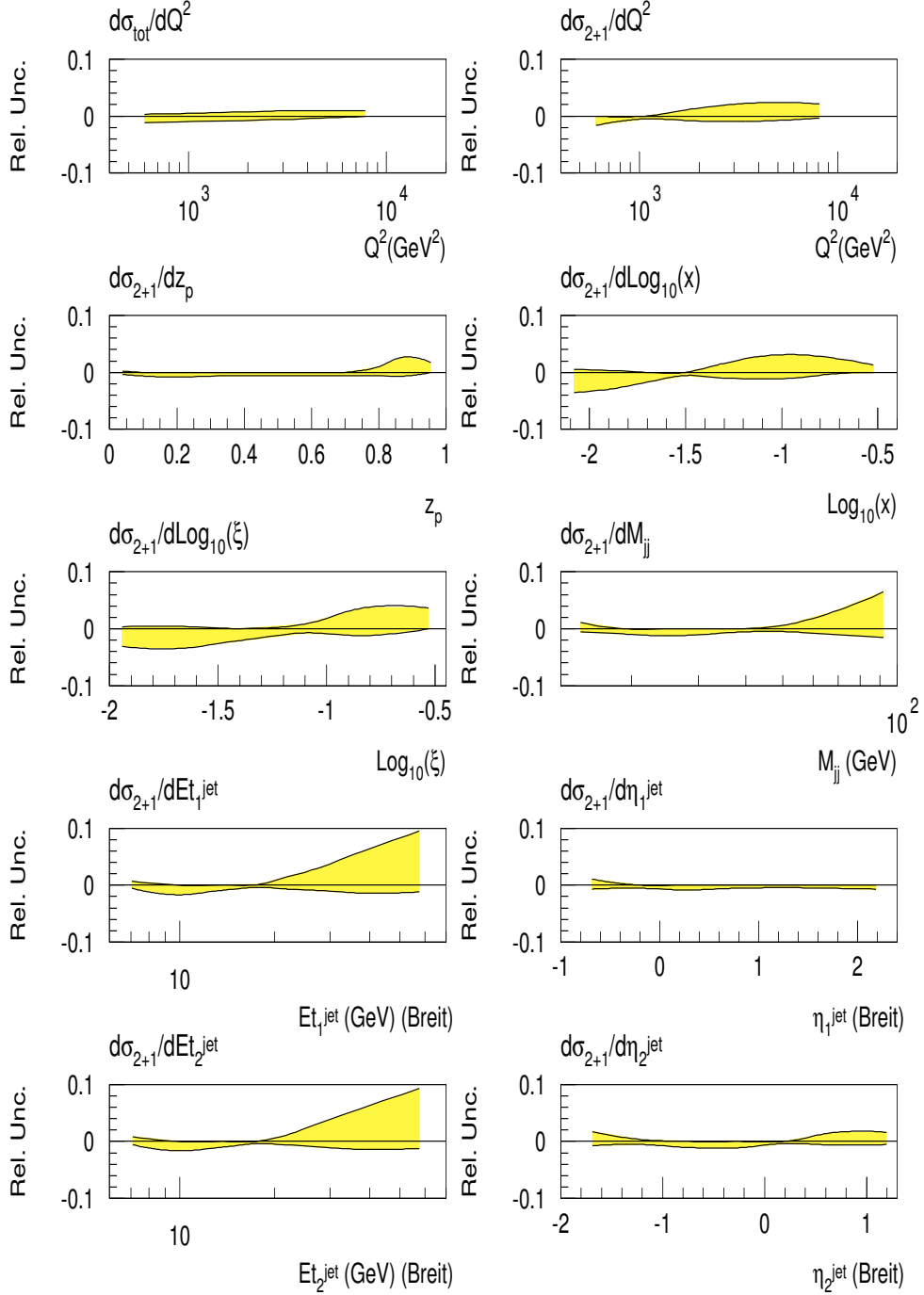
Figure 3.14: Relative uncertainties of the differential dijet cross sections obtained varying the renormalization scale *only* in the PDFs.
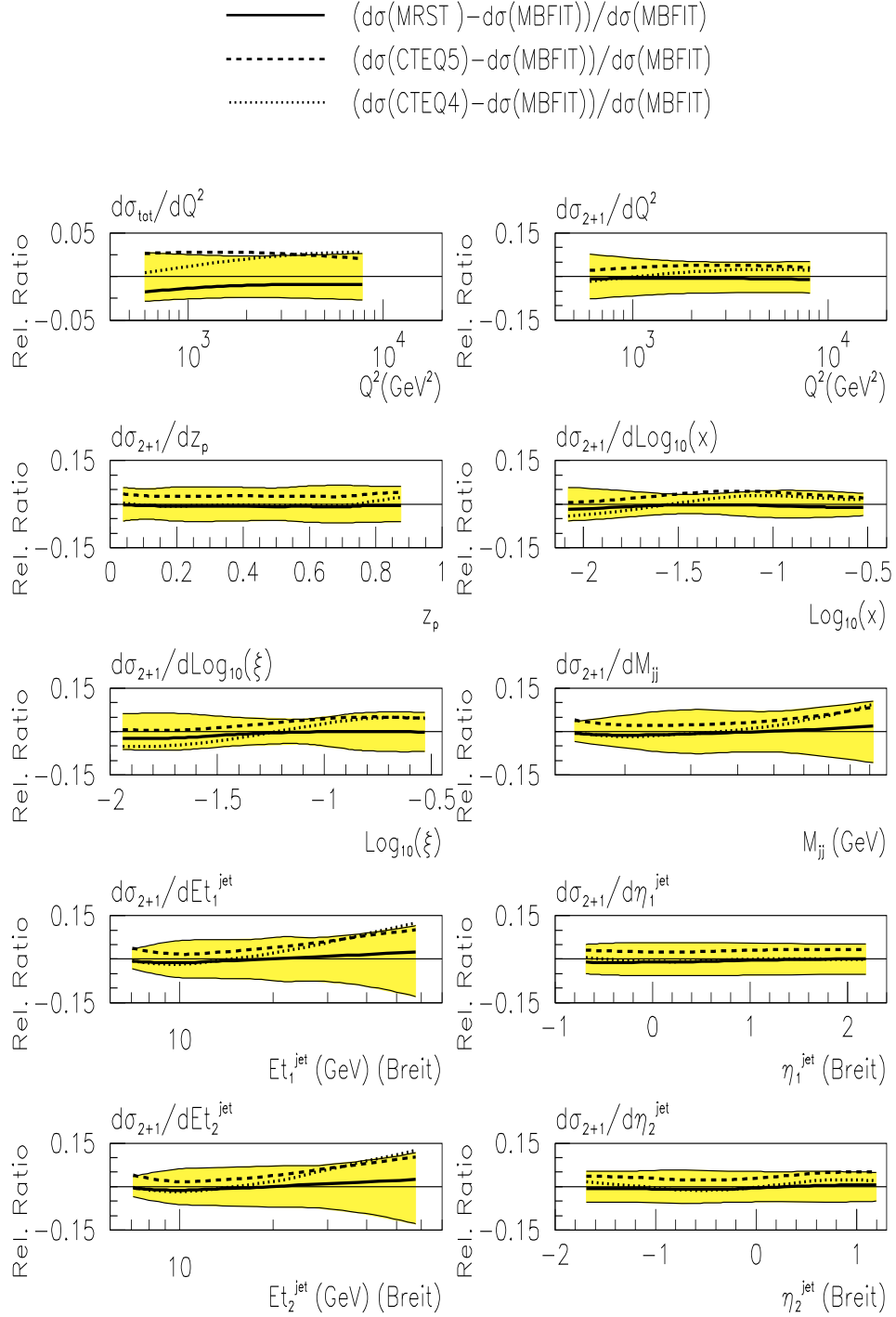
Figure 3.15: The total PDFs-related uncertainties on the NLO QCD differential cross sections. Also shown are the relative ratios, with respect to the MBFIT predictions, of the cross sections obtained using the CTEQ4, CTEQ5, and MRST PDFs.

Figure 3.16: The renormalization-scale dependence of the total dijet cross section. Shown is the ratio $\sigma_{2+1}(x_\mu \cdot \mu_{R,0})/\sigma_{2+1}(\mu_{R,0})$ in the region $0.1 < x_\mu < 10$ and for $\mu_{R,0} = \mu_{F,0} = Q$.
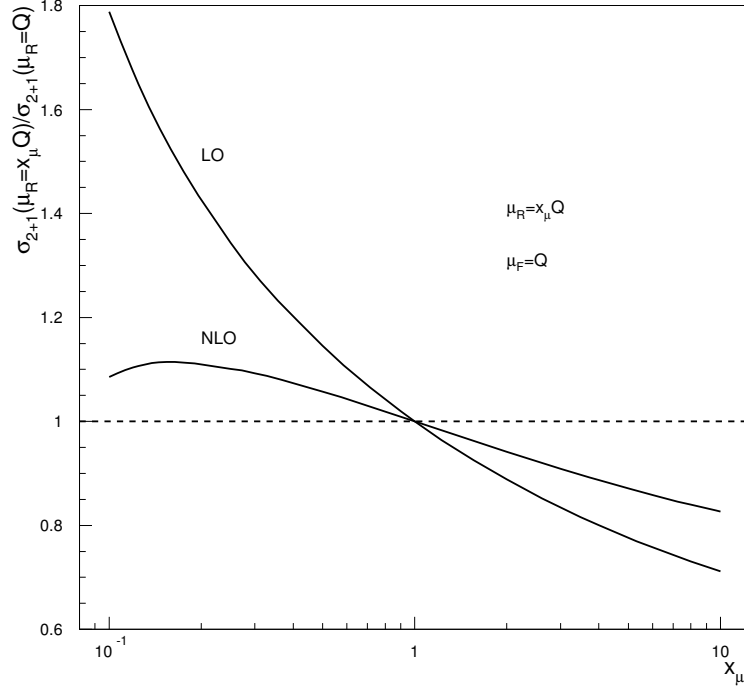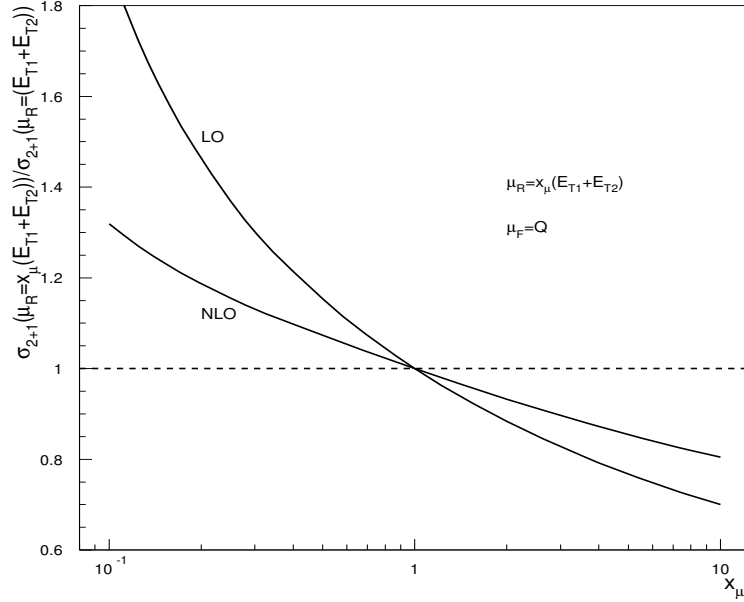

Figure 3.17: The renormalization-scale dependence of the total dijet cross section. Shown is the ratio $\sigma_{2+1}(x_\mu \cdot \mu_{R,0})/\sigma_{2+1}(\mu_{R,0})$ in the region $0.1 < x_\mu < 10$ and for $\mu_{R,0} = (E_{TB}^{jet,1} + E_{TB}^{jet,2})$ and $\mu_{F,0} = Q$.
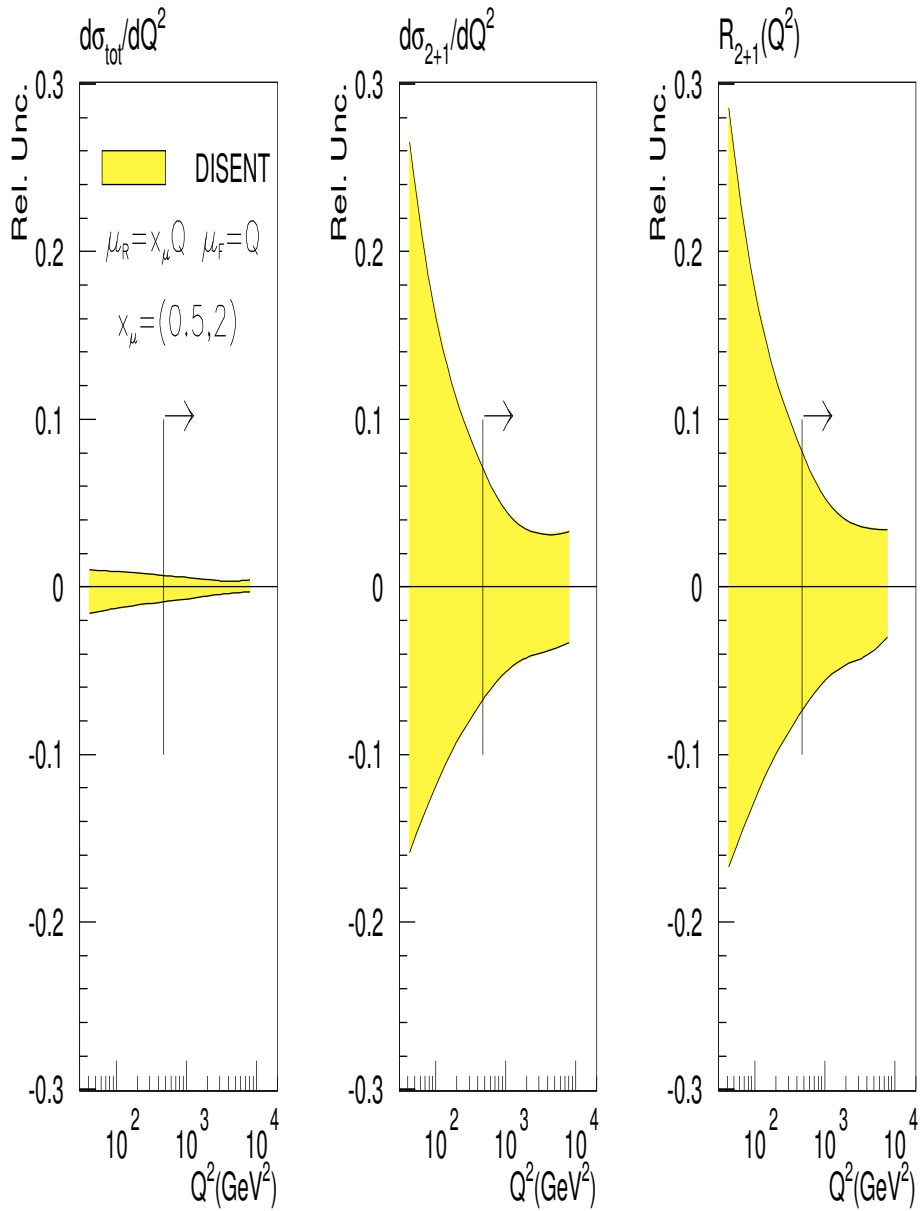
Figure 3.18: The μ_R-related uncertainty for the DIS inclusive and dijet differential cross sections, and for the dijet fraction as a function of Q^2. The arrows indicate the final Q^2 kinematic region used in this analysis.
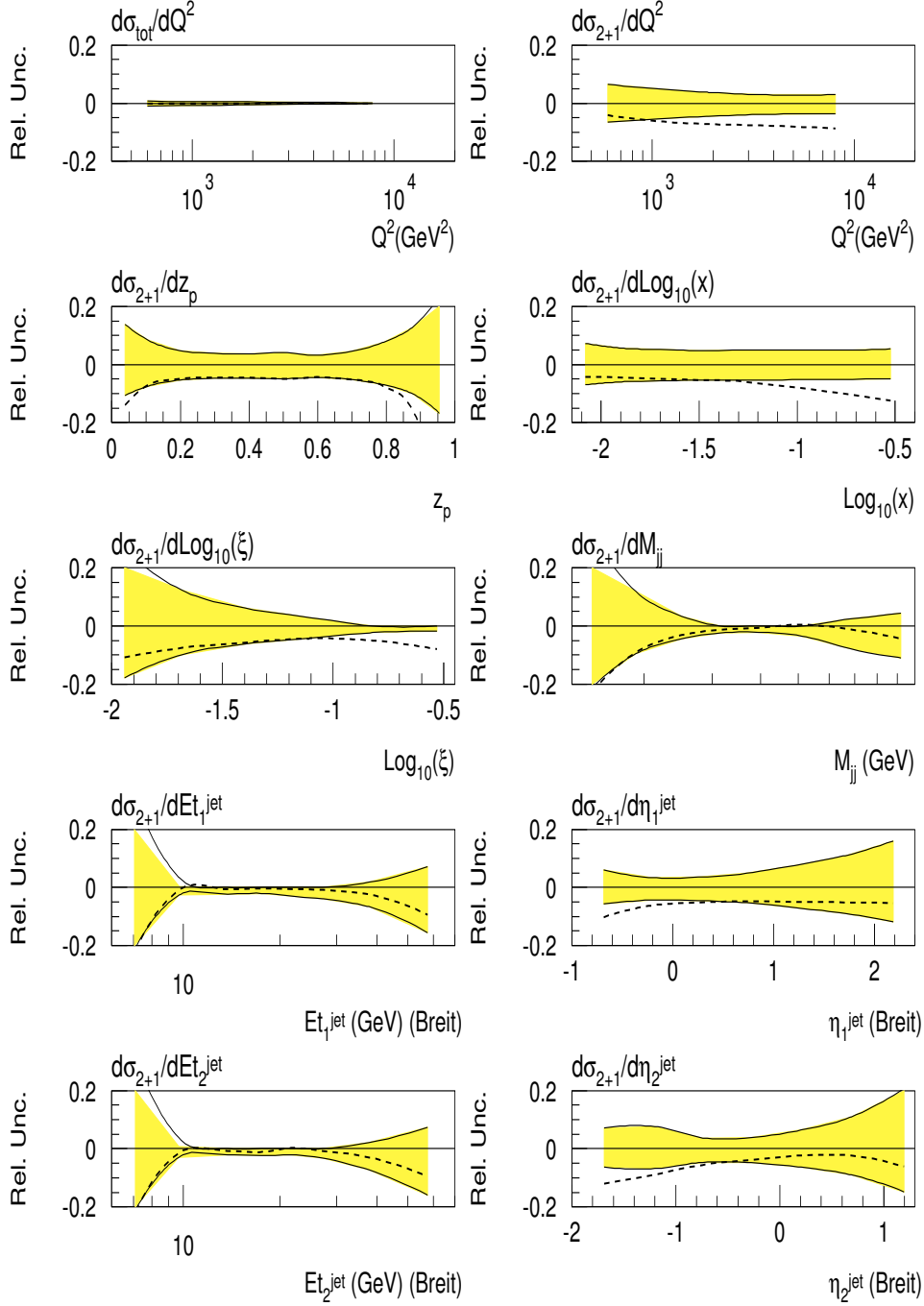
Figure 3.19: The μ_{R}-related uncertainty for the DIS inclusive and the dijet differential cross sections for $30 < Q^2 < 20000$ GeV^2. For comparison only the relative ratio $(d\sigma(\mu_{\mathrm{R}} = Q) - d\sigma(\mu_{\mathrm{R}} = E_{TB}^{jet,1} + E_{TB}^{jet,2}))/d\sigma(\mu_{\mathrm{R}} = Q)$ is also shown as a dashed line.
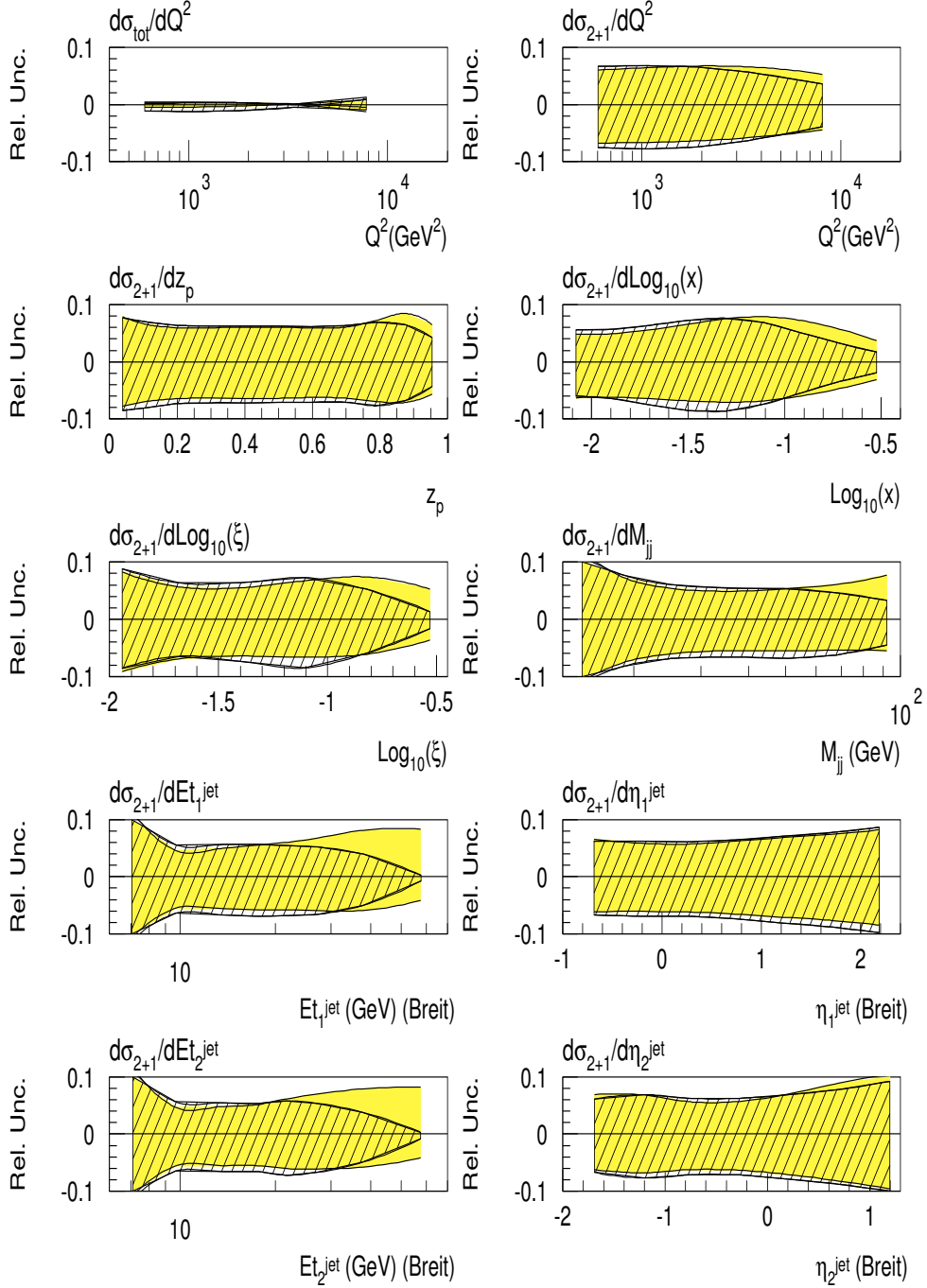
Figure 3.20: The relative uncertainties of the NLO QCD differential inclusive and dijet cross sections due to $\alpha_s(M_Z)$. The shaded (hatched) band shows the uncertainty obtained with the MBFIT(MRST)-α_s series corresponding to $\Delta\alpha_s = \pm 0.005$.

Figure 3.21: The cluster (left) and string (right) hadronisation models.

Figure 3.22: Cluster model: mass distribution of $q\bar{q}$ pairs.

Figure 3.23: The string model: space-time picture.

Figure 3.24: Particle yields in Z^0 decay.

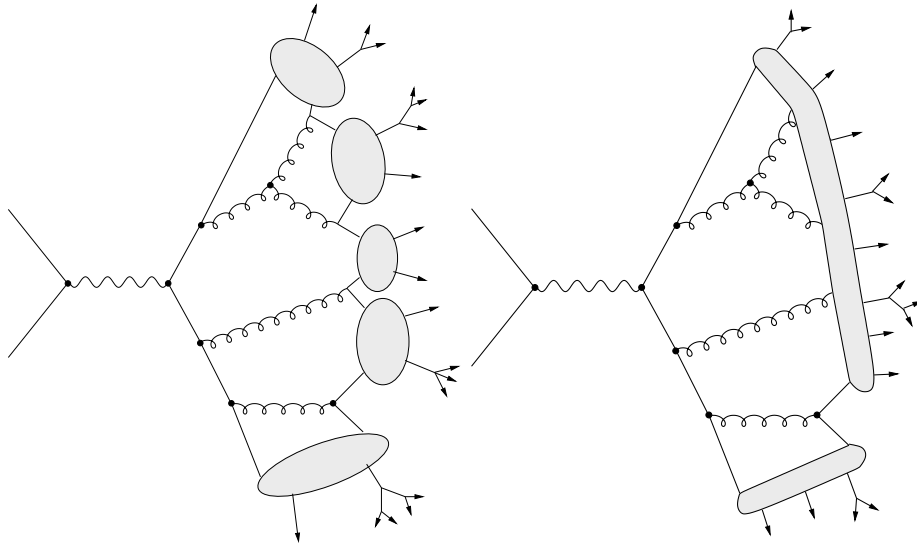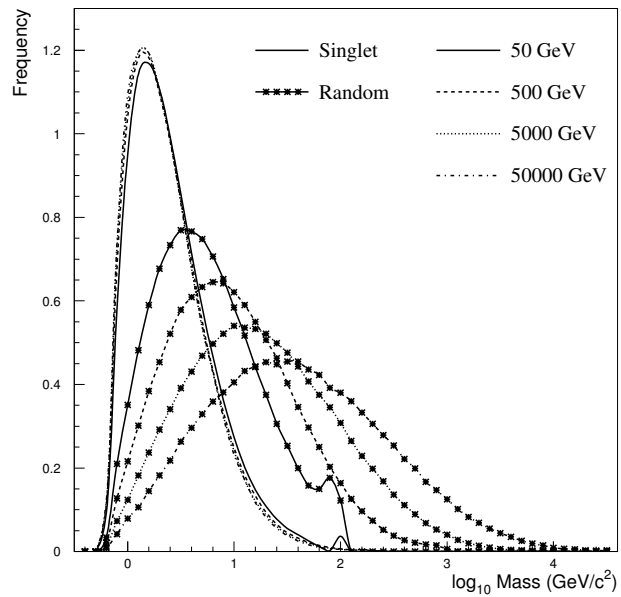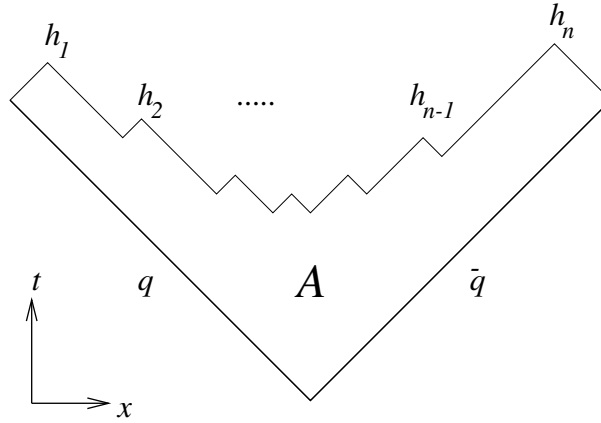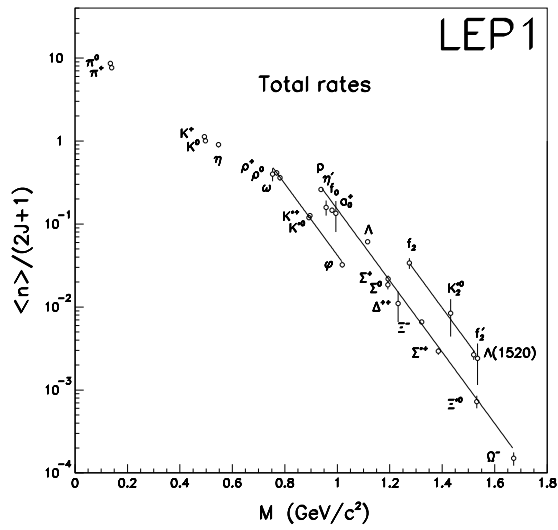| Particle	Multiplicity	HERWIG 5.9	JETSET 7.4	UCLA 7.4	Expts
Charged	20.96(18)	20.95	20.95	20.88	ADLMO
$\pi^\pm$	17.06(24)	17.41	16.95	17.04	ADO
π^0	9.43(38)	9.97	9.59	9.61	ADLO
$\boldsymbol{\eta}$	0.99(4)	1.02	1.00	<u>0.78</u>	ALO
$\rho(770)^0$	1.24(10)	1.18	1.50	1.17	AD
$\omega(782)$	1.09(9)	1.17	1.35	1.01	ALO
$\boldsymbol{\eta'(958)}$	0.159(26)	0.097	0.155	0.121	ALO
$\mathbf{f_0(980)}$	0.155(8)	<u>0.111</u>	$\sim$<u>0.1</u>	—	ADO
$a_0(980)^\pm$	0.14(6)	0.240	—	—	O
$\phi(1020)$	0.097(7)	0.104	<u>0.194</u>	<u>0.132</u>	ADO
$\mathbf{f_2(1270)}$	0.188(14)	0.186	~ 0.2	—	ADO
$f_2'(1525)$	0.012(6)	0.021	—	—	D
$K^\pm$	2.26(6)	2.16	2.30	2.24	ADO
$\mathbf{K^0}$	2.074(14)	2.05	2.07	2.06	ADLO
$K^*(892)^\pm$	0.718(44)	0.670	<u>1.10</u>	0.779	ADO
$K^*(892)^0$	0.759(32)	0.676	<u>1.10</u>	0.760	ADO
$K_2^*(1430)^0$	0.084(40)	0.111	—	—	DO
$D^\pm$	0.187(14)	<u>0.276</u>	0.174	0.196	ADO
D^0	0.462(26)	0.506	0.490	0.497	ADO
$D^*(2010)^\pm$	0.181(10)	0.161	<u>0.242</u>	<u>0.227</u>	ADO
$D_s^\pm$	0.131(20)	0.115	0.129	0.130	O
B^*	0.28(3)	0.201	0.260	0.254	D
$B_{u,d}^{**}$	0.118(24)	<u>0.013</u>	—	—	D
J/ψ	0.0054(4)	<u>0.0018</u>	0.0050	0.0050	ADLO
$\psi(3685)$	0.0023(5)	0.0009	0.0019	0.0019	DO
χ_{c1}	0.0086(27)	<u>0.0001</u>	—	—	DL

Table 3.4: The meson yields in Z^0 decay. Experiments: A=Aleph, D=Delphi, L=L3, M=Mark II, O=Opal. Bold: new data. Underlined: disagreement with data by more than 3σ.

Particle	Multiplicity	HERWIG 5.9	JETSET 7.4	UCLA 7.4	Expts
p	1.04(4)	<u>0.863</u>	<u>1.19</u>	1.09	ADO
Δ^{++}	0.079(15)	<u>0.156</u>	<u>0.189</u>	<u>0.139</u>	D
	0.22(6)	0.156	0.189	0.139	O
Λ	0.399(8)	0.387	0.385	0.382	ADLO
$\Lambda(1520)$	0.0229(25)	—	—	—	DO
$\Sigma^{\pm}$	0.174(16)	0.154	0.140	0.118	DO
Σ^0	0.074(9)	0.068	0.073	0.074	ADO
$\Sigma^{\star\pm}$	0.0474(44)	<u>0.111</u>	<u>0.074</u>	<u>0.074</u>	ADO
Ξ^-	0.0265(9)	<u>0.0493</u>	0.0271	<u>0.0220</u>	ADO
$\Xi(1530)^0$	0.0058(10)	<u>0.0205</u>	0.0053	0.0081	ADO
Ω^-	0.0012(2)	<u>0.0056</u>	0.00072	0.0011	ADO
Λ_c^+	0.078(17)	<u>0.0123</u>	0.059	<u>0.026</u>	O

Table 3.5: Baryon yields in Z^0 decay. Legend as in table Table 3.4.
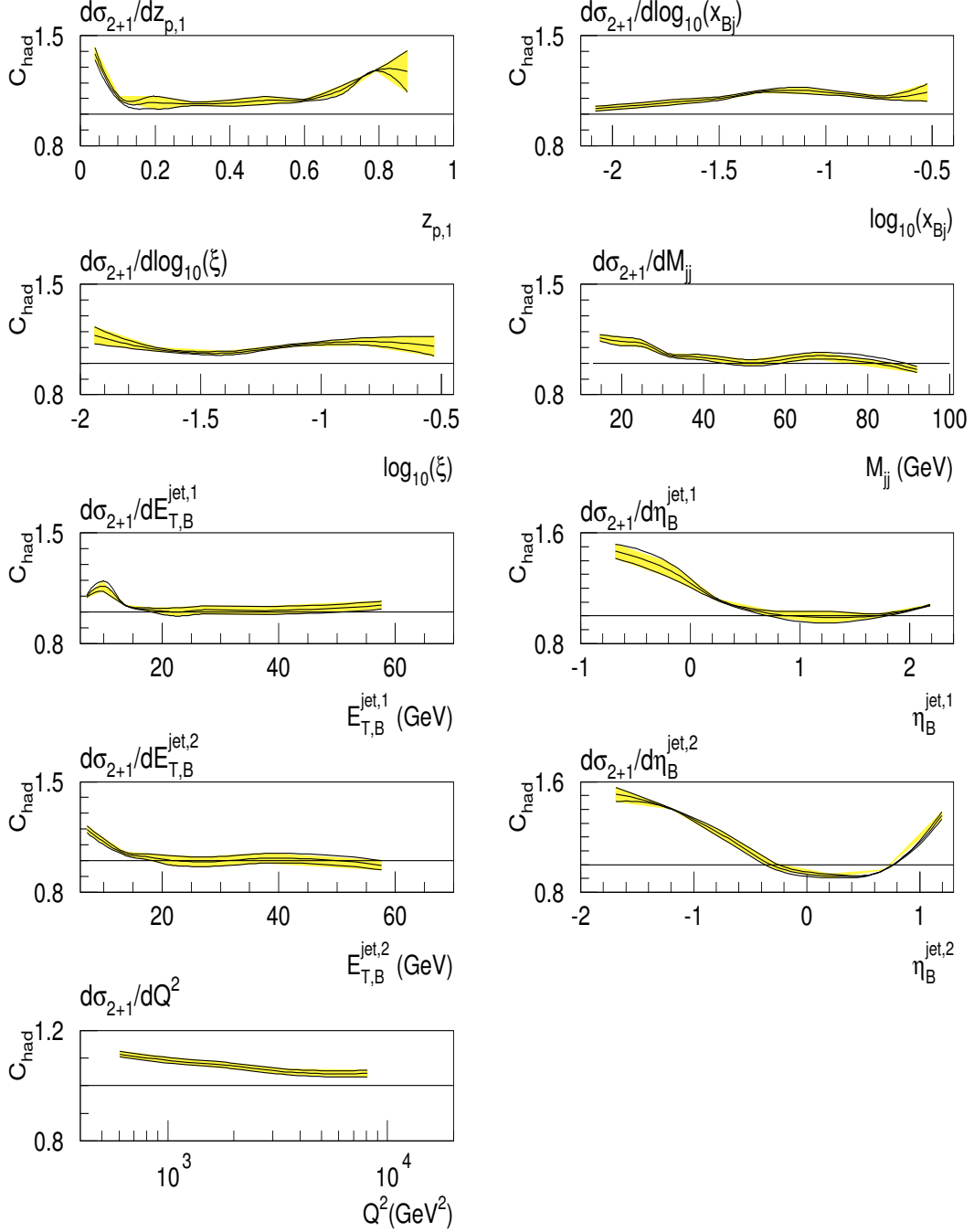
Figure 3.25: The Hadronisation-correction factors (and associated uncertainties) for the differential dijet cross sections.
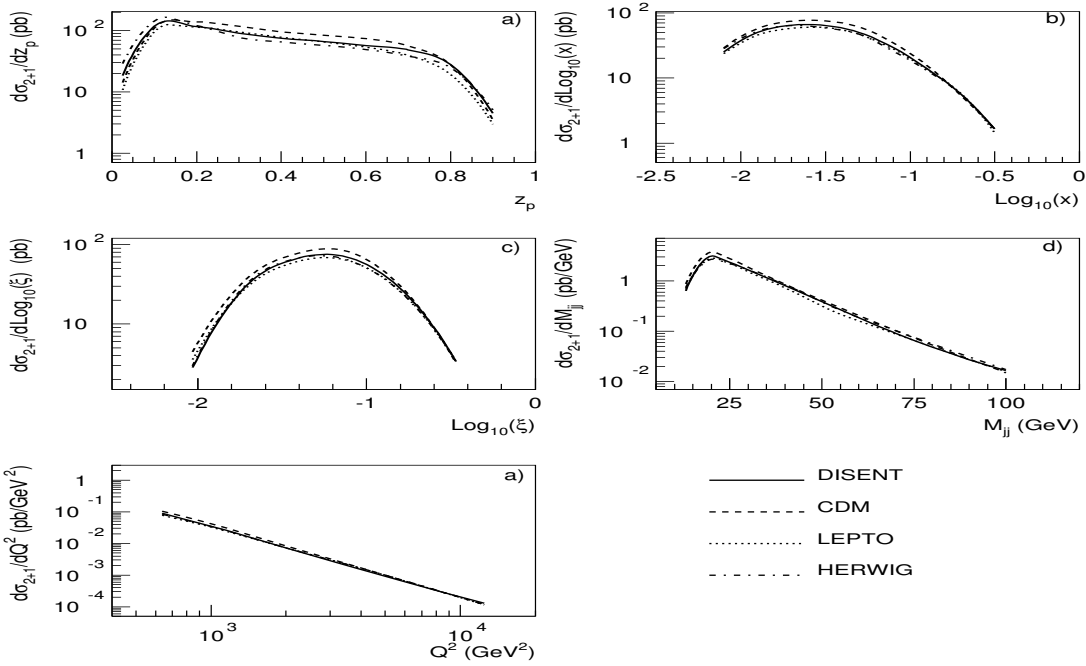
Figure 3.26: A comparison of the NLO QCD and parton-level MC differential dijet cross sections in NC DIS as a function of a) z_p, b) $Log_{10}(x)$, c) $Log_{10}(\xi)$, d) M_{jj} and e) Q^2. The parton level predictions are obtained with the ARIADNE, LEPTO and HERWIG MC programs.
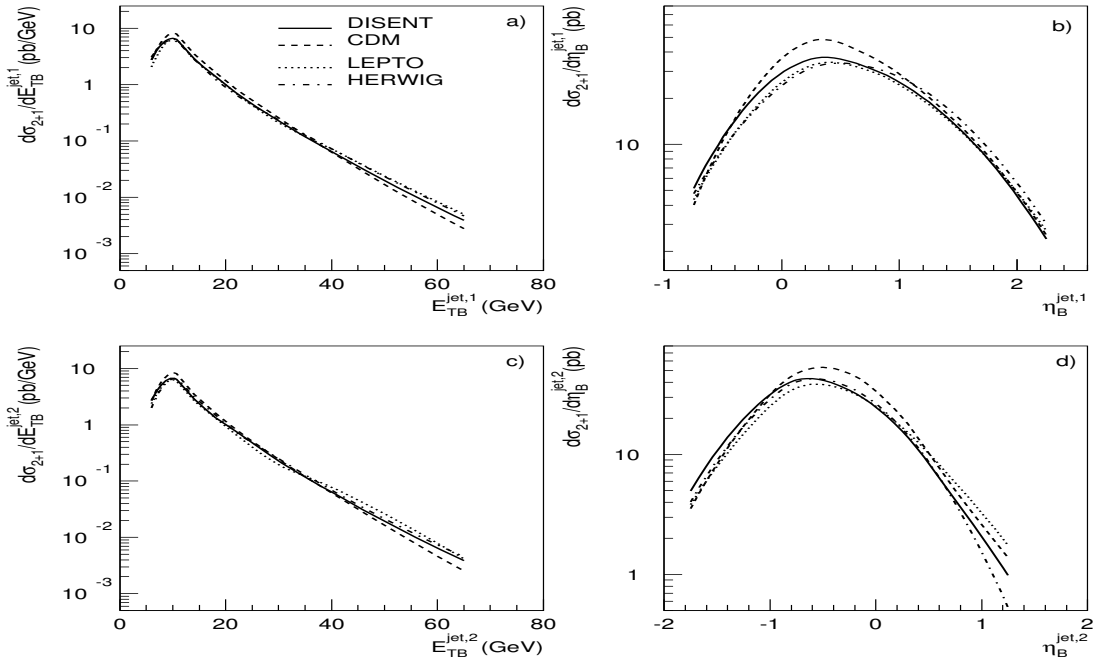
Figure 3.27: A comparison of the NLO QCD and parton-level MC differential dijet cross sections in NC DIS as a function of a) $E_{TB}^{jet,1}$, b) $\eta_B^{jet,1}$, c) $E_{TB}^{jet,2}$ and d) $\eta_B^{jet,2}$. The parton level predictions are obtained with the ARIADNE, LEPTO and HERWIG MC programs.
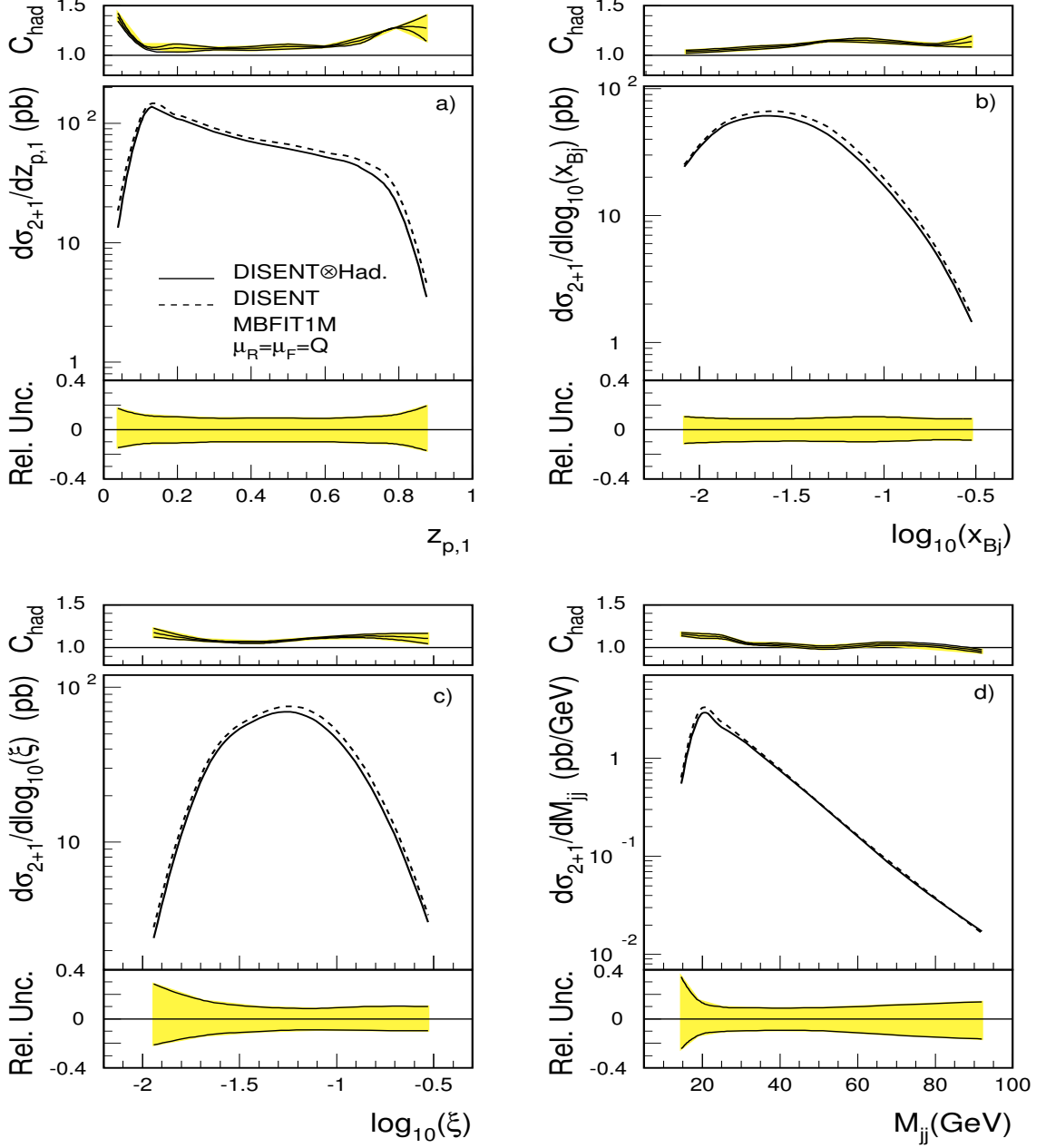
Figure 3.28: The QCD differential dijet cross sections in NC DIS as functions of a) z_p, b) $Log_{10}(x)$, c) $Log_{10}(\xi)$ and d) M_{jj}. The cross sections are obtained with the program DISENT using the MBFIT1M PDFs and $\mu_R = \mu_F = Q$. The dashed lines show the pure NLO QCD calculations. The solid lines show the NLO QCD calculations corrected for hadronisation effects. The relative total uncertainty of the QCD calculation is shown, as a shaded band, underneath each plot.
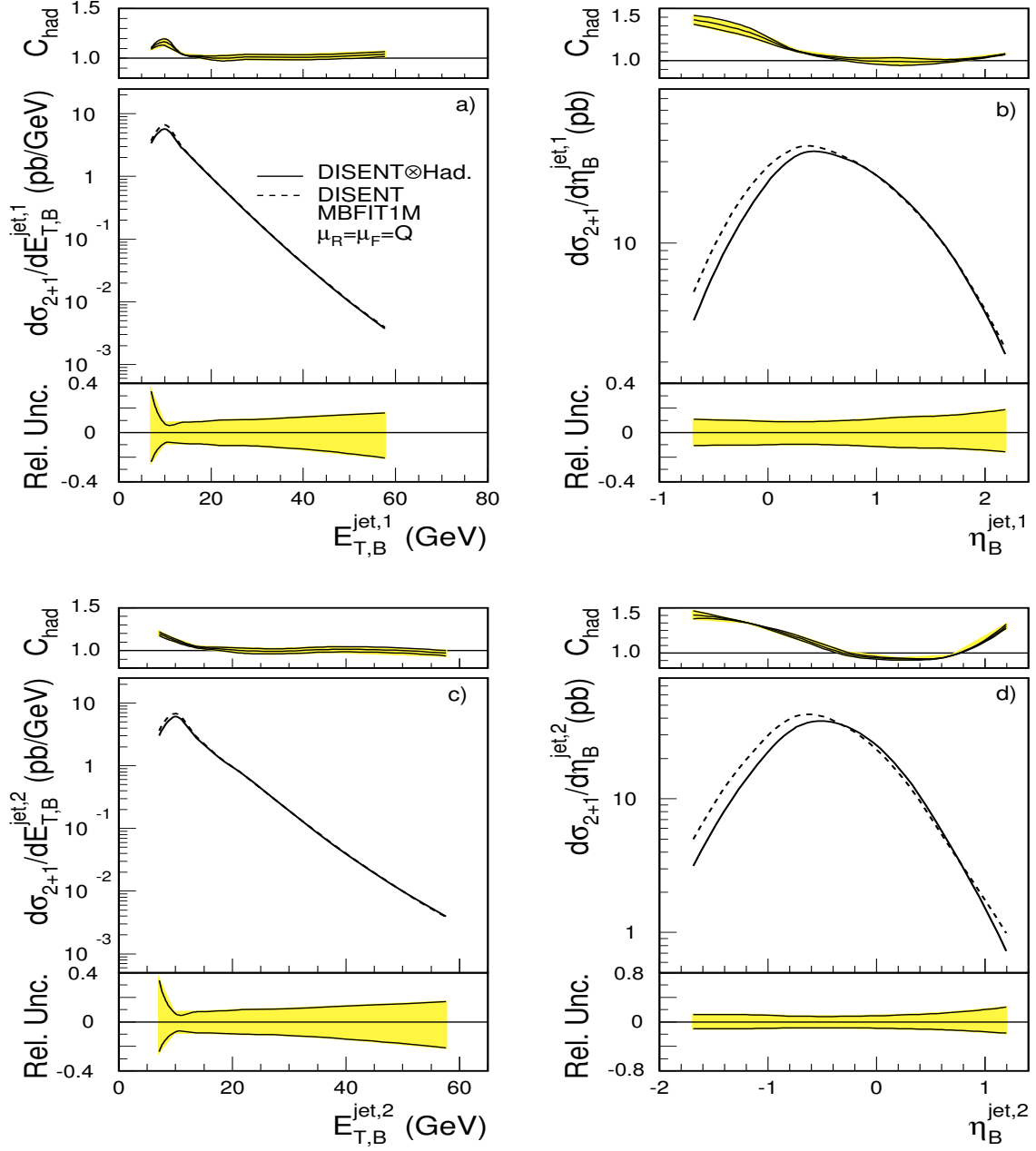
Figure 3.29: The QCD differential dijet cross sections in NC DIS as functions of a) $E_{TB}^{jet,1}$, b) $\eta_B^{jet,1}$, c) $E_{TB}^{jet,2}$ and d) $\eta_B^{jet,2}$. The cross sections are obtained with the program DISENT using the proton MBFIT1M PDFs and $\mu_R = \mu_F = Q$. The dashed lines show the pure NLO QCD calculations. The solid lines show the NLO QCD calculations corrected for hadronisation effects. The relative total uncertainty of the QCD calculation is shown, as a shaded band, underneath each plot.
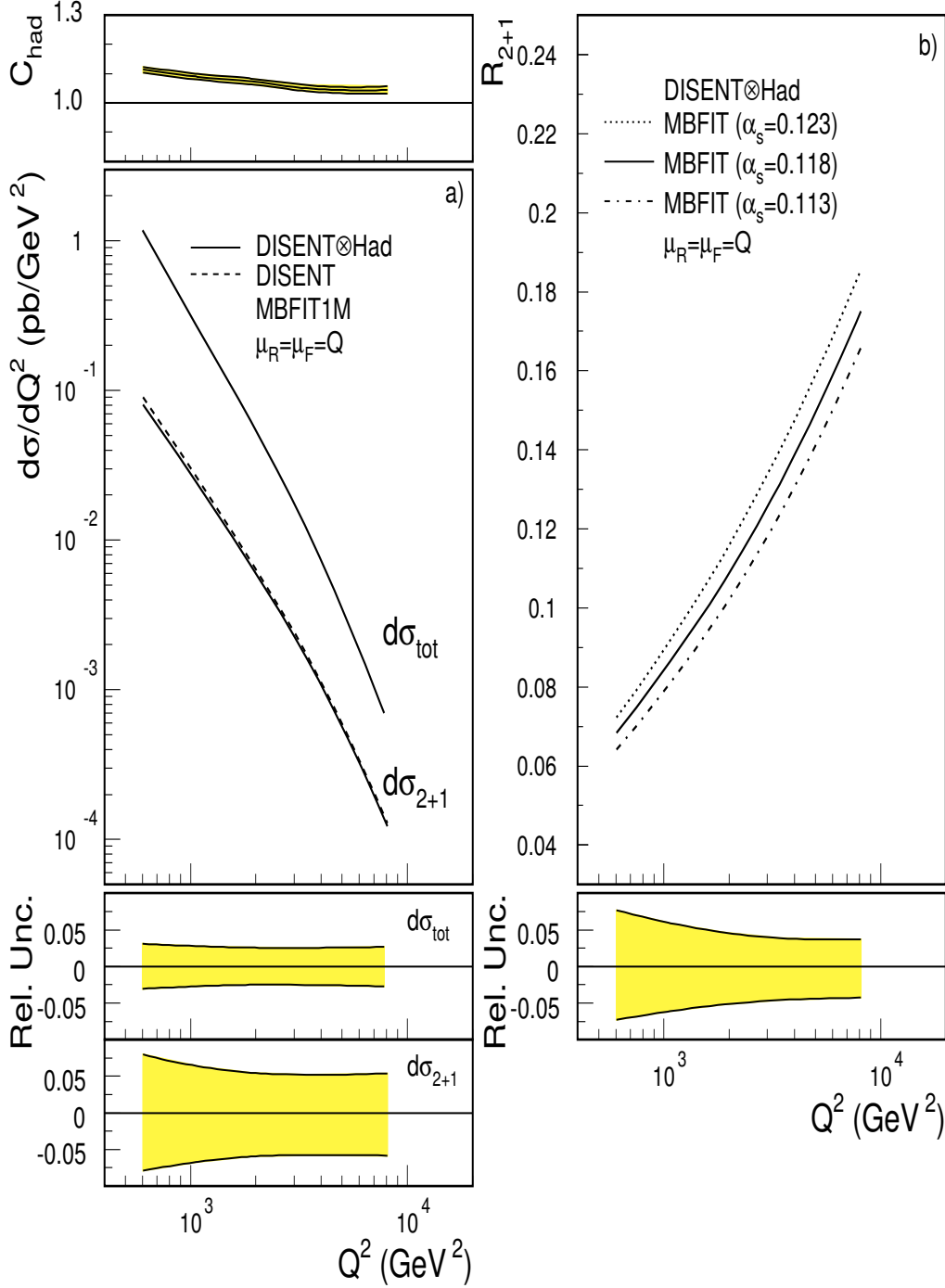
Figure 3.30: The QCD a) inclusive ($d\sigma_{tot}/dQ^2$) and dijet ($d\sigma_{2+1}/dQ^2$) differential cross sections and b) the dijet fraction $R_{2+1}(Q^2)$ in NC DIS as a function Q^2. The cross sections are obtained with program DISENT using the proton MBFIT PDFs and $\mu_R = \mu_F = Q$. The dashed lines show the pure NLO QCD calculations. The solid lines show the NLO QCD calculations corrected for hadronisation effects. For the dijet fraction the QCD predictions obtained for $\alpha_s(M_Z) = 0.123$ and 0.113 are also shown. The relative total uncertainty of the QCD calculation is shown, as a shaded band, underneath each plot.

Chapter 4

The ZEUS Detector at HERA

In this chapter we will briefly describe the HERA Collider and the ZEUS detector. In describing the detector we will focus on those components that are of particular relevance for this analysis. A description of the ZEUS trigger architecture is given at the end of the chapter.

4.1 The HERA Accelerator

The Hadron Electron Ring Accelerator, HERA, is the first lepton-proton collider in the world. It is designed to accelerate electrons or positrons and protons in the 6.3 km long ring to 30 GeV and 820 GeV, respectively[1]. The purpose of HERA is to enable the investigation of DIS in a region of phase space not accessible thus far to previous experiments.

HERA is located near the main site of the DESY laboratory in Hamburg, Germany. A view of the HERA layout is depicted in Fig. 4.1.

In the 1996-97 data-taking period HERA operated at a proton energy of 820 GeV and a positron energy of 27.52 GeV, resulting in a center of mass energy $\sqrt{s}$ of 300 GeV. To reach an equivalent center of mass energy with a fixed target proton would require an electron beam of 48 TeV.

During this period HERA operated with 153 ep bunches with typical beam currents of 30-40 mA for electrons and 70-80 mA for protons. Besides these colliding bunches there were also unpaired (or *pilot*) 17 proton- and 15 electron-pilot bunches as well as 25 empty bunches. The pilot bunches can be used to estimate beam related background rates, while empty bunches allow the estimation of background rates originating from cosmic rays or to study the noise characteristics of detector components. The design and performance parameters of the HERA machine are summarized in table 4.1.

The integrated luminosity delivered by HERA (see Fig. 4.2) has continuously increased, from about 30 nb^{-1} in the 1992 data taking period to almost 37 pb^{-1} in 1997.

4.2 The ZEUS Detector

The design, construction and operation of the ZEUS detector owes its successes to the hard work of almost 500 physicists and as many members of technical staff. This multinational collaboration is an assembly of more than 50 institutes coming from 12 different countries. The main detector, weighing 3600 tones and standing 12 meters in height, is located 30m underground in the South Experimental Hall of the main HERA ring.

The coordinate system of ZEUS is defined as a right-handed system with the origin at the nominal interaction point (IP). In this system, the incoming proton direction, referred to as the

---

[1]In the 1998-2000 running period, the proton energy in HERA was increased to 920 GeV.

forward direction, defines the z-axis and the x-axis is defined to point horizontally towards the center of HERA. Thus, the proton beam polar angle is 0°, whereas the electron beam polar angle is 180°. The azimuthal angle ϕ is measured w.r.t the positive x-axis (see Fig. 4.3).

ZEUS is a multi-purpose solenoid detector with a solid angle coverage of $> 99.6\%$ of 4π srad consisting of inner tracking detectors surrounded by a high resolution Uranium Calorimeter and a muon detection system. The longitudinal and transverse cross sections through the detector, showing the main components, are presented Fig. 4.4 and Fig. 4.5. The asymmetry of the detector on either side of the interaction point reflects the large momentum imbalance between the colliding beams.

The complete and detailed descriptions of the ZEUS detector may be found in the original technical proposal [87] and subsequent status reports [88]. The components of the detector essential for the present analysis are described in more detail in the following sections. A brief description of the ZEUS detector is given below.

Starting radially outward from the interaction point is the central tracking detector (CTD); a large drift chamber for charged particle identification and measurement. The CTD is surrounded by a super-conducting magnet providing a field of 1.43 T. Forward and rear tracking chambers (FTD and RTD) provide extra tracking information in the forward and rear directions. The tracking chambers are surrounded by a high resolution Uranium Calorimiter (UCAL). The UCAL is divided into three main sections; the FCAL in the forward (proton) direction, the BCAL a barrel section surrounding the central region and the RCAL in the rear (electron) direction. The UCAL is enclosed by muon chambers (FMUI, BMUI and RMUI) on the inner side of an iron yoke. The yoke itself serves as an absorber for the backing calorimeter (BAC), which measures the energy of late-showering particles and also provides the return path for the solenoid magnetic field flux. On the outer side of the yoke, the outer muon chambers are installed (FMUO, BMUO and RMUO). Downstream of the main detector in the electron direction at $z = -7.5$ m an iron-scintillator Vetowall is used to reject beam-related backgrounds. The C5 beam monitor, a small lead-scintillator counter, located around the beam pipe at $z = -3.15$ m, is used to determine the nominal interaction point and monitor the proton and electron bunch shapes from timing measurements. Upstream of the interaction point, the proton remnant tagger (PRT), a lead-scintillator counter, located at $z = 5.1$ m around the beam pipe provides information about high energy charged particles which are produced at very small angles and leave the main detector through the beam hole. The leading proton spectrometer (LPS) installed at intervals along the beam line (20-90 m) and forward neutron calorimeter (FNC) located at about 100 m in the forward direction detect protons and neutrons scattered through a very small angles, respectively.

The short time interval of 96 ns between the bunch crossings at HERA results in a nominal rate of 10 MHz. ZEUS employs a three-level triggering system to reduce the rate to a few Hz, a level at which data can be written to tape.

4.2.1 The Central Tracking Detector

The CTD [89] provides the direction and momentum information of charged particles with high precision and estimates the energy loss dE/dx used for particle identification. It is a cylindrical gas-filled drift chamber, covering an angular region from $15°$ to $164°$. The gas is a mixture of 83% argon, 5% CO_2, and 12% ethane bubbled through alcohol.

The chamber is organized radially into 9 superlayers. The odd-numbered superlayers are axial layers and have their sense wires parallel to the CTD axis, whereas the even-numbered superlayers are stereo layers and have their wires inclined at a small angle ($\pm 5°$) to the chamber axis. The resolution of the CTD is around 230 μm in $r\phi$, resulting in a transverse momentum resolution (for full-length tracks) of $\sigma_{p_t}/p_t = 0.0058p_t \oplus 0.0065 \oplus 0.0014/p_t$, with p_t in GeV.

4.2.2 The Uranium Calorimeter

The Uranium Calorimeter (UCAL) [90] is one of the most essential detector components at ZEUS for the reconstruction of *ep*-scattering events and plays a crucial role in the present analysis. The UCAL is a sampling calorimeter, consisting of alternating layers of depleted uranium as absorber and scintillator as active material for readout purposes. The thickness of the plates (2.6 mm scintillator and 3.3 mm = 1 X_0 uranium) has been chosen such that the calorimeter response to electrons and hadrons is the same ($e/h = 1 \pm 0.02$) over a wide range of energies, or in other words the calorimeter is said to be compensating. The compensation characteristic is particularly important for energy resolution of hadrons as hadronic showers have a statistically fluctuating electromagnetic component. The energy resolution of the ZEUS calorimeter, measured under test beam conditions, is $\sigma(E)/E = 18\%/\sqrt{E} \oplus 1\%$ for electrons and $\sigma(E)/E = 35\%/\sqrt{E} \oplus 2\%$ for hadrons, where energy is measured in GeV, and $\oplus$ means summation in quadrature.

The calorimeter is divided into three parts, the Forward (FCAL), the Barrel (BCAL) and the Rear (RCAL) (see Fig. 4.4). The depth of the calorimeter is determined by the maximum jet energy it needs to absorb, requiring 99% energy containment [87]. This energy is a function of polar angle, ranging from about 800 GeV in the forward direction, to about 30 GeV in the rear. The containment of very energetic jets is achieved by surrounding the uranium calorimeter by a much cheaper iron backing calorimeter.

The FCAL, covers polar angles from 2.2° to 36.7°. It is divided into 24 modules numbered with increasing x, each module (see Fig. 4.7) is further segmented into 20×20 cm^2 towers numbered with increasing y. The towers are segmented in depth into an electromagnetic section (EMC) and two hadronic (HAC) sections. Each of the hadronic sections of a tower is identified as a calorimeter cell. The EMC section, however, is divided vertically into four 20×5 cm^2 cells. The structure of the RCAL is very similar. However, the EMC section has two 20×10 cm^2 cells instead of four and there is only one hadronic section. The RCAL covers polar angles between 129.1° to 176.5°. In the outer region of the F- and RCAL are the HAC0 cells. There is no need for a finely segmented EMC sections there, as these regions are shadowed by the BCAL. The view of the UCAL geometry and FCAL face seen from the IP are shown in figure 4.8.

The BCAL covering the angles between the FCAL and the RCAL, consists of 32 wedge-shaped modules and has one EMC and two HAC sections. The modules are tilted 2.5° in ϕ. Each module is divided into 14 towers along the z-axis. The four EMC cells of each tower are projective in θ, where the HAC sections behind them are not projective.

Each calorimeter cell is read out on opposite sides by two photomultiplier tubes (PMTs) coupled to the scintillators via wavelength shifters. Comparison of the two PMT signals allows the determination of the impact point of the particle within a cell.

The calorimeter is calibrated on a channel-by-channel basis using the natural radioactivity of the depleted uranium, which provides stable and time independent reference signal. This calibration procedure is good to 1%. The PMTs can be calibrated via light emission of known intensity from LEDs. The rest of the electronic readout chain is calibrated using test pulses.

The calorimeter also provides accurate timing information with a time resolution better than about 1 ns for energy deposits greater than 4.5 GeV.

4.2.3 The Luminosity Monitor

The precise determination of the time-integrated luminosity is a crucial aspect of all cross section measurements. The *ep* luminosity at HERA is measured by the luminosity monitor using the rate of hard bremsstrahlung photons, $ep \to e'p\gamma$ from the Bethe-Heitler process [91]. The cross section for this process is high and is known from theoretical calculations to an accuracy of 0.5%.

The luminosity monitor [92] consists of two calorimeters, the electron calorimeter (LUMI-e) and the photon calorimeter (LUMI-γ).

The LUMI-e is a lead-scintillator calorimeter. It is located at $z = -34$ m and detects electrons that have lost part of their energy via bremsstrahlung and are deflected from the nominal beam orbit by the magnetic field of HERA. The geometrical acceptance is limited to the detection of electrons with $0.2 \cdot E_{beam} < E'_e < 0.8 \cdot E_{beam}$. The energy resolution is $\sigma(E)/E = 18\%/\sqrt{E}$ with E measured in GeV.

The LUMI-γ is a lead-scintillator calorimeter situated at $z = -104$ m and is protected against synchrotron radiation by a 3.5 X_0 carbon/lead filter. The energy resolution which under test beam conditions is $18\%/\sqrt{E}$, where E is in GeV, is reduced to $25\%/\sqrt{E}$ by the filter.

The measured luminosity uncertainty in 1996-97 data taking period was found to be about 1.6%, where the dominant sources of errors are due to energy scale uncertainties, cross section calculation, acceptance correction and beam gas background subtraction.

4.3   The ZEUS Trigger and Data Acquisition System

The short bunch crossing time at HERA of 96 ns, equivalent to a rate of approximately 10 MHz, is a technical challenge and puts stringent requirements on the ZEUS trigger and data acquisition system.

ZEUS employs a sophisticated three-level trigger system in order to select ep physics events efficiently while reducing the rate to a few Hz [93, 94]. A schematic diagram of the ZEUS trigger system is shown in figure 4.10.

The First Level Trigger (FLT) is a hardware trigger, designed to reduce the input rate below 1 kHz. Each detector component has its own FLT, which stores the data in a pipeline, and makes a trigger decision within 2 μs after the bunch crossing. The decision from the local FLTs are passed to the Global First Level Trigger (GFLT), which decides whether to accept or reject the event.

If the event is accepted, the data are transferred to the Second Level Trigger (SLT), which is software-based and runs on a network of Transputers. It is designed to reduce the rate below 100 Hz. Each component can also have its own SLT, which passes a trigger decision to the Global Second Level Trigger (GSLT) [95]. The GSLT decides then to accept or reject the event. If GSLT accepts the event then it is passed to an Event Builder.

The Event Builder [96] collects data from all detector components into a single event record and transfers it to the Third Level Trigger (TLT), which makes a decision based on the complete information. The TLT is software-based and includes parts of the offline reconstruction code. It runs on a farm of Silicon Graphics computers and is designed to reduce the rate to a few Hz.

Events accepted by the TLT are written to tape via a fiber-link (FLINK) connection. The size of an event is typically 100 kBytes. From here on events are available for full offline reconstruction and data analysis.

The trigger logic used for the online selection of DIS events, on which the present analysis are based, is described in chapter 5.

Parameter	Design Value	Average 1996-97
Proton energy E_p	820 GeV	820 GeV
lepton energy E_e	30 GeV	27.52 GeV
center-of-mass energy $\sqrt{s}$	314 GeV	300 GeV
$\mathcal{L}_{\mathrm{spec}}$ ($\mathrm{cm}^{-2}\mathrm{s}^{-1}\mathrm{mA}^{-2}$)	$3.2 \cdot 10^{29}$	$6.0 \cdot 10^{29}$
$\int \mathcal{L}$ (pb^{-1})/year	100	27
bunches ($ep + e + p$)	210	(153+15+17)
bunch crossing time	96 ns	96ns
p current	160 mA	75 mA
e current	60 mA	35 mA
$\#p$/bunch	$11.0 \cdot 10^{10}$	$3.1 \cdot 10^{10}$
$\#e$/bunch	$3.6 \cdot 10^{10}$	$2.6 \cdot 10^{10}$
I^e_{tot}/I^e_{pilot}	–	10.0
I^p_{tot}/I^p_{pilot}	–	10.1

Table 4.1: A compilation of some of the HERA design parameters and their actual values during the 1996-97 running period.
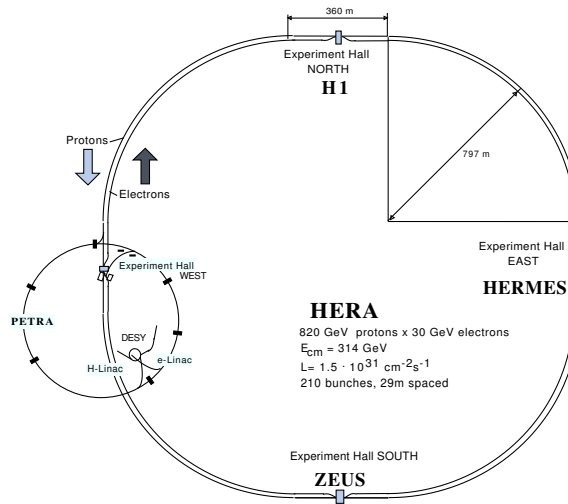
Figure 4.1: The HERA accelerator complex at DESY, Hamburg.
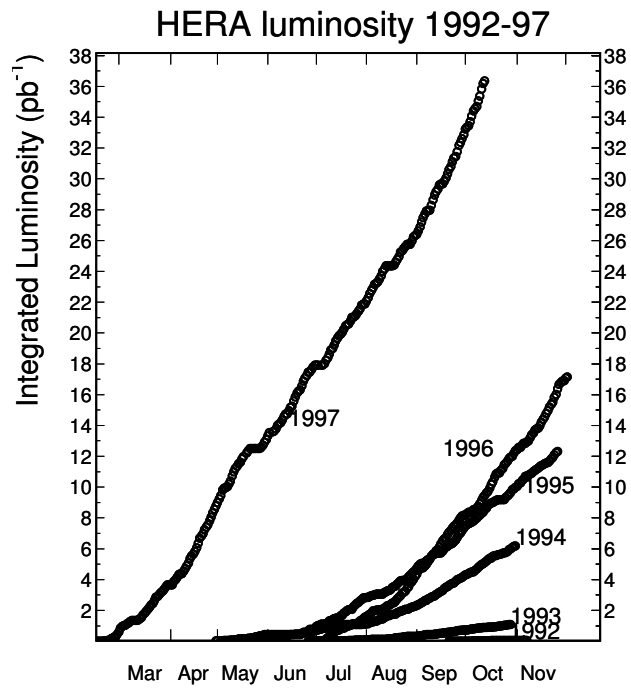
Figure 4.2: HERA delivered luminosity.
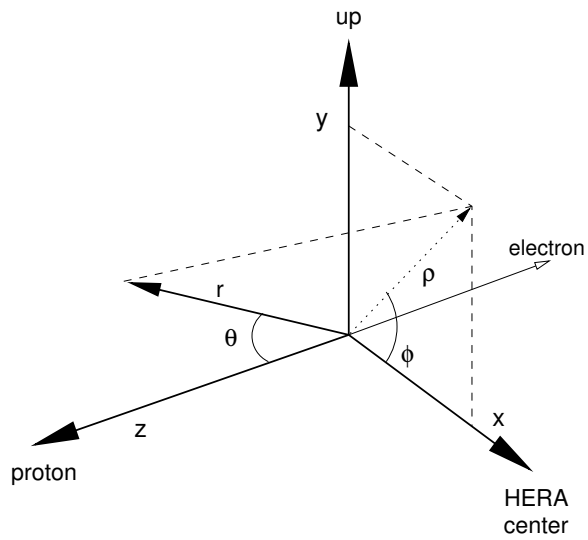
Figure 4.3: The ZEUS coordinate system.

Overview of the ZEUS Detector
(longitudinal cut)
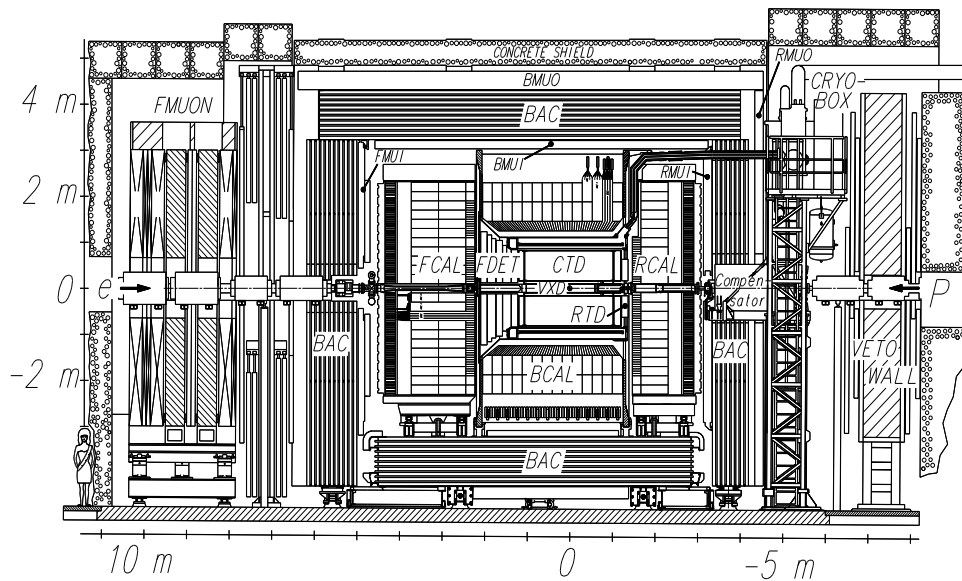
Figure 4.4: The longitudinal cross section trough the ZEUS detector. The main components are labeled and the directions of the incoming beam electrons and protons are also shown.

Overview of the ZEUS Detector
(cross section)
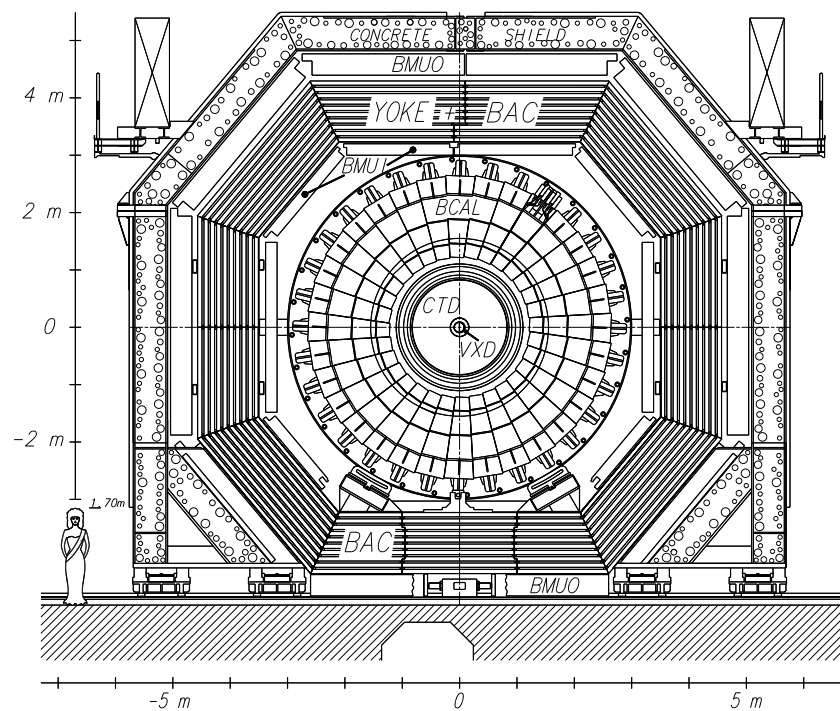
Figure 4.5: The transverse cross section trough the ZEUS detector. The main components are labeled and the directions of the incoming beam electrons and protons are also shown.

Figure 4.6: CTD octant

Figure 4.7: FCAL module

Figure 4.8: The view of the CAL geometry (left) and FCAL face seen from the IP (right).

Figure 4.9: The Lumi detector.

Figure 4.10: Schematic diagram of the ZEUS trigger and data acquisition system.

Chapter 5

Measured cross sections and related uncertainties

5.1 Introduction

In this chapter we describe the measurement of the NC e^+p DIS inclusive and dijet cross sections. After a short description of the kinematical characteristics of the high-Q^2 events considered here, the trigger requirements and the offline selection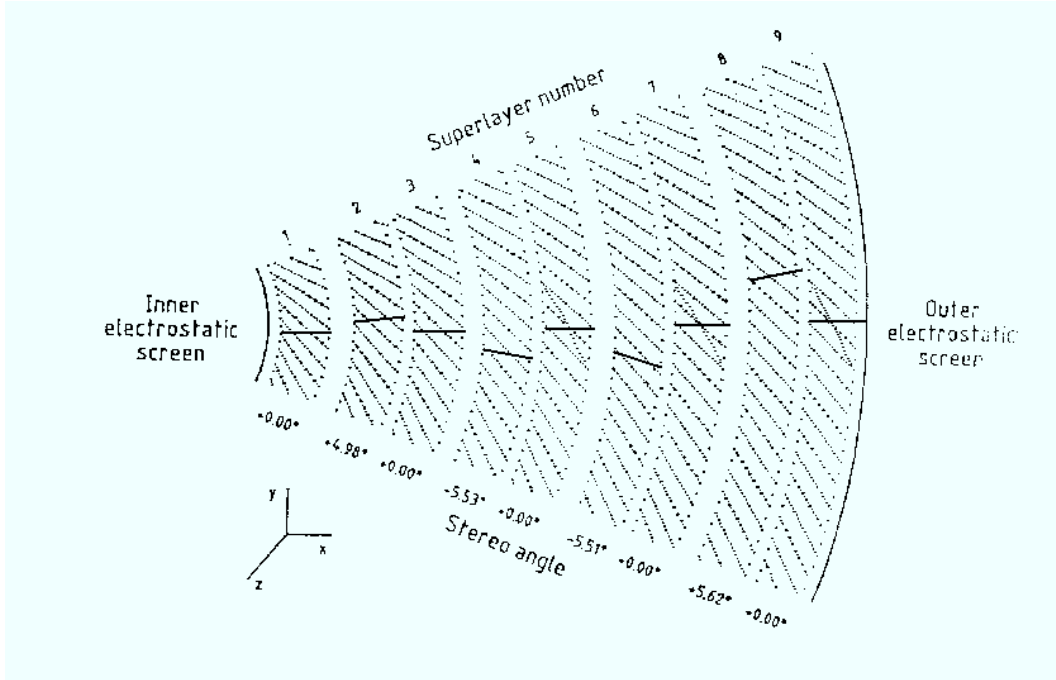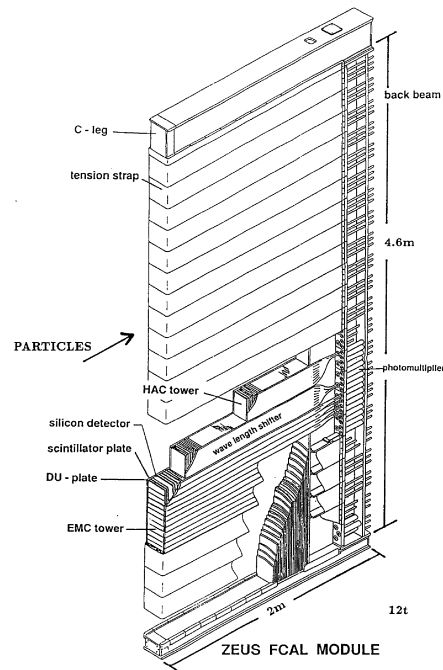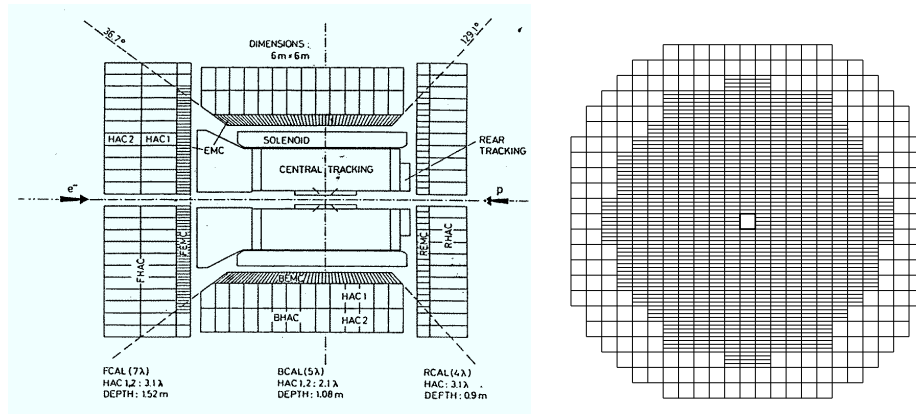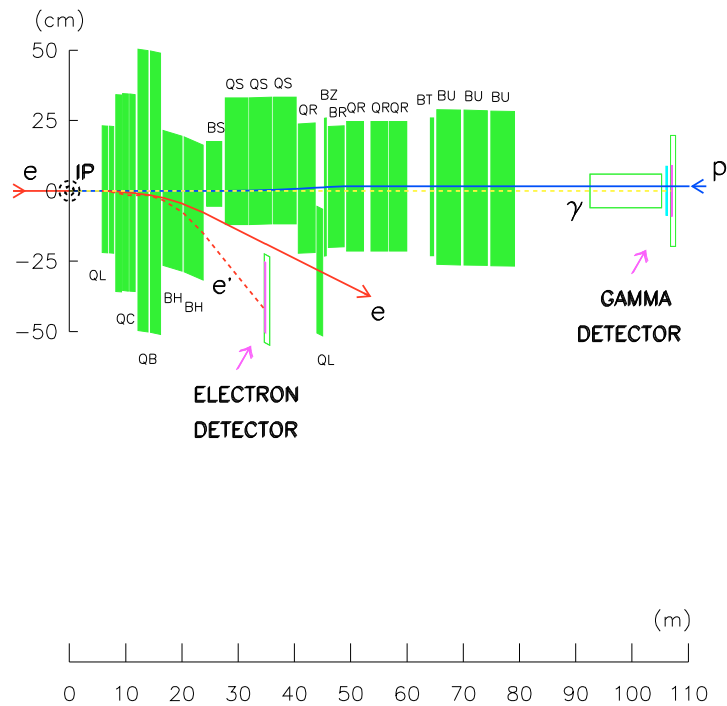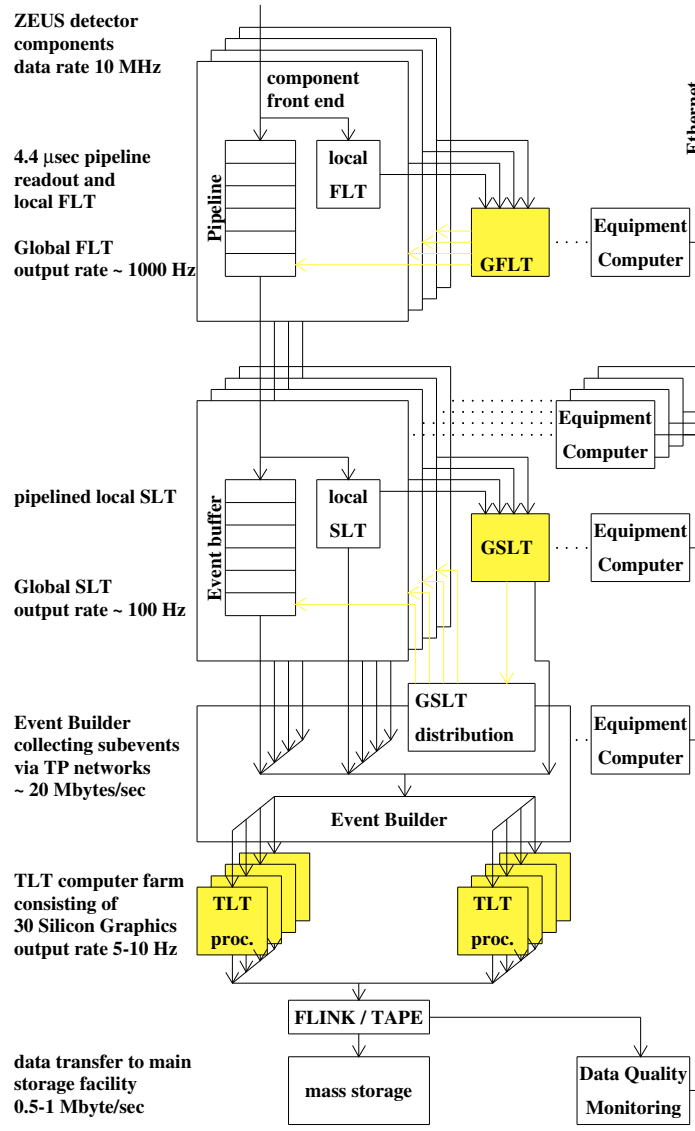 criteria used to select the NC DIS inclusive sample are outlined. The reconstruction of the DIS kinematic variables is then discussed.

Each event of the inclusive sample thus selected is then boosted into the Breit frame and a jet search is performed in this frame, using the $K_\perp$-cluster algorithm, in order to define the final dijet event sample. The accuracy of the reconstruction of the boost vector is described in detail as well as the estimate of the uncertainty associated with the absolute jet-energy scale.

This chapter ends with a description of the unfolding procedure and a study of the main sources of systematic uncertainty.

5.2 Monte Carlo samples

All the relevent distributions of the inclusive and dijet samples were compared, at the various stages of the selection procedure, to DIS Monte Carlo(MC) simulations. An adequate description by MC of these data samples is crucial in order to correctly determine the efficiency for selecting events, to determine the accuracy of the kinematic and jet reconstruction, to estimate the backgrounds, and to extrapolate the measured cross-sections to the full kinematic phase space.

NC DIS events, including QED radiative effects, were simulated using the HERACLES 4.5.2 [97] program with the DJANGO6 2.4 [98] interface to the QCD cascade and hadronisation programs. In HERACLES, corrections for initial- and final-state radiation, vertex and propagator corrections, and two-boson exchange were included. The QCD cascade was simulated using the colour-dipole model [99] including the LO QCD diagrams as implemented[1] in ARIADNE 4.08 [101] and, as a systematic check, with the MEPS model of LEPTO 6.5 [102]. The LEPTO event sample was generated without the soft colour interaction model. Both programs use the Lund string model [103] of JETSET 7.4 [104] to simulate the hadronisation effects.

For the above MC samples the ZEUS detector response was simulated with a program based on GEANT [107]. The generated events were passed through the simulated detector, subjected to the same trigger requirements as the data, and processed by the same reconstruction and offline programs. The ARIADNE (LEPTO) sample corresponds to an integrated luminosity of $L_{int} = 800(170)pb^{-1}$, that is a factor 20 (4) larger than the integrated luminosity of the ZEUS

---

[1]A modified treatment of parton radiation at high Q^2 [100] was included.

data sample used in the present analysis (see below).

Large samples of events were generated without Z^0 exchange processes and QED corrections to correct the measured cross sections for these effects, which at present are not included in the DISENT program. An additional sample of events was also generated with HERWIG 5.9 [105] program, in which the fragmentation is simulated according to a cluster model [106], in order to estimated, togheter with the ARIADNE sample, the hadronisation effects as discussed in chapter 3.

5.3   Selection of the DIS event sample

The selection of the DIS inclusive sample follows very closely the one used in a recent measurement of the inclusive e^+p cross section at large four-momentum transfer[108]. We have benefited very much from the detailed studies[109] performed in that context, which have improved significantly both the reconstruction of the scattered positron and that of the hadronic final state. In this section we give, as a consequence, only a brief description of the basic selection criteria and present the most relevant control distributions in order to demonstrate the quality of our reconstruction of the DIS inclusive events.

5.3.1   General event characteristics

Neutral-current DIS processes in the high-Q^2 phase-space region considered here produce striking events, relatively easy to distinguish from the potentially large backgrounds of quasi-real photoproduction ($Q^2 \sim 0$) and beam-gas interactions. The events are characterized by a high-energy isolated positron detected in the ZEUS Uranium calorimeter. For $Q^2 > 470$ GeV^2, most of the positrons have an energy close to the nominal beam energy (27.5 GeV) and are restricted to a polar angle below 140 degrees. As Q^2 increases, the positrons are produced with higher energies, up to several hundred GeV, and at smaller polar angles.

In addition to the energy and polar angle of the scattered positron, the variables δ, P_T and E_T were used for event selection. These are defined as:

$$\delta = \sum_i (E_i - E_i \cos \theta_i) = \sum_i (E - p_z)_i \tag{5.1}$$

$$P_T = \sqrt{P_x^2 + P_y^2} = \sqrt{\left(\sum_i E_i \sin \theta_i \cos \phi_i\right)^2 + \left(\sum_i E_i \sin \theta_i \sin \phi_i\right)^2} \tag{5.2}$$

$$E_T = \sum_i E_i \sin \theta_i \tag{5.3}$$

where the sums run over all calorimeter energy deposits E_i with polar angle θ_i and azimuthal angle ϕ_i. At the generator level $\delta = 55$ GeV, i.e. twice the positron beam energy, which follows from energy-momentum conservation. Undetected particles which escape through the forward beam hole give a negligible change in δ while particle loss through the the rear beam hole, e.g. from initial state bremsstrahlung, can lead to a substantial reduction of δ. High-Q^2 events in which the positron strikes the BCAL or FCAL ($Q^2 > 1000$ GeV^2) are characterized by large E_T values.

In the determination of the DIS kinematic variables (to be described below), the CAL energy deposits are separated into those associated with the identified scattered positron, and all other energy deposits. The sum of the latter will be referred to in the following as the hadronic energy.

Year	$\mathcal{L}(\text{pb}^{-1})$	$\delta\mathcal{L}/\mathcal{L}(\%)$
1996	10.71	1.1
1997	27.69	1.8
Total	38.40	1.6

Table 5.1: Luminosity $\mathcal{L}$ and relative error $\delta\mathcal{L}/\mathcal{L}$ for 1996 and 1997 positron data samples.

5.3.2 Data Samples and trigger requirements

Data Samples

The data samples employed in this analysis were collected with the ZEUS detector in the 1996 and 1997 running periods. Included in the analysis were only those runs for which the main detector components used here (CAL, CTD, and the luminosity monitors) were fully operational. The resulting data set correspond to an integrated luminosity of $\mathcal{L} = 38.4\text{pb}^{-1}$. The relative contributions from each of the two data taking years can be found in table 5.1. The uncertainty on the total integrated luminosity was determined via the fractional uncertainties for the two years $\frac{\delta\mathcal{L}}{\mathcal{L}}$, according to:

$$\left(\frac{\delta\mathcal{L}}{\mathcal{L}}\right)_{tot} = \frac{\sum_{i=1996}^{1997} \left(\frac{\delta\mathcal{L}}{\mathcal{L}}\right)_i \times \mathcal{L}_i}{\sum_{i=1996}^{1997} \mathcal{L}_i} \tag{5.4}$$

i.e. assuming maximum correlation.

Trigger requirements

For the portions of the trigger relevant to this analysis, the requirements were strictest during 1997 and are described here. The first-level trigger requires a total electromagnetic energy of at least 3.4 GeV in the RCAL or 4.8 GeV in the BCAL, or $E_T'' > 30$ GeV, where E_T'' is the total transverse energy excluding the two rings of calorimeter towers nearest to the forward beampipe. The E_T'' requirement is designed to tag high-Q^2 events by their large E_T while rejecting beam-gas background having large energy deposits at low polar angles. The major requirement at the second-level trigger is $\delta + 2E_\gamma > 29$ GeV, where E_γ is the energy measured in the luminosity monitor. This requirement suppresses photoproduction. Backgrounds are further reduced at the second-level trigger by removing events with calorimeter timing inconsistent with an *ep* interaction. For the third-level trigger, events are reconstructed on a computer farm, and the requirements are similar to the offline cuts described below, though looser and using a simpler and generally more efficient (but less pure) positron finder.

5.3.3 Positron identification and reconstruction

As mentioned above the key signature of the events under study is the presence of an isolated high-energy positron. Thus, a correct and efficient identification of the scattered positron as well as a precise reconstruction of its position and energy are important requirements in the selection of DIS events. In this analysis, in order to identify and reconstruct the positron, while rejecting events in which other final state particles mimic it, the Sira95[110] electron finder algorithm was used in conjunction with the tracking information provided by the CTD.

Sira95 electron finder

Sira95 is based on a feed-forward neural network algorithm (with back-propagation) trained to identify electromagnetic particles based upon their showering properties in the segmented

uranium calorimeter. In a first step, calorimeter clusters (tower islands[111]) are formed by grouping CAL cells that are contiguous to a cell with the local highest energy. The energy of each cluster, E_{clu}, is defined as the sum of the cell energies belonging to the cluster. The cluster angle, θ_{clu}, is set equal to the polar angle obtained from the center position of the cluster and the event vertex obtained from tracks measured with the CTD. A set of 16 rotationally invariant moments which characterise the geometrical structure of each cluster defined above are then used, together with the cluster's energy, as inputs of the neural network in the training phase. The neural network output is defined to represent the probability, P_{sira}, that a given calorimeter cluster is of electromagnetic ($P_{sira} \sim 1$) or non-electromagnetic ($P_{sira} \sim 0$) origin. The final calorimeter cluster associated to the scattered positron if defined as the one with the highest Sira95 probability. The performance of the electron finder can be evaluated in terms of the efficiency and purity for selecting the scattered positron. MC studies have demonstrated that these efficiencies and purities exceed 95% for $P_{sira} > 0.9$ and cluster energies $E_{clu} > 10$ GeV.

Track-matching

For clusters with polar angles[2] within the CTD acceptance ($\theta_{\mathrm{clu}} > 17.2°$), a matching track is required. A track is considered to match if the distance of closest approach (DCA) between the extrapolation of the track into the calorimeter and the position of the cluster center is less than 10 cm, where the r.m.s. resolution in the DCA is 1.8 cm.

Since the CAL energy resolution is better than that of the CTD for tracks above 10 GeV, for accepted candidates, the positron energy, E'_e, is set equal to the cluster energy, E_{clu}, comprising typically six cells. The positron angle, θ_e, is determined from the associated track if the positron cluster is within the CTD acceptance, and otherwise set equal to θ_{clu}. The resolution in θ_e is typically 0.1°.

Energy and non-uniformity corrections

The energy of the calorimeter cluster associated to the scattered positron was corrected for energy loss in the material between the interaction point and the calorimeter. All the positron clusters in BCAL and FCAL were corrected based on the material maps implemented in the detector simulation package. The presampler was used to correct positrons entering the RCAL. This correction is based on the measured positron energy, the amount of material in front of the RCAL and the presampler signal.

In addition to the above corrections for energy losses an additional correction was applied to the positron energy to remove a discrepancy between data and MC in the measured energy response at the boundaries of the calorimeter cells and modules.

Positron energy scale uncertainty

The uncertainty in the energy scale of the scattered positron, determined after applying the corrections described above, was studied in detail in [108]. For scattered positrons in low y region, the energy is strongly correlated with the scattering angle, and a comparison of the predicted energy to the measured energy in the calorimeter was made. In the range of $30° < \theta_e < 150°$, the momentum of the positrons can be determined by the CTD. The average track momentum minus calorimeter energy was used as an independent check of the energy measured in the CAL for energies up to 30 GeV. For positrons with energies above 30 GeV, or those scattered to extreme forward directions, a comparison of the energy predicted from double-angle variables

---

[2]We do not consider candidates with $\theta_{\mathrm{clu}} > 164°$ (which are also beyond the CTD acceptance limit), since they correspond to Q^2 values below the range of this analysis.

(see section 5.3.5) to the measured energy was made. In kinematic regions where the other methods can be used to check the CAL energy scale, the double-angle results are in agreement with the other methods to better than 0.5%. As a result of these studies, the uncertainty in the value of the energy of the scattered positron in the RCAL is 2% at 10 GeV, decreasing linearly to 1% at 27.5 GeV and above, 1% in the BCAL and 3% in the FCAL.

5.3.4 Reconstruction of the hadronic final state

Energy depositions of the hadronic final state are used to evaluate the angle γ_h. For this purpose calorimeter clusters are used as just described. The angle γ_h is then calculated for the event according to

$$\cos \gamma_h = \frac{P_{T,h}^2 - \delta_h^2}{P_{T,h}^2 + \delta_h^2}, \tag{5.5}$$

where $P_{T,h}$ and δ_h are calculated using (5.1) and (5.2) with sums running over the calorimeter clusters in the same manner as P_T and δ, but excluding the positron.

MC studies of the calorimeter response indicate that the uncorrected γ_h calculated with (5.5) is biased by redirected hadronic energy from interactions in material between the primary vertex and the calorimeter or by backsplash from the calorimeter (albedo)[112][3]. To minimize this bias, clusters with energy below 3 GeV and with polar angles larger than γ_{max} are removed. The value of γ_{max}, which is a function of γ_h, is derived from a NC MC sample by requiring that less than 1% of the clusters not related to the above effects be removed. This yields a reconstruction of γ_h closest to the true value as given by the MC. After this first pass of cluster removal the value of γ_h is re-calculated and the procedure is repeated until it converges, typically after two or three passes. Removing calorimeter clusters in this manner substantially improves the resolution and bias of the double-angle variables for small values of γ_h (corresponding to small values of y) and leaves them largely unchanged for large values of γ_h.

A study on the uncertainty in the scale of the hadronic energy will be presented together with an estimate of the uncertainty on the absolute jet-energy scale in section 5.4.2.

5.3.5 Reconstruction of the kinematics

The kinematic variables Q^2, x, and y were determined using the double angle (DA) method [114]:

$$Q_{\mathrm{DA}}^2 = 4E_e^2 \frac{\sin \gamma_h (1 + \cos \theta_e)}{\sin \gamma_h + \sin \theta_e - \sin(\gamma_h + \theta_e)} \tag{5.6}$$

$$x_{\mathrm{DA}} = \frac{E_e}{E_p} \frac{\sin \gamma_h + \sin \theta_e + \sin(\gamma_h + \theta_e)}{\sin \gamma_h + \sin \theta_e - \sin(\gamma_h + \theta_e)} \tag{5.7}$$

$$y_{\mathrm{DA}} = \frac{\sin \theta_e (1 - \cos \gamma_h)}{\sin \gamma_h + \sin \theta_e - \sin(\gamma_h + \theta_e)} \tag{5.8}$$

Being based on angular quantities the DA method is mostly insensitive to errors in the absolute energy scale of the calorimeter. It is however sensitive to QED radiation and an accurate simulation of the hadronic final state is necessary. At high Q^2 the hadronic final system is sufficiently energetic and model uncertainties in the fragmentation process are smaller than at lower Q^2.

To validate the performance of the double-angle method, the reconstructed kinematic variables of MC events were compared to the true hadron variables Q^2, x and y as defined by the

---

[3]High energy hadrons interacting in a calorimeter can produce with a non-negligible probability particles at large angles with respect to the direction of the main shower. Some of these particles travel backwards and generate energy deposits far away from their primary source in the calorimeter which is referred to as backsplash.

four-momentum transfer q to the hadronic system

$$Q^2 = -q^2, \ \ x = Q^2/(2p \cdot q), \ \ y = Q^2/(xs) \tag{5.9}$$

where P is the four-momentum of the initial proton and $s = 4E_pE_e$. The resolution in the kinematic variables is determined accordingly and demonstrates (not shown here) that the double-angle method performs better than other methods for $Q^2 > 400$ GeV^2.

5.3.6   Offline selection

The following criteria are applied offline:

- To ensure that event quantities can be accurately determined, a reconstructed vertex with $-50 < z_{vtx} < 50$ cm is required, a range consistent with the ep interaction region.

- To suppress photoproduction events where the scattered positron escapes through the beam hole in the RCAL, δ is required to be greater than 38 GeV. This cut also reduces the number of events with initial-state QED radiation. The requirement $\delta < 65$ GeV removes cosmic ray background.

- Positrons are identified based on calorimeter cluster quantities and tracking information as described above.

  - To ensure high purity, the positron is required to have an energy of at least 10 GeV; in this case the identification efficiency exceeds 96%, as shown by MC studies.

  - To reduce background, isolated positrons are selected by requiring no more than 5 GeV in calorimeter cells not associated with the scattered positron in an $\eta - \Phi$ cone of radius 0.8 centered on the positron.

  - In addition, each positron with $\theta_e > 17.2°$ must be matched to a charged track of at least 5 GeV momentum.

  - For positrons beyond the forward tracking acceptance ($\theta_e < 17.2°$), the tracking requirement in the positron selection is replaced by a cut on the transverse momentum of the positron $P_{T,e} > 30$ GeV and by the requirement $\delta > 44$ GeV.

  - A fiducial volume cut is applied to the positron position. This excludes the upper part of the central RCAL area (20×80 cm^2) occluded by the cryogenic supply for the solenoid magnet as well as the transition region between the CAL parts corresponding to a polar angle of the positron of $35.6° < \theta < 37.3°$ and $128.2° < \theta < 140.2°$.

  If more than one positron candidate in an event passes these cuts (7% of the events), the one with the highest probability is assumed to be the DIS positron.

- To further reduce background from photoproduction, y estimated from the positron energy and angle is required to be $y_e < 0.95$.

- The net transverse momentum P_T is expected to be close to zero and is measured with an error approximately proportional to $\sqrt{E_T}$. To remove cosmic rays and beam-related background, P_T is required to be less than $4\sqrt{E_T \, (\text{GeV})}$.

The efficiency of these cuts for selecting DIS events with $Q^2 > 470$ GeV^2 as determined by MC is, on average, 80%[4] It is approximately uniform over the kinematic phase space except

---

[4]The efficiencies and purities for all the measured cross sections (inclusive and dijet) will be presented in section 5.5.

for the region of high y and low Q^2 where the efficiency decreases due to the positron energy requirement. Uncertainties in the simulation of the efficiency arising from the diffractive contribution to the cross-section which is not included in the MC are neglected since the diffractive contribution is small for $Q^2 > 470$ GeV^2.

5.3.7 Monte Carlo and data comparison

To prove that the set of MC samples describe the inclusive data sample specified above, thus allowing to determine the data taking efficiency, the agreement between data and MC in the spectra of the most relevant quantities is checked.

The vertex is reconstructed using the CTD alone. The measured z vertex distribution is compared with the ARIADNE and LEPTO predictions in Fig. 5.1 after applying all analysis cuts except for the cut on the z coordinate of the vertex. A very good agreement between the data and the MC is observed except in the upstream region ($z_{vtx} < -70$ cm). This is presumably due to the presence of residual beam-gas background events. The vertex cut (described above) is applied to reject this background and to reduce acceptance uncertainties.

The comparison between the data and MC samples for the positron's related quantities is presented in Fig. 5.2 to Fig. 5.4. In Fig. 5.2 the positron coordinates at the CAL face are shown. The positron's energy (after correction or estimated with the DA method) and polar angle distributions are presented in Fig. 5.3. In Fig. 5.4 the energy (E_{cone}) in a η-ϕ cone of radius 0.8 that is not assigned to the positron together with the momentum of the track (p_e^{Trk}) matching the positron calorimeter cluster and the corresponding DCA are shown. For all the distributions an adequate description by the MC sample is seen.

A similar conclusion hold for the hadronic variables γ_h $P_{T,h}$ and δ_h (see Fig. 5.5), and the total and hadronic $E - P_z$ presented in Fig. 5.6.

Finally, the distribution of the final inclusive data sample as function of Q^2_{DA},x_{DA} and y_{DA} is compared with the LEPTO and ARIADNE MC samples in Fig. 5.7. An excellent agreement between data and MC is again observed.

5.4 Selection of the dijet sample

In this section we describe the selection of the final dijet sample. Having already motivated in chapter 3 our decision to perform the jet clustering in the Breit frame (using the longitudinally invariant $K_\perp$-cluster algorithm), emphasis will be placed here on the quality of the boost to the Breit frame and on the description by the ARIADNE and LEPTO MC event samples of the most relevant dijet distributions. In this section we will also address the problem of quantifying the uncertainty on the jet energy scale which represents one of the main sources of the experimental uncertainty of the measured jet cross sections.

5.4.1 Boost to the Breit frame

The Breit frame is defined as the one in which the four-momentum $\Sigma_B = 2xP + q$ has zero spatial components:

$$\mathbf{\Sigma}_B = 2x\mathbf{P} + \mathbf{q} = \mathbf{0} \ . \tag{5.10}$$

This four-vector has been reconstructed using the initial positron and proton four-momenta and the four-momentum of the scattered positron calculated according to the DA method:

$$(E'_e)_{\text{DA}} = 2E_e \frac{\sin \gamma_h}{\sin \gamma_h + \sin \theta_e - \sin(\gamma_h + \theta_e)} \tag{5.11}$$

$$(p'_{e,x})_{\text{DA}} = E'_{e\text{DA}} \sin(\theta_e) \cos(\phi_e) \tag{5.12}$$

$$(p'_{e,y})_{\text{DA}} = E'_{e\text{DA}} \sin(\theta_e) \sin(\phi_e) \tag{5.13}$$

$$(p'_{e,z})_{\text{DA}} = E'_{e\text{DA}} \cos(\theta_e) \tag{5.14}$$

where E_e is the nominal positron beam energy in the case of reconstructed events and the true one for the generator level events. The decision to use the DA method was motivated by the excellent resolutions obtained for the angular quantities θ_e, ϕ_e and γ_h in the selected DIS kinematic region. Being calculated from angular quantities only, the boost vector is also independent from uncertainties on the calorimeter energy scale.

Initial state photon radiation effects

The components of the four-momentum of the scattered positron calculated with the DA method (see Eq.) depend linearly on the positron beam energy. The emission of an energetic photon from the incoming positron[5] (initial state radiation, ISR) can lower considerably the beam positron energy w.r.t. the nominal value:

$$E_{e,\text{beam}} \longrightarrow E_{e,\text{beam}}^{\text{ISR}} = (1 - f_\gamma)E_{e,\text{beam}} \tag{5.15}$$

where f_γ is the fraction of the positron beam energy carried by the initial-state radiated photon. The cut $\delta > \delta_{min} = 38$ GeV we applied at the DIS selection stage puts an upper limit on the energy of a possible ISR photon. For a hermetic detector $\delta = 2E_{e,\text{beam}}$. If the ISR photon escapes detection the requirement $\delta > \delta_{min}$ limits the fraction f_γ to:

$$f_\gamma < 1 - \delta_{min}/(2E_{e,\text{beam}}) \simeq 0.3. \tag{5.16}$$

f_γ in the region $(0., 0.3)$ is shown in Fig. 5.8 In the DIS kinematical region of this analysis approximately 15% of the events have an ISR photon carrying between 2 and 30% of the energy of the incident positron.

In order to study the effects of these events on the measured dijet cross section two cross checks were performed:

1. In order to study the effect of assuming a nominal value of $E_{e,\text{beam}}$ for calculating the boost, all the hadron level MC dijet cross sections were calculate using the true incoming positron's energy and the nominal one. The ratios of these cross sections are presented in Fig. 5.10. For all the dijet cross sections, the ratios deviate from one by at most 10%.

2. At the reconstructed level (both in the data and in the MC) the boost was performed assuming for the incoming positron energy the nominal value. If the effect of ISR events is different between data and MC a bias could be produced. In order to check this f_γ was reconstructed in data and MC separately from the reconstructed Q^2 calculated with the electron and DA method. In general we have

$$Q^2_{true} = Q^2_e(1 - f_\gamma) = Q^2_{DA}(1 - f_\gamma)^2 \tag{5.17}$$

---

[5]Due to the comparatively large mass of the proton, ISR from the incoming proton can be safely neglected. In principle, photon emission by the scattered positron (final state radiation, FSR) will affect also the determination of the kinematics; in practice, if the scattered positron is detected in the calorimeter, the effect will be small because the signals from the positron and the FSR photon are summed.

and therefore

$$f_\gamma^{meas} = 1 - \frac{Q_e^2}{Q_{DA}^2} \tag{5.18}$$

The f_γ^{meas} distributions are presented in Fig. 5.9 and excellent agreement was found between data and MC.

The final measured dijet cross sections were corrected (according to the procedure decribed in the next section) for QED effects.

5.4.2 Jet-energy scale uncertainty

The uncertainty associated with the absolute jet-energy scale represents the main source of the experimental uncertainty on any measured jet cross section and deserves a detailed study. The method adopted here to determine such an uncertainty is based on a detailed comparison, in the laboratory frame, between the transverse momentum of the scattered positron, reconstructed with the DA method, with the transverse energy of the balancing jet.

In a first step a sample of NC DIS events characterised by the presence of a *single* high transverse energy jet, in the DIS kinematical region of the present analysis, was selected both in the data and MC samples according to:

$$E_{T,\text{Lab}}^{\text{jet}}(\text{Leading}) > 10 \text{ GeV} \quad \text{and} \quad -1 < \eta_{\text{Lab}}^{\text{jet}}(\text{Leading}) < 2$$
$$\text{and}$$
$$E_{T,\text{Lab}}^{\text{jet}}(\text{non} - \text{Leading}) < 5 \text{ GeV}$$

where the leading jet was defined as the one with highest transverse energy. In selecting the jet sample the jet clustering procedure was carried out in the laboratory frame and the transverse energy threshold for the leading jet was chosen in order to approximately resemble the transverse energy distribution of each jet selected in the Breit frame (according to the nominal cut in the Breit frame) after having boosted it in the laboratory frame.

For each sample the mean ($\langle r \rangle$) of the quantity:

$$r = \frac{E_T^{\text{jet}}}{p_{\text{T,e}}^{\text{DA}}} \tag{5.19}$$

was computed separately for data ($\langle r_D \rangle$) and MC ($\langle r_M \rangle$) (in the latter case both for the CDM and MEPS samples) as a function of the jet's pseudorapidity and transverse energy. The mean was evaluated using both the histogram and gaussian mean of the $E_T^{\text{jet}}/p_{\text{T,e}}^{\text{DA}}$ distribution.

In Fig. 5.14 to Fig. 5.17 the measured ratio r is compared to the MC samples in bins of $E_{T,\text{Lab}}^{\text{jet}}$ and $\eta_{\text{Lab}}^{\text{jet}}$. The ARIADNE and LEPTO MC samples give an adequate description of the measured distributions. In Fig. 5.18 to Fig. 5.21 the quantities $\langle r_D \rangle$, $\langle r_M \rangle$ and $\langle r_D \rangle/\langle r_M \rangle$ are presented as a function of the jet's transverse energy and pseudorapidity. For all the distributions data and MC agree within 2%.

As an additional cross check the same study was repeated using the total transverse momentum of the hadronic final state (P_T^{had}) instead of the jet transverse energy. The mean of the ratio

$$\rho = \frac{P_T^{\text{had}}}{p_{\text{T,e}}^{\text{DA}}} \tag{5.20}$$

was in this case computed in bins of γ_{had} and P_T^{had}, again for data and MC. Even in this case data and MC (see Fig. 5.22 to Fig. 5.25) agree within 2%.

5.4.3   Jet energy correction

The comparison of the reconstructed jet variables between jets of hadrons and jets of CAL cells in MC generated events showed no significant systematic shift in the angular variables η_B^{jet} and ϕ_B^{jet}. However, the jet transverse energy as measured by the CAL under-estimated that of the jet of hadrons by an average of $\approx 15\%$. This effect is due mainly to energy losses in the inactive material in front of the CAL and was corrected for using the samples of MC generated events[113].

5.4.4   Final djet sample and MC comparison

The final dijet sample refer to the following jet selection criteria:

$$E_{TB}^{jet,M} > 8 \text{ GeV} \text{ and } E_{TB}^{jet,m} > 5 \text{ GeV} \tag{5.21}$$

$$-1 < \eta^{jet} \, (Lab) < 2 \tag{5.22}$$

where $E_{TB}^{jet,M}$ ($E_{TB}^{jet,m}$) is the transverse energy of the jet in the Breit frame with the highest (second highest) transverse energy in the event. Only events with exactly two jets passing the above selection cuts were used to compute the cross sections.

In Fig. 5.11 to Fig. 5.13 the measured dijet uncorrected distributions are compared with the predictions of ARIADNE and LEPTO. Both MC samples give an adequate description of the shape of the measured distributions. LEPTO gives a somewhat better description of the jet pseudorapidity distributions and transverse distributions at high E_{TB}^{jet}. ARIADNE reproduces better the shape of the dijet cross section as a function of Q^2. Both programs give a very similar prediction for the detector correction factors.

5.5   Unfolding and experimental uncertainties

5.5.1   Correction procedure

In order to compare the measured inclusive and dijet cross sections and the dijet fraction with the corresponding NLO predictions (corrected for hadronisation effects) the observed distributions have to be corrected for detector, QED, and Z^0 effects. The correction for the latter two effects is necessary because the DISENT NLO predictions presently do not include QED and Z^0 effects. The adequate description of the observed distributions by the ARIDNE and LEPTO MC sample discusssed above allowed a simple bin-by-bin correction procedure to be applied. The final measured cross section (both inclusive or dijet), $\sigma_{\text{DATA}}^{\text{meas}}$, in a given bin was obtained correcting the observed cross section, $\sigma_{\text{DATA}}^{\text{obs}}$, in the same bin according to:

$$\sigma_{\text{DATA}}^{\text{meas}} = C_{\text{det}} \cdot C_{\text{qed}} \cdot C_{Z^0} \cdot \sigma_{\text{DATA}}^{\text{obs}} \tag{5.23}$$

with

$$C_{\text{det}} = \frac{\sigma_{\text{MC}}^{\text{had}}}{\sigma_{\text{MC}}^{\text{det}}}$$

$$C_{\text{qed}} = \frac{\sigma_{\text{MC}}^{\text{no-qed}}}{\sigma_{\text{MC}}^{\text{had}}} \tag{5.24}$$

$$C_{Z^0} = \frac{\sigma_{\text{MC}}^{\text{no-}Z^0}}{\sigma_{\text{MC}}^{Z^0}}$$

where

- $\sigma_{\rm MC}^{\rm had}$ is the MC hadron-level cross section including QED and Z^0 effects;

- $\sigma^{\rm det}$ is the MC detector-level cross section including QED and Z^0 effects;

- $\sigma^{\rm no-qed}$ is the MC hadron-level cross section without QED effects;

- σ^{Z^0} is the MC hadron-level cross section with Z^0 effects;

- $\sigma^{\rm no-Z^0}$ is the MC hadron-level cross section without Z^0 effects.

The detector correction factors ($C_{\rm det}$), computed both for the ARIADNE and the LEPTO MC samples, for all the measured cross sections, are shown in Fig. 5.26. For most of the cross sections they are flat and amount to $\approx 20\%$. The dijet cross sections as a function of the jet transverse energy slowly increase (up to 30%) with decreasing $E_{T,B}^{\rm jet}$. In Fig. 5.27 to Fig. 5.29 the ARIADNE hadron level predictions with and without QED effects are presented for the inclusive and dijet differential cross sections. The corresponding QED correction factors ($C_{\rm qed}$), which range between 5 and 10%, are shown underneath each plot. The corrections for the Z^0 effects (C_{Z^0}) affect mostly the inclusive and dijet cross section, as a function of Q^2, in the high-Q^2 region (see Fig. 5.30).

To ensure a reasonable choice of the bins, the purities and efficiencies in all the bins as well as the bin sizes compared to the resolutions in the quantities considered were checked. The purity and efficiency in a given bin is:

$$\text{Purity} = \frac{\text{Nr. of events generated and measured in the bin}}{\text{Nr. of events measured in the bin}} \tag{5.25}$$

$$\text{Efficiency} = \frac{\text{Nr. of events generated and measured in the bin}}{\text{Nr. of events generated in the bin}}. \tag{5.26}$$

The purities and efficiencies (estimated again both with the LEPTO and ARIADNE MC samples) are presented for all the measured cross sections in Fig. 5.31 and Fig. 5.32.

5.5.2 Experimental uncertainties

Various sources contribute to the uncertainties of the measured inclusive and dijet cross sections. In the following we give a short description of how the single contributions were evaluated and discuss which are correlated between single data points.

Statistical uncertainties

Statistical uncertainties arise from the limited number of events used in the determination of a given cross section. In this analysis they enter at three places: the limited amount of data events in the reconstructed distributions (1), the limited number of simulated and reconstructed MC events used to determine the correction factor for detector effects (2), and the number of generated events used to estimate the QED and Z^0 correction factors (3). As mentioned before the final statistical uncertainty in each bin was obtained by adding in quadrature all three contributions. Due to their statistical nature they are uncorrelated between different bins.

Uncertainty in the luminosity determination

The uncertainty associated with luminosity determination for the 1996-97 data taking periods used in this analysis was estimated to be 1.6%. This introduces a corresponding overall normalisation uncertainty on each measured cross section, which is correlated between all data points. The measured dijet fraction R_{2+1} is not affected by this source of uncertainty.

Uncertainty on the detector correction-factors

The uncertainty arising from the MC model dependence of the detector correction factors (which have already been presented in Fig. 5.26) was estimated as the difference between the cross sections obtained using the LEPTO and ARIADNE MC samples.

Uncertainty on the DIS selection

The following studies were performed in order to assess the uncertainty associated to the selection of the DIS inclusive sample:

- Positron's energy-scale uncertainty
  According to the studies described in [108] the uncertainty associated to the positron energy scale is 3, 1, and 2% for positrons in FCAL, BCAL, and RCAL respectively. In order to investigate the effect of these uncertainties on the electron finder performance, the entire analysis was repeated after correcting (in the data only) simultaneously the EMC F/B/RCAL cells' energies by (+3%,+1%,+2%) and (-3%,-1%,-2%).

- Positron's isolation cut
  The cut on the total energy from the CAL cells (not associated with the scattered positron) in an $\eta - \phi$ cone of radius 0.8 centered on the positron direction was varied by ± 2 GeV with respect to the nominal value.

- Vertex cut
  The cut on the z position of the event vertex was relaxed to $-100. < z_{\text{vtx}} < 100.$ cm, in order to study the effect on the cross sections from the satellites.

- y_e cut
  The upper cut on y_e was lowered to 0.9^6.

- $E - p_z$ cut
  The lower cut on the total $E - p_z$ was varied in the region between 35 and 40 GeV.

- Uncertainty on the calculation of the DA quantities
  The evaluate the uncertainty associated to the reconstruction of the kinematical variables the analysis was repeated after smearing the angles which are used in the calculation of the DA quantity according to their resolution. As a further cross-check only the electron method was used instead of the DA method to reconstruct the event kinematics.

Uncertainty on the dijet selection

The following studies were performed in order to assess the uncertainty associated to the selection of the dijet sample:

- Jet energy-scale uncertainty
  Following the results of the study on the jet energy-scale uncertainty the dijet cross sections were recalculated varying by ± 2% (in the MC sample only) the transverse energies of the jet.

- Uncertainty in the boost
  In addition to studies on the effects of ISR events, the following systematics checks were performed in order to demonstrate the reliability of the boost. In the first one the boost to the Breit frame was performed again (in the reconstructed MC sample only) after having

---

[6]The default $y_e < 0.95$ was already implemented at the trigger level and could not be raised

varied separately each of the three angles (θ_e, ϕ_e, γ_h), used in the reconstruction of the boost vector, according to its estimated resolutions. The boost was also performed after having smeared simultaneously three angles according to a normal distribution.

- Jets' transverse energy and pseudorapidity cuts
  The transverse energy of leading (non-leading) jet was varied, in both data and MC, in the range [6.5,9.5] ([4.0,6.0]). The jet pseudorapity cuts were varied by ± 0.1 units around the nominal values.
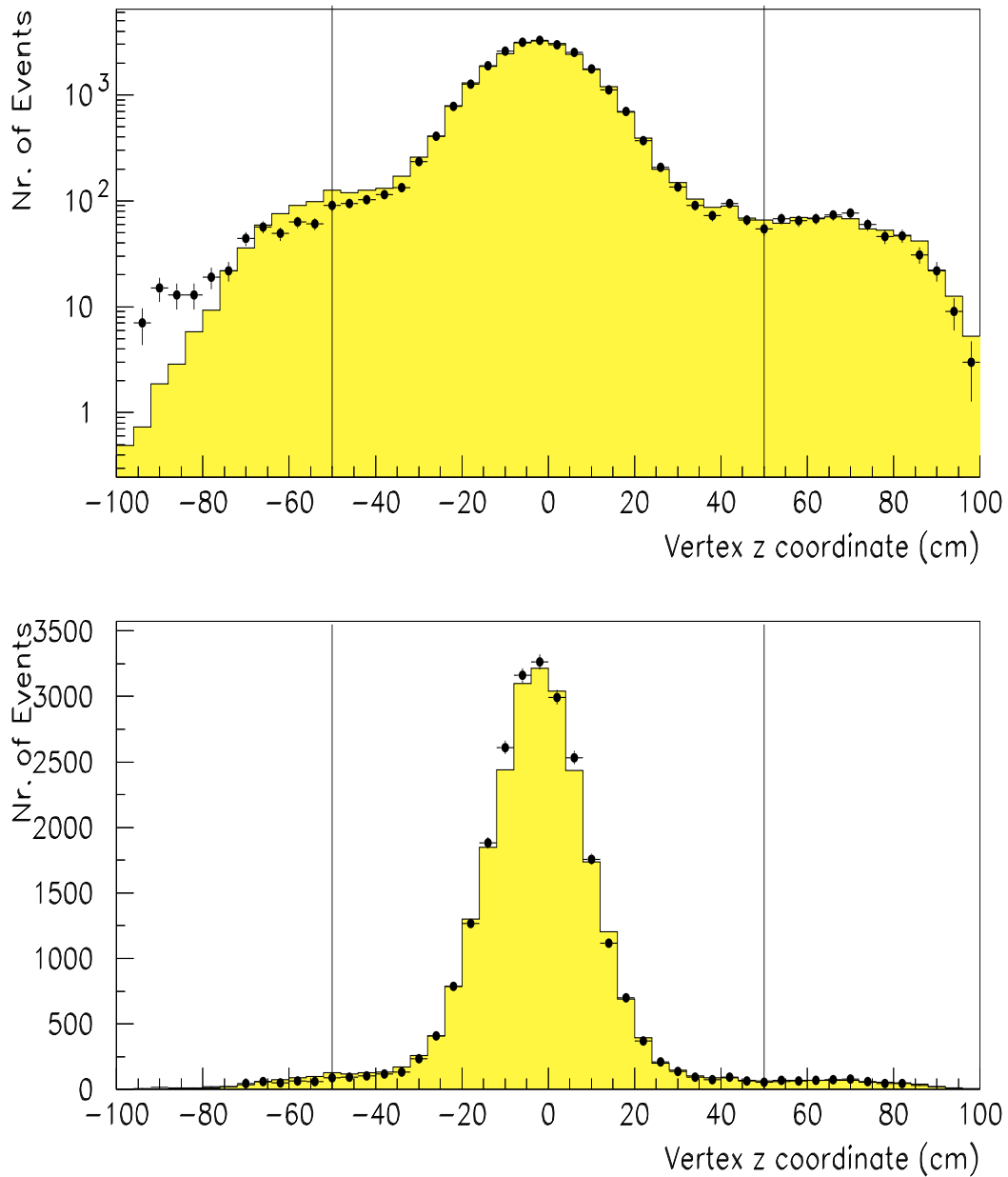
Figure 5.1: The z vertex distribution on a log and linear scale for data (dots) and ARIADNE (shaded histograms) and LEPTO (dashed lines) MC predictions.
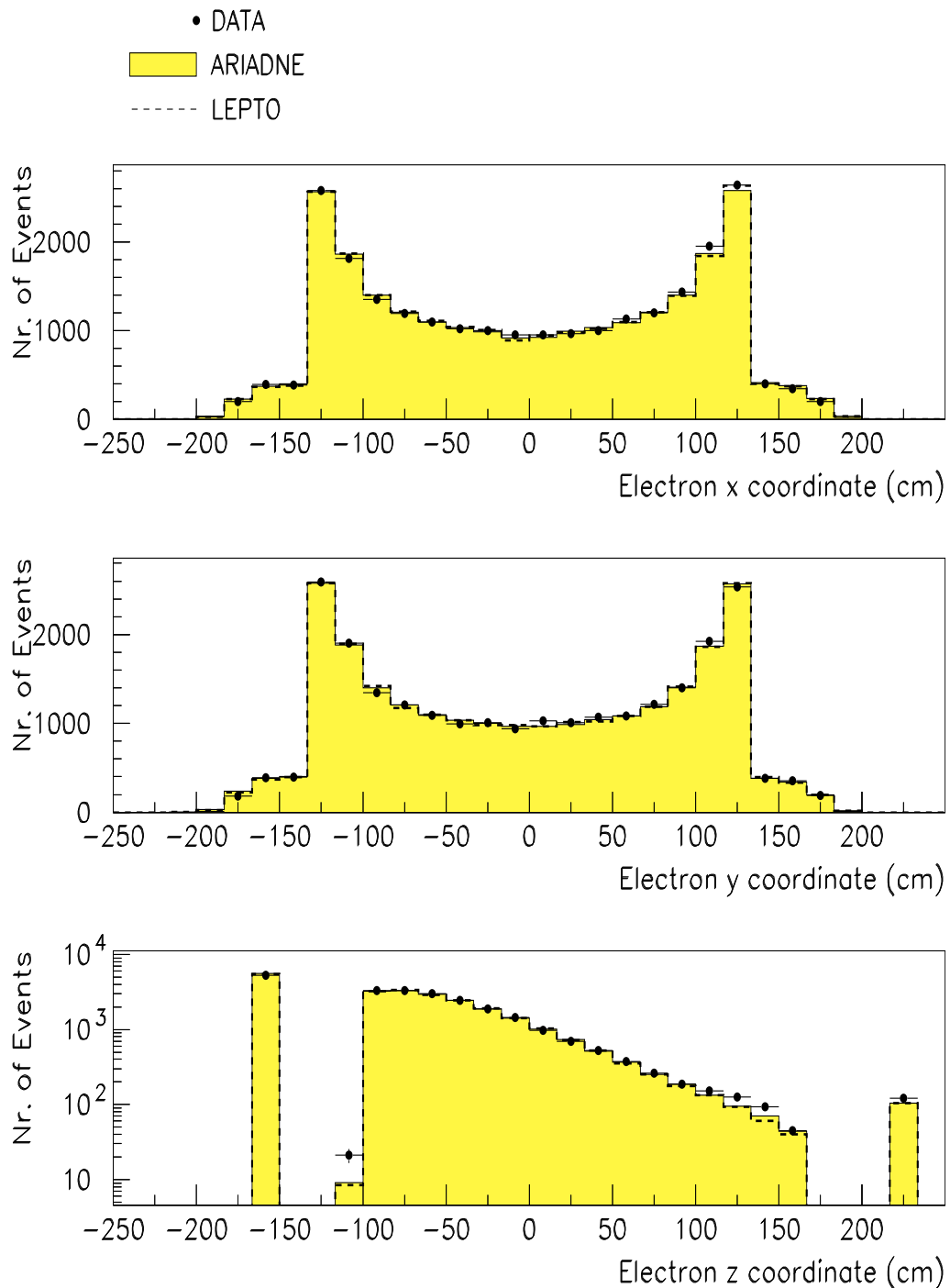
Figure 5.2: The positron coordinates at the CAL face for data (dots) and the ARIADNE (shaded histogram) and LEPTO (dashed histogram) MC program predictions.
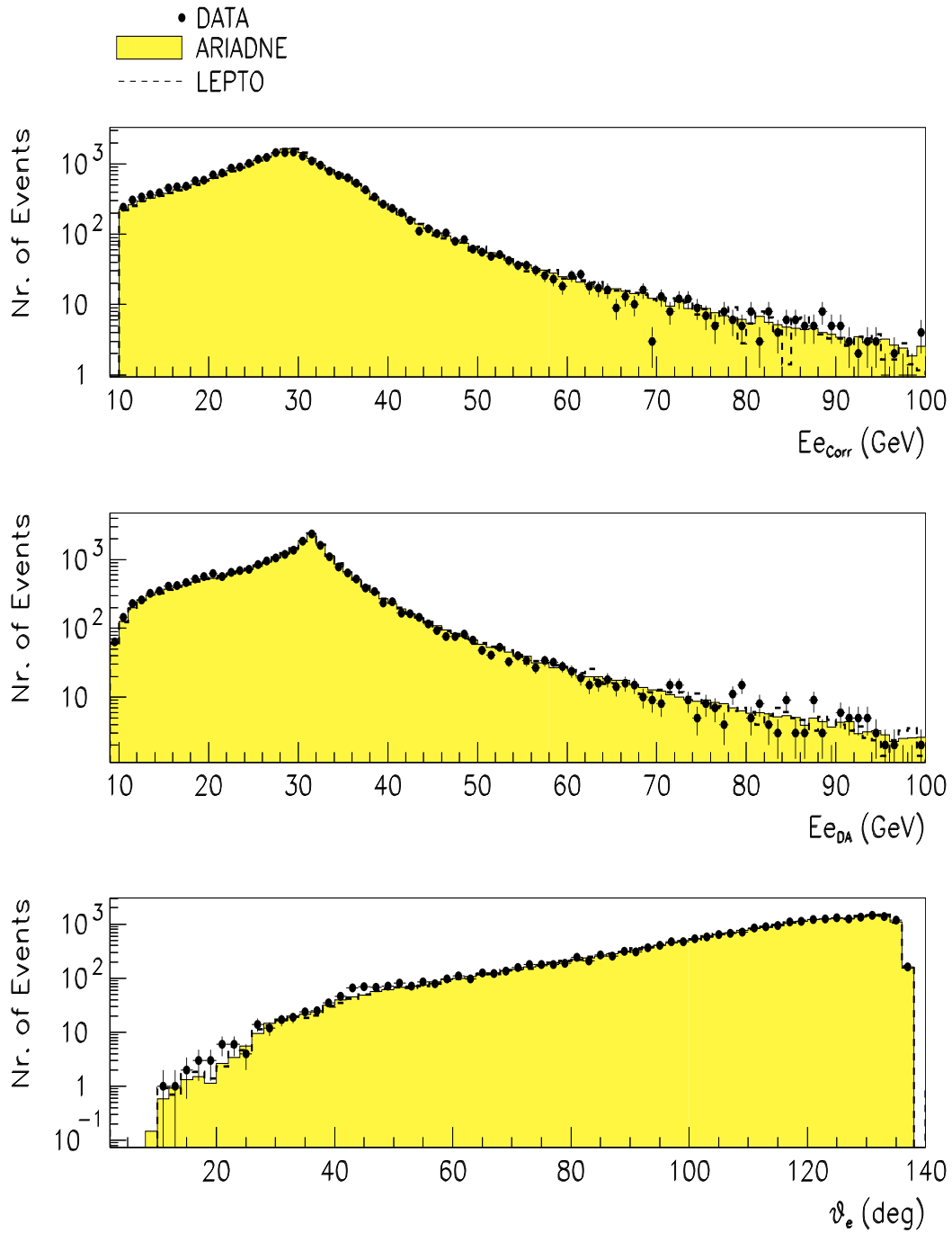
Figure 5.3: The positron's energy and polar angle. Shown are both the positron energy after correction (top) and estimated with the DA method.
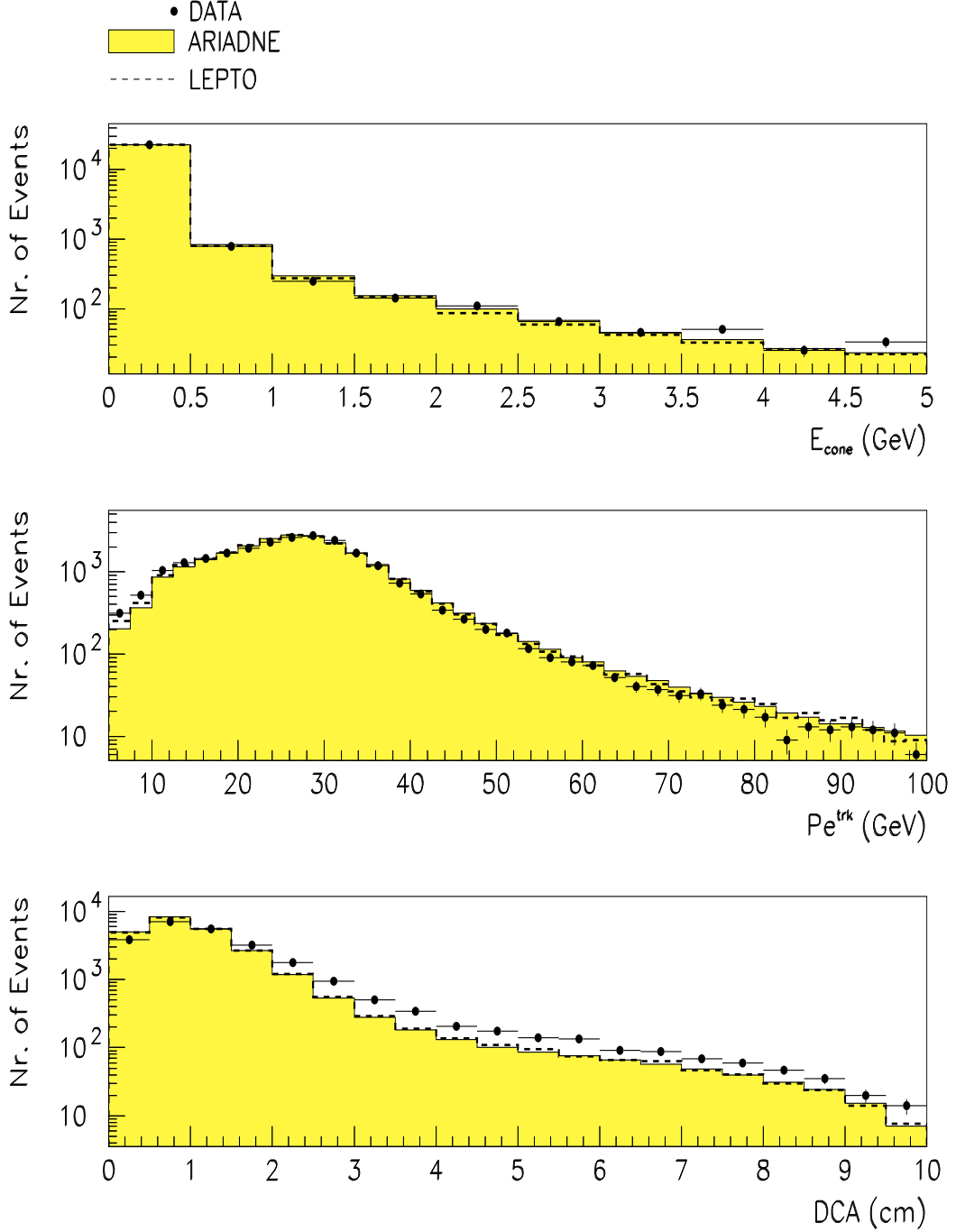
Figure 5.4: Upper plot: the distribution of the energy, E_{cone}, in a $\eta - \phi$ cone of radius 0.8 that is not assigned to the electron. Middle plot: the momentum of the track, p_e^{Trk}, matching the positron calorimeter cluster. Lower plot: the distance of closest approach (DCA) between the electron and the track assigned to it.
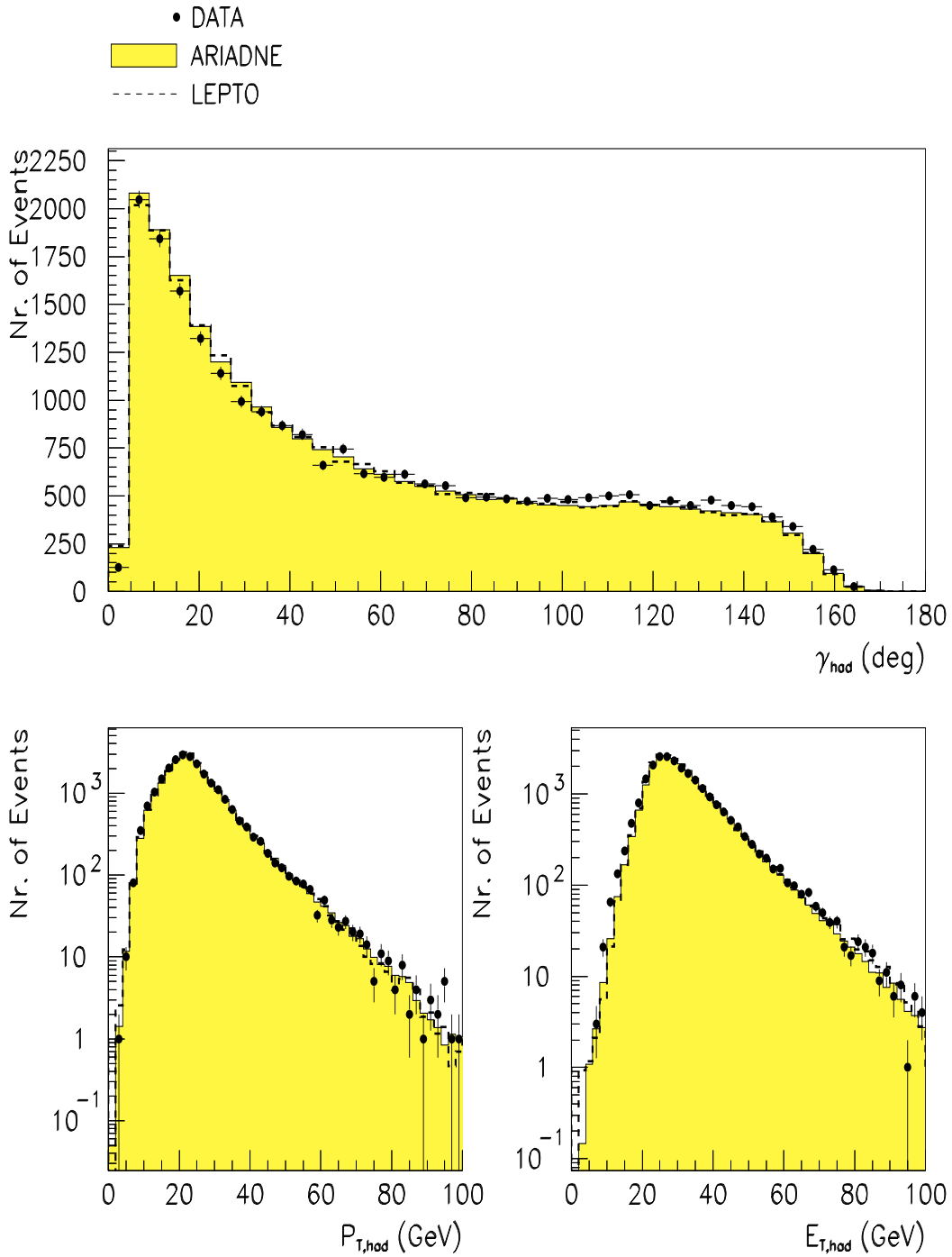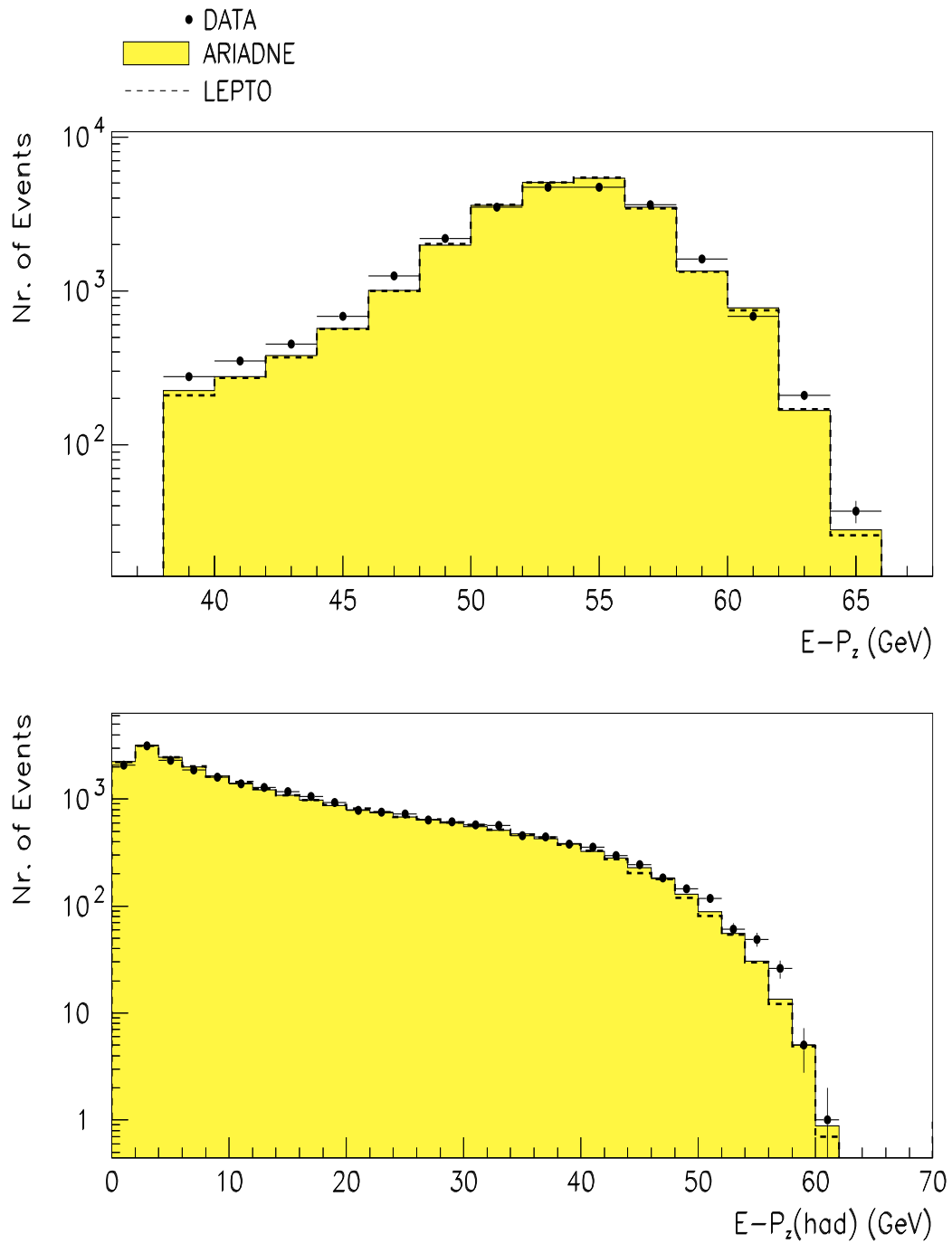
Figure 5.5: The hadronic variables: γ_h, $P_{T,hadr}$, and $E_{T,hadr}$.

Figure 5.6: The total (top plot) and hadronic (lower plot) $E - p_z$ distributions.
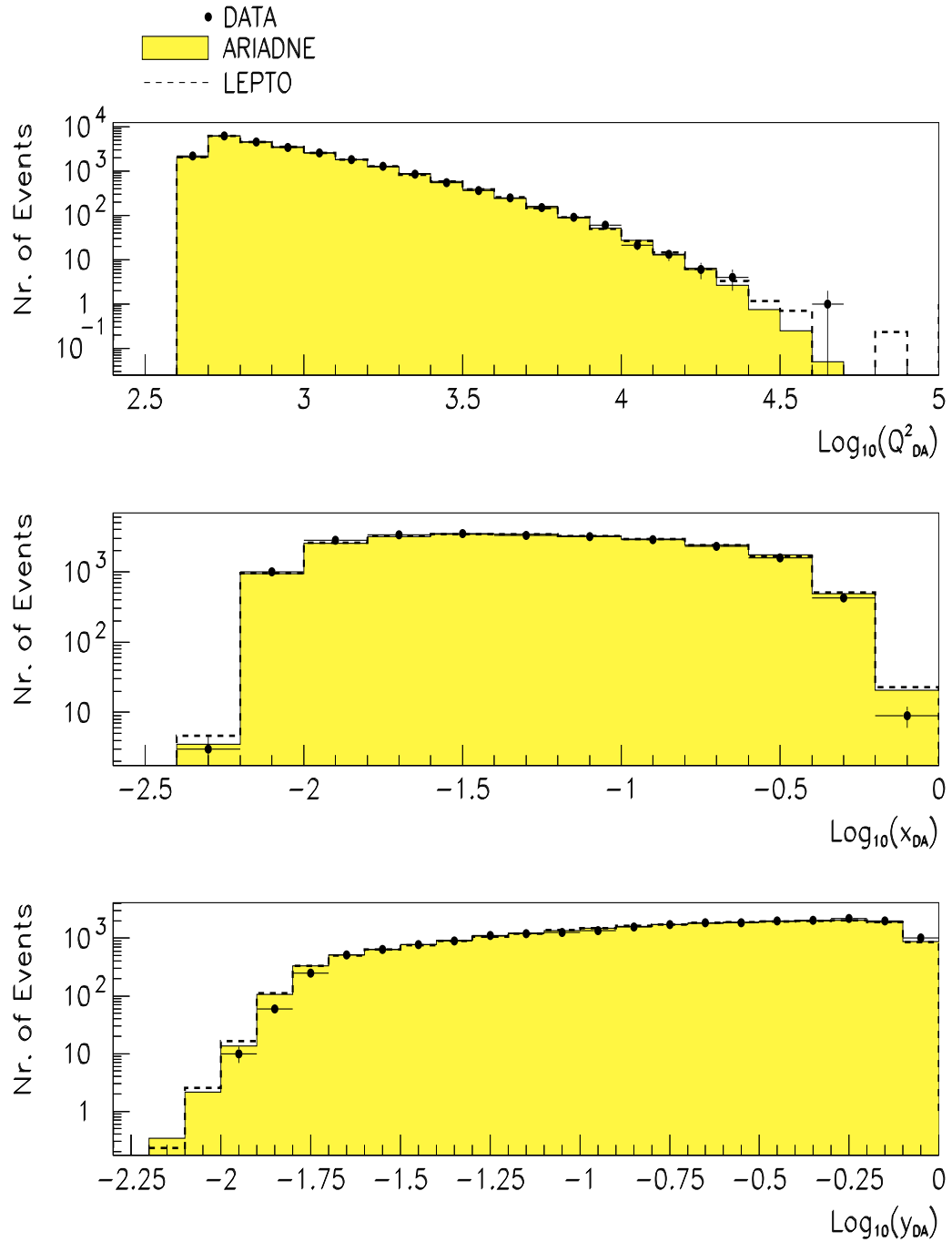
Figure 5.7: The kinematic variables Q^2, x, and y estimated with the double angle (DA) method.

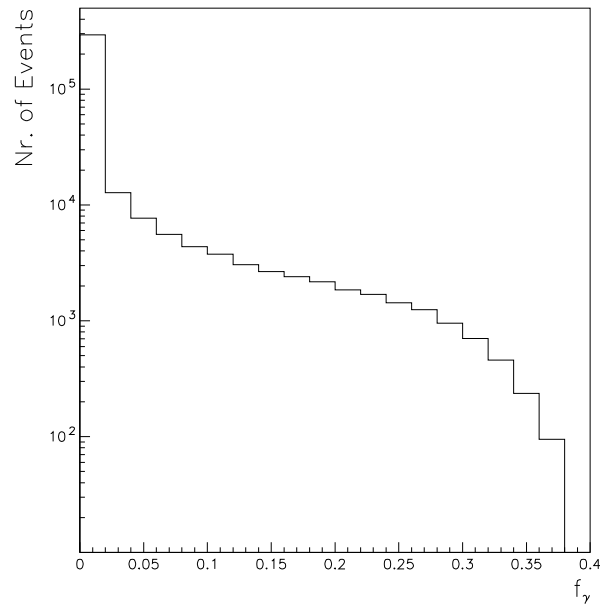Figure 5.8: The f_γ^{true} distribution.
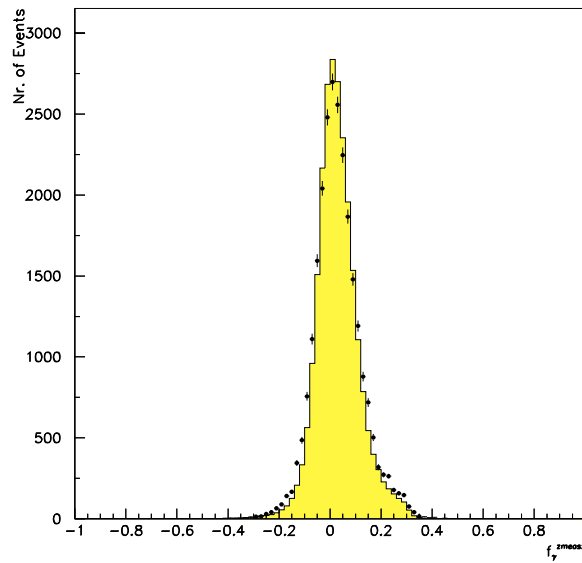
Figure 5.9: The f_γ^{meas} distribution for data and MC (ARIADNE).
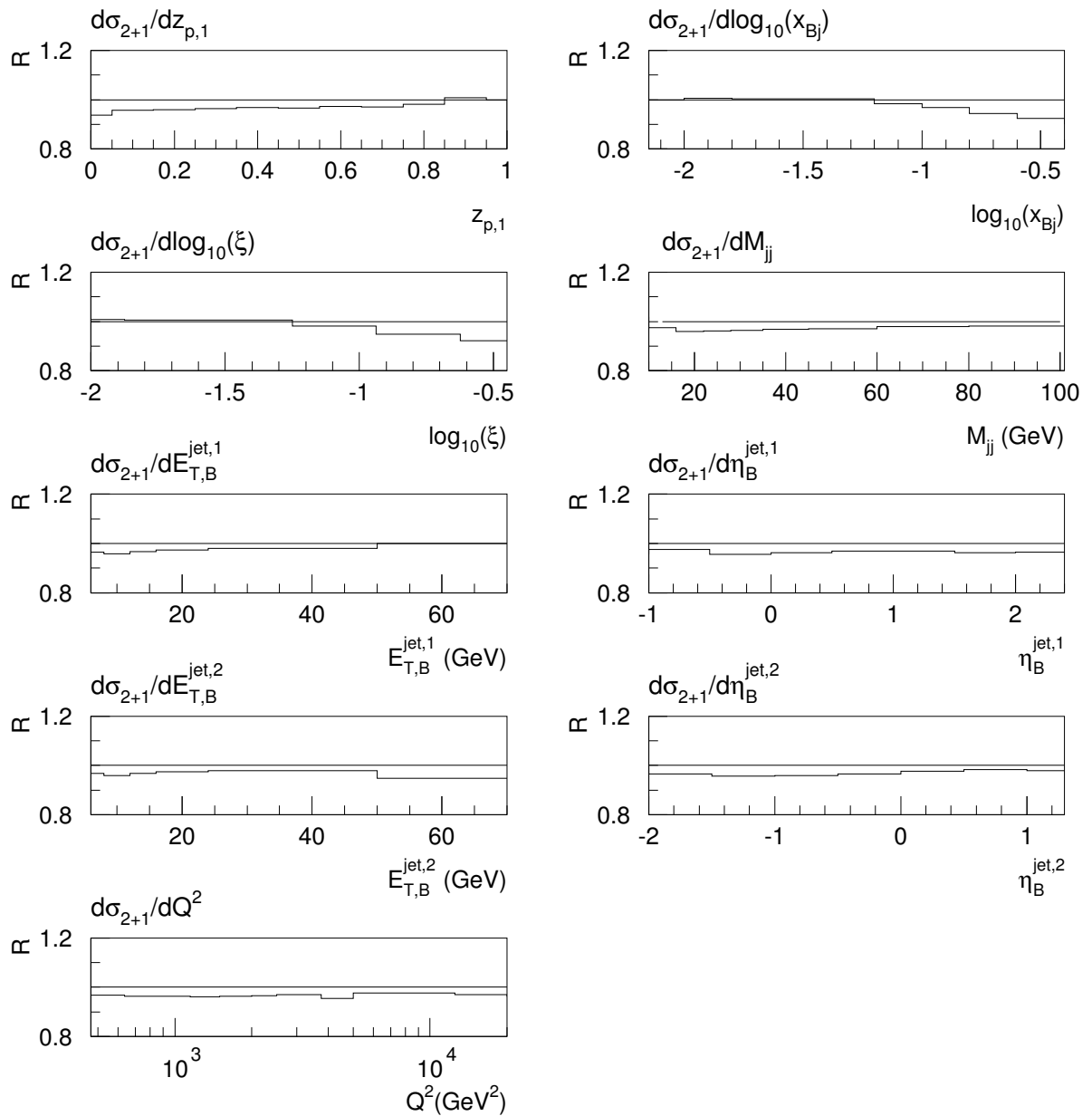
Figure 5.10: The ratio $R = \sigma_{2+1}(E_e^{nom})/\sigma_{2+1}(E_e^{true})$ for the MC (hadron level) dijet cross sections.
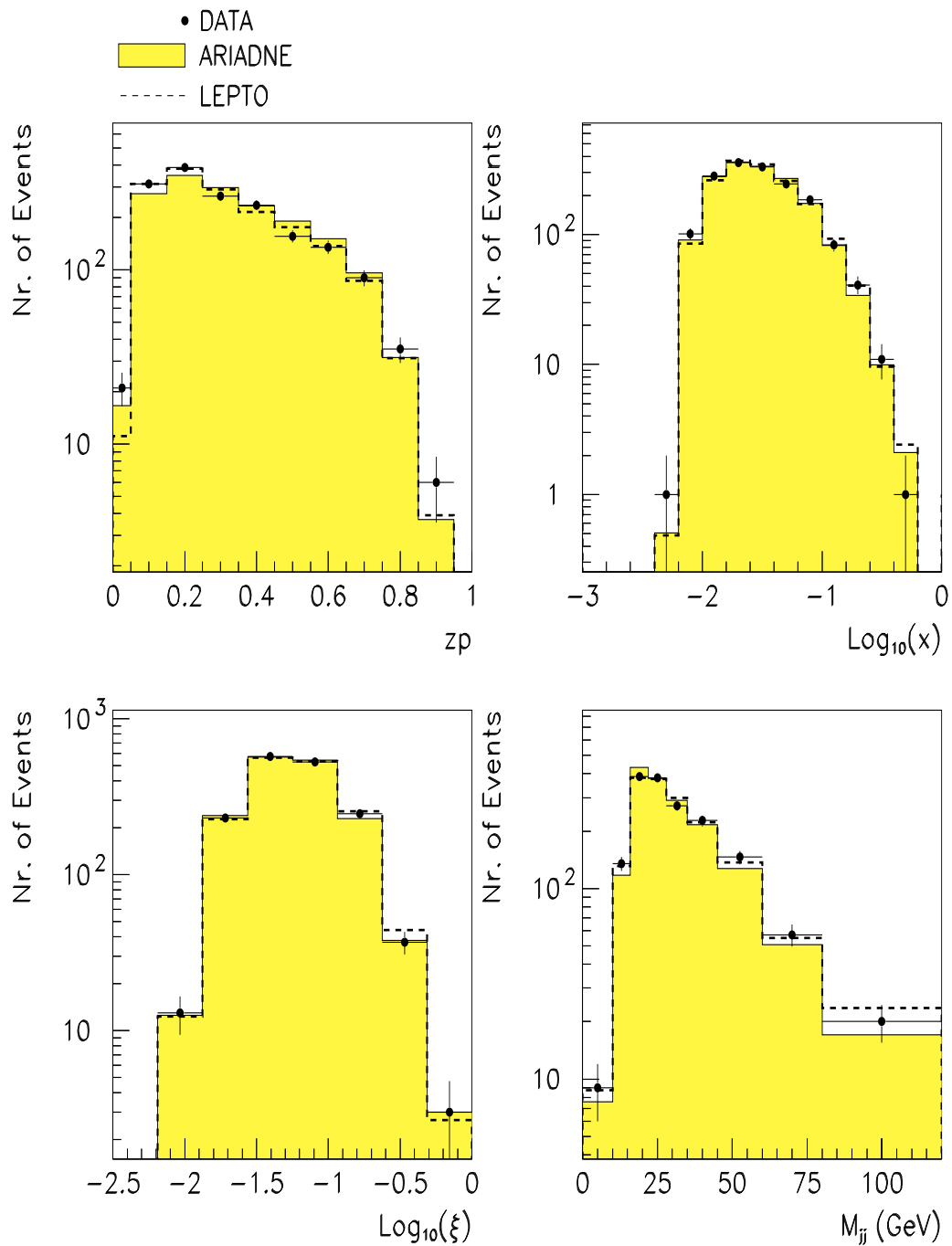
Figure 5.11: Data Monte Carlo shape comparison for the djet distributions as a function of z_p, $Log_{10}(x)$, $Log_{10}(\xi)$, and the dijet mass.
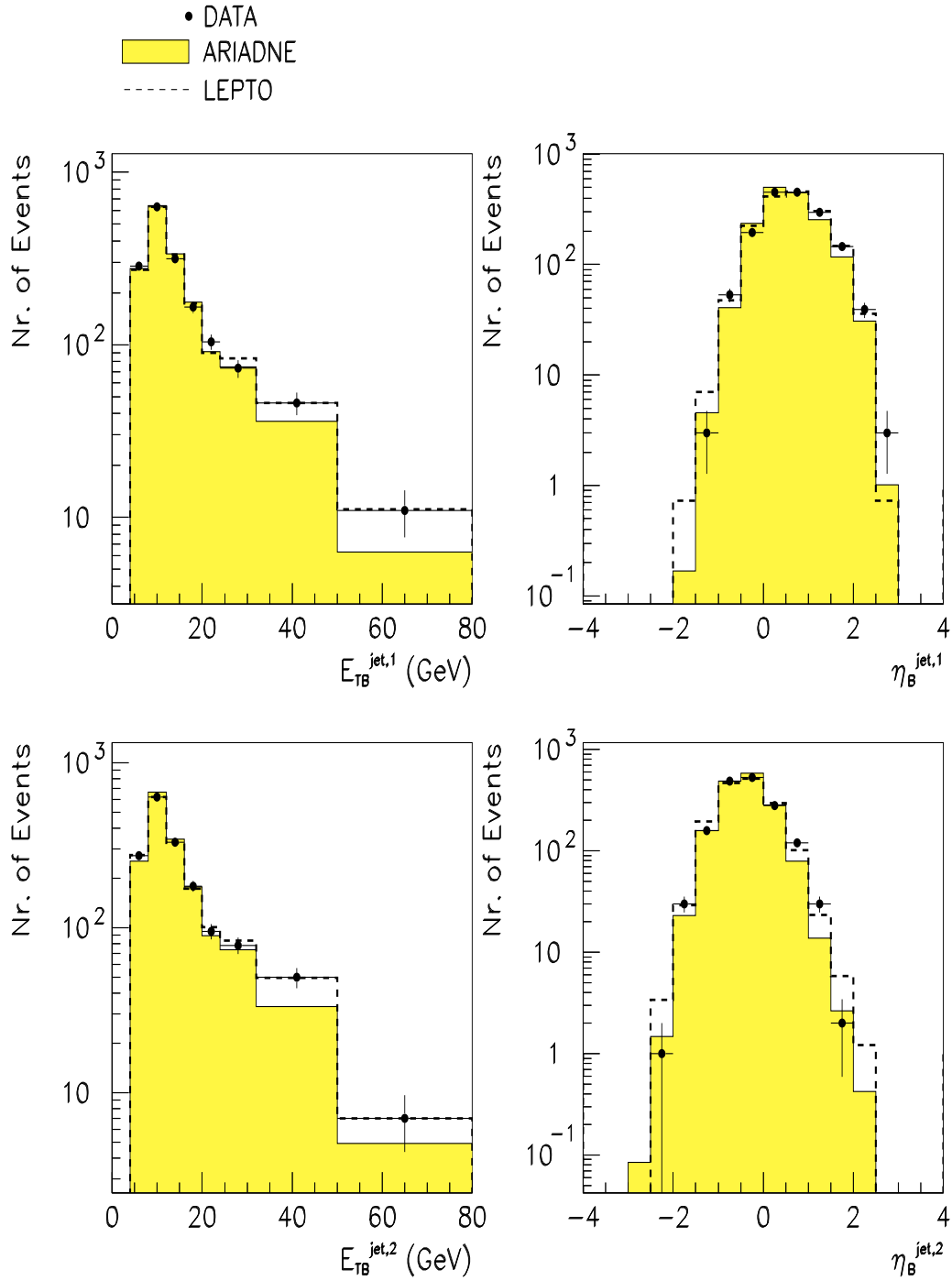
Figure 5.12: Data Monte Carlo shape comparison for the djet distributions as a function of $E_{TB}^{jet,1}$, $\eta_B^{jet,1}$, $E_{TB}^{jet,2}$ and $\eta_B^{jet,2}$.
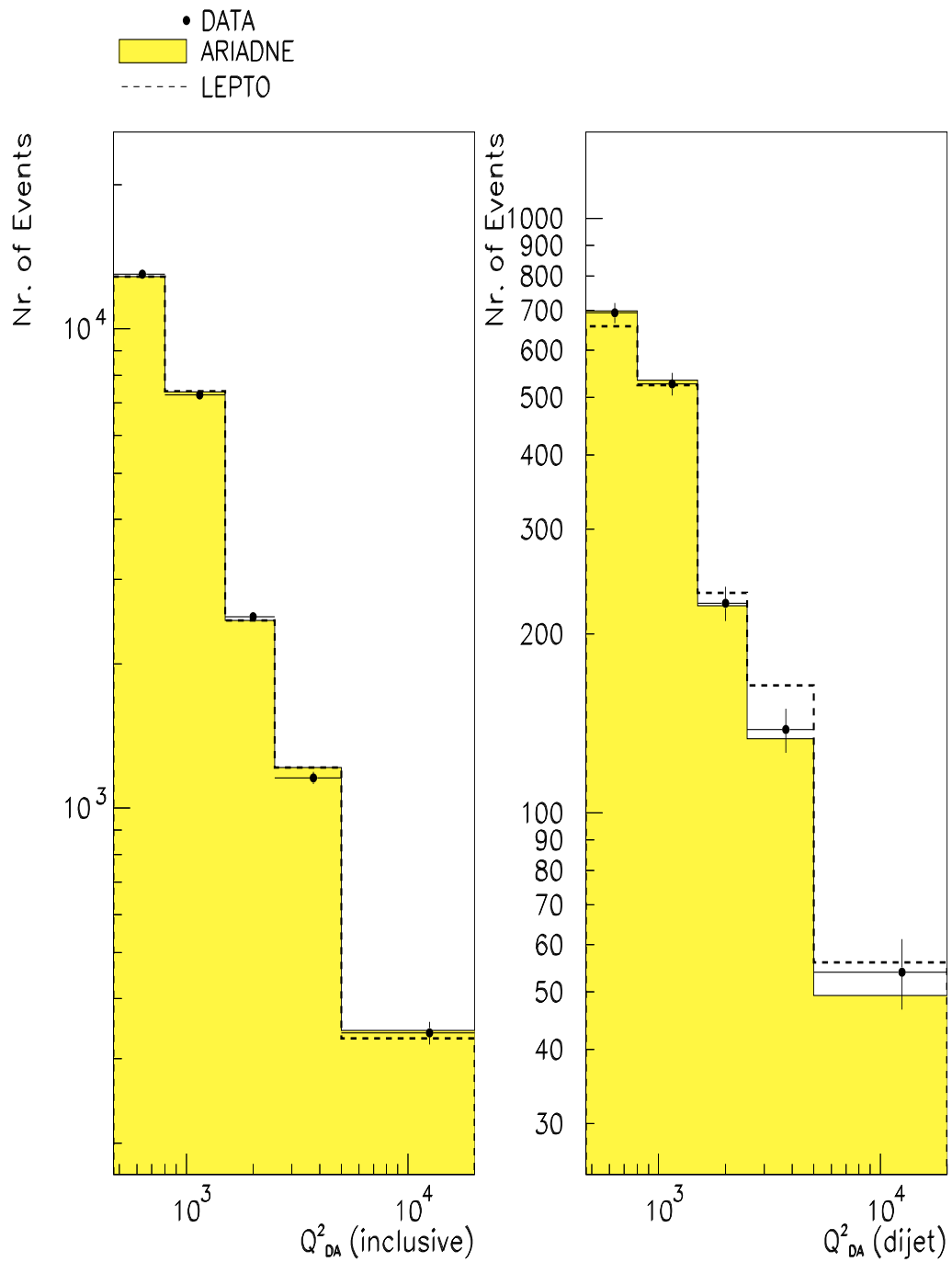
Figure 5.13: Data Monte Carlo shape comparison for $d\sigma_{tot}/dQ^2$ and $d\sigma_{2+1}/dQ^2$.
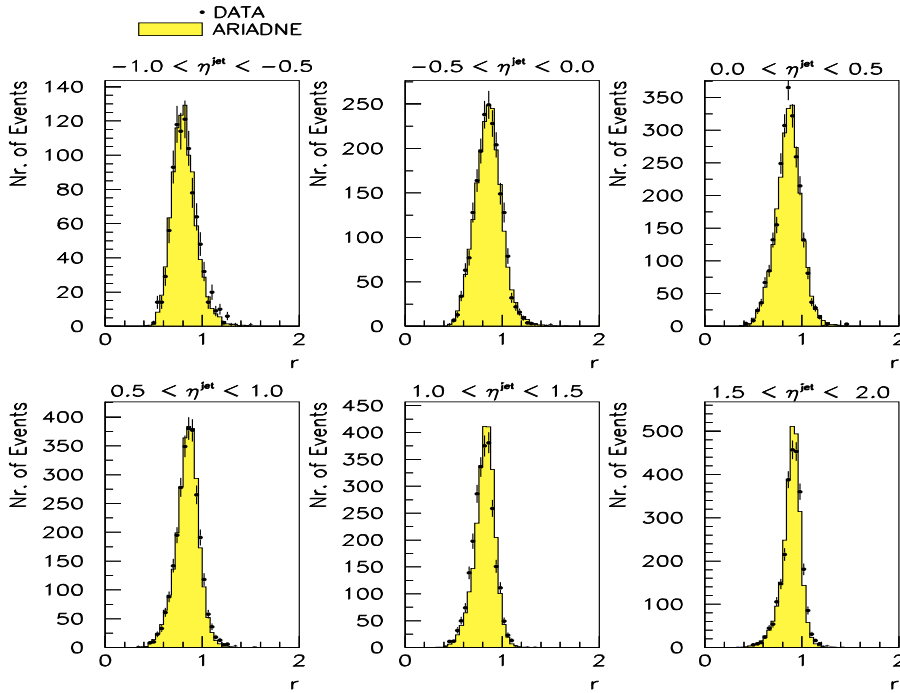
Figure 5.14: The ratio $r = E_T^{\text{jet}}/p_{\text{T,e}}^{\text{DA}}$ in bins of jet's pseudrapidity. The measured distributions are compared to the ARIADNE MC.
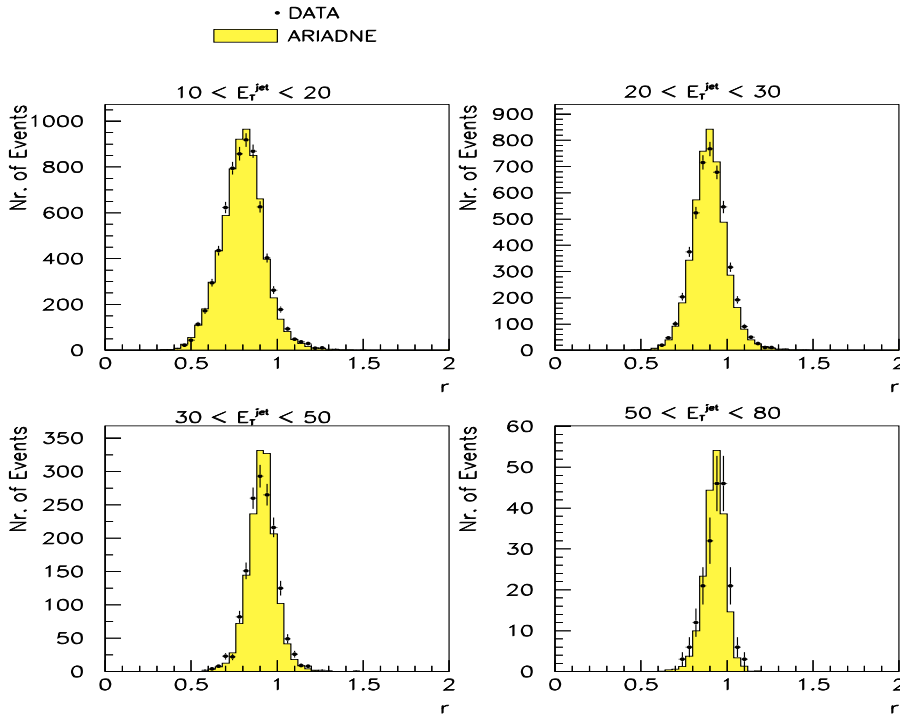
Figure 5.15: The ratio $r = E_T^{\text{jet}}/p_{\text{T,e}}^{\text{DA}}$ in bins of jet's transverse energy. The measured distributions are compared to the ARIADNE MC.
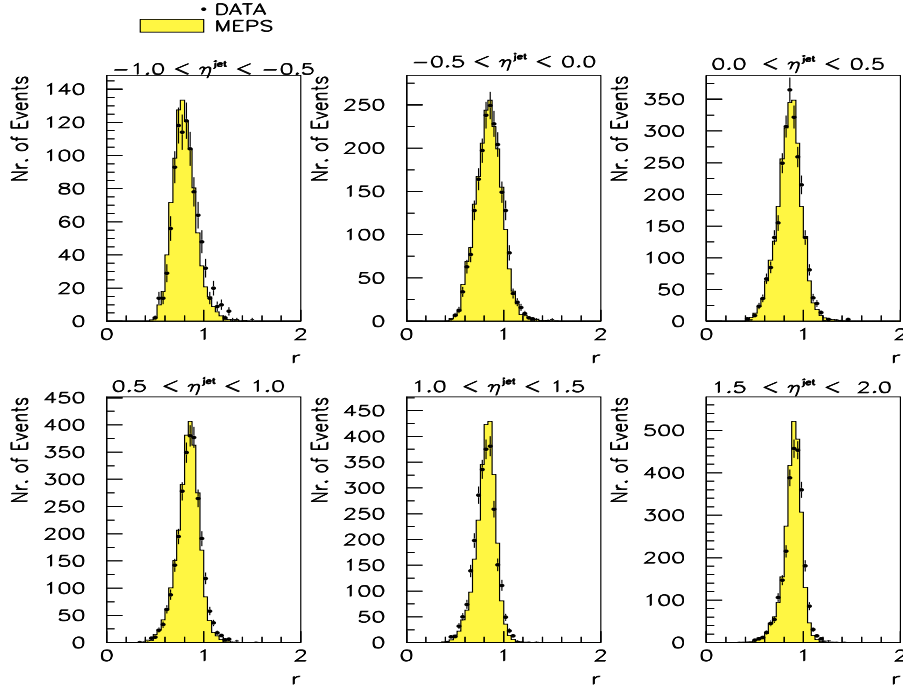
Figure 5.16: The ratio $r = E_T^{\text{jet}}/p_{\text{T,e}}^{\text{DA}}$ in bins of jet's pseudrapidity. The measured distributions are compared to the LEPTO MC.
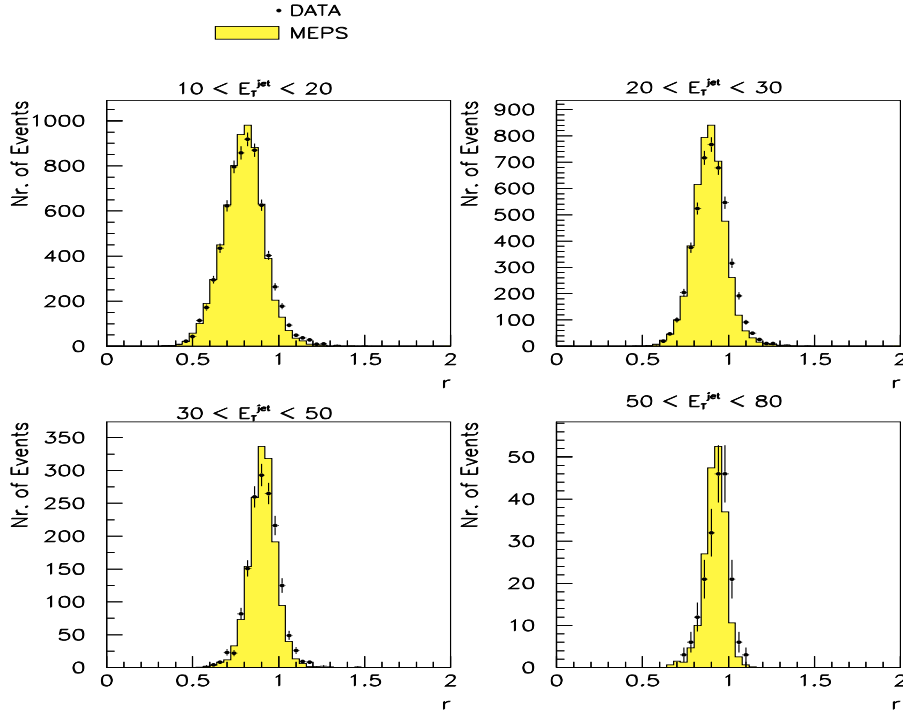
Figure 5.17: The ratio $r = E_T^{\text{jet}}/p_{\text{T,e}}^{\text{DA}}$ in bins of jet's transverse energy. The measured distributions are compared to the LEPTO MC.
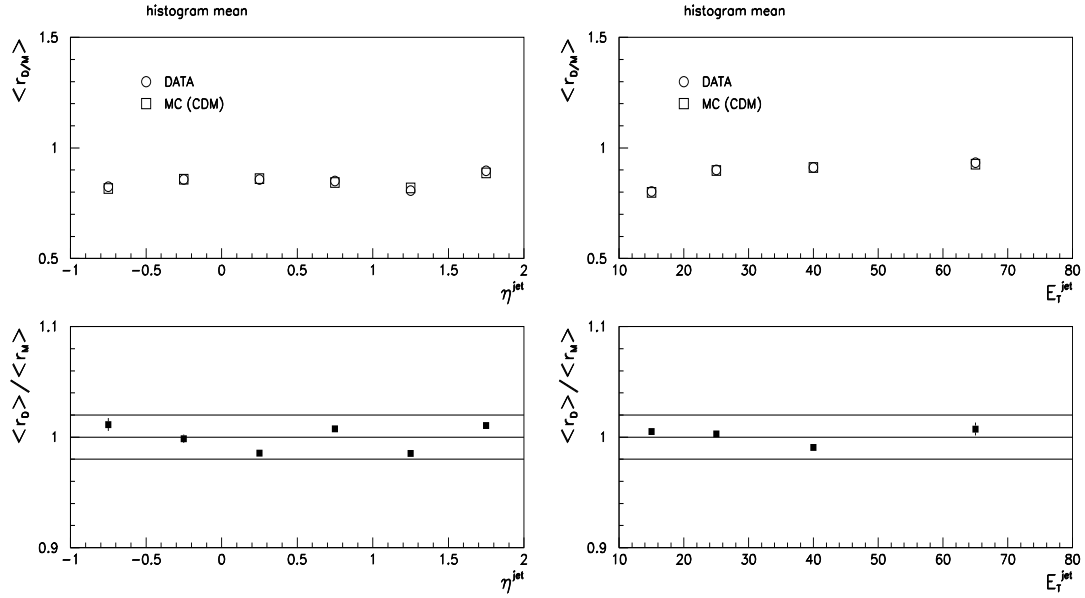
Figure 5.18: The mean ratios: $\langle r_D \rangle, \langle r_M \rangle$ (ARIADNE-CDM) and $\langle r_D \rangle / \langle r_M \rangle$ in bins of η^{jet} (left) and E_T^{jet} (right).
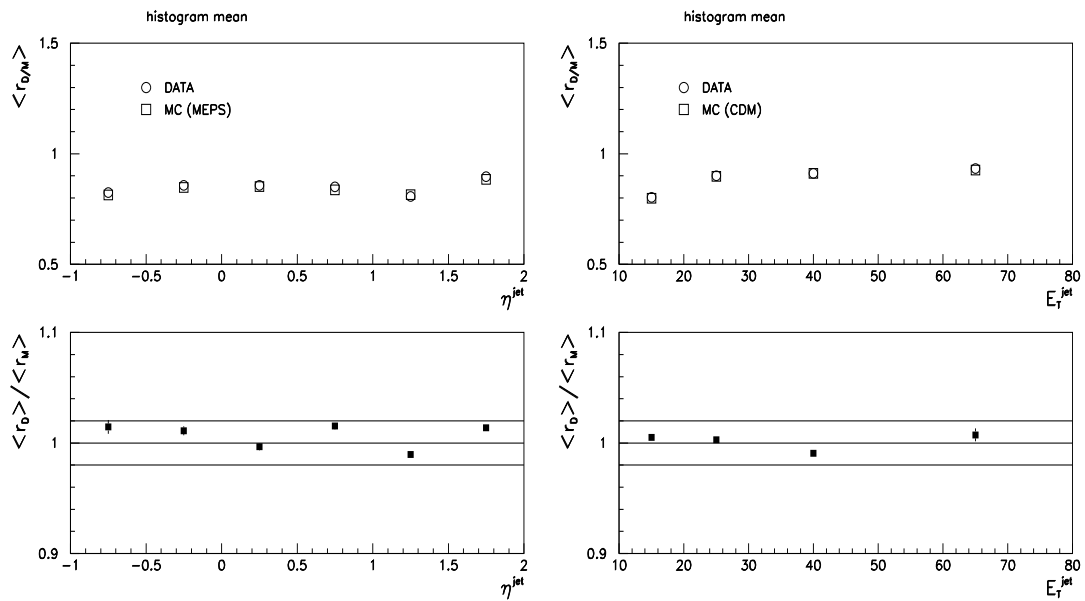
Figure 5.19: The histogram's mean ratios: $\langle r_D \rangle, \langle r_M \rangle$ (LEPTO) and $\langle r_D \rangle / \langle r_M \rangle$ in bins of η^{jet} (left) and E_T^{jet} (right).
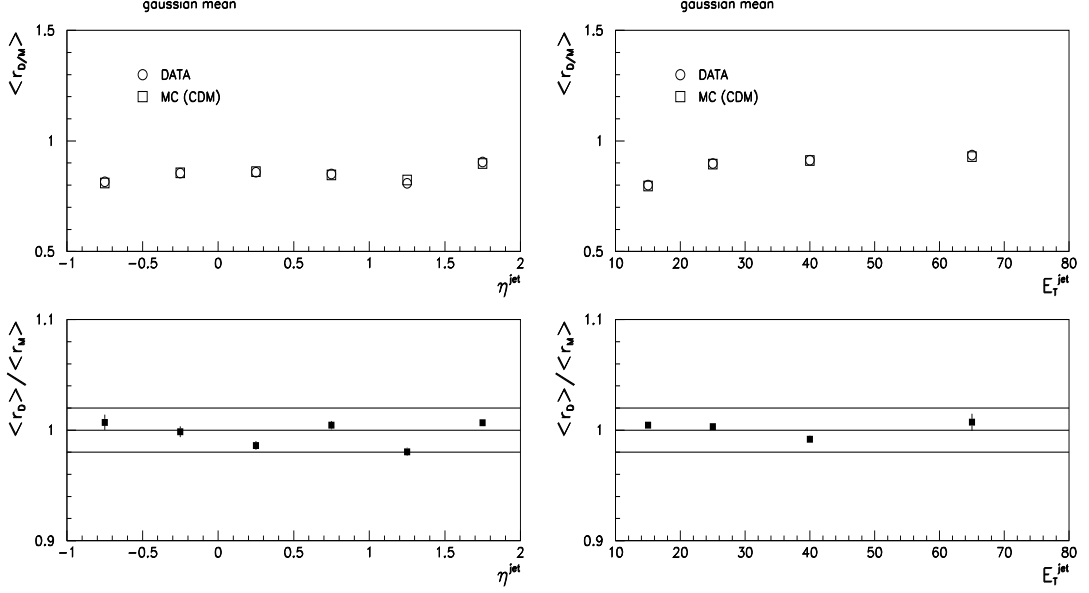
Figure 5.20: The histogram's mean ratios: $\langle r_D \rangle, \langle r_M \rangle$ (ARIADNE-CDM) and $\langle r_D \rangle / \langle r_M \rangle$ in bins of η^{jet} (left) and E_T^{jet} (right).
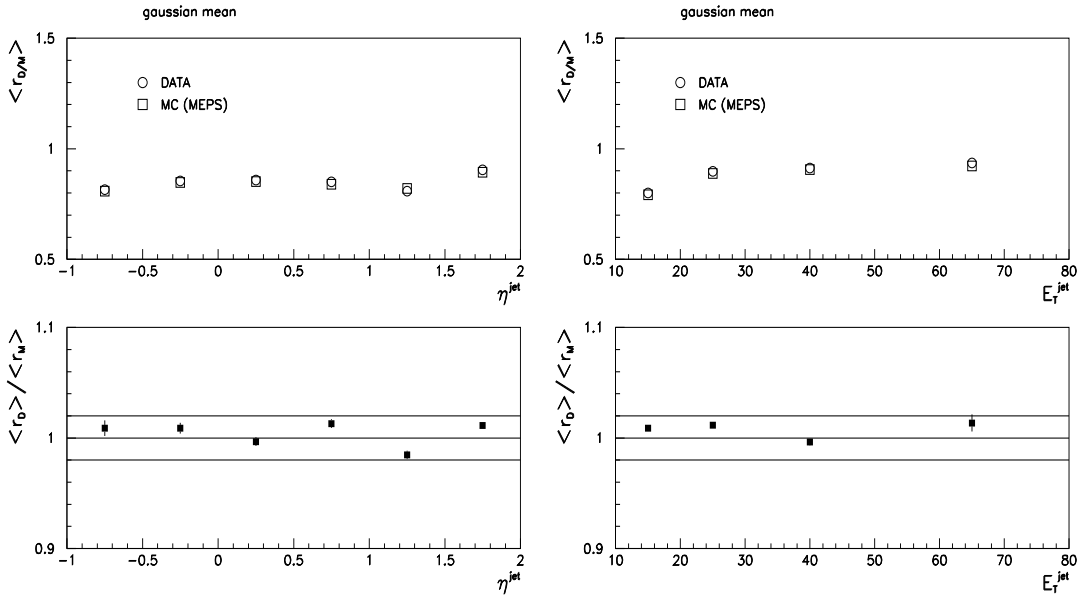
Figure 5.21: The histogram's mean ratios: $\langle r_D \rangle, \langle r_M \rangle$ (LEPTO) and $\langle r_D \rangle / \langle r_M \rangle$ in bins of η^{jet} (left) and E_T^{jet} (right).
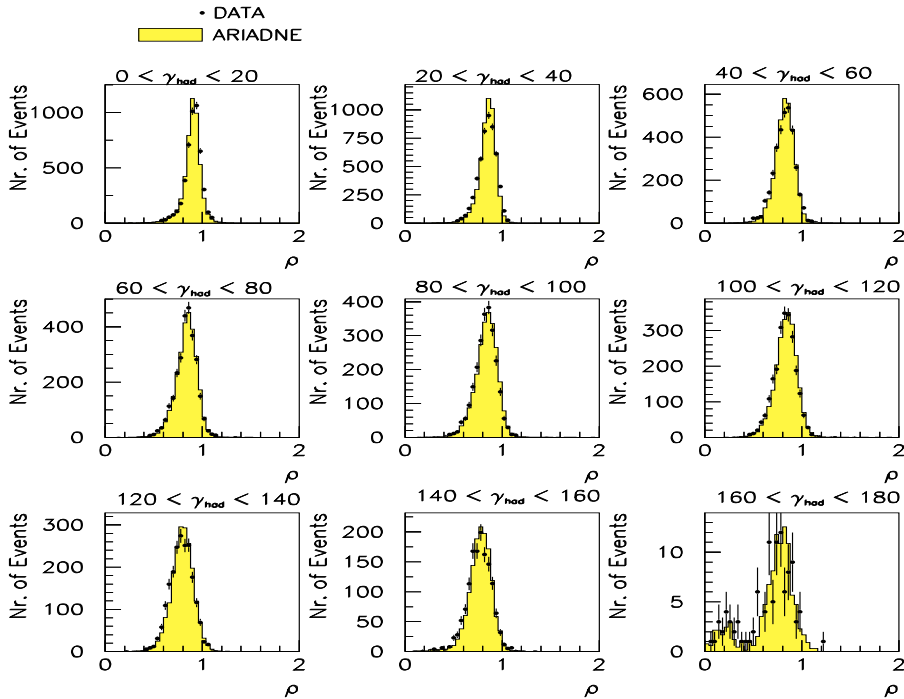
Figure 5.22: The ratio $\rho = P_{T,\mathrm{had}}/p_{\mathrm{T,e}}^{\mathrm{DA}}$ in bins of γ_{had}. The measured distributions are compared to the ARIADNE (CDM) MC.
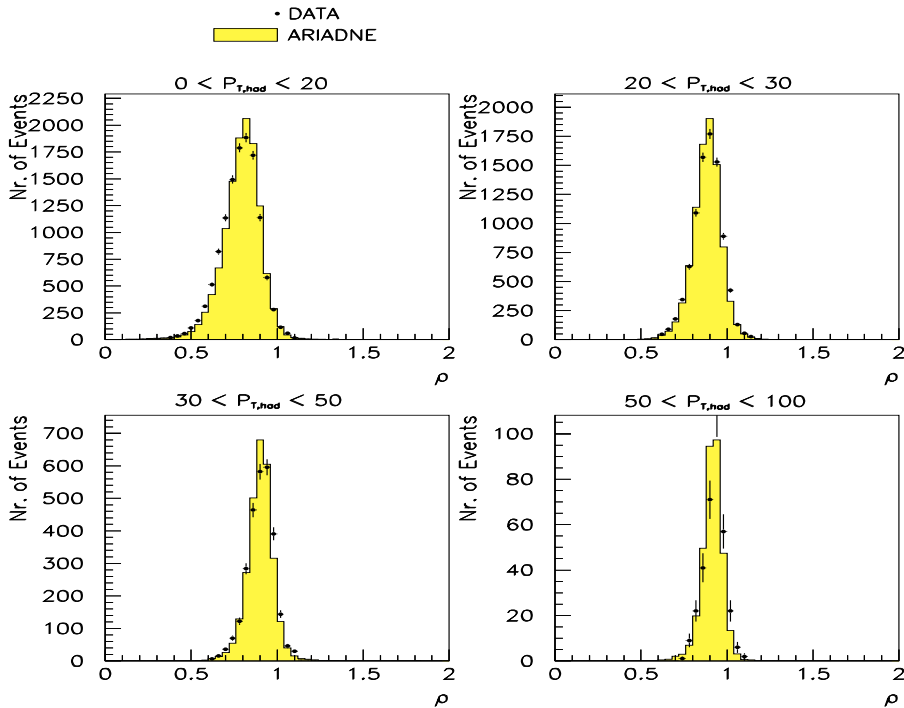
Figure 5.23: The ratio $\rho = P_{T,\mathrm{had}}/p_{\mathrm{T,e}}^{\mathrm{DA}}$ in bins of $P_{T,\mathrm{had}}$. The measured distributions are compared to the ARIADNE (CDM) MC.
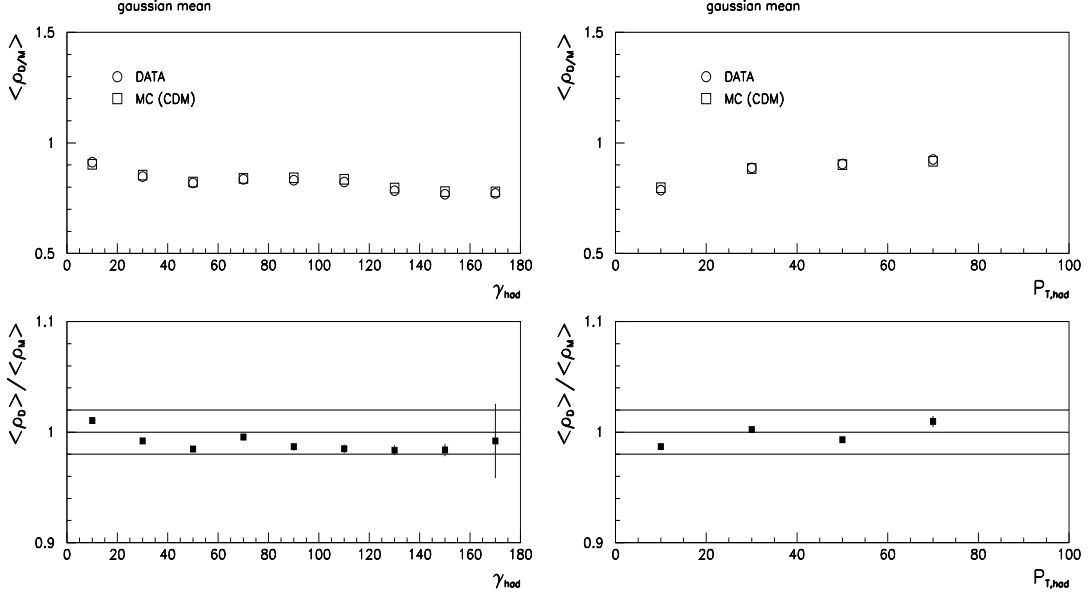
Figure 5.24: The histogram's mean ratios: $\langle\rho_D\rangle$, $\langle\rho_M\rangle$ (ARIADNE-CDM) and $\langle\rho_D\rangle/\langle\rho_M\rangle$ in bins of γ_{had} (left) and $P_{T,\text{had}}$ (right).
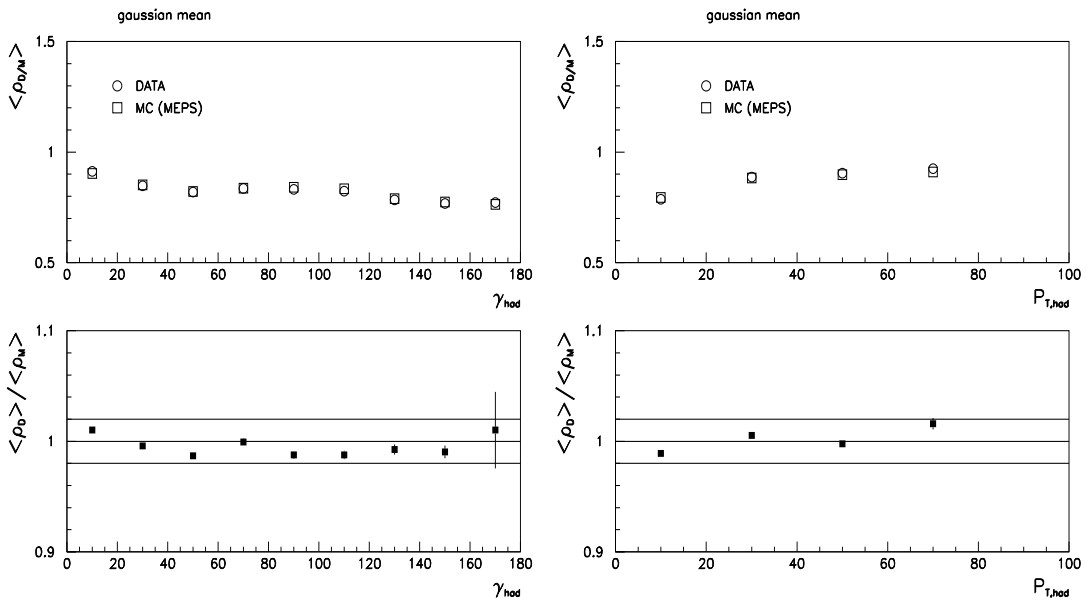
Figure 5.25: The histogram's mean ratios: $\langle\rho_D\rangle$, $\langle\rho_M\rangle$ (LEPTO) and $\langle\rho_D\rangle/\langle\rho_M\rangle$ in bins of γ_{had} (left) and $P_{T,\text{had}}$ (right).
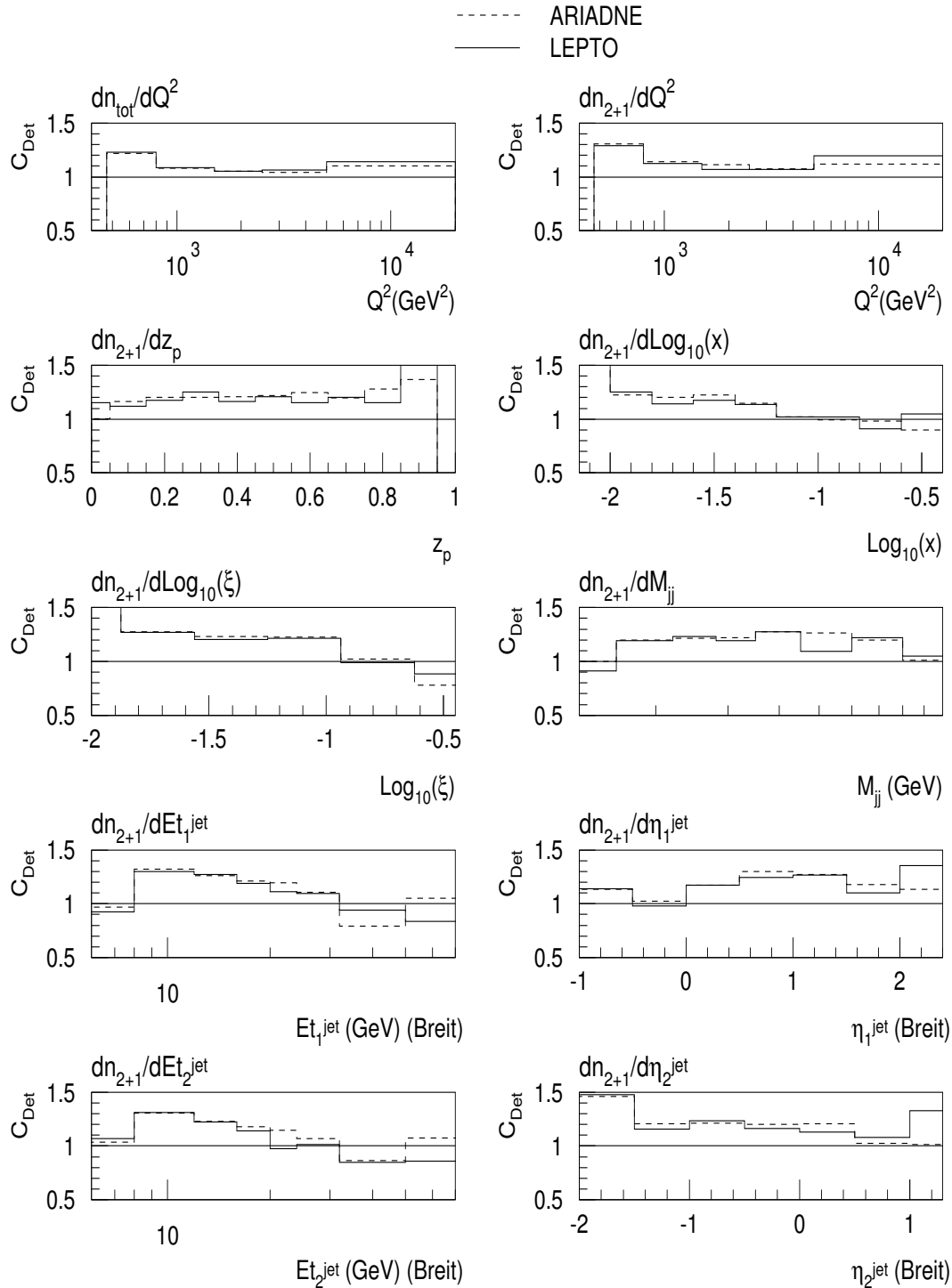
Figure 5.26: The detector-correction factors obtained with ARIADNE(dashed lines) and LEPTO (solid lines).

QED Corrections
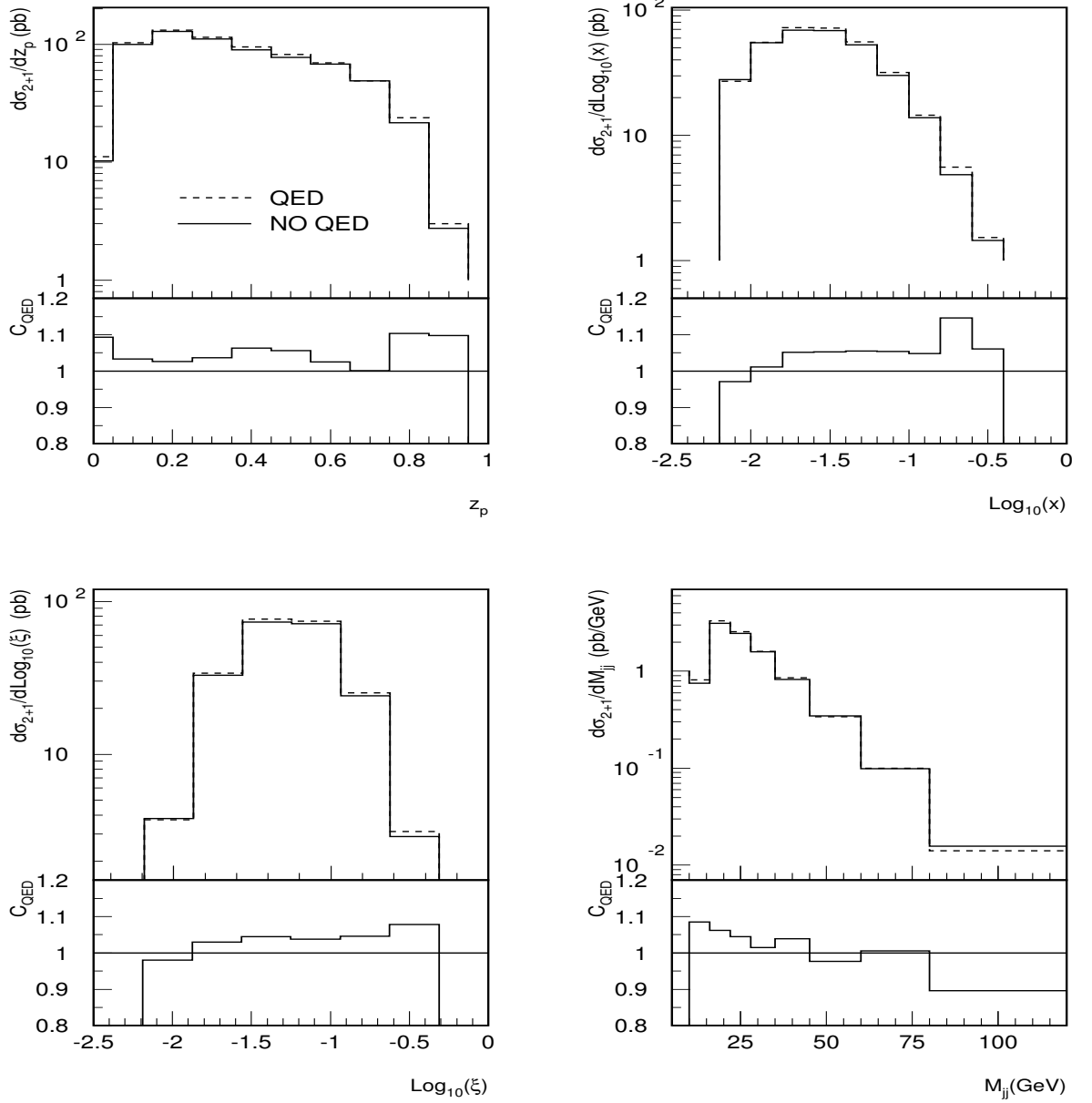
Figure 5.27: The MC dijet cross sections as a functions of z_p, $Log_{10}(x)$, $Log_{10}(\xi)$ and M_{jj} computed including (dashed lines) or excluding (solid lines) QED effects. Also shown are the corresponding QED-correction factors.
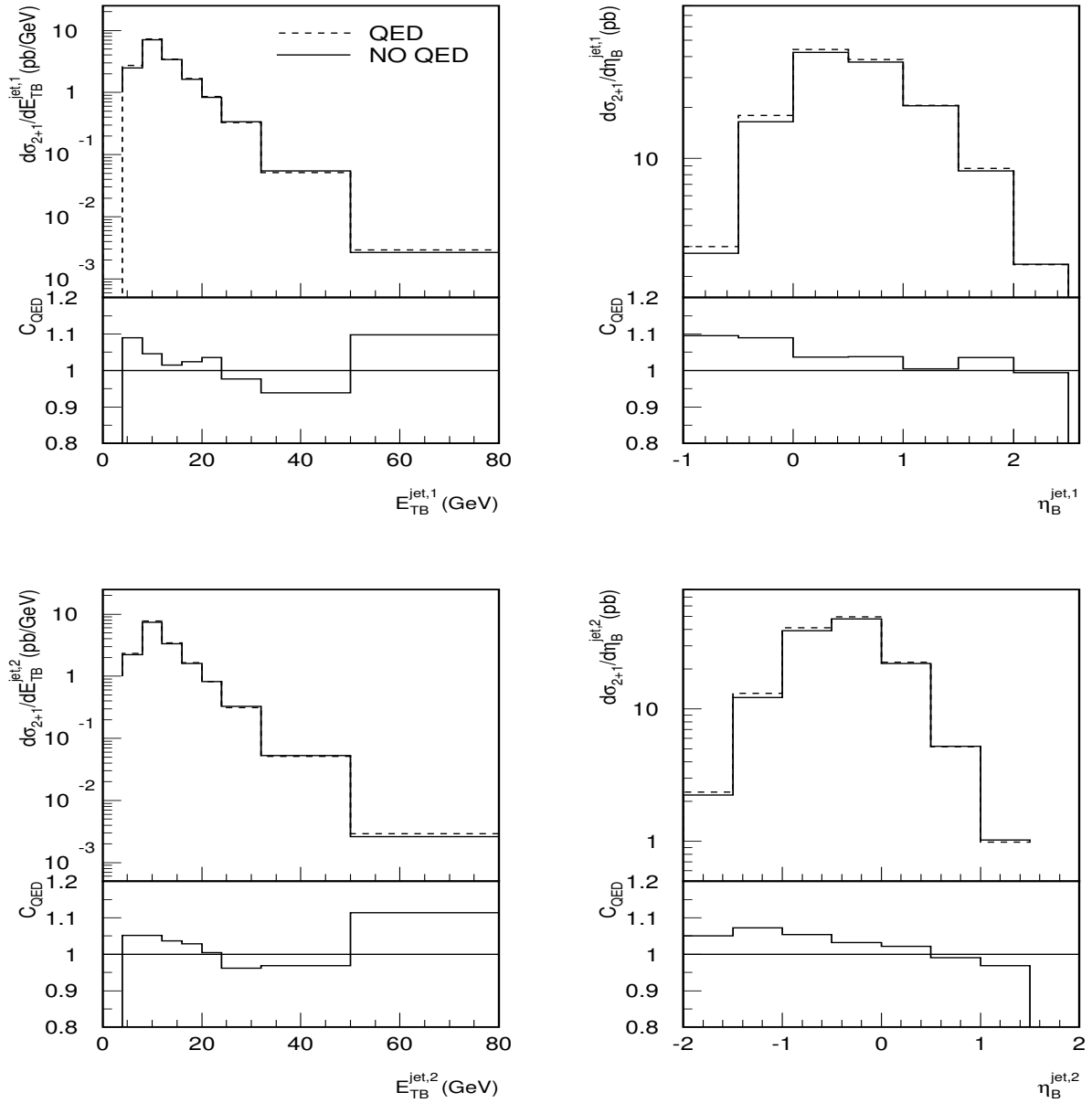
QED Corrections

Figure 5.28: The MC dijet cross sections as a functions of $E_{TB}^{jet,1}$, $\eta_B^{jet,1}$, $E_{TB}^{jet,2}$ and $\eta_B^{jet,2}$ computed including (dashed lines) or excluding (solid lines) QED effects. Also shown are the corresponding QED-correction factors.
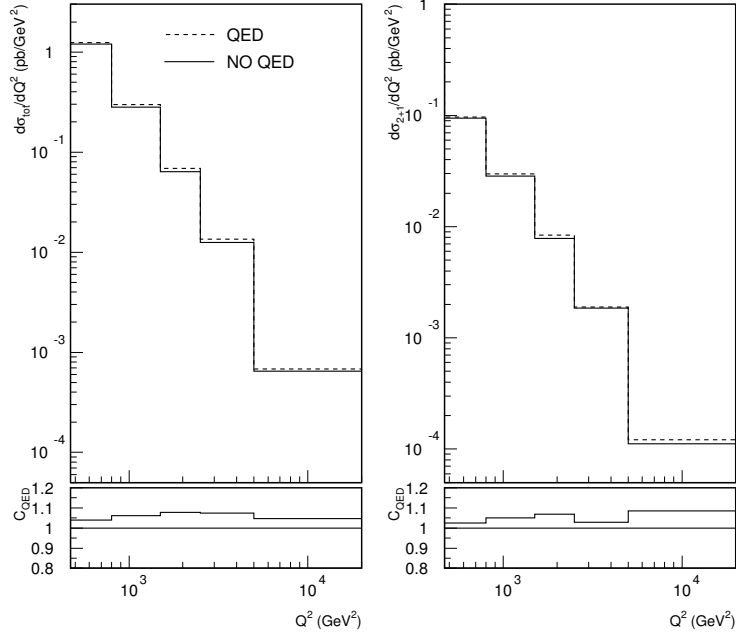
QED Corrections

Figure 5.29: The MC inclusive $(d\sigma_{tot}/dQ^2)$ and dijet $(d\sigma_{2+1}/dQ^2)$ cross sections as a function of Q^2 computed including (dashed lines) or excluding (solid lines) QED effects. Also shown are the corresponding QED-correction factors.
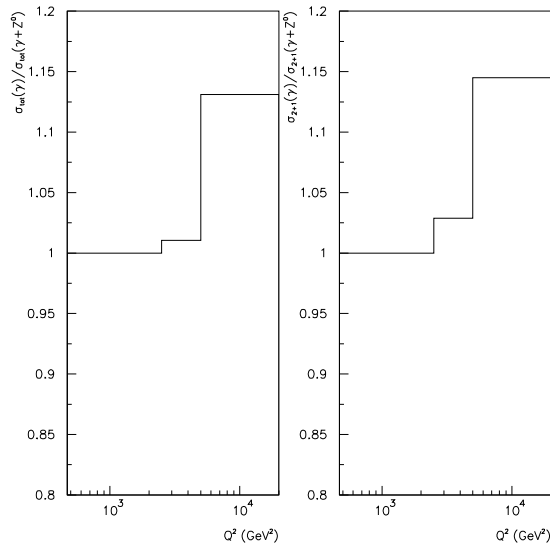
Figure 5.30: The Z^0 correction factors (C_{Z^0}) for the cross sections $(d\sigma_{tot}/dQ^2)$ and $(d\sigma_{2+1}/dQ^2)$.
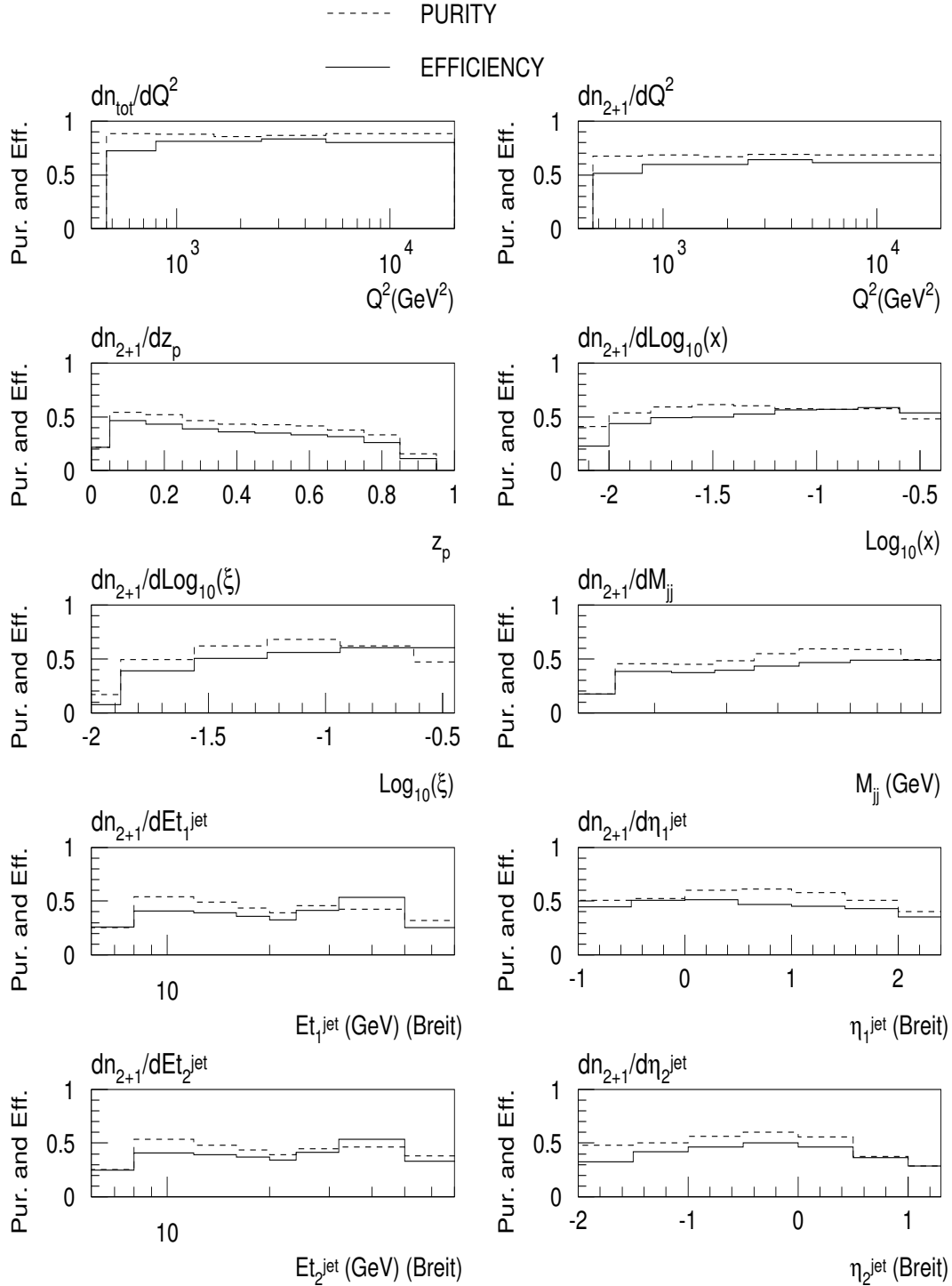
Figure 5.31: Purities and efficiencies obtained with ARIADNE.
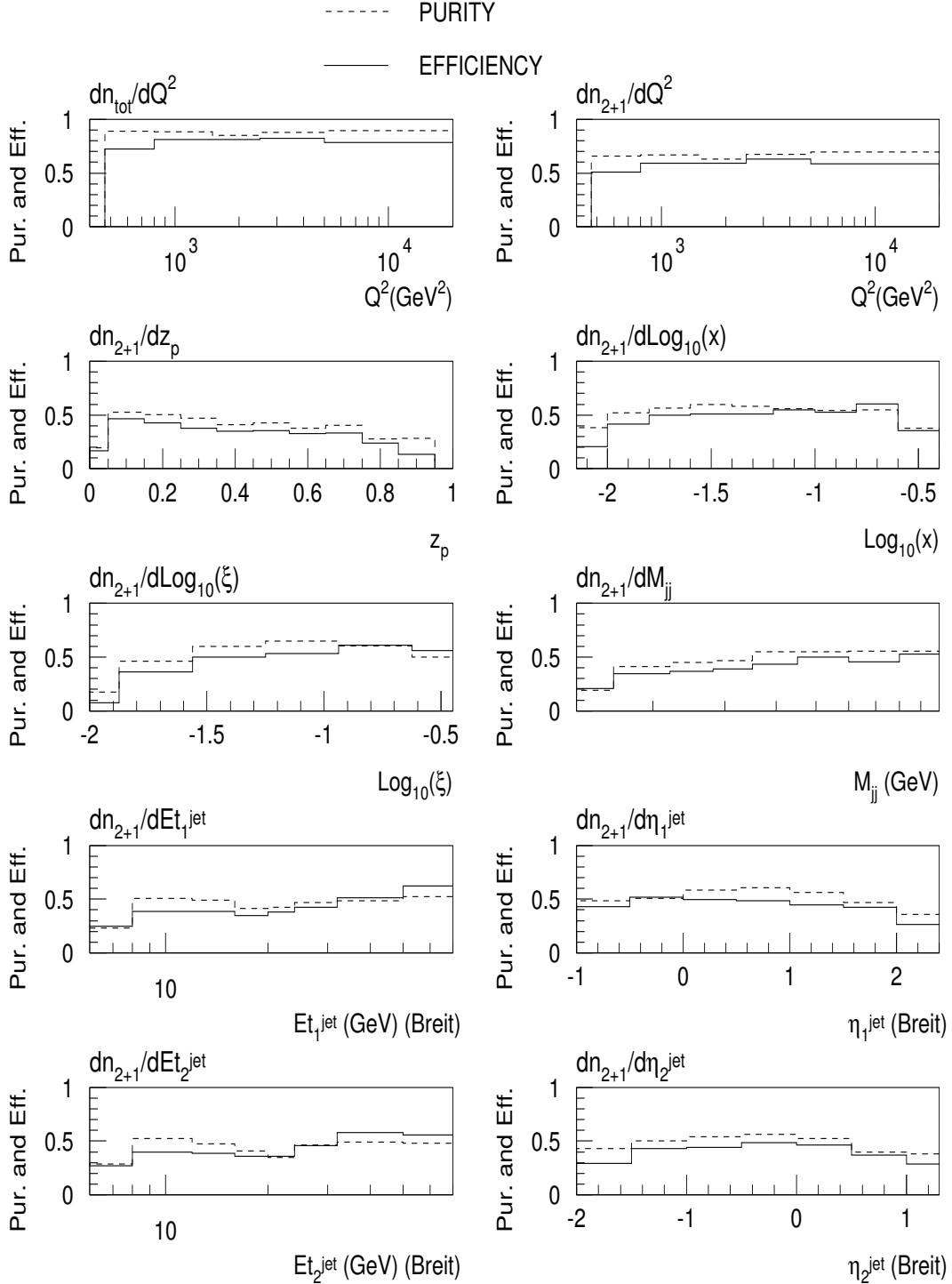
Figure 5.32: Purities and efficiencies obtained with LEPTO.

Chapter 6

Results

In this chapter we present the final results on the measured NC e^+p DIS dijet differential cross sections and on the dijet fraction R_{2+1}. The measured observables are compared to NLO QCD predictions after correcting the latter for hadronization effects. The dijet fraction, which is affected by the smallest theoretical and experimental uncertainties, is then used in a NLO QCD fit in order to determine α_s. The strong coupling constant is determined both at the reference mass scale of the Z^0 boson and as function of the virtuality (Q^2) of the exchanged boson.

6.1 Dijet differential cross sections and dijet fraction

6.1.1 Results

Using the data samples of inclusive and dijet events, selected according to the criteria described in the previous chapter, single differential cross sections and the dijet fraction are measured for exclusive dijet production in NC e^+p deep inelastic scattering at HERA.

The measured cross sections are corrected bin-by-bin for detector effects, QED radiative effects, and Z^0-exchange processes. They refer to the following DIS phase-space region

$$470 < Q^2 < 20000 \ \text{GeV}^2 \quad \text{and} \quad 0 < y < 1 \tag{6.1}$$

and the jet selection criteria:

$$E_{TB}^{jet,M} > 8 \ \text{GeV} \quad \text{and} \quad E_{TB}^{jet,m} > 5 \ \text{GeV} \tag{6.2}$$

$$-1 < \eta_{Lab}{}^{jet} < 2 \tag{6.3}$$

where $E_{TB}^{jet,M}$ ($E_{TB}^{jet,m}$) is the transverse energy of the jet in the Breit frame with the highest (second highest) transverse energy in the event. Both jets are required to lie in the pseudorapidity range between -1 and 2 in the laboratory frame. In the presented dijet cross sections, the two jets are ordered according to decreasing pseudorapidity in the Breit frame ($\eta_B^{jet,1} > \eta_B^{jet,2}$).

The measurements of the differential dijet cross sections as functions of z_p, $log_{10}(x)$, $log_{10}(\xi)$, the dijet invariant mass M_{jj}, and the jet transverse energies and pseudorapidities in the Breit frame are presented (as black dots) in Fig. 6.1 and 6.2. The inclusive ($d\sigma_{tot}/dQ^2$) and dijet ($d\sigma_{2+1}/dQ^2$) cross sections, as well as the dijet fraction

$$R_{2+1}(Q^2) \equiv \frac{d\sigma_{2+1}/dQ^2}{d\sigma_{tot}/dQ^2} \ ,$$

all as a function of Q^2, are shown in Fig. 6.3. The inner error bars represent the statistical uncertainties of the data, and the outer error bars show the statistical and systematic uncertainties − not associated with the uncertainty in the absolute energy scale of the jets − added in

quadrature. The uncertainty on the absolute energy scale which represents the dominant source of systematic error is strongly correlated between measurements at different points and is shown as a light shaded band in each figure.

The measured inclusive and dijet differential cross sections, and the dijet fraction $R_{2+1}(Q^2)$, are compared to DISENT NLO QCD predictions (the solid lines in Figs. 6.1 to 6.3) corrected for hadronisation effects and obtained according to the DISENT program settings described in chapter 3. The uncertainties associated to the QCD predictions, discussed at length and estimated again in chapter 3, are shown as a shaded band underneath each plot in Figs. 6.1 to 6.3. The uncertainty band in Fig. 6.3b) does not include the contribution due to $\alpha_s(M_Z)$; since the measurement of $R_{2+1}(Q^2)$ in Fig. 6.3b) was used to determine $\alpha_s(M_Z)$ (see next section), the band reflects the theoretical uncertainty of the calculation except that associated with $\alpha_s(M_Z)$. To quantify the effect of the hadronisation corrections on the central theoretical predictions, the pure NLO QCD cross sections are also shown (as dashed lines) in all the figures.

The complete results, in tabular form, of the measured cross sections and the theoretical predictions including a detailed information on the corresponding experimental and theoretical uncertainties are presented in the tables from Table 6.1 to Table 6.22.

6.1.2   Discussion of the results

The QCD predictions, which assume $\alpha_s(M_Z) = 0.118$, give overall a good description of the shape and magnitude of the measured cross sections. In particular, in the case of the cross sections as a function of the jet transverse energies and Q^2, the agreement between data and theory extend over four order of magnitudes. The dijet fraction is also very well described by the QCD calculations; it is found to increase with increasing Q^2. The only exception is represented by the cross section as of function of the pseudorapidity of the most backward jet in the Breit frame $(d\sigma_{2+1}/d\eta_B^{jet,2})$, where the data lie above the theoretical predictions in the forward region. It has to be pointed out however that (as noted in the chapter 3) the MC programs give a rather poor description of this observable which is also affected by large hadronisation corrections.

The proton PDFs used in the NLO QCD calculations were determined from DGLAP fits which included measurements of F_2 from ZEUS. On the other hand, exclusive dijet production represents a small fraction of the total DIS cross section (see $R_{2+1}(Q^2)$ in Fig. 6.3). Thus in summary, the observed agreement in normalization between the measured dijet fraction and the theoretical predictions is non-trivial and shows that pQCD is able to reproduce quantitatively the rate for exclusive dijet production in the phase-space region considered here. The agreement in the differential cross sections demonstrates the validity of the description of the dynamics of dijet production by the underlying QCD hard processes (up to $O(\alpha_s^2)$) at the $\approx 10\%$ level.

6.2   Determination of the strong coupling

In chapter 3 we have demonstrated how the use of the dijet fraction is particular effective in reducing the theoretical uncertainty due to the NLO PDFs, the relative uncertainty on $R_{2+1}(Q^2)$ being only $1 - 1.5\%$. In addition in the measured ratio $R_{2+1}(Q^2)$ some of the systematic uncertainties (as for example the uncertainty on the luminosity determination) largely cancel. This makes the use of this observable particularly suitable for a QCD analysis aiming at a determination α_s. In the next two sections the dijet fraction $R_{2+1}(Q^2)$ will be used in a QCD fit to the corresponding NLO QCD predictions in order to determine α_s. The strong coupling constant is determined both at reference scale of the Z^0 boson mass and as function of the virtuality (Q^2) of the exchanged boson.

6.2.1 Determination of $\alpha_s(M_Z)$

The measured dijet fraction as a function of Q^2, $R_{2+1}(Q^2)$, was used to determine $\alpha_s(M_Z)$. The sensitivity of the measurements to the value of $\alpha_s(M_Z)$ is exemplified in Fig. 6.3 by the comparison between the measured $R_{2+1}(Q^2)$ and the NLO QCD calculations for three values of $\alpha_s(M_Z)$.

The procedure to determine the value of $\alpha_s(M_Z)$ was as follows:

- NLO QCD calculations of $R_{2+1}(Q^2)$ were performed for three sets of the MBFIT proton PDFs which were obtained assuming different values of $\alpha_s(M_Z)$: 0.113, 0.118 and 0.123. In each of these calculations, the value of $\alpha_s(M_Z)$ used in the partonic cross section was the one associated with the corresponding set of PDFs. The renormalization and factorization scales were set equal to $\mu_R = \mu_F = Q$;

- for each value of Q^2, the NLO QCD calculations mentioned above, corrected for hadronisations effects, were used to parameterise the $\alpha_s(M_Z)$-dependence of the dijet fraction according to the functional form:

$$R_{2+1}(Q^2, \alpha_s(M_Z)) = A_1(Q^2) \cdot \alpha_s(M_Z) + A_2(Q^2) \cdot \alpha_s^2(M_Z) \tag{6.4}$$

  a parameterisation that allows a simple description of the $\alpha_s(M_Z)$-dependence of $R_{2+1}(Q^2)$ over the entire $\alpha_s(M_Z)$-range spanned by the MBFIT PDF sets, while using only three NLO calculations of the dijet fraction. Its validity rests only on the assumption of a smooth behaviour of $R_{2+1}(Q^2)$ in the considered $\alpha_s(M_Z)$-range. The parameterisation of $R_{2+1}(Q^2, \alpha_s(M_Z))$, together with the NLO calculations used to obtain it, is presented for each Q^2 bin in Fig. 6.4;

- the value of $\alpha_s(M_Z)$ was then determined by a χ^2-fit of the parameterisation of Eq. 6.4 to the measured $R_{2+1}(Q^2)$.

This procedure provides for the correct handling of the complete $\alpha_s(M_Z)$-dependence of the NLO differential cross sections (the explicit dependence coming from the partonic cross sections and the implicit one coming from the PDFs) during the fit, while preserving the built-in correlation between $\alpha_s(M_Z)$ and the PDFs. Its stability was checked with respect to variations in the PDFs and $\alpha_s(M_Z)$, as well as alternative parameterisations of $R_{2+1}(Q^2, \alpha_s(M_Z))$ (see below).

Taking into account only the statistical errors on the measured dijet fraction, the result of the fit is:

$$\alpha_s(M_Z) = 0.1166 \pm 0.0019 \text{ (stat)} \tag{6.5}$$

The uncertainty on the value of $\alpha_s(M_Z)$ due to the experimental systematic uncertainties of the measured dijet rate was evaluated by repeating the analysis above for each systematic check. In the ratio $R_{2+1}(Q^2)$ some of the systematic uncertainties largely cancel. The individual uncertainties were added in quadrature to give a total experimental systematic uncertainty on the value of $\alpha_s(M_Z)$ of $^{+0.0024}_{-0.0033}$. This uncertainty is mostly dominated by the uncertainty on the jet energy-scale.

The following sources of theoretical uncertainties and cross-checks on the extracted value of $\alpha_s(M_Z)$ were considered:

- missing higher-order terms: they were estimated by repeating the analysis using $\mu_R = Q/2$ and $\mu_R = 2Q$. The factorization scale was kept fixed to $\mu_F = Q$. The resulting values are $\alpha_s(M_Z) = 0.1124 \pm 0.0020$ ($\mu_R = Q/2$) and $\alpha_s(M_Z) = 0.1221 \pm 0.0018$ ($\mu_R = 2Q$);

- uncertainties in the proton PDFs: they were estimated by repeating the fit using DISENT calculations obtained from the central ones by offsetting the latter according to the total

PDF-related uncertainty on the dijet fraction. The resulting uncertainty in the value of $\alpha_s(M_Z)$ is $^{+0.0012}_{-0.0011}$;

- uncertainty on the hadronisation effects: this was estimated by repeating the QCD fit taking into account the uncertainty on the hadronisation correction factors estimated as half the spread between the results obtained from the string and cluster hadronisation models. The resulting uncertainty on $\alpha_s(M_Z)$ is ± 0.0005.

- the dependence of the result on the use of a renormalization scale that involves the jet variables: the analysis was repeated with $\mu_R = (E_{TB}^{jet,1} + E_{TB}^{jet,2})$. The result is $\alpha_s(M_Z) = 0.1125 \pm 0.0018$ (stat), which is essentially identical to that obtained with $\mu_R = Q/2$. For this reason, this was not included in the total theoretical uncertainty;

- the fit procedure: this was cross-checked by repeating the $\alpha_s(M_Z)$ determination using the five (three) sets of proton PDFs of the CTEQ4- (MRST)-α_s series; the resulting parameterisations of $R_{2+1}(Q^2, \alpha_s(M_Z))$ are shown in Fig. 6.5 and Fig. 6.6. The results are: $\alpha_s(M_Z) = 0.1159 \pm 0.0021$ (stat) (CTEQ4) and $\alpha_s(M_Z) = 0.1161 \pm 0.0020$ (stat) (MRST). Both are in good agreement with the central value determined above. As an additional cross-check the fit was repeated assuming a linear (instead of a quadratic) ansazt for the Eq. (6.4); the resulting $\alpha_s(M_Z)$ was essentially identical to the central value quoted above.

The total theoretical uncertainty was obtained by adding in quadrature the uncorrelated uncertainties on $\alpha_s(M_Z)$ due to the first three items mentioned above and amounts to $^{+0.0057}_{-0.0044}$.

The value of $\alpha_s(M_Z)$ as determined from the measured $R_{2+1}(Q^2)$ is therefore:

$$\alpha_s(M_Z) = 0.1166 \pm 0.0019 \text{ (stat.)}^{+0.0024}_{-0.0033} \text{ (exp.)}^{+0.0057}_{-0.0044} \text{ (th.)} \qquad (6.6)$$

This result is consistent with the current PDG world average, $\alpha_s(M_Z) = 0.1181 \pm 0.0020$ [22], a review from Bethke [23], and recent determinations by the H1 Collaboration [24].

6.2.2   The energy scale dependence of α_s

A consistency test for the scale dependence of the renormalised strong coupling constant predicted by the renormalisation group equation was carried out by repeating the QCD fit of the dijet fraction in five Q^2 bins. The principle of the fit is the same as outlined above, with the only difference being that the α_s dependence of the dijet fraction in Eq. (6.4) was parameterised not in terms of $\alpha_s(M_Z)$ but in terms of $\alpha_s(\langle Q \rangle)$, where $\langle Q \rangle$ is the mean value of Q in each bin. The measured $\alpha_s(\langle Q \rangle)$ values, with their experimental and theoretical systematic uncertainties estimated as for $\alpha_s(M_Z)$, are shown in Fig. 6.7 and Table 6.23. The measurements are compared with the renormalisation group predictions obtained from the PDG $\alpha_s(M_Z)$ value and its associated uncertainty. The values are in good agreement with the predicted running of the strong coupling constant over a large range in Q.

6.3   Summary

Differential dijet cross sections have been measured in neutral current deep inelastic e^+p scattering for $470 < Q^2 < 20000$ GeV^2 with the ZEUS detector at HERA. The measurements were performed in a kinematic region where both theoretical and experimental uncertainties are small. Next-to-leading-order QCD calculations give a good description of the shape and magnitude of the measurements; the observed agreement is a non-trivial test of NLO pQCD predictions and demonstrates the validity of the description of dijet production by the underlying QCD hard

processes (up to $O(\alpha_s^2)$) at the $\approx 10\%$ level. A QCD fit of the measured dijet fraction as a function of Q^2 allows both a precise determination of the strong coupling constant and a test of its energy-scale dependence. A comprehensive analysis of the uncertainties of the calculations has been carried out which takes into account the dependence of the proton PDFs on the assumed value of α_s and the statistical and correlated systematic uncertainties from each data set used in the determination of the proton PDFs. The value of $\alpha_s(M_Z)$ as determined by fitting the measured dijet fraction with next-to-leading-order QCD calculations is:

$$\alpha_s(M_Z) = 0.1166 \pm 0.0019 \text{ (stat.)}^{+0.0024}_{-0.0033} \text{ (exp.)}^{+0.0057}_{-0.0044} \text{ (th.) },$$

in good agreement with the PDG world average. The value of α_s as a function of Q is in good agreement, over a wide range of Q, with the running of α_s as predicted by QCD.

ZEUS
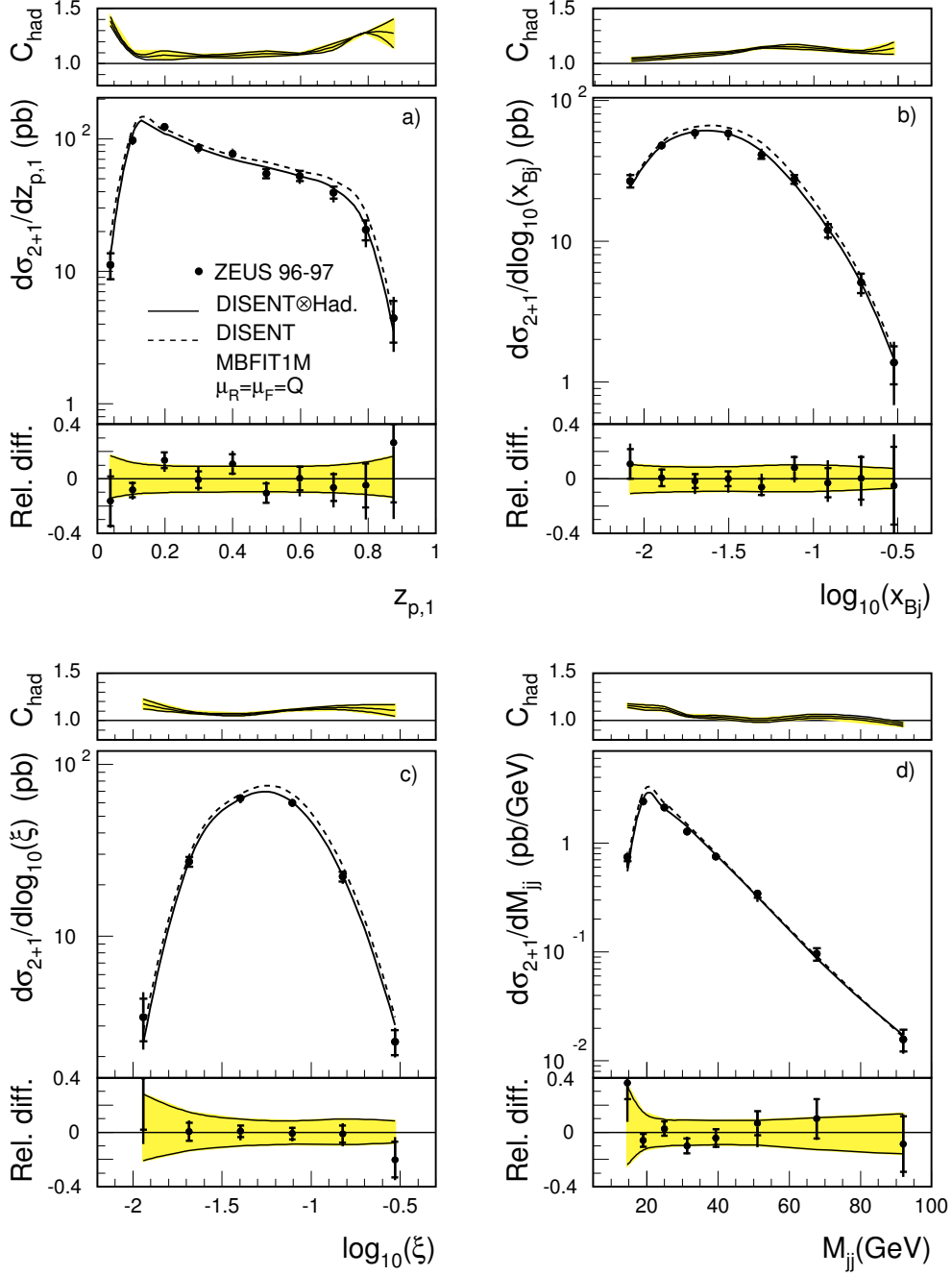
Figure 6.1: The measured differential dijet cross sections in NC DIS as functions of a) $z_{p,1}$, b) $\log_{10} x_{Bj}$, c) $\log_{10} \xi$ and d) dijet invariant mass M_{jj}. The inner error bars represent the statistical errors of the data. The outer error bars show the statistical errors and systematic uncertainties − except those associated with the uncertainty in the absolute energy scale of the jets − added in quadrature. For comparison, pure NLO QCD calculations (dashed lines) and NLO QCD calculations corrected for hadronisation effects (solid lines), obtained using the proton MBFIT PDFs and $\mu_R = \mu_F = Q$, are shown. The relative differences of the measured differential cross sections over the NLO QCD predictions corrected for hadronisation effects are shown underneath each plot; the shaded band represents the uncertainty of the QCD calculation (see text). The hadronisation correction (C_{had}) together with its uncertainty are shown above each plot.
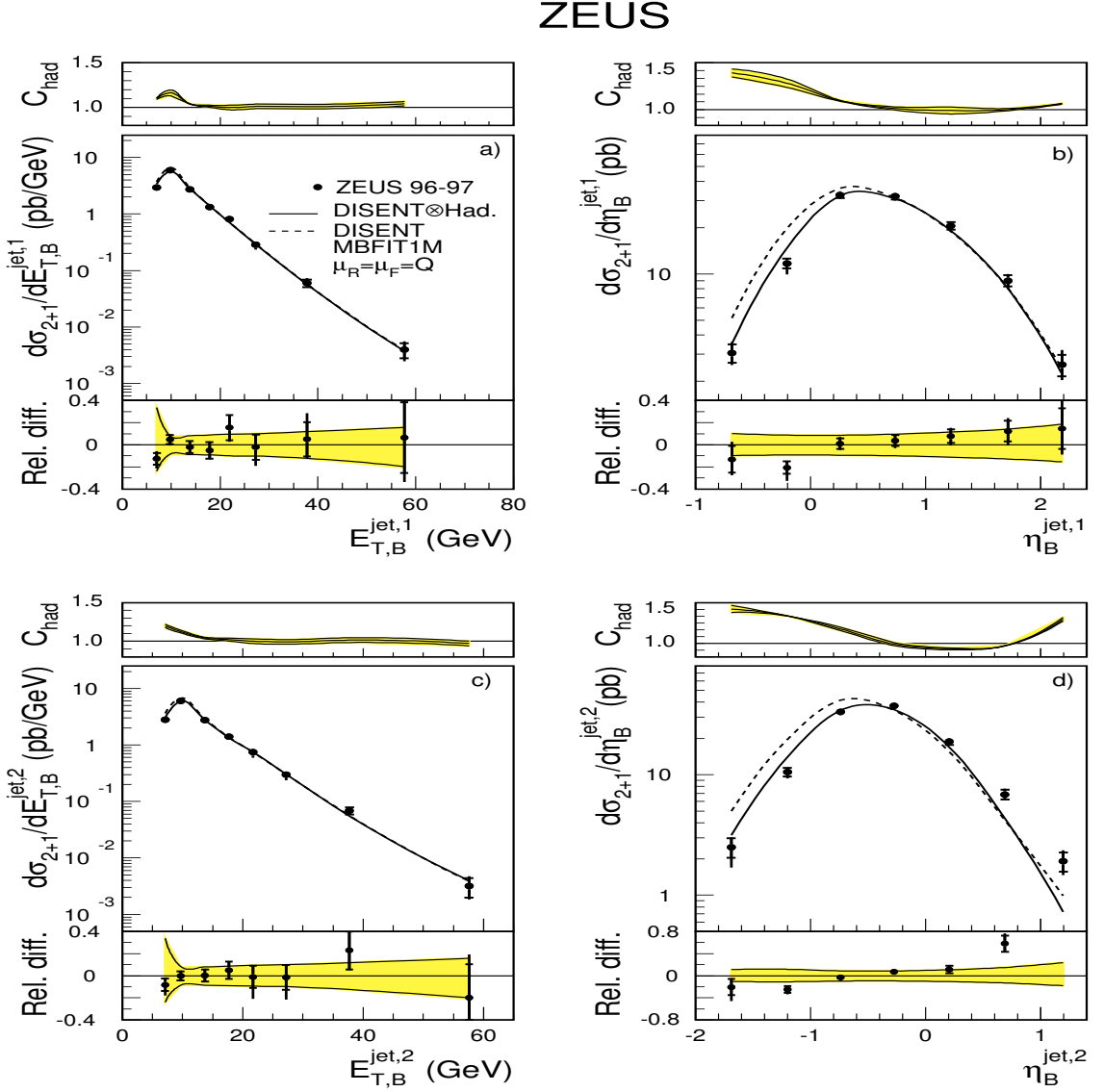
ZEUS

Figure 6.2: The measured differential dijet cross sections in NC DIS as functions of a) $E_{T,B}^{\mathrm{jet,1}}$, b) $\eta_B^{\mathrm{jet,1}}$, c) $E_{T,B}^{\mathrm{jet,2}}$ and d) $\eta_B^{\mathrm{jet,2}}$. Other details are as described in the caption to Fig. 6.1.
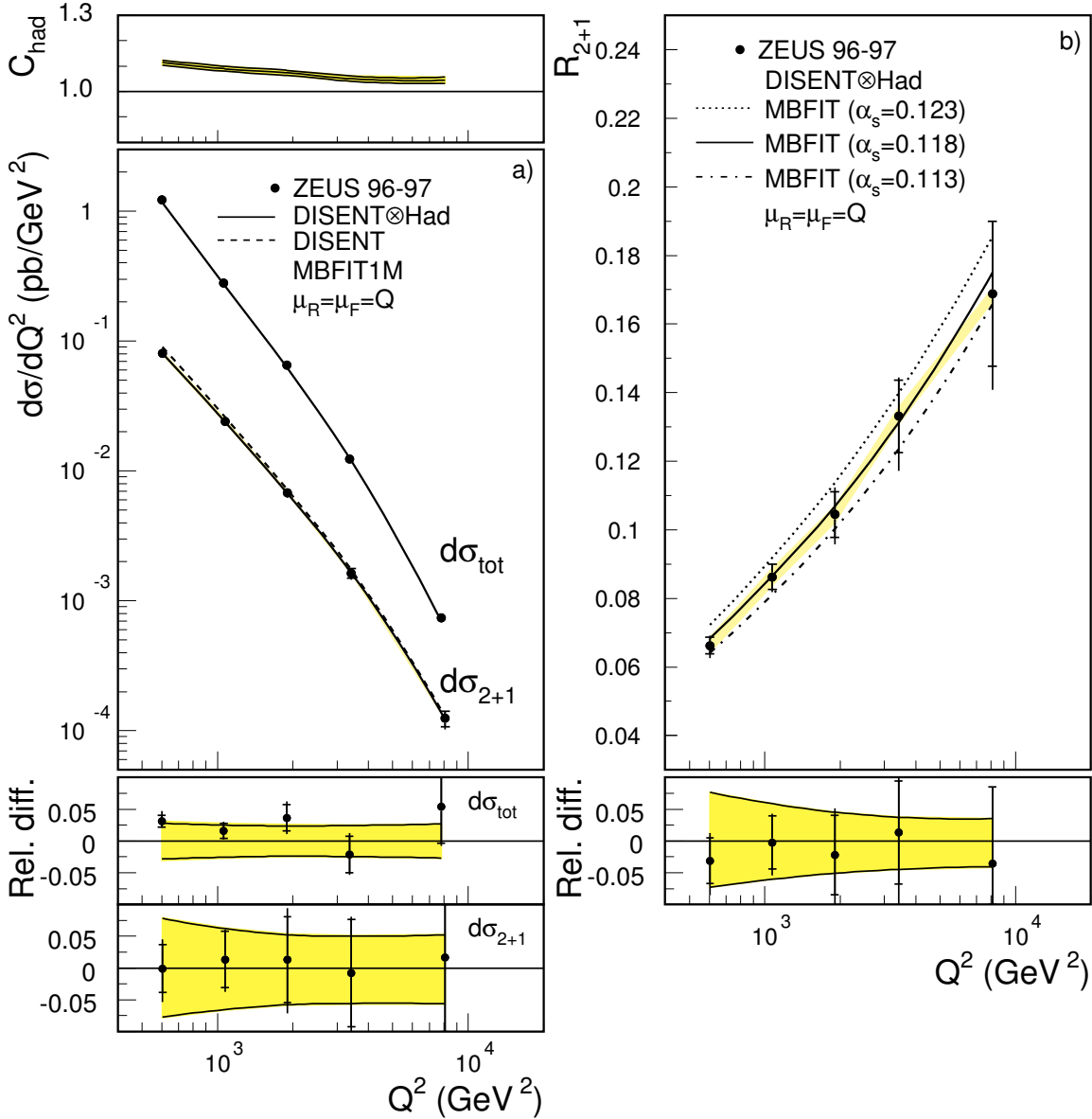
Figure 6.3: a) The measured inclusive $(d\sigma_{tot}/dQ^2)$ and dijet $(d\sigma_{2+1}/dQ^2)$ differential cross sections in NC DIS as a function of Q^2. The hadronisation correction (C_{had}), shown above the figure, refers to the dijet cross section. b) The dijet fraction, $R_{2+1}(Q^2)$, in NC DIS as a function of Q^2. The light shaded band displays the uncertainty due to the absolute energy scale of the jets. For comparison, the QCD predictions using MBFIT proton PDFs determined assuming $\alpha_s(M_Z) = 0.113$ and 0.123 [41] are also shown. The bands showing the theoretical uncertainty on the cross sections and dijet fraction do not include the uncertainty associated with $\alpha_s(M_Z)$. Other details are as described in the caption to Fig. 6.1.
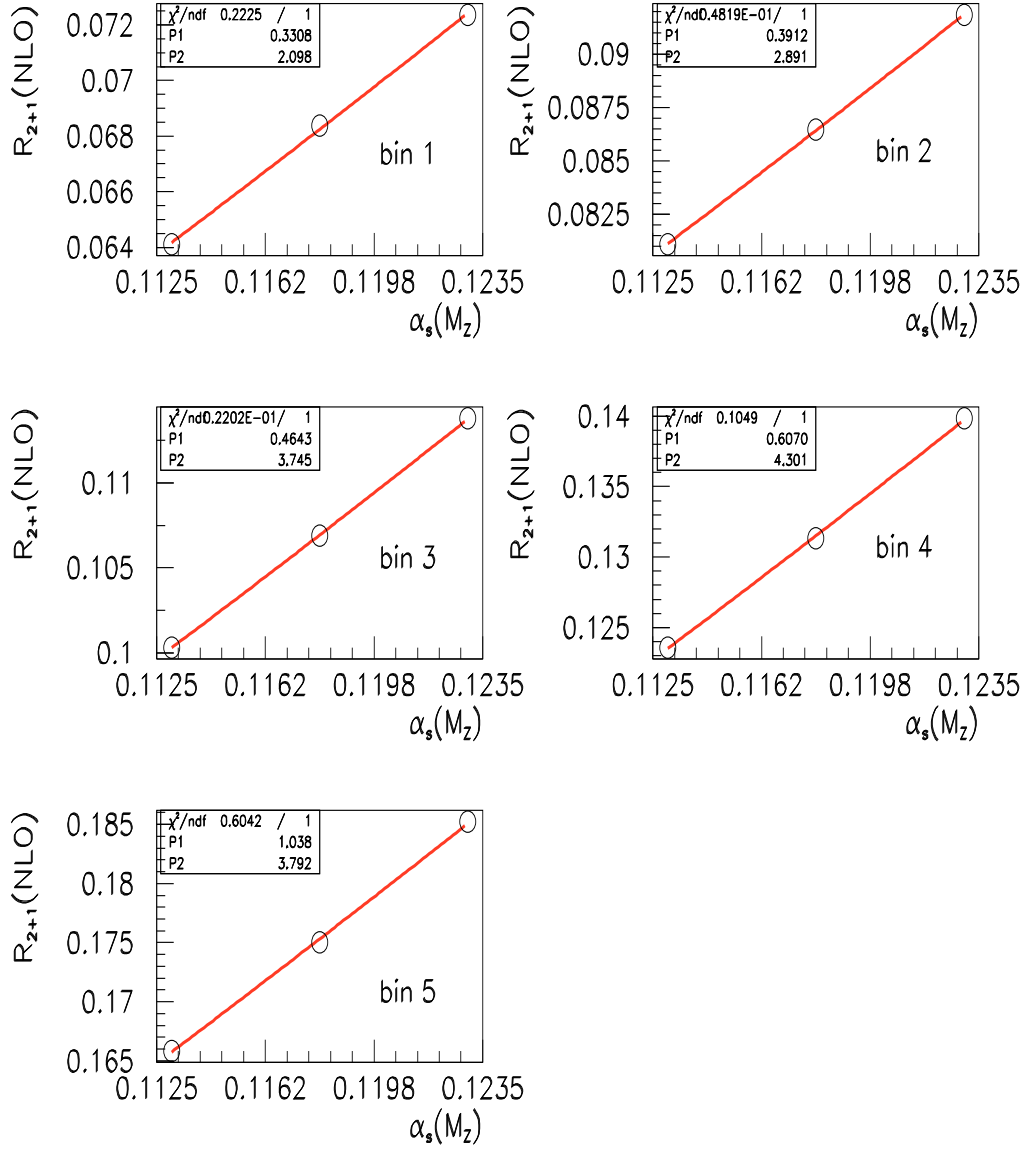
Figure 6.4: The parameterisation of the QCD predictions for $R_{2+1}(Q^2)$ as a function of $\alpha_s(M_Z)$ in different Q^2 bins. The QCD predictions are those obtained with the MBFIT α_s-series.
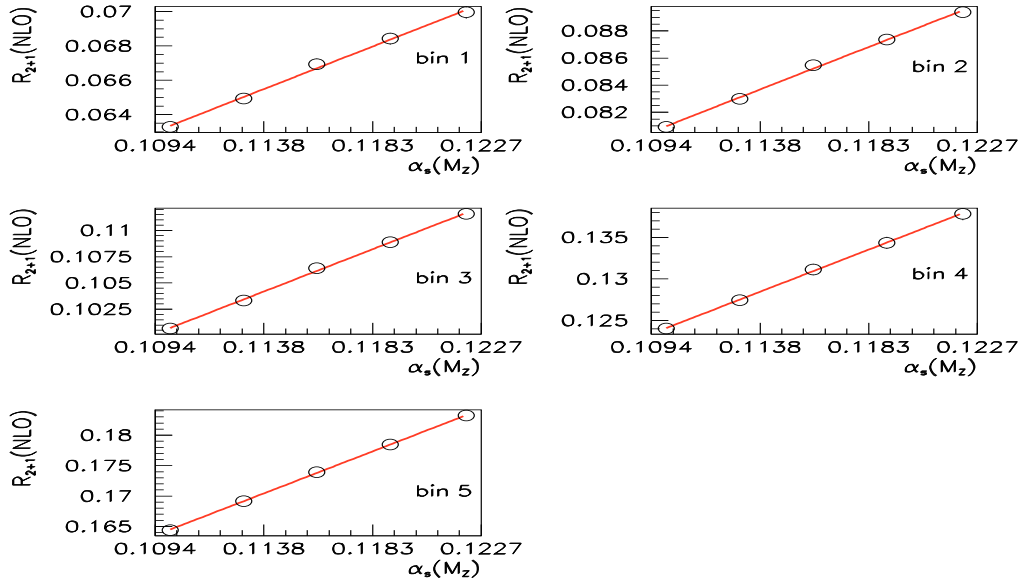
Figure 6.5: The parameterisation of the QCD predictions for $R_{2+1}(Q^2)$ as a function of $\alpha_s(M_Z)$ in different Q^2 bins. The QCD predictions are those obtained with the CTEQ4 α_s-series.
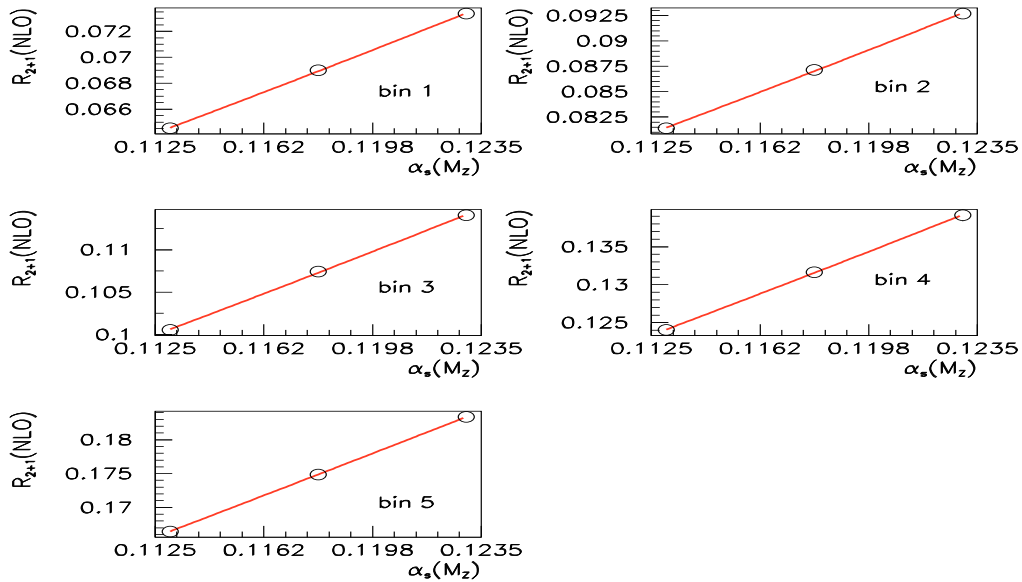
Figure 6.6: The parameterisation of the QCD predictions for $R_{2+1}(Q^2)$ as a function of $\alpha_s(M_Z)$ in different Q^2 bins. The QCD predictions are those obtained with the MRST α_s-series.

ZEUS
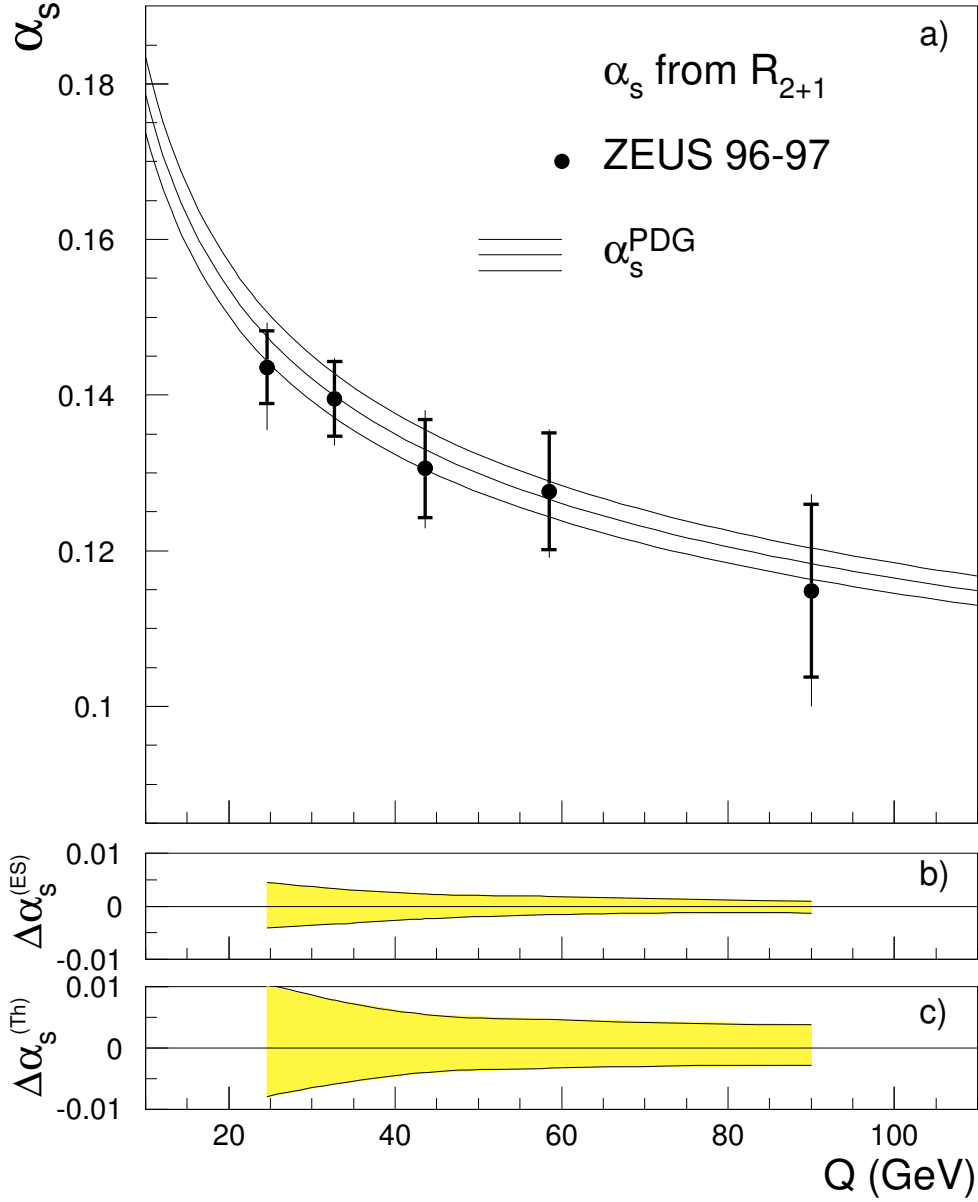
Figure 6.7: a) The $\alpha_s(Q)$ values determined from the QCD fit of the measured dijet fraction, $R_{2+1}(Q^2)$, as a function of Q. The inner error bars represent the statistical errors of the data. The outer error bars show the statistical errors and systematic uncertainties − except those associated with the uncertainty in the absolute energy scale of the jets − added in quadrature. The three curves indicate the renormalisation group predictions obtained from the PDG $\alpha_s(M_Z)$ value and its associated uncertainty. b) The uncertainty on α_s due to the absolute energy scale of the jets, $\Delta\alpha_s^{ES}$. c) The total theoretical uncertainty associated with the determination of α_s, $\Delta\alpha_s^{\mathrm{Th}}$.

$z_{p,1}$ range	$d\sigma_{2+1}/dz_{p,1}$ [pb]	Δ_{stat}	Δ_{syst}	Δ_{ES}
$0.00 - 0.05$	$1.118 \cdot 10^1$	$(\pm 0.244) \cdot 10^1$	$\left(^{+0.203}_{-0.097}\right) \cdot 10^1$	$\left(^{+0.089}_{-0.089}\right) \cdot 10^1$
$0.05 - 0.15$	$9.777 \cdot 10^1$	$(\pm 0.555) \cdot 10^1$	$\left(^{+0.365}_{-0.519}\right) \cdot 10^1$	$\left(^{+0.365}_{-0.400}\right) \cdot 10^1$
$0.15 - 0.25$	$1.233 \cdot 10^2$	$(\pm 0.063) \cdot 10^2$	$\left(^{+0.024}_{-0.068}\right) \cdot 10^2$	$\left(^{+0.038}_{-0.033}\right) \cdot 10^2$
$0.25 - 0.35$	$8.469 \cdot 10^1$	$(\pm 0.520) \cdot 10^1$	$\left(^{+0.625}_{-0.482}\right) \cdot 10^1$	$\left(^{+0.207}_{-0.158}\right) \cdot 10^1$
$0.35 - 0.45$	$7.738 \cdot 10^1$	$(\pm 0.505) \cdot 10^1$	$\left(^{+0.425}_{-0.268}\right) \cdot 10^1$	$\left(^{+0.170}_{-0.144}\right) \cdot 10^1$
$0.45 - 0.55$	$5.473 \cdot 10^1$	$(\pm 0.438) \cdot 10^1$	$\left(^{+0.288}_{-0.145}\right) \cdot 10^1$	$\left(^{+0.125}_{-0.133}\right) \cdot 10^1$
$0.55 - 0.65$	$5.259 \cdot 10^1$	$(\pm 0.453) \cdot 10^1$	$\left(^{+0.156}_{-0.525}\right) \cdot 10^1$	$\left(^{+0.138}_{-0.148}\right) \cdot 10^1$
$0.65 - 0.75$	$3.938 \cdot 10^1$	$(\pm 0.415) \cdot 10^1$	$\left(^{+0.240}_{-0.451}\right) \cdot 10^1$	$\left(^{+0.167}_{-0.135}\right) \cdot 10^1$
$0.75 - 0.85$	$2.064 \cdot 10^1$	$(\pm 0.349) \cdot 10^1$	$\left(^{+0.076}_{-0.416}\right) \cdot 10^1$	$\left(^{+0.135}_{-0.137}\right) \cdot 10^1$
$0.85 - 0.95$	4.436	± 1.537	$^{+1.261}_{-1.232}$	$^{+0.522}_{-0.325}$

Table 6.1: The differential dijet cross section $d\sigma_{2+1}/dz_{p,1}$. For each bin in $z_{p,1}$, the measured cross section, the statistical uncertainty, Δ_{stat}, and the systematic uncertainty (not) associated with the energy scale of the jets, Δ_{ES} (Δ_{syst}), are given. The overall normalisation uncertainty of 1.6% due to the luminosity determination is not included.

$\log_{10}(x_{Bj})$ range	$d\sigma_{2+1}/d\log_{10}(x_{Bj})$ [pb]	Δ_{stat}	Δ_{syst}	Δ_{ES}
-2.20 − -2.00	$2.681 \cdot 10^1$	$(\pm 0.267) \cdot 10^1$	$\left(^{+0.241}_{-0.093}\right) \cdot 10^1$	$\left(^{+0.072}_{-0.064}\right) \cdot 10^1$
-2.00 − -1.80	$4.794 \cdot 10^1$	$(\pm 0.286) \cdot 10^1$	$\left(^{+0.139}_{-0.118}\right) \cdot 10^1$	$\left(^{+0.114}_{-0.115}\right) \cdot 10^1$
-1.80 − -1.60	$5.902 \cdot 10^1$	$(\pm 0.312) \cdot 10^1$	$\left(^{+0.143}_{-0.472}\right) \cdot 10^1$	$\left(^{+0.162}_{-0.166}\right) \cdot 10^1$
-1.60 − -1.40	$5.821 \cdot 10^1$	$(\pm 0.319) \cdot 10^1$	$\left(^{+0.110}_{-0.497}\right) \cdot 10^1$	$\left(^{+0.175}_{-0.180}\right) \cdot 10^1$
-1.40 − -1.20	$4.105 \cdot 10^1$	$(\pm 0.263) \cdot 10^1$	$\left(^{+0.341}_{-0.141}\right) \cdot 10^1$	$\left(^{+0.146}_{-0.138}\right) \cdot 10^1$
-1.20 − -1.00	$2.750 \cdot 10^1$	$(\pm 0.203) \cdot 10^1$	$\left(^{+0.112}_{-0.181}\right) \cdot 10^1$	$\left(^{+0.095}_{-0.070}\right) \cdot 10^1$
-1.00 − -0.80	$1.195 \cdot 10^1$	$(\pm 0.131) \cdot 10^1$	$\left(^{+0.155}_{-0.112}\right) \cdot 10^1$	$\left(^{+0.041}_{-0.034}\right) \cdot 10^1$
-0.80 − -0.60	5.078	± 0.793	$^{+0.323}_{-0.670}$	$^{+0.176}_{-0.105}$
-0.60 − -0.40	1.373	± 0.414	$^{+0.363}_{-0.552}$	$^{+0.042}_{-0.023}$

Table 6.2: The differential dijet cross section $d\sigma_{2+1}/d\log_{10}(x_{Bj})$. Other details are as described in the caption to Table 6.1.

$\log_{10}(\xi)$ range	$d\sigma_{2+1}/d\log_{10}(\xi)$ [pb]	Δ_{stat}	Δ_{syst}	Δ_{ES}
-2.1875 – -1.8750	3.386	± 0.939	$^{+0.970}_{-0.736}$	$^{+0.093}_{-0.078}$
-1.8750 – -1.5625	$2.726 \cdot 10^1$	$(\pm 0.179) \cdot 10^1$	$\left(^{+0.126}_{-0.045}\right) \cdot 10^1$	$\left(^{+0.021}_{-0.037}\right) \cdot 10^1$
-1.5625 – -1.2500	$6.379 \cdot 10^1$	$(\pm 0.266) \cdot 10^1$	$\left(^{+0.085}_{-0.334}\right) \cdot 10^1$	$\left(^{+0.147}_{-0.136}\right) \cdot 10^1$
-1.2500 – -0.9375	$5.997 \cdot 10^1$	$(\pm 0.260) \cdot 10^1$	$\left(^{+0.156}_{-0.224}\right) \cdot 10^1$	$\left(^{+0.199}_{-0.189}\right) \cdot 10^1$
-0.9375 – -0.6250	$2.232 \cdot 10^1$	$(\pm 0.142) \cdot 10^1$	$\left(^{+0.105}_{-0.154}\right) \cdot 10^1$	$\left(^{+0.126}_{-0.108}\right) \cdot 10^1$
-0.6250 – -0.3125	2.434	± 0.400	$^{+0.305}_{-0.229}$	$^{+0.177}_{-0.123}$

Table 6.3: The differential dijet cross section $d\sigma_{2+1}/d\log_{10}(\xi)$. Other details are as described in the caption to Table 6.1.

M_{jj} range [GeV]	$d\sigma_{2+1}/dM_{jj}$ [pb/GeV]	Δ_{stat}	Δ_{syst}	Δ_{ES}
10.00 – 16.00	$7.462 \cdot 10^{-1}$	$(\pm 0.642) \cdot 10^{-1}$	$\left(^{+0.562}_{-1.434}\right) \cdot 10^{-1}$	$\left(^{+0.016}_{-0.005}\right) \cdot 10^{-1}$
16.00 – 22.00	2.404	± 0.122	$^{+0.055}_{-0.055}$	$^{+0.034}_{-0.035}$
22.00 – 28.00	2.127	± 0.109	$^{+0.048}_{-0.041}$	$^{+0.057}_{-0.053}$
28.00 – 35.00	1.272	± 0.077	$^{+0.060}_{-0.038}$	$^{+0.046}_{-0.042}$
35.00 – 45.00	$7.494 \cdot 10^{-1}$	$(\pm 0.497) \cdot 10^{-1}$	$\left(^{+0.090}_{-0.309}\right) \cdot 10^{-1}$	$\left(^{+0.256}_{-0.246}\right) \cdot 10^{-1}$
45.00 – 60.00	$3.430 \cdot 10^{-1}$	$(\pm 0.284) \cdot 10^{-1}$	$\left(^{+0.100}_{-0.484}\right) \cdot 10^{-1}$	$\left(^{+0.270}_{-0.195}\right) \cdot 10^{-1}$
60.00 – 80.00	$9.605 \cdot 10^{-2}$	$(\pm 1.272) \cdot 10^{-2}$	$\left(^{+0.326}_{-0.419}\right) \cdot 10^{-2}$	$\left(^{+0.619}_{-0.709}\right) \cdot 10^{-2}$
80.00 – 120.00	$1.578 \cdot 10^{-2}$	$(\pm 0.353) \cdot 10^{-2}$	$\left(^{+0.122}_{-0.219}\right) \cdot 10^{-2}$	$\left(^{+0.117}_{-0.145}\right) \cdot 10^{-2}$

Table 6.4: The differential dijet cross section $d\sigma_{2+1}/dM_{jj}$. Other details are as described in the caption to Table 6.1.

$E_{T,B}^{jet,1}$ range [GeV]	$d\sigma_{2+1}/dE_{T,B}^{jet,1}$ [pb/GeV]	Δ_{stat}	Δ_{syst}	Δ_{ES}
5.00 – 8.00	2.956	± 0.175	$^{+0.154}_{-0.243}$	$^{+0.072}_{-0.081}$
8.00 – 12.00	5.977	± 0.238	$^{+0.105}_{-0.201}$	$^{+0.094}_{-0.090}$
12.00 – 16.00	2.736	± 0.154	$^{+0.039}_{-0.033}$	$^{+0.083}_{-0.081}$
16.00 – 20.00	1.327	± 0.103	$^{+0.055}_{-0.030}$	$^{+0.072}_{-0.026}$
20.00 – 24.00	$8.165 \cdot 10^{-1}$	$(\pm 0.801) \cdot 10^{-1}$	$\left(^{+0.096}_{-0.397}\right) \cdot 10^{-1}$	$\left(^{+0.245}_{-0.566}\right) \cdot 10^{-1}$
24.00 – 32.00	$2.848 \cdot 10^{-1}$	$(\pm 0.333) \cdot 10^{-1}$	$\left(^{+0.077}_{-0.355}\right) \cdot 10^{-1}$	$\left(^{+0.236}_{-0.183}\right) \cdot 10^{-1}$
32.00 – 50.00	$5.960 \cdot 10^{-2}$	$(\pm 0.879) \cdot 10^{-2}$	$\left(^{+0.997}_{-0.449}\right) \cdot 10^{-2}$	$\left(^{+0.572}_{-0.497}\right) \cdot 10^{-2}$
50.00 – 80.00	$3.991 \cdot 10^{-3}$	$(\pm 1.203) \cdot 10^{-3}$	$\left(^{+1.086}_{-0.902}\right) \cdot 10^{-3}$	$\left(^{+0.548}_{-0.472}\right) \cdot 10^{-3}$

Table 6.5: The differential dijet cross section $d\sigma_{2+1}/dE_{T,B}^{jet,1}$. Other details are as described in the caption to Table 6.1.

$\eta_B^{jet,1}$ range	$d\sigma_{2+1}/d\eta_B^{jet,1}$ [pb]	Δ_{stat}	Δ_{syst}	Δ_{ES}
-1.00 – -0.50	3.051	±0.419	$^{+0.360}_{-0.277}$	$^{+0.155}_{-0.141}$
-0.50 – 0.00	$1.170 \cdot 10^1$	$(\pm0.084) \cdot 10^1$	$(^{+0.025}_{-0.158}) \cdot 10^1$	$(^{+0.060}_{-0.051}) \cdot 10^1$
0.00 – 0.50	$3.260 \cdot 10^1$	$(\pm0.154) \cdot 10^1$	$(^{+0.116}_{-0.105}) \cdot 10^1$	$(^{+0.102}_{-0.091}) \cdot 10^1$
0.50 – 1.00	$3.204 \cdot 10^1$	$(\pm0.151) \cdot 10^1$	$(^{+0.084}_{-0.147}) \cdot 10^1$	$(^{+0.068}_{-0.075}) \cdot 10^1$
1.00 – 1.50	$2.054 \cdot 10^1$	$(\pm0.119) \cdot 10^1$	$(^{+0.083}_{-0.104}) \cdot 10^1$	$(^{+0.046}_{-0.049}) \cdot 10^1$
1.50 – 2.00	9.035	±0.748	$^{+0.570}_{-0.742}$	$^{+0.229}_{-0.194}$
2.00 – 2.50	2.561	±0.410	$^{+0.491}_{-0.324}$	$^{+0.061}_{-0.058}$

Table 6.6: The differential dijet cross section $d\sigma_{2+1}/d\eta_B^{jet,1}$. Other details are as described in the caption to Table 6.1.

$E_{T,B}^{jet,2}$ range [GeV]	$d\sigma_{2+1}/dE_{T,B}^{jet,2}$ [pb/GeV]	Δ_{stat}	Δ_{syst}	Δ_{ES}
5.00 – 8.00	2.775	±0.168	$^{+0.098}_{-0.235}$	$^{+0.074}_{-0.082}$
8.00 – 12.00	5.971	±0.240	$^{+0.142}_{-0.154}$	$^{+0.103}_{-0.092}$
12.00 – 16.00	2.762	±0.152	$^{+0.074}_{-0.071}$	$^{+0.088}_{-0.076}$
16.00 – 20.00	1.403	±0.105	$^{+0.011}_{-0.034}$	$^{+0.062}_{-0.050}$
20.00 – 24.00	$7.437 \cdot 10^{-1}$	$(\pm0.763) \cdot 10^{-1}$	$(^{+0.144}_{-1.274}) \cdot 10^{-1}$	$(^{+0.397}_{-0.406}) \cdot 10^{-1}$
24.00 – 32.00	$2.995 \cdot 10^{-1}$	$(\pm0.339) \cdot 10^{-1}$	$(^{+0.070}_{-0.507}) \cdot 10^{-1}$	$(^{+0.182}_{-0.198}) \cdot 10^{-1}$
32.00 – 50.00	$6.834 \cdot 10^{-2}$	$(\pm0.966) \cdot 10^{-2}$	$(^{+0.641}_{-0.239}) \cdot 10^{-2}$	$(^{+0.551}_{-0.452}) \cdot 10^{-2}$
50.00 – 80.00	$3.189 \cdot 10^{-3}$	$(\pm1.205) \cdot 10^{-3}$	$(^{+0.981}_{-0.621}) \cdot 10^{-3}$	$(^{+0.203}_{-0.251}) \cdot 10^{-3}$

Table 6.7: The differential dijet cross section $d\sigma_{2+1}/dE_{T,B}^{jet,2}$. Other details are as described in the caption to Table 6.1.

$\eta_B^{jet,2}$ range	$d\sigma_{2+1}/d\eta_B^{jet,2}$ [pb]	Δ_{stat}	Δ_{syst}	Δ_{ES}
-2.00 – -1.50	2.507	±0.458	$^{+0.219}_{-0.670}$	$^{+0.202}_{-0.190}$
-1.50 – -1.00	$1.054 \cdot 10^1$	$(\pm0.084) \cdot 10^1$	$(^{+0.043}_{-0.084}) \cdot 10^1$	$(^{+0.069}_{-0.067}) \cdot 10^1$
-1.00 – -0.50	$3.328 \cdot 10^1$	$(\pm0.151) \cdot 10^1$	$(^{+0.080}_{-0.170}) \cdot 10^1$	$(^{+0.154}_{-0.134}) \cdot 10^1$
-0.50 – 0.00	$3.735 \cdot 10^1$	$(\pm0.163) \cdot 10^1$	$(^{+0.067}_{-0.130}) \cdot 10^1$	$(^{+0.073}_{-0.066}) \cdot 10^1$
0.00 – 0.50	$1.885 \cdot 10^1$	$(\pm0.112) \cdot 10^1$	$(^{+0.062}_{-0.066}) \cdot 10^1$	$(^{+0.012}_{-0.014}) \cdot 10^1$
0.50 – 1.00	6.868	±0.627	$^{+0.504}_{-0.252}$	$^{+0.070}_{-0.080}$
1.00 – 1.50	1.914	±0.349	$^{+0.288}_{-0.273}$	$^{+0.066}_{-0.057}$

Table 6.8: The differential dijet cross section $d\sigma_{2+1}/d\eta_B^{jet,2}$. Other details are as described in the caption to Table 6.1.

Q^2 range [GeV^2]	$d\sigma_{\rm tot}/dQ^2$ [pb/GeV^2]	$\Delta_{\rm stat}$	$\Delta_{\rm syst}$
$470. - 800.$	1.217	± 0.011	$^{+0.015}_{-0.006}$
$800. - 1500.$	$2.800 \cdot 10^{-1}$	$(\pm 0.033) \cdot 10^{-1}$	$\left(^{+0.023}_{-0.019}\right) \cdot 10^{-1}$
$1500. - 2500.$	$6.509 \cdot 10^{-2}$	$(\pm 0.130) \cdot 10^{-2}$	$\left(^{+0.103}_{-0.090}\right) \cdot 10^{-2}$
$2500. - 5000.$	$1.230 \cdot 10^{-2}$	$(\pm 0.036) \cdot 10^{-2}$	$\left(^{+0.022}_{-0.020}\right) \cdot 10^{-2}$
$5000. - 20000.$	$7.378 \cdot 10^{-4}$	$(\pm 0.400) \cdot 10^{-4}$	$\left(^{+0.051}_{-0.163}\right) \cdot 10^{-4}$

Table 6.9: The differential inclusive cross section $d\sigma_{\rm tot}/dQ^2$. Other details are as described in the caption to Table 6.1.

Q^2 range [GeV^2]	$d\sigma_{2+1}/dQ^2$ [pb/GeV^2]	$\Delta_{\rm stat}$	$\Delta_{\rm syst}$	$\Delta_{\rm ES}$
$470. - 800.$	$8.061 \cdot 10^{-2}$	$(\pm 0.306) \cdot 10^{-2}$	$\left(^{+0.212}_{-0.294}\right) \cdot 10^{-2}$	$\left(^{+0.287}_{-0.256}\right) \cdot 10^{-2}$
$800. - 1500.$	$2.415 \cdot 10^{-2}$	$(\pm 0.105) \cdot 10^{-2}$	$\left(^{+0.039}_{-0.061}\right) \cdot 10^{-2}$	$\left(^{+0.071}_{-0.072}\right) \cdot 10^{-2}$
$1500. - 2500.$	$6.802 \cdot 10^{-3}$	$(\pm 0.453) \cdot 10^{-3}$	$\left(^{+0.300}_{-0.343}\right) \cdot 10^{-3}$	$\left(^{+0.159}_{-0.160}\right) \cdot 10^{-3}$
$2500. - 5000.$	$1.637 \cdot 10^{-3}$	$(\pm 0.139) \cdot 10^{-3}$	$\left(^{+0.046}_{-0.124}\right) \cdot 10^{-3}$	$\left(^{+0.033}_{-0.028}\right) \cdot 10^{-3}$
$5000. - 20000.$	$1.246 \cdot 10^{-4}$	$(\pm 0.170) \cdot 10^{-4}$	$\left(^{+0.006}_{-0.139}\right) \cdot 10^{-4}$	$\left(^{+0.013}_{-0.018}\right) \cdot 10^{-4}$

Table 6.10: The differential dijet cross section $d\sigma_{2+1}/dQ^2$. Other details are as described in the caption to Table 6.1.

Q^2 range [GeV^2]	R_{2+1}	$\Delta_{\rm stat}$	$\Delta_{\rm syst}$	$\Delta_{\rm ES}$
$470. - 800.$	$6.625 \cdot 10^{-2}$	$(\pm 0.245) \cdot 10^{-2}$	$\left(^{+0.168}_{-0.278}\right) \cdot 10^{-2}$	$\left(^{+0.236}_{-0.210}\right) \cdot 10^{-2}$
$800. - 1500.$	$8.627 \cdot 10^{-2}$	$(\pm 0.362) \cdot 10^{-2}$	$\left(^{+0.144}_{-0.267}\right) \cdot 10^{-2}$	$\left(^{+0.255}_{-0.256}\right) \cdot 10^{-2}$
$1500. - 2500.$	$1.045 \cdot 10^{-1}$	$(\pm 0.066) \cdot 10^{-1}$	$\left(^{+0.043}_{-0.057}\right) \cdot 10^{-1}$	$\left(^{+0.024}_{-0.025}\right) \cdot 10^{-1}$
$2500. - 5000.$	$1.331 \cdot 10^{-1}$	$(\pm 0.106) \cdot 10^{-1}$	$\left(^{+0.039}_{-0.119}\right) \cdot 10^{-1}$	$\left(^{+0.027}_{-0.023}\right) \cdot 10^{-1}$
$5000. - 20000.$	$1.688 \cdot 10^{-1}$	$(\pm 0.211) \cdot 10^{-1}$	$\left(^{+0.008}_{-0.185}\right) \cdot 10^{-1}$	$\left(^{+0.017}_{-0.024}\right) \cdot 10^{-1}$

Table 6.11: The dijet fraction $R_{2+1}(Q^2)$. Other details are as described in the caption to Table 6.1.

$z_{p,1}$ range	$< z_{p,1} >$	$d\sigma_{2+1}^{NLO}/dz_{p,1}$ [pb]	Δ_{μ_r}	Δ_{α_s}	$\Delta_{pdf}^{\mathrm{exp}}$	$\Delta_{pdf}^{\mathrm{theo}}$	$C_{\mathrm{had}} \pm \Delta C_{\mathrm{had}}$
$0.00 - 0.05$	0.04	$1.854 \cdot 10^1$	$\left(^{+0.256}_{-0.197}\right) \cdot 10^1$	$\left(^{+0.147}_{-0.143}\right) \cdot 10^1$	$(\pm 0.105) \cdot 10^1$	$\left(^{+0.023}_{-0.027}\right) \cdot 10^1$	1.38 ± 0.04
$0.05 - 0.15$	0.10	$1.172 \cdot 10^2$	$\left(^{+0.100}_{-0.088}\right) \cdot 10^2$	$\left(^{+0.078}_{-0.082}\right) \cdot 10^2$	$(\pm 0.060) \cdot 10^2$	$\left(^{+0.014}_{-0.014}\right) \cdot 10^2$	1.10 ± 0.01
$0.15 - 0.25$	0.20	$1.167 \cdot 10^2$	$\left(^{+0.056}_{-0.062}\right) \cdot 10^2$	$\left(^{+0.070}_{-0.075}\right) \cdot 10^2$	$(\pm 0.067) \cdot 10^2$	$\left(^{+0.015}_{-0.014}\right) \cdot 10^2$	1.08 ± 0.04
$0.25 - 0.35$	0.30	$9.100 \cdot 10^1$	$\left(^{+0.351}_{-0.432}\right) \cdot 10^1$	$\left(^{+0.542}_{-0.577}\right) \cdot 10^1$	$(\pm 0.529) \cdot 10^1$	$\left(^{+0.120}_{-0.118}\right) \cdot 10^1$	1.07 ± 0.01
$0.35 - 0.45$	0.40	$7.481 \cdot 10^1$	$\left(^{+0.280}_{-0.349}\right) \cdot 10^1$	$\left(^{+0.454}_{-0.477}\right) \cdot 10^1$	$(\pm 0.421) \cdot 10^1$	$\left(^{+0.100}_{-0.097}\right) \cdot 10^1$	1.07 ± 0.02
$0.45 - 0.55$	0.50	$6.667 \cdot 10^1$	$\left(^{+0.275}_{-0.327}\right) \cdot 10^1$	$\left(^{+0.403}_{-0.425}\right) \cdot 10^1$	$(\pm 0.361) \cdot 10^1$	$\left(^{+0.089}_{-0.085}\right) \cdot 10^1$	1.09 ± 0.02
$0.55 - 0.65$	0.60	$5.711 \cdot 10^1$	$\left(^{+0.185}_{-0.250}\right) \cdot 10^1$	$\left(^{+0.339}_{-0.356}\right) \cdot 10^1$	$(\pm 0.349) \cdot 10^1$	$\left(^{+0.074}_{-0.070}\right) \cdot 10^1$	1.09 ± 0.01
$0.65 - 0.75$	0.70	$4.858 \cdot 10^1$	$\left(^{+0.219}_{-0.248}\right) \cdot 10^1$	$\left(^{+0.294}_{-0.308}\right) \cdot 10^1$	$(\pm 0.309) \cdot 10^1$	$\left(^{+0.061}_{-0.058}\right) \cdot 10^1$	1.15 ± 0.03
$0.75 - 0.85$	0.79	$2.776 \cdot 10^1$	$\left(^{+0.215}_{-0.194}\right) \cdot 10^1$	$\left(^{+0.202}_{-0.193}\right) \cdot 10^1$	$(\pm 0.168) \cdot 10^1$	$\left(^{+0.037}_{-0.036}\right) \cdot 10^1$	1.28 ± 0.00
$0.85 - 0.95$	0.88	4.466	$^{+0.573}_{-0.445}$	$^{+0.377}_{-0.318}$	± 0.265	$^{+0.049}_{-0.072}$	1.27 ± 0.13

Table 6.12: The QCD predictions for the differential dijet cross section as a function of $z_{p,1}$. For each bin in $z_{p,1}$ the following quantities are given: the weighted mean value $< z_{p,1} >$, the pure NLO QCD cross section, the uncertainty due to the renormalization scale, Δ_{μ_r}, the uncertainty due to $\alpha_s(M_Z)$, Δ_{α_s}, the uncertainty due to the proton PDFs (experimental), $\Delta_{pdf}^{\mathrm{exp}}$, the uncertainty due to the proton PDFs (theoretical), $\Delta_{pdf}^{\mathrm{theo}}$, and the hadronisation correction, C_{had}, with its associated uncertainty, ΔC_{had}.

$\log_{10}(x_{Bj})$ range	$< \log_{10}(x_{Bj}) >$	$d\sigma_{2+1}^{NLO}/d\log_{10}(x_{Bj})$ [pb]	Δ_{μ_r}	Δ_{α_s}	Δ_{pdf}^{exp}	Δ_{pdf}^{theo}	$C_{had} \pm \Delta C_{had}$
$-2.2 - -2.0$	-2.08	$2.509 \cdot 10^1$	$\left(^{+0.184}_{-0.173}\right) \cdot 10^1$	$\left(^{+0.121}_{-0.157}\right) \cdot 10^1$	$(\pm 0.140) \cdot 10^1$	$\left(^{+0.036}_{-0.040}\right) \cdot 10^1$	1.04 ± 0.02
$-2.0 - -1.8$	-1.90	$5.025 \cdot 10^1$	$\left(^{+0.285}_{-0.297}\right) \cdot 10^1$	$\left(^{+0.246}_{-0.311}\right) \cdot 10^1$	$(\pm 0.248) \cdot 10^1$	$\left(^{+0.064}_{-0.072}\right) \cdot 10^1$	1.06 ± 0.01
$-1.8 - -1.6$	-1.70	$6.477 \cdot 10^1$	$\left(^{+0.336}_{-0.361}\right) \cdot 10^1$	$\left(^{+0.363}_{-0.419}\right) \cdot 10^1$	$(\pm 0.256) \cdot 10^1$	$\left(^{+0.076}_{-0.078}\right) \cdot 10^1$	1.08 ± 0.02
$-1.6 - -1.4$	-1.50	$6.403 \cdot 10^1$	$\left(^{+0.311}_{-0.341}\right) \cdot 10^1$	$\left(^{+0.423}_{-0.436}\right) \cdot 10^1$	$(\pm 0.205) \cdot 10^1$	$\left(^{+0.079}_{-0.068}\right) \cdot 10^1$	1.10 ± 0.01
$-1.4 - -1.2$	-1.31	$5.003 \cdot 10^1$	$\left(^{+0.247}_{-0.266}\right) \cdot 10^1$	$\left(^{+0.377}_{-0.353}\right) \cdot 10^1$	$(\pm 0.165) \cdot 10^1$	$\left(^{+0.072}_{-0.059}\right) \cdot 10^1$	1.14 ± 0.01
$-1.2 - -1.0$	-1.11	$2.935 \cdot 10^1$	$\left(^{+0.148}_{-0.155}\right) \cdot 10^1$	$\left(^{+0.231}_{-0.201}\right) \cdot 10^1$	$(\pm 0.122) \cdot 10^1$	$\left(^{+0.044}_{-0.037}\right) \cdot 10^1$	1.15 ± 0.02
$-1.0 - -0.8$	-0.91	$1.391 \cdot 10^1$	$\left(^{+0.070}_{-0.071}\right) \cdot 10^1$	$\left(^{+0.100}_{-0.083}\right) \cdot 10^1$	$(\pm 0.064) \cdot 10^1$	$\left(^{+0.017}_{-0.017}\right) \cdot 10^1$	1.13 ± 0.01
$-0.8 - -0.6$	-0.72	5.604	$^{+0.283}_{-0.282}$	$^{+0.322}_{-0.263}$	± 0.244	$^{+0.041}_{-0.069}$	1.11 ± 0.01
$-0.6 - -0.4$	-0.52	1.650	$^{+0.088}_{-0.082}$	$^{+0.061}_{-0.051}$	± 0.062	$^{+0.000}_{-0.023}$	1.14 ± 0.05

Table 6.13: The QCD predictions for the differential dijet cross section as a function of $\log_{10}(x_{Bj})$. Other details are as described in the caption to Table 6.12.

$\log_{10}(\xi)$ range	$< \log_{10}(\xi) >$	$d\sigma_{2+1}^{NLO}/d\log_{10}(\xi)$ [pb]	Δ_{μ_r}	Δ_{α_s}	Δ_{pdf}^{exp}	Δ_{pdf}^{theo}	$C_{had} \pm \Delta C_{had}$
$-2.1875 - -1.8750$	-1.94	2.825	$^{+0.737}_{-0.503}$	$^{+0.233}_{-0.258}$	± 0.166	$^{+0.047}_{-0.051}$	1.18 ± 0.05
$-1.8750 - -1.5625$	-1.68	$2.951 \cdot 10^1$	$\left(^{+0.363}_{-0.290}\right) \cdot 10^1$	$\left(^{+0.167}_{-0.205}\right) \cdot 10^1$	$(\pm 0.180) \cdot 10^1$	$\left(^{+0.043}_{-0.048}\right) \cdot 10^1$	1.09 ± 0.01
$-1.5625 - -1.2500$	-1.40	$6.736 \cdot 10^1$	$\left(^{+0.416}_{-0.416}\right) \cdot 10^1$	$\left(^{+0.372}_{-0.434}\right) \cdot 10^1$	$(\pm 0.318) \cdot 10^1$	$\left(^{+0.075}_{-0.076}\right) \cdot 10^1$	1.06 ± 0.01
$-1.2500 - -0.9375$	-1.11	$6.746 \cdot 10^1$	$\left(^{+0.198}_{-0.282}\right) \cdot 10^1$	$\left(^{+0.453}_{-0.448}\right) \cdot 10^1$	$(\pm 0.273) \cdot 10^1$	$\left(^{+0.085}_{-0.069}\right) \cdot 10^1$	1.11 ± 0.01
$-0.9375 - -0.6250$	-0.82	$2.569 \cdot 10^1$	$\left(^{+0.002}_{-0.059}\right) \cdot 10^1$	$\left(^{+0.190}_{-0.157}\right) \cdot 10^1$	$(\pm 0.162) \cdot 10^1$	$\left(^{+0.041}_{-0.040}\right) \cdot 10^1$	1.14 ± 0.02
$-0.6250 - -0.3125$	-0.53	3.378	$^{+0.000}_{-0.059}$	$^{+0.177}_{-0.122}$	± 0.220	$^{+0.027}_{-0.067}$	1.11 ± 0.06

Table 6.14: The QCD predictions for the differential dijet cross section as a function of $\log_{10}(\xi)$. Other details are as described in the caption to Table 6.12.

M_{jj} range [GeV]	$< M_{jj} >$	$d\sigma_{2+1}^{NLO}/dM_{jj}$ [pb/GeV]	Δ_{μ_r}	Δ_{α_s}	$\Delta_{pdf}^{\text{exp}}$	$\Delta_{pdf}^{\text{theo}}$	$C_{\text{had}} \pm \Delta C_{\text{had}}$
10. – 16.	14.65	$6.351 \cdot 10^{-1}$	$(^{+2.017}_{-1.355}) \cdot 10^{-1}$	$(^{+0.751}_{-0.684}) \cdot 10^{-1}$	$(\pm 0.190) \cdot 10^{-1}$	$(^{+0.099}_{-0.112}) \cdot 10^{-1}$	1.16 ± 0.02
16. – 22.	19.03	2.914	$^{+0.346}_{-0.278}$	$^{+0.208}_{-0.216}$	± 0.149	$^{+0.038}_{-0.036}$	1.14 ± 0.03
22. – 28.	24.98	2.331	$^{+0.079}_{-0.104}$	$^{+0.126}_{-0.141}$	± 0.161	$^{+0.028}_{-0.026}$	1.13 ± 0.02
28. – 35.	31.32	1.487	$^{+0.000}_{-0.035}$	$^{+0.073}_{-0.083}$	± 0.112	$^{+0.017}_{-0.016}$	1.05 ± 0.01
35. – 45.	39.42	$8.119 \cdot 10^{-1}$	$(^{+0.000}_{-0.174}) \cdot 10^{-1}$	$(^{+0.403}_{-0.446}) \cdot 10^{-1}$	$(\pm 0.567) \cdot 10^{-1}$	$(^{+0.095}_{-0.091}) \cdot 10^{-1}$	1.04 ± 0.02
45. – 60.	51.11	$3.227 \cdot 10^{-1}$	$(^{+0.000}_{-0.111}) \cdot 10^{-1}$	$(^{+0.174}_{-0.179}) \cdot 10^{-1}$	$(\pm 0.223) \cdot 10^{-1}$	$(^{+0.042}_{-0.041}) \cdot 10^{-1}$	1.00 ± 0.02
60. – 80.	67.73	$9.154 \cdot 10^{-2}$	$(^{+0.216}_{-0.712}) \cdot 10^{-2}$	$(^{+0.553}_{-0.493}) \cdot 10^{-2}$	$(\pm 0.767) \cdot 10^{-2}$	$(^{+0.155}_{-0.164}) \cdot 10^{-2}$	1.05 ± 0.02
80. – 120.	92.06	$1.657 \cdot 10^{-2}$	$(^{+0.072}_{-0.182}) \cdot 10^{-2}$	$(^{+0.128}_{-0.091}) \cdot 10^{-2}$	$(\pm 0.170) \cdot 10^{-2}$	$(^{+0.040}_{-0.050}) \cdot 10^{-2}$	0.96 ± 0.02

Table 6.15: The QCD predictions for the differential dijet cross section as a function of M_{jj}. Other details are as described in the caption to Table 6.12.

$E_{T,B}^{jet,1}$ range [GeV]	$< E_{T,B}^{jet,1} >$	$d\sigma_{2+1}^{NLO}/dE_{T,B}^{jet,1}$ [pb/GeV]	Δ_{μ_r}	Δ_{α_s}	$\Delta_{pdf}^{\text{exp}}$	$\Delta_{pdf}^{\text{theo}}$	$C_{\text{had}} \pm \Delta C_{\text{had}}$
5. – 8.	7.06	3.722	$^{+1.174}_{-0.790}$	$^{+0.429}_{-0.397}$	± 0.108	$^{+0.056}_{-0.062}$	1.10 ± 0.01
8. – 12.	9.72	6.637	$^{+0.023}_{-0.176}$	$^{+0.304}_{-0.366}$	± 0.407	$^{+0.075}_{-0.065}$	1.16 ± 0.03
12. – 16.	13.77	2.905	$^{+0.000}_{-0.067}$	$^{+0.145}_{-0.163}$	± 0.190	$^{+0.034}_{-0.031}$	1.04 ± 0.00
16. – 20.	17.83	1.420	$^{+0.000}_{-0.030}$	$^{+0.079}_{-0.083}$	± 0.096	$^{+0.018}_{-0.019}$	1.01 ± 0.01
20. – 24.	21.92	$7.071 \cdot 10^{-1}$	$(^{+0.000}_{-0.218}) \cdot 10^{-1}$	$(^{+0.426}_{-0.411}) \cdot 10^{-1}$	$(\pm 0.535) \cdot 10^{-1}$	$(^{+0.105}_{-0.107}) \cdot 10^{-1}$	1.00 ± 0.03
24. – 32.	27.28	$2.951 \cdot 10^{-1}$	$(^{+0.001}_{-0.118}) \cdot 10^{-1}$	$(^{+0.199}_{-0.175}) \cdot 10^{-1}$	$(\pm 0.214) \cdot 10^{-1}$	$(^{+0.051}_{-0.056}) \cdot 10^{-1}$	1.01 ± 0.03
32. – 50.	37.77	$5.730 \cdot 10^{-2}$	$(^{+0.098}_{-0.381}) \cdot 10^{-2}$	$(^{+0.464}_{-0.339}) \cdot 10^{-2}$	$(\pm 0.482) \cdot 10^{-2}$	$(^{+0.128}_{-0.173}) \cdot 10^{-2}$	1.01 ± 0.03
50. – 80.	57.65	$3.908 \cdot 10^{-3}$	$(^{+0.280}_{-0.609}) \cdot 10^{-3}$	$(^{+0.324}_{-0.162}) \cdot 10^{-3}$	$(\pm 0.441) \cdot 10^{-3}$	$(^{+0.094}_{-0.244}) \cdot 10^{-3}$	1.04 ± 0.03

Table 6.16: The QCD predictions for the differential dijet cross section as a function of $E_{TB}^{jet,1}$. Other details are as described in the caption to Table 6.12.

$\eta_B^{jet,1}$ range	$< \eta_B^{jet,1} >$	$d\sigma_{2+1}^{NLO}/d\eta_B^{jet,1}$ [pb]	Δ_{μ_r}	Δ_{α_s}	Δ_{pdf}^{exp}	Δ_{pdf}^{theo}	$C_{had} \pm \Delta C_{had}$
-1.0 – -0.5	-0.68	5.156	$^{+0.305}_{-0.294}$	$^{+0.335}_{-0.316}$	± 0.257	$^{+0.054}_{-0.046}$	1.47± 0.05
-0.5 – 0.0	-0.21	$1.972 \cdot 10^1$	$\left(^{+0.066}_{-0.086}\right) \cdot 10^1$	$\left(^{+0.115}_{-0.120}\right) \cdot 10^1$	$(\pm 0.109) \cdot 10^1$	$\left(^{+0.024}_{-0.022}\right) \cdot 10^1$	1.34± 0.05
0.0 – 0.5	0.26	$3.596 \cdot 10^1$	$\left(^{+0.126}_{-0.163}\right) \cdot 10^1$	$\left(^{+0.205}_{-0.222}\right) \cdot 10^1$	$(\pm 0.197) \cdot 10^1$	$\left(^{+0.046}_{-0.044}\right) \cdot 10^1$	1.11± 0.01
0.5 – 1.0	0.73	$3.136 \cdot 10^1$	$\left(^{+0.152}_{-0.168}\right) \cdot 10^1$	$\left(^{+0.194}_{-0.205}\right) \cdot 10^1$	$(\pm 0.171) \cdot 10^1$	$\left(^{+0.041}_{-0.041}\right) \cdot 10^1$	1.02± 0.02
1.0 – 1.5	1.22	$1.888 \cdot 10^1$	$\left(^{+0.144}_{-0.132}\right) \cdot 10^1$	$\left(^{+0.129}_{-0.134}\right) \cdot 10^1$	$(\pm 0.099) \cdot 10^1$	$\left(^{+0.025}_{-0.026}\right) \cdot 10^1$	0.99± 0.04
1.5 – 2.0	1.71	8.064	$^{+0.884}_{-0.724}$	$^{+0.596}_{-0.617}$	± 0.413	$^{+0.106}_{-0.112}$	1.00± 0.01
2.0 – 2.5	2.18	2.406	$^{+0.384}_{-0.287}$	$^{+0.197}_{-0.204}$	± 0.120	$^{+0.031}_{-0.033}$	1.08± 0.01

Table 6.17: The QCD predictions for the differential dijet cross section as a function of $\eta_B^{jet,1}$. Other details are as described in the caption to Table 6.12.

$E_{TB}^{jet,2}$ range [GeV]	$< E_{T,B}^{jet,2} >$	$d\sigma_{2+1}^{NLO}/dE_{T,B}^{jet,2}$ [pb/GeV]	Δ_{μ_r}	Δ_{α_s}	Δ_{pdf}^{exp}	Δ_{pdf}^{theo}	$C_{had} \pm \Delta C_{had}$
5. – 8.	7.10	3.623	$^{+1.148}_{-0.771}$	$^{+0.425}_{-0.390}$	± 0.109	$^{+0.056}_{-0.063}$	1.20± 0.02
8. – 12.	9.69	6.737	$^{+0.053}_{-0.196}$	$^{+0.315}_{-0.376}$	± 0.398	$^{+0.076}_{-0.066}$	1.13± 0.02
12. – 16.	13.75	2.877	$^{+0.000}_{-0.062}$	$^{+0.139}_{-0.159}$	± 0.185	$^{+0.033}_{-0.031}$	1.04± 0.01
16. – 20.	17.70	1.367	$^{+0.000}_{-0.033}$	$^{+0.071}_{-0.076}$	± 0.094	$^{+0.017}_{-0.016}$	1.02± 0.02
20. – 24.	21.70	$7.527 \cdot 10^{-1}$	$\left(^{+0.000}_{-0.154}\right) \cdot 10^{-1}$	$\left(^{+0.464}_{-0.455}\right) \cdot 10^{-1}$	$(\pm 0.527) \cdot 10^{-1}$	$\left(^{+0.106}_{-0.108}\right) \cdot 10^{-1}$	1.00± 0.03
24. – 32.	27.18	$3.020 \cdot 10^{-1}$	$\left(^{+0.000}_{-0.098}\right) \cdot 10^{-1}$	$\left(^{+0.210}_{-0.184}\right) \cdot 10^{-1}$	$(\pm 0.212) \cdot 10^{-1}$	$\left(^{+0.052}_{-0.057}\right) \cdot 10^{-1}$	0.99± 0.03
32. – 50.	37.71	$5.643 \cdot 10^{-2}$	$\left(^{+0.117}_{-0.410}\right) \cdot 10^{-2}$	$\left(^{+0.446}_{-0.327}\right) \cdot 10^{-2}$	$(\pm 0.476) \cdot 10^{-2}$	$\left(^{+0.125}_{-0.165}\right) \cdot 10^{-2}$	1.02± 0.03
50. – 80.	57.61	$3.867 \cdot 10^{-3}$	$\left(^{+0.288}_{-0.618}\right) \cdot 10^{-3}$	$\left(^{+0.315}_{-0.161}\right) \cdot 10^{-3}$	$(\pm 0.440) \cdot 10^{-3}$	$\left(^{+0.093}_{-0.225}\right) \cdot 10^{-3}$	0.97± 0.03

Table 6.18: The QCD predictions for the differential dijet cross section as a function of $E_{TB}^{jet,2}$. Other details are as described in the caption to Table 6.12.

$\eta_B^{jet,2}$ range	$< \eta_B^{jet,2} >$	$d\sigma_{2+1}^{NLO}/d\eta_B^{jet,2}$ [pb]	Δ_{μ_r}	Δ_{α_s}	Δ_{pdf}^{exp}	Δ_{pdf}^{theo}	$C_{had} \pm \Delta C_{had}$
-2.0 – -1.5	-1.69	4.973	$^{+0.354}_{-0.317}$	$^{+0.343}_{-0.309}$	± 0.264	$^{+0.054}_{-0.051}$	1.51 ± 0.05
-1.5 – -1.0	-1.20	$1.972 \cdot 10^1$	$(^{+0.151}_{-0.135}) \cdot 10^1$	$(^{+0.135}_{-0.133}) \cdot 10^1$	$(\pm 0.104) \cdot 10^1$	$(^{+0.024}_{-0.022}) \cdot 10^1$	1.40 ± 0.00
-1.0 – -0.5	-0.74	$4.169 \cdot 10^1$	$(^{+0.154}_{-0.194}) \cdot 10^1$	$(^{+0.234}_{-0.258}) \cdot 10^1$	$(\pm 0.238) \cdot 10^1$	$(^{+0.051}_{-0.048}) \cdot 10^1$	1.21 ± 0.03
-0.5 – 0.0	-0.28	$3.427 \cdot 10^1$	$(^{+0.132}_{-0.164}) \cdot 10^1$	$(^{+0.195}_{-0.216}) \cdot 10^1$	$(\pm 0.180) \cdot 10^1$	$(^{+0.044}_{-0.043}) \cdot 10^1$	0.99 ± 0.02
0.0 – 0.5	0.20	$1.558 \cdot 10^1$	$(^{+0.100}_{-0.099}) \cdot 10^1$	$(^{+0.109}_{-0.110}) \cdot 10^1$	$(\pm 0.077) \cdot 10^1$	$(^{+0.023}_{-0.024}) \cdot 10^1$	0.92 ± 0.01
0.5 – 1.0	0.69	4.185	$^{+0.459}_{-0.377}$	$^{+0.371}_{-0.342}$	± 0.209	$^{+0.071}_{-0.079}$	0.96 ± 0.00
1.0 – 1.5	1.19	$9.857 \cdot 10^{-1}$	$(^{+2.051}_{-1.459}) \cdot 10^{-1}$	$(^{+1.041}_{-0.945}) \cdot 10^{-1}$	$(\pm 0.454) \cdot 10^{-1}$	$(^{+0.170}_{-0.201}) \cdot 10^{-1}$	1.36 ± 0.03

Table 6.19: The QCD predictions for the differential dijet cross section as a function of $\eta_B^{jet,2}$. Other details are as described in the caption to Table 6.12.

Q^2 range [GeV^2]	$< Q^2 >$	$d\sigma_{tot}^{NLO}/dQ^2$ [pb/GeV^2]	Δ_{μ_r}	Δ_{α_s}	Δ_{pdf}^{exp}	Δ_{pdf}^{theo}
470. – 800.	599.	1.180	$^{+0.008}_{-0.011}$	$^{+0.002}_{-0.006}$	± 0.032	$^{+0.017}_{-0.014}$
800. – 1500.	1059.	$2.756 \cdot 10^{-1}$	$(^{+0.016}_{-0.021}) \cdot 10^{-1}$	$(^{+0.006}_{-0.012}) \cdot 10^{-1}$	$(\pm 0.067) \cdot 10^{-1}$	$(^{+0.034}_{-0.026}) \cdot 10^{-1}$
1500. – 2500.	1890.	$6.282 \cdot 10^{-2}$	$(^{+0.028}_{-0.036}) \cdot 10^{-2}$	$(^{+0.014}_{-0.015}) \cdot 10^{-2}$	$(\pm 0.146) \cdot 10^{-2}$	$(^{+0.064}_{-0.046}) \cdot 10^{-2}$
2500. – 5000.	3363.	$1.257 \cdot 10^{-2}$	$(^{+0.004}_{-0.005}) \cdot 10^{-2}$	$(^{+0.001}_{-0.000}) \cdot 10^{-2}$	$(\pm 0.030) \cdot 10^{-2}$	$(^{+0.009}_{-0.007}) \cdot 10^{-2}$
5000. – 20000.	7801.	$7.003 \cdot 10^{-4}$	$(^{+0.010}_{-0.012}) \cdot 10^{-4}$	$(^{+0.057}_{-0.035}) \cdot 10^{-4}$	$(\pm 0.188) \cdot 10^{-4}$	$(^{+0.003}_{-0.031}) \cdot 10^{-4}$

Table 6.20: The QCD predictions for the differential inclusive cross section as a function of Q^2. Other details are as described in the caption to Table 6.12.

Q^2 range [GeV^2]	$< Q^2 >$	$d\sigma^{NLO}_{2+1}/dQ^2$ [pb/GeV^2]	Δ_{μ_r}	Δ_{α_s}	$\Delta^{\exp}_{pdf}$	$\Delta^{\text{theo}}_{pdf}$	$C_{\text{had}} \pm \Delta C_{\text{had}}$
470. – 800.	604.	$8.985 \cdot 10^{-2}$	$\left(^{+0.583}_{-0.577}\right) \cdot 10^{-2}$	$\left(^{+0.539}_{-0.606}\right) \cdot 10^{-2}$	$(\pm 0.388) \cdot 10^{-2}$	$\left(^{+0.118}_{-0.121}\right) \cdot 10^{-2}$	1.11 ± 0.01
800. – 1500.	1071.	$2.597 \cdot 10^{-2}$	$\left(^{+0.128}_{-0.139}\right) \cdot 10^{-2}$	$\left(^{+0.167}_{-0.172}\right) \cdot 10^{-2}$	$(\pm 0.098) \cdot 10^{-2}$	$\left(^{+0.034}_{-0.031}\right) \cdot 10^{-2}$	1.09 ± 0.01
1500. – 2500.	1901.	$7.208 \cdot 10^{-3}$	$\left(^{+0.270}_{-0.324}\right) \cdot 10^{-3}$	$\left(^{+0.484}_{-0.460}\right) \cdot 10^{-3}$	$(\pm 0.263) \cdot 10^{-3}$	$\left(^{+0.095}_{-0.080}\right) \cdot 10^{-3}$	1.07 ± 0.01
2500. – 5000.	3420.	$1.734 \cdot 10^{-3}$	$\left(^{+0.051}_{-0.067}\right) \cdot 10^{-3}$	$\left(^{+0.114}_{-0.101}\right) \cdot 10^{-3}$	$(\pm 0.070) \cdot 10^{-3}$	$\left(^{+0.022}_{-0.019}\right) \cdot 10^{-3}$	1.05 ± 0.01
5000. – 20000.	8095.	$1.281 \cdot 10^{-4}$	$\left(^{+0.038}_{-0.046}\right) \cdot 10^{-4}$	$\left(^{+0.068}_{-0.057}\right) \cdot 10^{-4}$	$(\pm 0.055) \cdot 10^{-4}$	$\left(^{+0.008}_{-0.014}\right) \cdot 10^{-4}$	1.04 ± 0.01

Table 6.21: The QCD predictions for the differential dijet cross section as a function of Q^2. Other details are as described in the caption to Table 6.12.

Q^2 range [GeV^2]	$< Q^2 >$	R_{2+1}	Δ_{μ_r}	Δ_{α_s}	$\Delta^{\exp}_{pdf}$	$\Delta^{\text{theo}}_{pdf}$	$C_{\text{had}} \pm \Delta C_{\text{had}}$
470. – 800.	604.	$7.615 \cdot 10^{-2}$	$\left(^{+0.569}_{-0.538}\right) \cdot 10^{-2}$	$\left(^{+0.443}_{-0.475}\right) \cdot 10^{-2}$	$(\pm 0.122) \cdot 10^{-2}$	$\left(^{+0.000}_{-0.017}\right) \cdot 10^{-2}$	1.11 ± 0.01
800. – 1500.	1071.	$9.424 \cdot 10^{-2}$	$\left(^{+0.539}_{-0.556}\right) \cdot 10^{-2}$	$\left(^{+0.583}_{-0.586}\right) \cdot 10^{-2}$	$(\pm 0.122) \cdot 10^{-2}$	$\left(^{+0.007}_{-0.025}\right) \cdot 10^{-2}$	1.09 ± 0.01
1500. – 2500.	1901.	$1.148 \cdot 10^{-1}$	$\left(^{+0.050}_{-0.056}\right) \cdot 10^{-1}$	$\left(^{+0.074}_{-0.071}\right) \cdot 10^{-1}$	$(\pm 0.015) \cdot 10^{-1}$	$\left(^{+0.003}_{-0.004}\right) \cdot 10^{-1}$	1.07 ± 0.01
2500. – 5000.	3420.	$1.380 \cdot 10^{-1}$	$\left(^{+0.047}_{-0.058}\right) \cdot 10^{-1}$	$\left(^{+0.089}_{-0.081}\right) \cdot 10^{-1}$	$(\pm 0.022) \cdot 10^{-1}$	$\left(^{+0.007}_{-0.007}\right) \cdot 10^{-1}$	1.05 ± 0.01
5000. – 20000.	8095.	$1.829 \cdot 10^{-1}$	$\left(^{+0.057}_{-0.069}\right) \cdot 10^{-1}$	$\left(^{+0.106}_{-0.096}\right) \cdot 10^{-1}$	$(\pm 0.029) \cdot 10^{-1}$	$\left(^{+0.011}_{-0.012}\right) \cdot 10^{-1}$	1.04 ± 0.01

Table 6.22: The QCD predictions for the dijet fraction as a function of Q^2. Other details are as described in the caption to Table 6.12.

$\langle Q \rangle$ [GeV]	$\alpha_s(\langle Q \rangle)$	$\Delta\alpha_s^{\text{stat}}$	$\Delta\alpha_s^{\text{syst}}$	$\Delta\alpha_s^{\text{ES}}$	$\Delta\alpha_s^{\text{Th}}$
24.6	0.1436	0.0047	$+0.0032$ -0.0066	$+0.0045$ -0.0041	$+0.0105$ -0.0079
32.7	0.1396	0.0048	$+0.0019$ -0.0036	$+0.0034$ -0.0034	$+0.0078$ -0.0059
43.6	0.1306	0.0063	$+0.0041$ -0.0044	$+0.0023$ -0.0024	$+0.0054$ -0.0040
58.5	0.1276	0.0075	$+0.0027$ -0.0041	$+0.0019$ -0.0016	$+0.0046$ -0.0033
90.0	0.1149	0.0111	$+0.0056$ -0.0099	$+0.0009$ -0.0013	$+0.0037$ -0.0028

Table 6.23: The α_s values as determined from the QCD fit to the measured dijet fraction R_{2+1} as a function of Q. For each bin in Q^2, the mean value $\langle Q \rangle$, the extracted value of the strong coupling constant, $\alpha_s(\langle Q \rangle)$, the statistical uncertainty, $\Delta\alpha_s^{\text{stat}}$, the systematic uncertainty (not) associated with the energy scale of the jets, $\Delta\alpha_s^{\text{ES}}$ ($\Delta\alpha_s^{\text{syst}}$), and the total theoretical uncertainty, $\Delta\alpha_s^{\text{Th}}$, are given.

Chapter 7

Summary and outlook

7.1 Summary

In this dissertation we have presented measurements of exclusive differential dijet cross sections in neutral current deep inelastic e^+p scattering. The measurements, which were performed with the ZEUS detector at HERA, refer to a phase-space region carefully selected in order to minimize experimental uncertainties as well as the uncertainties associated to the pQCD predictions.

Next-to-leading-order QCD calculations give a good description of the shape and magnitude of the measurements. The observed agreement is a non-trivial test of NLO pQCD predictions and demonstrates the validity of the description of dijet production by the underlying QCD hard processes (up to $O(\alpha_s^2)$) at the $\approx 10\%$ level.

A comprehensive and detailed analysis of the uncertainties of the calculations has been carried out which in particular, for the first time, takes into account the statistical and correlated systematic uncertainties from each data set used in the determination of the proton PDFs.

A QCD fit of the measured dijet fraction as a function of Q^2, which consistently includes the dependence of the proton PDFs on the value of $\alpha_s(M_Z)$ assumed in the DGLAP equations, allowed both a precise determination of the strong coupling constant and a test of its energy-scale dependence.

The value of $\alpha_s(M_Z)$ as determined by fitting the measured dijet fraction with next-to-leading-order QCD calculations is:

$$\alpha_s(M_Z) = 0.1166 \pm 0.0019 \text{ (stat.)}^{+0.0024}_{-0.0033} \text{ (exp.)}^{+0.0057}_{-0.0044} \text{ (th.)}.$$

in good agreement with the PDG world average. The value of α_s has been determined as a function of $<Q>$; its behaviour is compatible with the running of α_s as predicted by QCD.

7.2 Outlook

The analysis presented in this thesis had to be performed in a rather limited region of the phase space. As discussed in chapter 3 in the low Q^2 region the NLO jet cross sections are affected by very large uncertainties, the largest being, by far, the one related to the residual dependence on the renormalisation scale. This large theoretical uncertainty affecting the NLO jet cross sections at low Q^2 have preclude presently the inclusion of the dijet cross section in any quantitative QCD analysis in this region.

This is a particular unfortune circumstance because in this region the jet cross sections if included in a global DGLAP analysis, in conjuction with the already very precise measurements of the inclusive DIS cross sections, could add valuable and complementary information on the parton distribution functions of the proton (on the gluon density in particular) and on the

strong coupling constant. These theoretical limitations are going to become more and more severe taking into account the large data samples that the H1 and ZEUS experiments will collect after the (presently underway) HERA upgrade program, that will improve significantly the statistical precision of the measured dijet cross sections and also, presumably (due to the possibility of performing better detector calibrations and simiulation studies), also the systematic uncertainties.

In order to fully exploit the information on QCD carried by the dijet cross sections measured at HERA it will be hence mandatory to extend the pQCD predictions to next-to-next-to leading order accuracy in the strong coupling constant.

Although this is a tremendous theoretical effort the last two years have witnessed a remarkable progress towards the achievement of this goal.

There are in conclusion good reasons to belief that the post-HERA upgrade QCD phenomenological analyses could be carried out within a complete NNLO calculational paradigm thus allowing the possibility to perform even more stringent test of QCD in the high-energy perturbative regime and further improve our understanding of the internal structure of the proton.

Bibliography

[1] ZEUS Collab., J. Breitweg et al., Phys. Lett. B 507 (2001) 70.

[2] D.J. Gross and F. Wilczek, Phys. Rev. Lett. 30 (1973) 1343; Phys. Rev. D 8 (1973) 3633;
H.D. Politzer, Phys. Rev. Lett. 30 (1973) 1346.

[3] D.R.T. Jones, Nucl. Phys. B 75 (1974) 531;
W.E. Caswell, Phys. Rev. Lett. 33 (1974) 244;
É.Sh. Egoryan and O.V. Tarasov, TMF 41 (1979) 26; TMP 41 (1979) 863.

[4] O.V. Tarasov, A.A. Vladimirov, and A.Yu. Zharkov, Phys. Lett. B 93 (1980) 429;
S.A. Larin and J.A.M. Vermaseren, Phys. Lett. B 303 (1993) 334.

[5] T. van Ritbergen, J.A.M. Vermaseren, and S.A. Larin, Phys. Lett. B 400 (1997) 379.

[6] C.G. Bollini and J.J. Giambiagi, Phys. Lett. B 40 (1972) 566;
G. 't Hooft and M. Veltman, Nucl. Phys. B 44 (1972) 189;
G. 't Hooft, Nucl. Phys. B 61 (1973) 455.

[7] W.A. Bardeen, A.J. Buras, D.W. Duke, and T. Muta, Phys. Rev. D 18 (1978) 3998.

[8] G. 't Hooft, Nucl. Phys. B 61 (1973) 455;
W.A. Bardeen, A.J. Buras, D.W. Duke, and T. Muta, Phys. Rev. D 18 (1978) 3998.

[9] W. Furmanski and R. Petronzio, Z. Phys. C 11 (1982) 293.

[10] K.G. Chetyrkin, B.A. Kniehl, and M. Steinhauser, Phys. Rev. Lett. 79 (1997) 2184.

[11] T. Appelquist and J. Carazzone, Phys. Rev. D 11 (1975) 2856.

[12] S. Weinberg, Phys. Lett. B 91 (1980) 51;
B.A. Ovrut and H.J. Schnitzer, Phys. Lett. B 100 (1981) 403.

[13] W. Wetzel, Nucl. Phys. B 196 (1982) 259;
W. Bernreuther and W. Wetzel, Nucl. Phys. B 197 (1982) 228;
W. Bernreuther, Ann. Phys. 151 (1983) 127; Z. Phys. C 20 (1983) 331.

[14] S.A. Larin, T. van Ritbergen and J.A.M. Vermaseren, Nucl. Phys. B 438 (1995) 278.

[15] K.G. Chetyrkin, B.A. Kniehl, and M. Steinhauser, Nucl. Phys. B 510 (1998) 61.

[16] See e.g. J.C. Collins, D.E. Soper and G. Sterman, in *Perturbative Quantum Chromodynamics*, edited by A.H. Mueller (World Scientific, Singapore, 1989), p. 1 and references therein.

[17] V.N. Gribov and L.N. Lipatov, Sov. J. Nucl. Phys. 15 (1972) 438;
L.N. Lipatov, Sov. J. Nucl. Phys. 20 (1975) 94;
Y.L. Dokshitzer, Sov. Phys. JETP 46 (1977) 641;
G. Altarelli and G. Parisi, Nucl. Phys. B 126 (1977) 298.

[18] E. G. Floratos, D. A. Ross and C. T. Sachrajda, Nucl. Phys. B 129 (1977) 66, E ibid. B139 (1978) 545, Nucl. Phys. B 152 (1979) 493;
A. Gonzalez-Arroyo, C. Lopez and F. J. Yndurain, JournalNucl. Phys. B1531979161;
A. Gonzalez-Arroyo and C. Lopez, Nucl. Phys. B 166 (1980) 429;
G. Curci, W. Furmanski and R. Petronzio, Nucl. Phys. B 175 (1980) 27;
W. Furmanski and R. Petronzio, Phys. Lett. B 97 (1980) 437;
E. G. Floratos, C. Kounnas and R. Lacaze, Nucl. Phys. B 192 (1981) 417.

[19] T. Kinoshita, J. Math. Phys. 3 (1962) 650;
T.D. Lee and M. Nauenberg, Phys. Rev. 133 B 133 (1964) 1549.

[20] D. Amati and G. Veneziano, Phys. Lett. B 83 (1979) 87;
A. Bassetto, M. Ciafaloni and G. Marchesini, Phys. Lett. B 83 (1979) 207;
G. Marchesini, L. Trentadue and G. Veneziano, Nucl. Phys. B 181 (1980) 335;
Ya. I. Azimov et al.,Phys. Lett. B 165 (1985) 147; Z. Phys. C 27 (1985) 65.

[21] S. Catani and M. H. Seymour, Nucl. Phys. B 485 (1997) 291 and Erratum B 510 (1997) 503.

[22] Particle Data Group, D.E. Groom et al., Eur. Phys. J. C 15 (2000) 1.

[23] S. Bethke, J. Phys. G26 (2000) R27.

[24] H1 Collaboration, C. Adloff et al., DESY 00-145 (2000) and DESY 00-181 (2000).

[25] R.P. Feynman, *"Photon-Hadron Interactions"*, Benjamin, N.Y. (1972);
K.H. Streng, T.F. Walsh and P.M. Zerwas, Z. Phys. C 2 (1979) 237.

[26] S. Catani et al., Nucl. Phys. B 406 (1993) 187.

[27] S.D. Ellis and D.E. Soper, Phys. Rev. D 48 (1993) 3160.

[28] B.R. Webber, J. Phys. G19 (1993) 1567.

[29] M. Wobisch and T. Wengler, hep-ph/9907280.

[30] E. Mirkes and D. Zeppenfeld, Phys. Lett. B 380 (1996) 205;
E. Mirkes, TTP-97-39 (hep-ph/9711224).

[31] S. Catani and M. H. Seymour, Nucl. Phys. B 485 (1997) 291.

[32] D. Graudenz, hep-ph/9710244.

[33] B. Pötter, Comp. Phys. Comm. 119 (1999) 45.

[34] C. Duprel et al., hep-ph/9910448.

[35] M. Klasen and G. Kramer, Phys. Lett. B 366 (1996) 385;
S. Frixione and G. Ridolfi, Nucl. Phys. B 507 (1997) 315;
B. Pötter, hep-ph/9911221.

[36] M. Glück, E. Reya, and A. Vogt, Z. Phys. C67 (1995) 433.

[37] A.D. Martin, R.G. Roberts, and W.J. Stirling, Int. J. Mod. Phys. A10 (1995) 2885.

[38] A.D. Martin, R.G. Roberts, W.J. Stirling, and R.S. Thorne, Eur. Phys. J. C4 (1998) 463.

[39] H.L. Lai et al., Phys. Rev. D51 (1995) 4763.

[40] H.L. Lai et al., Phys. Rev. D55 (1997) 1280.

[41] M. Botje, Eur. Phys. J. C 14 (2000) 285.

[42] M. Botje, 'Fast access to parton densitie, errors and correlations. EPDFLIB Version 1.0' ZEUS 99-048

[43] ZEUS Collab., M. Derrick et al., Z. Phys. C72 (1996) 399.

[44] H1 Collab., S. Aid et al., Nucl. Phys. B470 (1996) 3.

[45] E665 Collab., M.R. Adams et al., Phys. Rev. D54 (1996) 3006.

[46] NMC, M. Arneodo et al., Nucl. Phys. B483 (1997) 3.

[47] BCDMS Collab., A.C. Benvenuti et al., Phys. Lett. B223 (1989) 485 and Phys. Lett. B237 (1990) 592.

[48] SLAC, L.W. Whitlow et al., Phys. Lett. B282 (1992) 475.

[49] NMC, M. Arneodo et al., Nucl. Phys. B487 (1997) 3.

[50] CCFR Collab., W. Seligman et al., Phys. Rev. Lett 79 (1997) 1213.

[51] E866 Collab., E.A. Hawker et al., Phys. Rev. Lett. 80 (1998) 3715.

[52] K.J. Eskola, V.J. Kolhinen and C.A. Salgado, JYFL-8/98, US-FT/14-98, hep-ph/9807297; K.J. Eskola, V.J. Kolhinen and P.V. Ruuskanen, Nucl. Phys. 535 (1998) 351.

[53] J. Gomez et al., Phys. Rev. D49 (1994) 4348.

[54] M. Virchaux and A. Milsztajn, Phys. Lett. B274 (1992) 221.

[55] H. Georgi and D. Politzer, Phys. Rev. D14 (1976) 1829.

[56] R.M. Barnett, Phys. Rev. Lett. 36 (1976) 1163.

[57] W. Seligman, Ph.D. Thesis (Columbia University), Nevis Report 292 (1997).

[58] G. Gurci, W. Furmanski and R. Petronzio, Nucl. Phys. B175 (1980) 27; W. Furmanski and R. Petronzio, Phys. Lett. 97B (1980) 437 and Z. Phys. C11 (1982) 293.

[59] A.D Martin, W.J. Stirling and R.G. Roberts, Phys. Rev. D50 (1994) 6734.

[60] ZEUS Collab., M. Derrick et al., Phys. Lett. B354 (1995) 576.

[61] ZEUS Collab., J. Breitweg et al., Eur. Phys. J. C7 (1999) 609.

[62] S. Riemersma et al., Phys. Lett. B347 (1995) 143 and references therein.

[63] Particle Data Group, S. Caso et al., Eur. Phys. J. C3 (1998) 1.

[64] CCFR Collab., A.O. Bazarko et al., Z. Phys. C65 (1995) 189.

[65] M. Botje, QCDNUM version 16.12, ZEUS 97-066.

[66] F. James, Minuit Version 94.1, CERN Program Library Long Writeup D506.

[67] U.K. Yang and A. Bodek, Phys. Rev. Lett. 82 (1999) 2467.

[68] See e.g. S. Catani, in Proceedings of the 17th Workshop of the INFN Eloisatron Project, QCD at 200 TeV, Erice, Italy, 1991. Report N. CERN-TH. 6281/91, 1991 (unpublished).

[69] P.M. Stevenson, Phys. Rev. D23 (1981) 2916.

[70] G. Grunberg, Phys. Rev. D29 (1984) 2315.

[71] S.J. Brodsky, G.P. Lepage, P.B. Mackenziee, Phys. Rev. D28 (1983) 228.

[72] DELPHI Collaboration, P. Abreu et al., hep-ex/0002026

[73] M. Botje, 'QCD fits to ZEUS and fixed target F_2 data', ZEUS 98-062.

[74] C. Pascaud and F. Zomer, preprint LAL 95-05.

[75] A.D. Martin, R.G. Roberts, W.J. Stirling and R.S. Thorne, Phys. Lett. B443 (1998) 301.

[76] CTEQ Collab., H.L. Lai et al., hep-ph/9903282 (1999).

[77] G. Altarelli and G. Martinelli, Phys. Lett. B76 (1978) 89.

[78] E. Zijlstra and W.L. van Neerven, Nucl. Phys. B383 (1992) 525.

[79] NMC, A. Amaudruz et al., Nucl. Phys. B441 (1995) 3; M. Arneodo et al., Nucl. Phys. B441 (1995) 12.

[80] I. Redondo, presented at the DIS99 Workshop, Zeuthen, Germany, April 19–23, 1999.

[81] G. Ingelman et al., Proc. HERA Workshop, ed. R.D. Peccei, Hamburg (1987) p.3;
J. Blümlein et al., *ibid.* p.67;
D. Roberts, 'The Structure of the Proton', Cambridge University Press (1990).

[82] ZEUS Collab., S. Chekanov et al., DESY-01-064, submitted to The European Physical Journal.

[83] K. Gottfried and V. Weisskopf, 'Concepts of Particle Physics', Oxford University Press, 1984, Vol. 1 p.137.

[84] U. Katz, 'Deep-Inelastic Positron-Proton Scattering in the High Momentum-Transfer Regime of HERA', to appear in Springer Tracts in Modern Physics (1999).

[85] A. Arbuzov et al., 'HECTOR 1.00', Comput. Phys. Commun. 94 (1996) 128.

[86] M. Botje, 'ZPDFLIB: Access to the ZEUS NLO QCD fit results', ZEUS-Note 98-063.

[87] ZEUS Coll., The ZEUS Detector, Technical Proposal 1986.

[88] ZEUS Coll., The ZEUS Detector, Status Report 1993.

[89] B. Foster et al., Nucl. Instr. and Meth. A 338 (1994) 254.

[90] M. Derrick et al., Nucl. Instr. and Meth. A 309 (1991) 77.

[91] H. Bethe and W. Heitler, Proc. Roy. Soc. A146 (1934) 83.

[92] K. Piotrzkowski, Dissertation, DESY F35D-93-06.

[93] C. Youngman, The ZEUS Data Acquisition System, DESY 92-150A.

[94] W. H. Smith et al., ZEUS-Note 89-084.

[95] H. Uijterwaal, Ph.D. Thesis, University of Amsterdam 1992.

[96] U. Behrens et al., Nucl. Instr. and Meth. A 336 (1993) 23

[97] K. Kwiatkowski, H. Spiesberger and H.-J. Möhring, Comp. Phys. Comm. 69 (1992) 155.

[98] K. Charchuła, G.A. Schuler, and H. Spiesberger, Comp. Phys. Comm. 81 (1994) 381.

[99] Y. Azimov et al., Phys. Lett. B 165 (1985) 147;
      G. Gustafson, Phys. Lett. B 175 (1986) 453;
      G. Gustafson and U. Petersson, Nucl. Phys. B 306 (1988) 746;
      B. Andersson, G. Gustafson and L. Lönnblad, Z. Phys. C 43 (1989) 625.

[100] L. Lönnblad, in *Proc. Workshop on Monte Carlo Generators for HERA Physics, Apr. 1998*, eds. A.T. Doyle, G. Grindhammer, G. Ingelman and H. Jung, p. 47, Hamburg, Germany, DESY (1999) and hep-ph/9908368.

[101] L. Lönnblad, Comp. Phys. Comm. 71 (1992) 15; Z. Phys. C 65 (1995) 285.

[102] G. Ingelman, A. Edin and J. Rathsman, Comp. Phys. Comm. 101 (1997) 108.

[103] B. Andersson et al., Phys. Rep. 97 (1983) 31.

[104] H.-U. Bengtsson and T. Sjöstrand, Comp. Phys. Comm. 46 (1987) 43;
      T. Sjöstrand, Comp. Phys. Comm. 82 (1994) 74.

[105] G. Marchesini et al., Comp. Phys. Comm. 67 (1992) 465.

[106] B.R. Webber, Nucl. Phys. B 238 (1984) 492.

[107] R. Brun et al., CERN-DD/EE/84-1 (1987).

[108] ZEUS Collaboration, J. Breitweg et al., Eur. Phys. J. C 11 (1999) 427.

[109] J. Edmonds, J. Grosse-Knetter and A. Quadt, ZEUS-Note 99-016.

[110] R. Sinkus, Nucl. Instr. and Meth. A 361 (1995) 290.

[111] L. L. Wai, Ph. D. Thesis, Columbia University (1995).

[112] J. Groesse-Knetter, ZEUS-Note 98-031.

[113] ZEUS Collab., J. Breitweg et al., Eur. Phys. J. C 8 (1999) 367.

[114] S. Bentvelsen, J. Engelen, and P. Kooijman, in *Proc. Workshop on Physics at HERA, Oct. 1991*, Volume 1, W. Buchmüller and G. Ingelman (eds.), DESY (1992), p. 23;
      K. C. Hoeger, *ibid.*, p. 43.